# Causal discovery of Atlantic-Pacific interactions in observations and CMIP6 models

Doctoral Dissertation of
Soufiane Karmouche


**January 2024**

# Causal discovery of Atlantic-Pacific interactions in observations and CMIP6 models

Am Institut für Umweltphysik
vom Fachbereich für Physik und Elektrotechnik
der Universität Bremen

*zur Erlangung des akademisches Grades*
**Doktor der Naturwissenschaften (Dr. rer. nat.)**
*genehmigte Dissertation*

von

Soufiane Karmouche

| | |
|---|---|
| Erste Gutachterin: | Prof. Dr. Veronika Eyring |
| Zweiter Gutachter: | Prof. Dr. Thomas Jung |
| Eingereicht am: | 4. Oktober 2023 |
| Tag des Promotionskolloquiums: | 26. Januar 2024 |

# Abstract

In a world of rapid climate change, a deeper comprehension of the Earth's climate system is central to accurate climate projections. In this regard, understanding the dynamics governing the climate system is important. The changing climate processes are influenced by a variety of factors including both natural and anthropogenic forcings, which modulate the interactions between major modes of climate variability. These interactions, particularly the teleconnections between the Atlantic and Pacific oceans, have a profound impact on global and regional climate patterns, necessitating a detailed exploration to grasp the complex networks of interrelated impacts. In this thesis, causal discovery approaches are applied to unravel the causal relationships for these interactions, aiming to enhance the understanding of the processes governing the climate system.

The first part of this Ph.D. thesis delves into this complex system by applying an algorithm for causal discovery to analyze observational and reanalysis datasets, in addition to large ensemble simulations from a collection of models participating in the sixth phase of the Coupled Model Intercomparison Project (CMIP). Dependent on the phases of the Pacific Decadal Variability (PDV) and the Atlantic Multidecadal Variability (AMV), different regimes with characteristic causal relationships (fingerprints) are identified in observations (and reanalyses) as well as in CMIP6. A regime-oriented causal model evaluation is then performed to assess the capability of CMIP6 models in representing observed changing interactions between PDV, AMV, and their extratropical teleconnections. Causal networks from observations show both opposite-sign and same-sign responses between AMV and PDV under specific conditions. Historical CMIP6 simulations exhibit varying skill in simulating the observed causal patterns but overall perform better when PDV and AMV are out of phase. Additionally, the two largest ensembles, (in terms of number of realizations) were found to contain realizations with most similar causal fingerprints to observations. For most regimes, these same models also showed higher network similarity when compared to each other.

In the second part of this thesis, the focus is on examining the tropical and extra-tropical routes connecting Pacific and Atlantic modes of variability on seasonal to interannual timescales. Following up on recent studies, this analysis characterizes two distinctive phases: the Pacific-driven regime (1950-1983) and the Atlantic-driven regime (1985-2014), spotlighting the varying role of El Niño-Southern Oscillation (ENSO) in shaping sea surface temperature variability in the tropical Atlantic. Guided by the results of the first study, the use of large ensemble simulations in this second study intends to separate the contributions of external forcings from natural internal variability. A comparative analysis examines results from observations (and reanalysis) in contrast to those from Pacific pacemaker simulations, unveiling effects

of anthropogenic external forcing, especially in the most recent decades. Specifically, the 1985-2014 results suggest that human-induced anomalous tropical north Atlantic warming greatly contributed to La Niña-like cooling over the tropical Pacific through the strengthening of the Pacific Walker circulation. On the other hand, the causal analysis of the pre-industrial control run emphasizes the importance of natural internal variability on decadal timescales in modulating the interplay between interannual climate variability modes over the two basins. Generally, the results presented in this thesis demonstrate the large potential of causal discovery for process-oriented model evaluation that can substantially enhance our understanding of climate variability and provide robust diagnostics for refining climate models. Furthermore, this thesis underscores the role of the intricate interplay between natural variability and external forcings in shaping climate patterns, and advocates for further research to precisely attribute the observed changes in the climate system. The insights gained are hence significant for formulating more accurate and informed climate projections as well as adaptation and mitigation strategies.

# Integrated Author's References

Parts of this thesis (text, figures, and tables) are already published in peer-reviewed studies.

## Publications as first author

**Karmouche**, **S.**, Galytska, E., Runge, J., Meehl, G. A., Phillips, A. S., Weigel, K., & Eyring, V. (2023a). Regime-oriented causal model evaluation of Atlantic–Pacific teleconnections in CMIP6. *Earth System Dynamics*, *14*(2), 309–344. https://doi.org/10.5194/esd-14-309-2023

**Karmouche**, **S.**, Galytska, E., Meehl, G. A., Runge, J., Weigel, K., & Eyring, V. (2023b). Changing effects of external forcing on Atlantic-Pacific interactions. *EGUsphere*, *2023*, 1–36. https://doi.org/10.5194/egusphere-2023-1861

## Contributions to IPCC Assessment Report 6

I also had the honor of being an acknowledged graphic developer for Chapter 3 (Eyring et al. 2021a) of the latest Intergovernmental Panel on Climate Change (IPCC) Sixth Assessment Report (IPCC 2021b).

Eyring, V., Gillett, N., Achuta Rao, K., Barimalala, R., Barreiro Parrillo, M., Bellouin, N., Cassou, C., Durack, P., Kosaka, Y., McGregor, S., Min, S., Morgenstern, O., & Sun, Y. (2021a). Human Influence on the Climate System. In V. Masson-Delmotte, P. Zhai, A. Pirani, S. Connors, C. Péan, S. Berger, N. Caud, Y. Chen, L. Goldfarb, M. Gomis, M. Huang, K. Leitzell, E. Lonnoy, J. Matthews, T. Maycock, T. Waterfield, O. Yelekçi, R. Yu, & B. Zhou (Eds.), *Climate Change 2021: The Physical Science Basis. Contribution of Working Group I to the Sixth Assessment Report of the Intergovernmental Panel on Climate Change* (pp. 423–552). Cambridge University Press. https://doi.org/10.1017/9781009157896.005

# Contents

# 1. Introduction

## 1.1. Motivation

Climate change is a pressing reality with profound implications for both human societies and the natural world. While the impact of anthropogenic climate change is well-recognized, it is equally crucial to understand the role of natural climate variability, driven by internal mechanisms within the Earth system. Modes of natural climate variability, such as El Niño-Southern Oscillation (ENSO), the Pacific Decadal Variability (PDV), and the Atlantic Multidecadal Variability (AMV), are integral components of the Earth's climate system. These modes can induce shifts in weather patterns, ocean currents, and atmospheric circulation, causing significant climatic impacts at both regional and global scales. In terms of statistical properties, climate models have shown tremendous improvements in simulating internal variability throughout the different phases of the Coupled Model Intercomparison Project (CMIP). However, accurately evaluating their ability to do so remains a formidable challenge (Eyring et al. 2019). The limited duration and uncertainties associated with observational datasets, particularly pre-satellite era records affected by data errors (Eyring et al. 2021b; Fasullo et al. 2020; Phillips et al. 2014), further complicate the assessment process. While climate models are often compared to reanalysis datasets to gauge their capacity to reproduce internal variability, this approach can still reveal systematic errors (**Karmouche** et al. 2023a). One of the central parts of this thesis focuses on analyzing modes of internal variability and how the interactions between them changed over the observed historical record. This is crucial to qualitatively assess the ability of climate models to reproduce the observed teleconnections during specific time periods and to enhance understanding of the underlying processes. Nonetheless, distinguishing the effects of internal climate variability from external forcings and quantifying their respective impacts presents a significant challenge. External forcings encompass changes to the climate system caused by natural factors such as volcanic eruptions, solar radiation, as well as human-induced emissions of greenhouse gases (GHGs) and aerosols. On the other hand, internal climate variability refers to inherent fluctuations resulting from complex interactions among the atmosphere, oceans, land, and cryosphere (IPCC 2021a). This dissertation is motivated by the necessity to address the complex effects of a changing climate on interactions between different modes of climate variability while isolating internal variability from external forcing. It also aims to advance climate model evaluation beyond conventional spatial and spectral properties and utilize novel causal discovery methods to examine whether these models accurately simulate the observed regime-dependent lagged teleconnections between geographically distant regions. By analyzing causal relationships derived from time series data, the thesis

assesses the models' capacity to capture unique dynamical dependencies within the climate system and determine whether specific phenomena are faithfully represented. Furthermore, the thesis aims to investigate the impact of a changing climate on these teleconnections and interactions. By scrutinizing the influence of external forcing and considering the varying states of the climate system under different regimes of long-term internal variability, this work seeks to deepen our understanding of how these teleconnections may evolve under changing climatic conditions.

## 1.2. Objective of the thesis

The primary objective of this Ph.D. thesis is to advance the understanding of the Earth's climate system by utilizing novel causal discovery approaches in combination with a variety of reanalysis datasets and large ensemble simulations from the CMIP phase 6 (CMIP6, Eyring et al. 2016). The thesis aims to investigate and evaluate the complex interactions between major modes of climate variability, focusing on the teleconnections between the Atlantic and Pacific oceans. In particular, the thesis provides insights into the driving mechanisms between modes of variability over the two basins and their phase-dependent causal relationships and identifies particular regimes with distinctive causal fingerprints. Additionally, the research seeks to explore the influence of a changing climate on these interactions, specifically considering the effects of external forcing and different regimes of long-term internal variability. By integrating these research dimensions, the thesis aspires to provide a deeper understanding of the climate system and enhance climate model evaluation, ultimately contributing to more accurate climate change projections.

## 1.3. Structure of the Thesis

Note that the results of this thesis are based on two publications: Chapter 4 and Section 3.5.3 are published in **Karmouche** et al. 2023a, while Section 3.5.2 and Chapter 5 are part of the recently submitted article (**Karmouche** et al. 2023b) to the same peer-reviewed journal *(Earth System Dynamics)*. These papers are two studies where the author of this thesis was the first author. He designed and organized the study, led the interpretation of the results and the writing of the paper, performed all data processing and analysis, and prepared all figures and tables. Throughout this thesis, when presenting material from these studies, the pronoun "we" is often used. This choice is made to enhance readability by reducing the use of passive voice and to acknowledge all contributors who were involved in these studies (Chapters 4 and 5, Sections 3.5.2 and 3.5.3, and Appendices A and B). However, all the content, including text, figures, and tables, and supplementary material derived from these papers (**Karmouche** et al. 2023a; **Karmouche** et al. 2023b), and thus included in this thesis, is the work of the author of the thesis. For a detailed breakdown of the author's contributions to these studies, please refer to the corresponding chapters.

This thesis is organized to facilitate a detailed, yet accessible examination of Atlantic-Pacific interactions within the climate system. Here is a breakdown of the structure: Following this section, Chapter 2 presents a scientific background offering a substantive exploration of the climate system and its variability. The initial section explores the fundamental principles of atmospheric and ocean circulation in addition to an introduction to Earth system modeling (Sections 2.1.1–2.1.2), before delving into ocean-atmosphere interactions (Section 2.1.3). The latter portion discusses climate variability, elaborating on its main modes and exploring teleconnections with a focus on Atlantic-Pacific interactions (Section 2.2.1). Chapter 3 is dedicated to outlining the methodological approach and the data sources consulted in the research. This includes general introductions to CMIP6 (Section 3.1), reanalysis and observational datasets (Section 3.2), empirical orthogonal function (EOFs) in Section 3.3, a tool for climate variability diagnostics (Section 3.4), and the causal discovery scheme in Section 3.5. The latter section also presents a proof of concept for the causal discovery method to be utilized in the following chapters (Section 3.5.2). Section 3.5.3 presents the metric used for comparing networks in the causal model model evaluation in the next chapter. In Chapter 4, the focus narrows down to a detailed analysis of decadal Atlantic-Pacific interactions within the context of CMIP6. It outlines the methodologies and data employed (Section 4.1), presents the results of the regime-oriented causal model evaluation (Section 4.2), and culminates in a discussion and summary, articulating the implications of the findings (Sections 4.3–4.4). Moving on to Chapter 5, the analysis extends to examine the evolving impacts of external forces on the Atlantic-Pacific interactions on the seasonal to interannual timescale. This chapter outlines the data and methodologies employed Section 5.1, explores the findings from various analyses (Section 5.2), specifically from observations Section 5.2.1, pacemaker simulations Section 5.2.2 and pre-industrial control run (Section 5.2.3, and ends with a discussion and conclusion that integrates the insights derived from the study (Section 5.3). Finally, Chapter 6 concludes with a summary encapsulating the most important findings from the preceding chapters (Section 6.1), and projects potential pathways for future research in the field in an "Outlook" section (Section 6.2).

# 2. Scientific Background

## 2.1. The Climate System

While our comprehension of weather and climate often centers on parameters such as mean temperature, wind speed, humidity, cloud coverage, and solar radiation, the climate system's complexity surpasses these elementary variables. The climate encompasses intricate interactions between the atmosphere, ocean currents, land masses, and other factors such as albedo, vegetation, and solar irradiance. To grasp Earth's climate and predict alterations induced by human activities, a comprehensive consideration of these interconnected components and their associated processes within the climate system is essential. In a broader context, the term "climate" includes both the statistical variations of the climate system as well as its overall condition, encapsulating a comprehensive understanding of prevailing weather conditions, including not only average states but also seasonal fluctuations and the potential for extreme events. The World Meteorological Organization (WMO) recommends a 30-year timeframe for defining climate statistically. However, when examining distant epochs like the last glacial maximum, longer time scales are necessary. It's important to recognize that despite the possibility of rapid climate changes, substantial durations are imperative to discern disparities between different eras (Goosse 2015). A broader perspective is emerging in the realm of climate definition, which entails a statistical depiction of the entire climate system. This entails the scrutiny of five crucial components: the atmosphere, hydrosphere, cryosphere, land surface, and biosphere (Goosse 2015). The interactions among the mentioned components encompass a range of physical, chemical, and biological processes, contributing to the complex nature of the climate system. Notably, investigating the intricate interplay between the ocean and the atmosphere is crucial, as it profoundly influences weather patterns and shapes climate dynamics at both regional and global scales. The exchange of heat, moisture, and energy between these two components serves as a pivotal driver of atmospheric circulation patterns, subsequently influencing the distribution of temperature and precipitation across diverse regions. The different components of the climate system are influenced by external forces, with the most significant one being the Sun. Some of the radiative energy provided by the Sun is in the form of 'shortwave' radiation and is either reflected back to space by clouds, aerosols, or the surface, or absorbed in the atmosphere or at the land or ocean surface where it is converted to heat and re-radiated in the form of infra-red or 'longwave' radiation. The difference between the incoming and outgoing radiation is called the radiative imbalance (Masson-Delmotte et al. 2021). Solar energy is not supplied uniformly due to the Earth's spherical shape, resulting in varying energy input near the equator and poles. The daily cycle due to Earth's rotation and

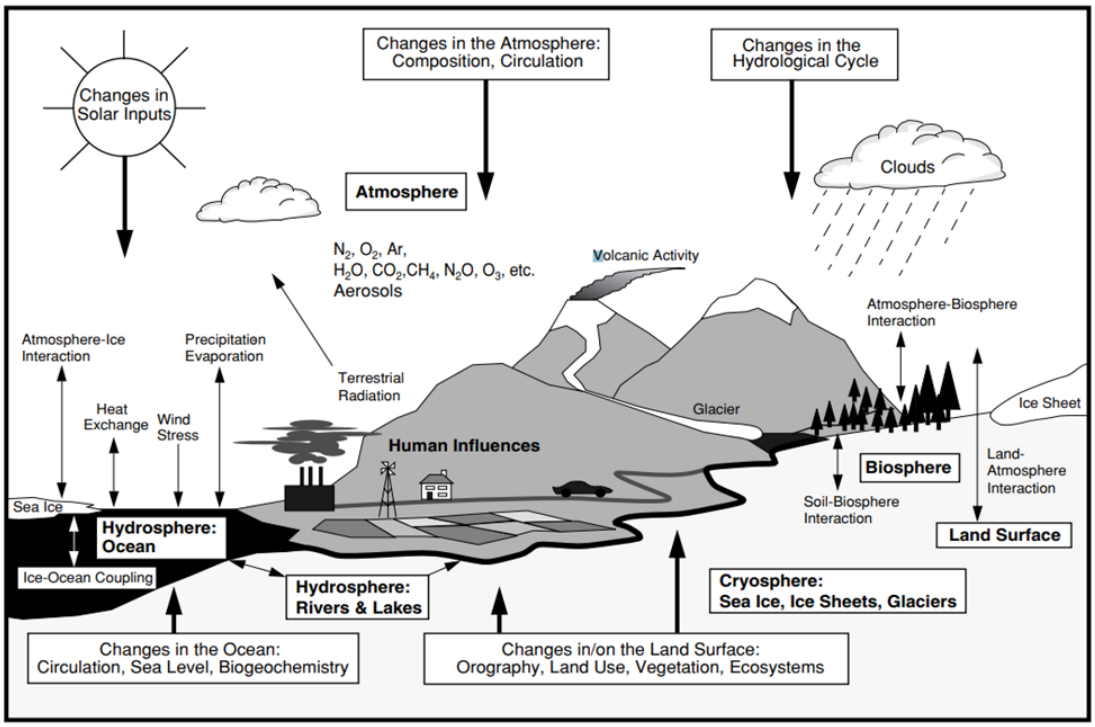


**Figure 2.1.:** A schematic view of the major components of the global climate system (highlighted in bold), illustrating their processes and interactions (indicated by thin arrows). It also highlights certain aspects that could undergo changes (shown by bold arrows). Figure from (Houghton et al. 2001)

the seasonal changes due to Earth's orbit around the sun add temporal variations to the solar energy received by the Earth. This solar heating imbalance drives large-scale atmospheric circulation, winds, and heat transport (Flato et al. 2013). The interactions continue with evaporation from land and oceans providing water vapor to the atmosphere, which condenses to form clouds altering solar radiation absorption and reflection. Condensed water vapor falls as precipitation, changing surface reflectivity and moisture content, thus contributing to climate variability (Flato et al. 2013). Human activities also have a direct impact on the climate system and are considered external forcing. Figure 2.1, from the Intergovernmental Panel on Climate Change (IPCC) Third Assessment Report (Houghton et al. 2001), illustrates a schematic view of the key components of the global climate system along with their processes and interactions and identifies specific aspects that have the potential to change. This visualization provides an overview of the complex dynamics within the climate system and has long served as a simplistic reference for understanding its interconnections.

**The atmosphere** is the most dynamic part of the system and contains various gases. While gases like nitrogen ($N_2$), oxygen ($O_2$), and argon (Ar) have limited interaction with solar and infrared radiation, GHGs such as carbon dioxide ($CO_2$), methane ($CH_4$), nitrous oxide ($N_2O$), and ozone ($O_3$) play a crucial role in the Earth's energy budget by absorbing and emitting infrared radiation. Water vapor ($H_2O$), another GHG, also contributes significantly to the climate system as it absorbs both infrared and solar short-wave radiation (Bridgman and Oliver 2006).

**The hydrosphere** includes all liquid water bodies on Earth, both fresh and saline. Over 70% of the Earth's surface is made up of oceans, which are essential for storing and transmitting energy as well as storing and dissolving enormous amounts of $CO_2$. The slower circulation of the oceans, driven by wind and density contrasts, acts as a regulator of the Earth's climate and contributes to natural climate variability. Ocean sea water density exhibits dependence on both salinity and pressure, with density rising as both parameters increase, and decreases with increasing temperature. In a simplified perspective, temperature influences density shifts at higher temperatures, whereas salinity plays a more substantial role at lower temperatures. The strong connection between the ocean and the overlying atmospheric layer plays a major role in different climate phenomena, encompassing weather patterns, heat exchange, and the modulation of Earth's energy budget (Goosse 2015).
**The cryosphere**, encompassing ice sheets, glaciers, sea ice, and permafrost, reflects solar radiation and plays a critical role in driving deep ocean water circulation. Changes in the volume of ice sheets can potentially lead to sea level variations (Bridgman and Oliver 2006).
**The land**, including vegetation and soils, influences how energy from the Sun is returned to the atmosphere. Vegetation absorbs $CO_2$ through photosynthesis, making it essential in the carbon cycle and affecting atmospheric chemistry and aerosol formation, which impact climate. **The biospheres**, marine and terrestrial, influence the atmosphere's composition through their uptake and release of GHGs. They play a central role in the carbon cycle and affect the budgets of various gases. Fossils, tree rings, and other biotic indicators from Earth's biosphere provide valuable information about past climates (Gettelman and Rood 2016).

The interactions between these components above result in the exchange of mass, energy, and momentum, leading to fluctuations in climate variables, including temperature, sea level pressure (SLP), and precipitation.

### 2.1.1. Primitive equations for atmospheric and ocean circulation

Based on fundamental concepts of fluid dynamics, the primitive equations are a collection of equations that describe the motion of a fluid, e.g. air in the atmosphere or water in the ocean. Modeling and simulating atmospheric and oceanic phenomena including weather patterns and climate dynamics are done using such equations. This section follows explanations from Wallace and Hobbs 2006a who explore how the dynamic processes described by the primitive equations of atmospheric motion influence the initial stages of an atmospheric model simulation. The atmosphere's vertical structure is characterized by hydrostatic equilibrium. Equatorial regions, heated intensely by the Sun, experience the ascent of less dense air, which subsequently moves poleward at higher altitudes. The Earth's rotation adds complexity to atmospheric circulation. The formation of Hadley cells, driven by air ascending at the equator and descending at approximately 30° latitude, illustrates this complexity. This phenomenon contributes to the establishment of the Intertropical Convergence Zone (ITCZ), a prominent atmospheric feature. The ITCZ is characterized by the convergence of ascending winds illustrated through a band of clouds and thunderstorms that form near the equator, where

the trade winds meet and rise. The rising air creates a low-pressure zone that attracts more wind from the subtropics. The ITCZ also shifts seasonally, following the sun's position and the thermal equator. This band of ascending motion, typically positioned around 5°N, plays a significant role in affecting wind patterns and precipitation distribution in tropical regions. The Coriolis force, due to Earth's rotation causes the deflection of surface winds and gives rise to unique wind patterns not only near the equator. The Ferrell cell, a weaker circulation compared to the Hadley cell, governs the mid-latitude atmospheric flow. Beyond the equatorial region and the surface boundary layer, geostrophic equilibrium plays a crucial role in shaping atmospheric circulation patterns. This equilibrium explains clockwise wind rotations around high-pressure systems and counterclockwise rotations around low-pressure systems in the Northern Hemisphere (and vice versa in the Southern Hemisphere). By capturing the underlying physical principles governing the motion of air masses, temperature variations, and pressure gradients, the primitive equations enable us to study the complex behaviors of the atmosphere. The comprehensive derivations of these equations are shown in textbooks (e.g. Holton and Hakim 2012; Vallis 2017; Wallace and Hobbs 2006a). In a simplified form, the primitive equations consist of:

**The horizontal equation of motion**: represents the rate of change in the velocity vector $\mathbf{V}$ of a fluid element with respect to time ($\frac{d\mathbf{V}}{dt}$). It describes its motion in a gravitational field considering several forces acting on it, including the pressure gradient force and the Coriolis force. Considering the horizontal wind field is defined on constant pressure surfaces, Equation (2.1) can be written as:

$$\frac{d\mathbf{V}}{dt} = -\nabla\Phi - f\mathbf{k} \times \mathbf{V} + \mathbf{F} \tag{2.1}$$

where $\frac{d\mathbf{V}}{dt}$ is the Lagrangian time derivative of the horizontal velocity component of a moving air parcel. Using the hydrostatic equation (Wallace and Hobbs 2006a), the pressure gradient force can be represented by the term $-\nabla\Phi$ where $\Phi$ is the gravitational potential. The second term on the right-hand side, $f\mathbf{k} \times \mathbf{V}$, is the Coriolis force where $f$ is the Coriolis parameter and $\mathbf{k}$ is the local vertical unit vector, defined as positive upward. The third term, $\mathbf{F}$, denotes any external forces acting on the fluid (e.g. frictional forces).

**The hypsometric equation**: is a mathematical relationship between the change in geopotential height ($\Phi$) with respect to atmospheric pressure ($p$). Equation (2.2) is given by:

$$\frac{\partial\Phi}{\partial p} = \frac{-RT}{p} \tag{2.2}$$

here, $R$ represents the gas constant for dry air, and $T$ signifies the air temperature. The equation indicates that as pressure diminishes, geopotential height increases, and vice versa. The negative sign indicates that higher pressure corresponds to lower geopotential height. Equation (2.2) is commonly used in meteorology and atmospheric science to calculate atmospheric layer thickness and estimate pressure surface heights.

**The thermodynamic energy equation**: describes how the temperature of a system changes over time. The equation is given in the form of a differential equation, where $\frac{dT}{dt}$ represents

the rate of change of temperature with respect to time and equals to:

$$\frac{dT}{dt} = \frac{\kappa T}{p}\omega + \frac{J}{c_p} \tag{2.3}$$

Here, in Equation (2.3), the first term on the right-hand side of the equation, $\frac{\kappa T}{p}\omega$, reflects the rate of temperature change resulting from adiabatic expansion or compression where $\kappa$ is the ratio of the gas constant to the specific heat at constant pressure, $p$ is the pressure, and $\omega$ is the vertical velocity. The second term describes the effects of diabatic heat sinks and sources. The absorption of solar radiation, the emission of longwave radiation, and the release of latent heat are all included under this term where $J$ is the heating rate per unit mass and $c_p$ is the specific heat at constant pressure. The continuity equation: describes the conservation of mass and is given by:

$$\frac{\partial \omega}{\partial p} = -\nabla \cdot \mathbf{V} \tag{2.4}$$

Equation (2.4) is a vectorial form of the relationship between the vertical velocity of air parcels ( $\omega$) and the divergence of the horizontal wind field ($\nabla \cdot \mathbf{V}$). Due to frictional drag, air parcels in the atmospheric boundary layer often travel across isobars towards lower pressure. As a result, low-level flow converges into regions of low pressure and diverges out of regions of high pressure. **The bottom boundary condition**: is described by Margules' pressure tendency equation:

$$\frac{\partial p_s}{\partial t} = -\mathbf{V}_s \cdot \nabla p - w_s \frac{\partial p}{\partial z} - \int_0^{p_s} (\nabla \cdot \mathbf{V}) dp \tag{2.5}$$

It states that, for the Earth's surface (where $p = p_s \approx$1000 hPa), the rate of change of pressure ($\frac{\partial p_s}{\partial t}$) is equal to the sum of the advection of pressure by the surface wind ($-\mathbf{V_s} \cdot \nabla p$), the vertical advection of pressure due to surface motion ($-w_s \frac{\partial p}{\partial z}$), and the integral of the divergence of the horizontal velocity from the surface to the pressure level ($\int_0^{p_s} (\nabla \cdot \mathbf{V}) dp$).

Considering that the system of primitive equations includes two components for horizontal motion, it forms a set of five equations corresponding to five dependent variables: $u$, $v$, $\omega$, $\Phi$, and $T$. Including diabatic heating field ($J$) and friction field ($F$) necessitates their specification or parameterization as functions of the dependent variables. The thermodynamic energy equation (2.3), the bottom boundary pressure equation (2.5), and the horizontal equation of motion (2.1), are all "prognostic" equations because they all contain time derivatives. The interrelations between the dependent variables at every given time instant are defined by the residual "diagnostic" equations. Numerical solutions can be employed for the primitive equations. These equations are organized on a horizontal grid with uniform spacing and several vertical levels. Even though latitudinal spacing may not be constant, grid points in global models frequently line up with latitude and longitude lines. In order to make computation easier on a fixed set of grid points and levels without requiring the grid to change with air trajectories, the equations are translated into the Eulerian form. The initial conditions for the dependent variables are determined at time $t_0$ while ensuring that

the diagnostic relationships between the variables are maintained (e.g. the geopotential field in hydrostatic conformity with the temperature field). The coefficients of orthogonal analytic functions known as spherical harmonics are used to analyze expressions involving the horizontal and vertical derivatives. Subsequently, time derivative terms ($\frac{d\mathbf{V}}{dt}$, $\frac{\partial T}{\partial t}$, and $\frac{\partial p_s}{\partial t}$) are computed, and their three-dimensional fields are advanced through a short time increment $\Delta t$. Diagnostic equations are then applied to compute dynamically consistent fields of other dependent variables at time $t_0 + \Delta t$. This iterative process is repeated across subsequent time steps to show the evolution of dependent variable fields. To avoid the creation of fictitious small-scale patterns brought on by numerical problems, the time increment $t$ must be small. The acceptable time step decreases as the spatial resolution of the model increases, requiring more calculations such as $u(t_0 + \Delta t) \approx u(t_0) + \frac{\Delta u}{\Delta t}$ for each time step (for the example of the u-component of the velocity field). As a result, along with increasing model spatial resolution, the computational resources needed for numerical weather prediction and climate modeling also significantly increase. Two significant breakthroughs around the mid-20th century greatly enhanced our understanding of the general circulation. First, the discovery of baroclinic instability, which creates baroclinic waves and extratropical cyclones, was made by Charney 1947 and Eady 1949. Second, the introduction of general circulation models (GCMs) allowed numerical representation of global atmospheric circulation using the primitive equations. These models enable the study of long-term wind patterns, precipitation, and wind steadiness. Let's consider a simulation starting from a state of rest, where the atmosphere is stable and pressure and temperature are uniform horizontally. At time $t = 0$, the model is activated, causing differential heating between the tropics and polar regions that resemble the temperature differences in the real atmosphere. Initially, the warming of the tropics and cooling of the polar areas lead to distinct changes in pressure. The upper pressure surfaces bulge upwards due to heat expansion in the tropics, while they bend downward over the polar regions (see Figure 2.2a). This leads to a pressure gradient between the equator and the pole at higher altitudes which drives a poleward flow. This flow becomes more pronounced in the second time step. The poleward mass movement results in a redistribution of mass across latitudes, causing surface pressure to drop in low latitudes and rise in high latitudes (Wallace and Hobbs 2006b). This change in surface pressure creates a pressure gradient between the equator and the pole at lower altitudes, initiating equatorward flow at these levels. This initial response results in the establishment of a circulation cell from the equator to the pole (Figure 2.2b). The Coriolis force causes the equatorward flow to move westward and the poleward flow to move eastward (Figure 2.2c). With each subsequent time step, the flow becomes more horizontal. The Coriolis force balances the pressure gradient force and the vertical wind shear between low-level easterly winds and upper-level westerly winds increases due to the stronger temperature contrast between the equator and the pole caused by meridional heating differences. The Coriolis force is essential in building this vertical shear. Friction limits the strength of surface easterly winds, while upper-level westerly winds become stronger over time. Questions about why winds blow in certain directions and why trade winds are more consistent than westerlies are crucial for understanding large-scale atmospheric mo-

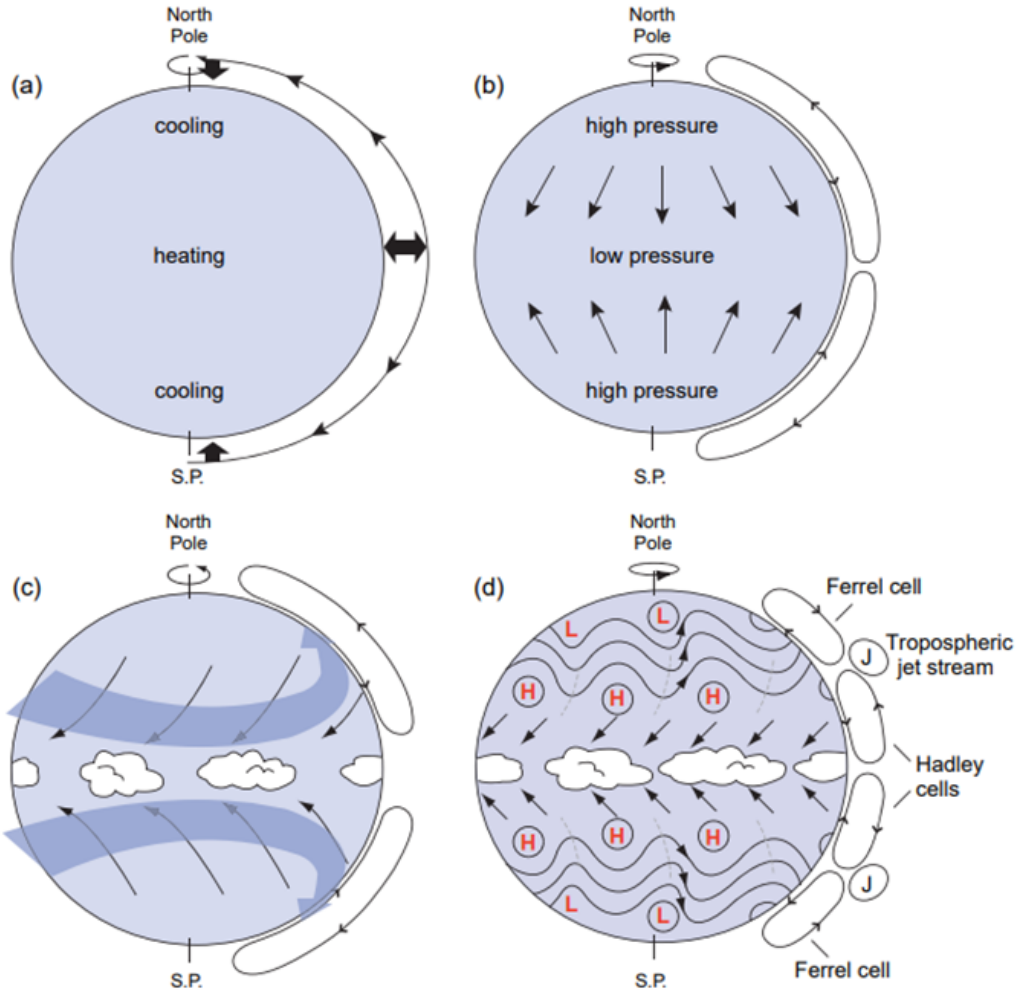


**Figure 2.2.:** Schematic showing the evolution of the atmospheric circulation from a state of stillness within a climate model, under simplistic equinox conditions, and without the influence of land-sea difference. Figure from (Wallace and Hobbs 2006b)

tions globally (Wallace and Hobbs 2006a). On the basis of the straightforward dynamical logic described by the primitive equations, the developments that follow could never have been predicted. The significance of the mid-20th-Century advancements becomes clear as the numerical integration introduced in the last section is extended forward in time. Results replicated from various GCMs show that, as the temperature difference between the equator and the pole reaches a critical point, baroclinic instability emerges in mid-latitudes. This introduces wave-like features to the flow. These waves lead to a circulation pattern similar to that shown in Figure 2.2d. Within the forming waves, warm and moist subtropical air masses are traveling toward the pole ahead of eastward-moving surface cyclones. Concurrently, cold and dry polar air masses travel equatorward behind these cyclones. This interchange of warm and cold air masses over the 45° latitude circle results in a recognizable movement of heat,

both sensible and latent, in a poleward direction. As a result, this heat exchange mitigates the intensification of the temperature difference between the equator and the pole. Following generations of these waves, originating in the lower troposphere of midlatitudes and moving upward towards the jet stream level before heading equatorward into the tropics (Wallace and Hobbs 2006b). The tilted features of the wave during its equatorward movement result in westerly winds in poleward-moving air, creating a net poleward transfer of momentum. This momentum transfer leads to a shift from easterly to westerly surface winds in midlatitudes, similar to real-world atmospheric conditions. Additionally, these waves induce weak mean meridional circulation cells in both hemispheres, i.e. the "Ferrel cells". In the latitude of the storm tracks ( 45°), these cells exhibit poleward, frictionally generated Ekman drift, ascent on the poleward side, and descent on the equatorward side. As baroclinic waves emerge, the Hadley cells retreat toward the tropics, creating subtropical anticyclones around 30° latitude (Wallace and Hobbs 2006b). These anticyclones define the boundary between tropical trade winds and extratropical westerlies, as many of the world's deserts are situated in this latitude zone. This subtropical high-pressure belt hosts the pressure centers of major modes of atmospheric variability which will be discussed in Section 2.2.1.

### 2.1.2. Earth system modeling

The climate we experience, including the averages and statistics of the ever-varying temperature and rainfall, wind and ocean currents, and all the other attributes of the Earth System in which we live, is a result of a complex chain of interactions, as discussed in Section 2.1. These complex processes interconnect Earth System components in ways that prevent their isolation, hence, the need for sophisticated models incorporating the diversity of Earth system processes. For example is how atmospheric circulation leads to surface winds driving ocean currents, which transport heat and moisture. This connection forms feedback loops, crucial in climate variability, enhancing or suppressing processes (Flato et al. 2013). Moreover, biogeochemical processes, including biology and chemistry, extend this network of interactions beyond physical components. Human impacts on climate, such as $CO_2$ emissions from fossil fuels, involve biogeochemical processes closely linked to the physical processes (Flato et al. 2013). This is to say that the processes within the climate system can be far more complex and not simply understood from simple GCMs with only a few components (e.g. ocean-atmosphere only). Earth system model (ESM) development has followed a path of gradual progress, evolving from basic numerical weather prediction models of the 1960s. These initial models focused on weather forecasts and were limited in scope. Over time, the models became more complex, connecting the behavior of the atmosphere and oceans. A significant milestone arrived with the emergence of fully coupled models, which can simulate climate changes over extended timeframes, from historical periods to future predictions (Flato et al. 2013). This was possible thanks to advancements in computer capabilities, allowing for more detailed and accurate representations of Earth's system behaviors (Flato et al. 2013). Collaborative efforts, such as CMIP, played an essential role in shaping ESM development (WCRP 2022).

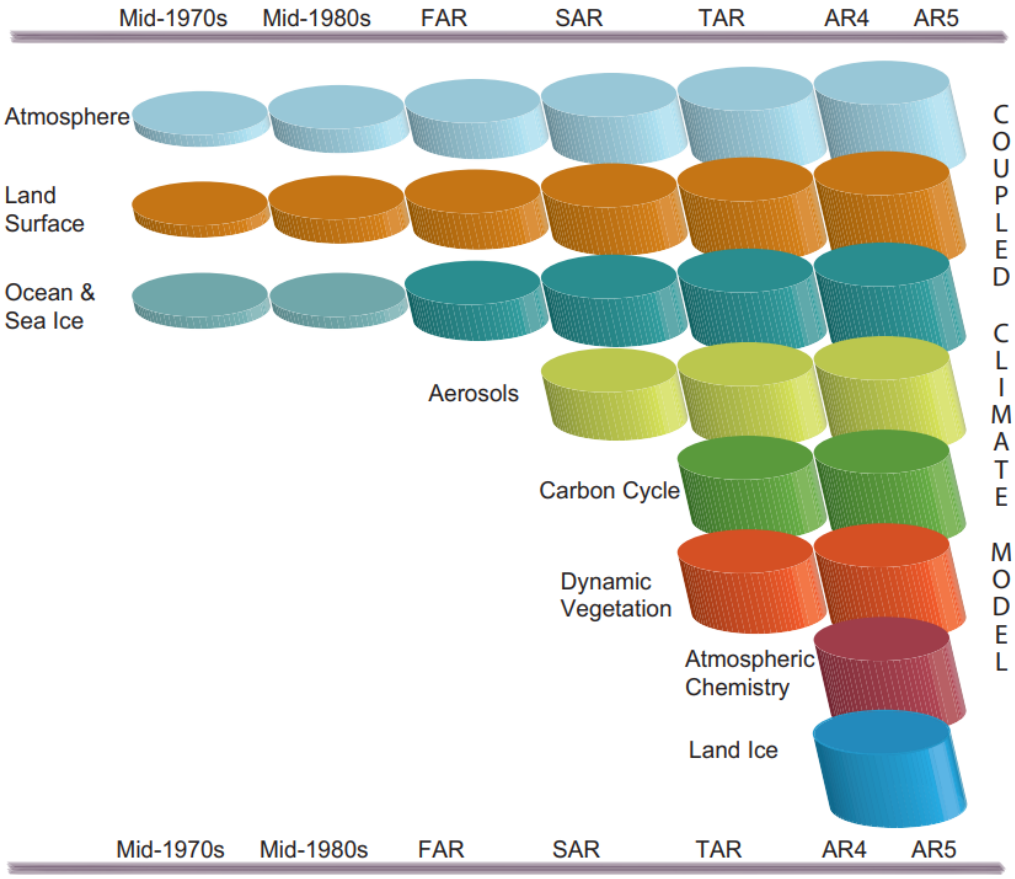


**Figure 2.3.:** Over the past decades, climate models have evolved by integrating various components into comprehensive models. This development is evident in the increasing complexity and diversity of processes in different aspects of the Earth's systems, such as the atmosphere. This progression is visually depicted by growing cylinders, signifying the advancement in process understanding. Figure from (IPCC 2013)

CMIP standardized the setup and evaluation of ESMs, enabling scientists to work together and compare outcomes. These projects revealed important insights, such as the ocean's role in heat retention and the cooling effects of aerosols on climate (WCRP 2022). The graphical representation, as depicted in Figure 2.3 from the IPCC's Fifth Assessment Report (AR5, IPCC 2013), provides a visual account of the progression of climate models over the past few decades. The figure illustrates how various components of these models have been gradually integrated into comprehensive climate models over time, with each aspect consisting of a range of intricate processes. Over the years, there has been a noticeable increase in the complexity and diversity of these processes, as symbolized by the growing size of the cylinders in the diagram. This implies that our understanding of Earth's processes and the ability to represent them within models have significantly improved. CMIP and similar frameworks have been crucial in extending modeling capabilities and investigating Earth's intricacies (Eyring et al. 2016). A noteworthy advancement highlighted in the figure corresponds to the enhancement of both horizontal and vertical resolution in the models. For example, the spectral models'

resolution has remarkably advanced from approximately 500 km horizontal resolution and 9 vertical levels in the 1970s to less than 25 km horizontal resolution and 95 vertical levels in the present. Additionally, ensemble techniques are increasingly prevalent in the domain of Earth system modeling. Such techniques involve multiple calculations to enhance statistical robustness, accommodate natural variability, and address uncertainty in model formulations. This is done by utilizing larger sample sizes and diverse approaches to generate samples, encompassing variations in models, physics, and initial conditions. Furthermore, the refinement of ocean grids and the integration of sophisticated grids in both oceanic and atmospheric models have also contributed to more accurate simulations. In light of the sophistication of modern ESMs, which now incorporate not just physical, but also biological and chemical processes, understanding the complexities of anthropogenic climate change becomes a multi-faceted endeavor (Flato et al. 2013). Significant progress has been made in the portrayal of Earth system processes, including key interactions like radiation-aerosol-cloud dynamics, cryosphere behavior, and carbon cycle representation. Such advancements, validated against observational and paleoclimate data, underscore the continual refinement of these models and spotlight the imperative to address inherent uncertainties and variabilities.

### 2.1.3. Ocean-Atmosphere interactions

All components mentioned in Section 2.1 interact through various physical, chemical, and biological processes, making the climate system highly complex. For example, the atmosphere and oceans exchange water vapor and heat through evaporation and precipitation, while precipitation affects the ocean's salinity and thermohaline circulation. Sea ice also affects the exchanges between the atmosphere and oceans, and the biosphere influences atmospheric $CO_2$ concentration through photosynthesis and respiration. Any change, whether natural or human-induced, in the components or interactions of the climate system, or in external forcing, can lead to climate variations. Understanding these interactions and feedbacks is crucial to comprehending the climate system's behavior and predicting climate changes accurately. Ocean-atmosphere interactions are influenced by a combination of physical processes, including changes in sea surface temperature (SST), ocean currents, wind patterns, and atmospheric circulation. The exchange of heat and moisture between the ocean and the atmosphere is a critical factor in driving these interactions. For example, warm ocean surface waters can lead to the development of weather systems such as tropical cyclones through enhanced atmospheric convection. Conversely, atmospheric circulation patterns can influence ocean currents and temperature distributions. These interactions play a crucial role in generating and modulating internal climate variability, impacting various climate phenomena across different temporal and spatial scales. Both atmospheric and oceanic processes exert significant influence on SSTs. Key factors governing energy exchange at the sea surface encompass wind speed, air temperature, cloud cover, and atmospheric humidity. SST is notably affected by heat transfer via currents, vertical mixing, and the depth of the boundary layer on the oceanic

side. To characterize the heat budget of the upper-ocean mixed layer, equations from (Deser et al. 2010) can be employed:

$$\frac{\partial T}{\partial t} = \frac{Q_{\text{net}}}{\rho C_p H} + (\vec{U}_{\text{geo}} + \vec{U}_{\text{ek}}) \cdot \vec{\nabla} T + \frac{W_e + W_{\text{ek}}}{H}(T - T_b) \tag{2.6}$$

In equation Equation (2.6), the symbols denote the following: $\rho$ represents seawater density, $C_p$ stands for the specific heat of seawater, $H$ signifies the depth of the mixed layer, $T$ denotes mixed-layer temperature, $Q_{\text{net}}$ represents the net surface energy flux, and $\vec{U}_{\text{geo}}$ and $\vec{U}_{\text{ek}}$ correspond to geostrophic and Ekman current velocities, respectively. Additionally, $W_e$ signifies vertical entrainment rate, $W_{\text{ek}}$ denotes Ekman pumping velocity, and $T_b$ stands for the temperature of water entrained from depth into the mixed layer. The net surface energy flux $Q_{\text{net}}$ can be decomposed into:

$$Q_{net} = Q_{sh} + Q_{lh} + Q_{sw} + Q_{lw} \tag{2.7}$$

In Equation (2.7), $Q_{sh}$ represents sensible heat flux, $Q_{lh}$ stands for latent heat flux, $Q_{sw}$ denotes downward solar radiative flux minus the portion penetrating the mixed layer, and $Q_{lw}$ signifies longwave radiative flux. Turbulent energy flux, represented by $Q_{sh} + Q_{lh}$, is directly proportional to wind speed and the difference in air-sea temperature or humidity. In contrast, radiative fluxes $Q_{sw} + Q_{lw}$ depend on air temperature, humidity, and cloudiness. Well-established references like Peixoto and Oort 1992 and Hartmann 1994 provide comprehensive formulations for these air-sea fluxes. Contributions from Ekman and geostrophic currents to the heat budget occur through horizontal advection, while entrainment and Ekman pumping affect SST through vertical advection (Pond and Pickard 1983; Vallis 2006). Figure 2.4, presented by (Deser et al. 2010), illustrates the influence of random atmospheric forcing on slow SST variations. The figure depicts a stochastic climate model paradigm, showcasing how the mixed-layer temperature responds to randomly varying surface heat fluxes (top panel) at two different ocean depths: shallow (50 m, middle panel) and deep (500 m, bottom panel). SST fluctuations are observed to occur over a couple of years at the shallow layer, while they take decades to oscillate at the deep layer.

Hasselmann 1976 proposed a stochastic climate model that divides the Earth System into a rapidly varying "weather" system, primarily represented by the atmosphere, and a slowly responding "climate" system, encompassing the ocean, cryosphere, land vegetation, and more. The interaction between these systems leads to climate variability, with the ocean integrating atmospheric noise. The atmosphere is treated as white noise, while the ocean, with its higher heat capacity, acts as a low-pass filter, especially at mid-latitudes. As a result, SST-anomaly feedbacks at the mixed layer have a characteristic feedback time of approximately 6 months (Frankignoul and Hasselmann 1977).

To achieve a truly coupled atmosphere-ocean mode of variability, oceanic SST must induce atmospheric heat and momentum fluxes to strengthen the coupling (Gill 1982; Mechoso et al. 2021). Tropical SST has a dominant effect on the atmosphere over midlatitude SST, contributing to stronger coupling in tropical modes compared to midlatitude modes. Oceans play a

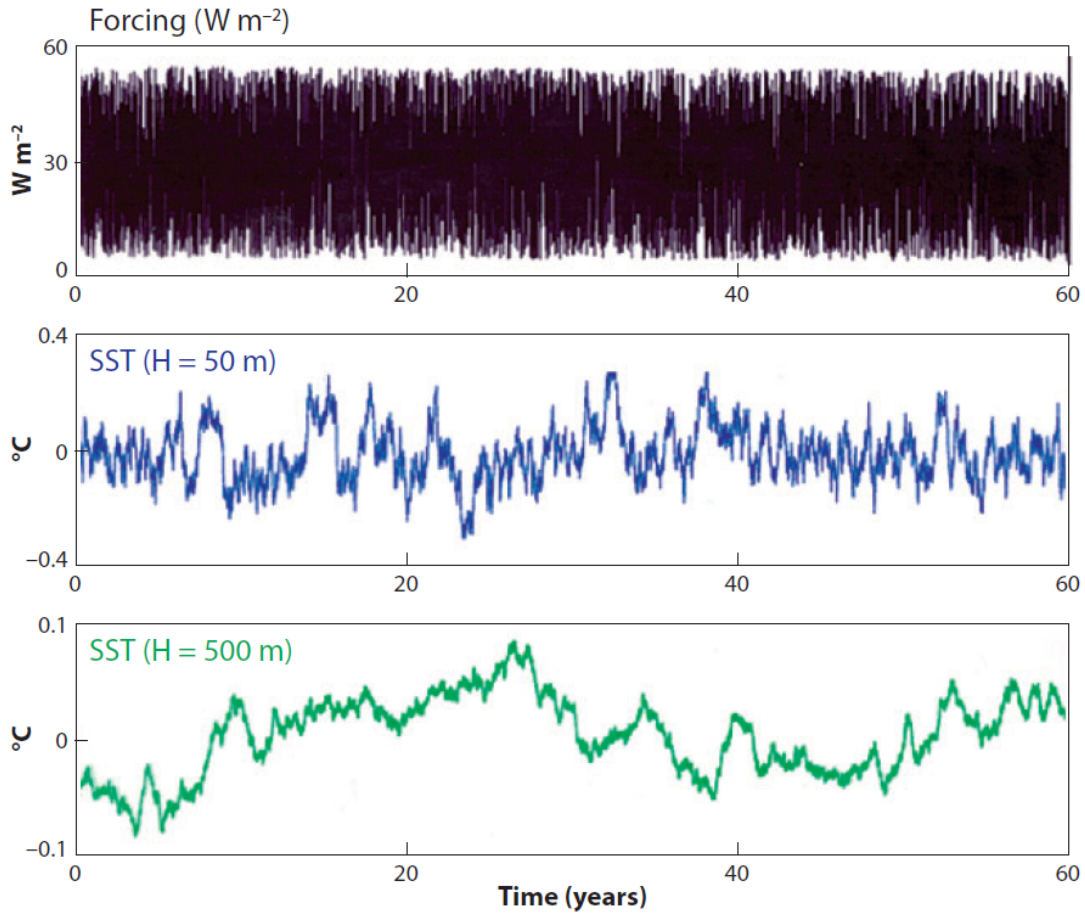


**Figure 2.4.:** Time series of random atmospheric heat flux forcing (top) and the resulting response in the upper-ocean mixed-layer temperature for two different mixed-layer depths: 50 m (middle) and 500 m (bottom). Figure from (Deser et al. 2010).

significant role in providing thermal inertia and transferring it to the overlying atmosphere mainly through turbulent fluxes of sensible and latent heat at the surface. As mentioned earlier, these turbulent fluxes depend not only on SST but also on various atmospheric parameters, such as near-surface wind speed, air temperature, and relative humidity (Deser et al. 2003). At this point, it is beneficial to refer to the Clausius–Clapeyron equation (Clapeyron 1834; Clausius 1850), given by:

$$\frac{dP}{dT} = \frac{L}{T(V_g - V_l)} \tag{2.8}$$

where $\frac{dP}{dT}$ is the rate of change of saturation vapor pressure with respect to temperature, $L$ is the latent heat of vaporization, $T$ is the temperature, and $V_g$ and $V_l$ are the molar volumes of the gas and liquid phases, respectively. This equation illustrates the exponential relationship between the temperature and the saturation vapor pressure of water, highlighting how an increase in SST can augment the atmosphere's moisture-holding capacity, thereby influencing the latent heat fluxes at the ocean-atmosphere interface.

The Bjerknes feedback (Bjerknes 1969), is central to understanding the amplification of certain phenomena in ocean-atmosphere interactions, including ENSO which will be discussed in more detail later Section 2.2.1. This feedback involves a positive loop between SSTs and atmospheric circulation. When the SSTs in the central/eastern equatorial Pacific warm, the temperature contrast between the eastern and western tropical Pacific decreases. This change weakens the east-to-west pressure gradient across the Pacific, leading to a reduction in the strength of the easterly trade winds. The weaker winds reduce the upwelling of cold, nutrient-rich waters in the eastern Pacific, enhancing the warming effect. This feedback loop between ocean warming and weakened trade winds amplifies the initial warming (Neelin et al. 1998; Philander 1990).

The weakening or strengthening of the easterly winds is associated with another fundamental atmospheric circulation pattern, called the Walker circulation (Walker and Bliss 1932), which is also inextricably linked to ENSO. In normal conditions over the equatorial Pacific, this circulation is characterized by a continuous loop, with the lower part flowing from east to west near the surface across much of the tropics, and the upper part moving from west to east at higher altitudes. The Pacific Walker circulation (PWC) involves rising air over the warm western Pacific and sinking air in the eastern Pacific, connecting the flow in one large loop. As illustrated through the schematic in Figure 2.5, the strongest upward branch of this circulation is found over the Maritime Continent, north of Australia, with weaker branches over eastern Africa and northern South America, areas associated with significant precipitation during the northern hemisphere winter. Understanding the Walker circulation is vital in grasping the broader picture of ocean-atmosphere interactions, and it sets the stage for discussing more complex phenomena such as ENSO and its teleconnection to the Atlantic, as will be further discussed in later sections.

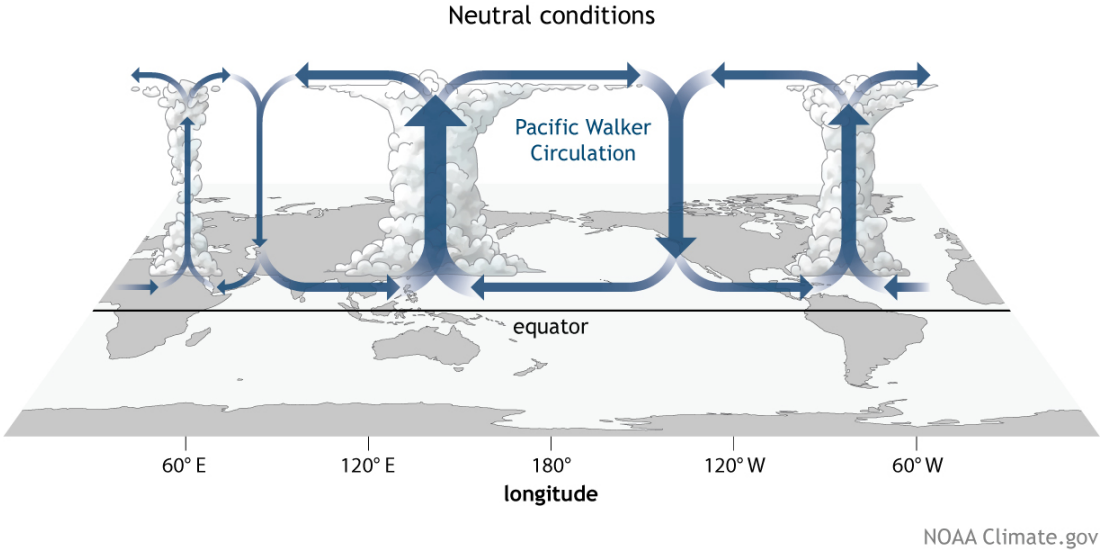


**Figure 2.5.:** Typical Walker Circulation in winter under ENSO-neutral conditions. The diagram illustrates the areas of convection linked with the ascending branches of the Walker Circulation, prominently observed over the Maritime continent, northern South America, and eastern Africa. National Oceanic and Atmospheric Administration (NOAA) Climate.gov drawings by Fiona Martin.

This "overturning cell" is maintained through a SST gradient, with warmer surface waters in the west and cooler waters in the east. Above the warmer waters, air rises, creating a region of low pressure, while above the cooler waters, the air is dry and descends, creating a region of high pressure. This process is facilitated by the trade winds that blow from east to west, pushing seawater towards the west side of ocean basins, and warming it along the (Bjerknes 1969; Meng et al. 2012).

## 2.2. Climate Variability

As discussed in Section 2.1, the term "climate" pertains to the average condition of the Earth's atmosphere and its interconnected components. It's also employed to discuss prolonged atmospheric fluctuations that extend beyond the predictability range of typical atmospheric forecasting. The average state, which encompasses daily and seasonal oscillations over a specified averaging period, is termed the "climatological mean". Any deviations from this standard state are termed climate "anomalies" that happen over different time scales such as weeks, years, and decades. The difference between climate "variability" and climate "change" lies in the time frame; i.e. variability involves fluctuations within a specific time period, while change involves differences between two different, sufficiently long time periods. The concept of climate variability refers to extended variations or modifications in the average state. It can be broken down as follows:

- Intraseasonal climate variability applies to month-to-month fluctuations around the seasonally fluctuating climatological mean that occur within the same season. This could involve, for example, distinguishing between an unusually warm July and an exceptionally cold August.
- Interannual variability captures year-to-year changes in annual or seasonal averages. This might be featured by contrasting mean temperatures of successive summer seasons over a certain region (e.g. Europe or the North Pacific).
- The terms "decadal", "multidecadal", "century-scale", and so on, refer to fluctuations spanning periods of decades, multiple decades, centuries, and beyond.

To grasp the reasons and characteristics of year-to-year climate variability, researchers have deployed computer simulations with atmospheric models, e.g. Coupled Earth ESMs. Early numerical experiments utilizing various models have been carried out during the recent decades, yielding some interesting results, summarized according to (Wallace and Hobbs 2006a) as follows:

- The year-to-year variability of the tropical atmosphere is mainly influenced by external factors, particularly variations in prescribed boundary conditions like SSTs over tropical oceans. Realistic models show that simulated tropical climate variations closely resemble observed variations.

- Climate variability in extratropical latitudes is influenced by both external boundary conditions (not as strongly as in the tropics) and internal atmospheric dynamics. Tropical SSTs are crucial for northern hemisphere winter climate, while variations in soil moisture and vegetation contribute to summer climate anomalies.

- Year-to-year variations in extratropical sea-ice extent and SST have subtler impacts. Running simulations with varied initial conditions but the same boundary-forcing conditions reveals weak externally forced signals within the internally generated noise.

- The majority of intraseasonal variability in extratropical wintertime circulation appears to originate internally within the atmosphere, indicating that the atmosphere itself generates this variability.

The conclusions from above highlight that climate variability arising from interactions generated by the atmosphere is coupled to gradually changing components of the Earth system. Next, we introduce well-recognized patterns of atmospheric (Section 2.2.1) and coupled modes of climate variability (Section 2.2.1). Moreover, climate variability can also arise from external forcing agents, such as volcanic eruptions, fluctuations in solar activity, or alterations in atmospheric composition driven by human activities. Externally forced variability is introduced in Section 2.2.2.

### 2.2.1. Main modes of climate variability

This section introduces the central modes of climate variability, characterized by recurring spatial patterns in atmospheric and ocean parameters over the different timescales discussed above. These modes represent significant and recurrent patterns in the climate system and can be identified through the analysis of anomalies over specific regions, often using techniques such as empirical orthogonal functions (EOFs), later discussed in Chapter 3 (see Section 3.3). Depicted by distinctive spatial and temporal patterns, the modes introduced in this section are central to understanding the complex dynamics of climate variability connecting the Pacific and Atlantic basins, and thus set the stage for a deeper analysis in Chapters 4 and 5.

#### Atmospheric modes of variability

This section introduces atmospheric modes of climate variability which are characterized by recurring and persistent patterns in atmospheric pressure, temperature, and circulation. Here, results are shown based on diagnostics provided by the Climate Variability Diagnostic Package for Large Ensembles (CVDP-LE); Phillips et al. 2020 (see also Section 3.4) using SLP data from the 20th Century Atmospheric Reanalysis extended with ERA5 (ERA20C-ERA5), disseminated by the European Centre for Medium-Range Weather Forecasts (ECMWF) and incorporating observations of surface pressure. Below are some of the most prominent atmospheric modes relevant to the scope of Atlantic-Pacific interactions:

- **The North Atlantic Oscillation (NAO):** The NAO dominates North Atlantic atmospheric variability and is characterized by alternating SLP changes between the Azores High and the Icelandic Low (Hurrell et al. 2003). Its positive phase involves a strengthened Azores High, deepened Icelandic Low, and a northward-shifted jet stream. The NAO significantly influences temperature, precipitation, winds, storm tracks, and extreme events over North Atlantic-European areas (Matthews et al. 2014; Woollings et al. 2014). An index representing the time evolution of NAO can be obtained as the principal-component (PC) time series associated with the leading EOF of area-weighted SLP anomalies over the North Atlantic region [20-80°N, 90°W-40°E] (Hurrell and Deser 2010). Figure 2.6a shows the NAO index using mean winter (DJF) SLP anomalies for the historical 1900-2014 period. Linearly regressing the DJF SLP anomalies (north of 20°N) onto the PC time series in 2.6a reveals the distinctive NAO pattern (Azores High in red and Icelandic Low in blue, as shown in 2.6b). The percent variance explained (*pcvar* in 2.6b) implies that over 41% in the variability of North Atlantic winter SLP anomalies can be explained by the leading EOF (i.e. NAO).

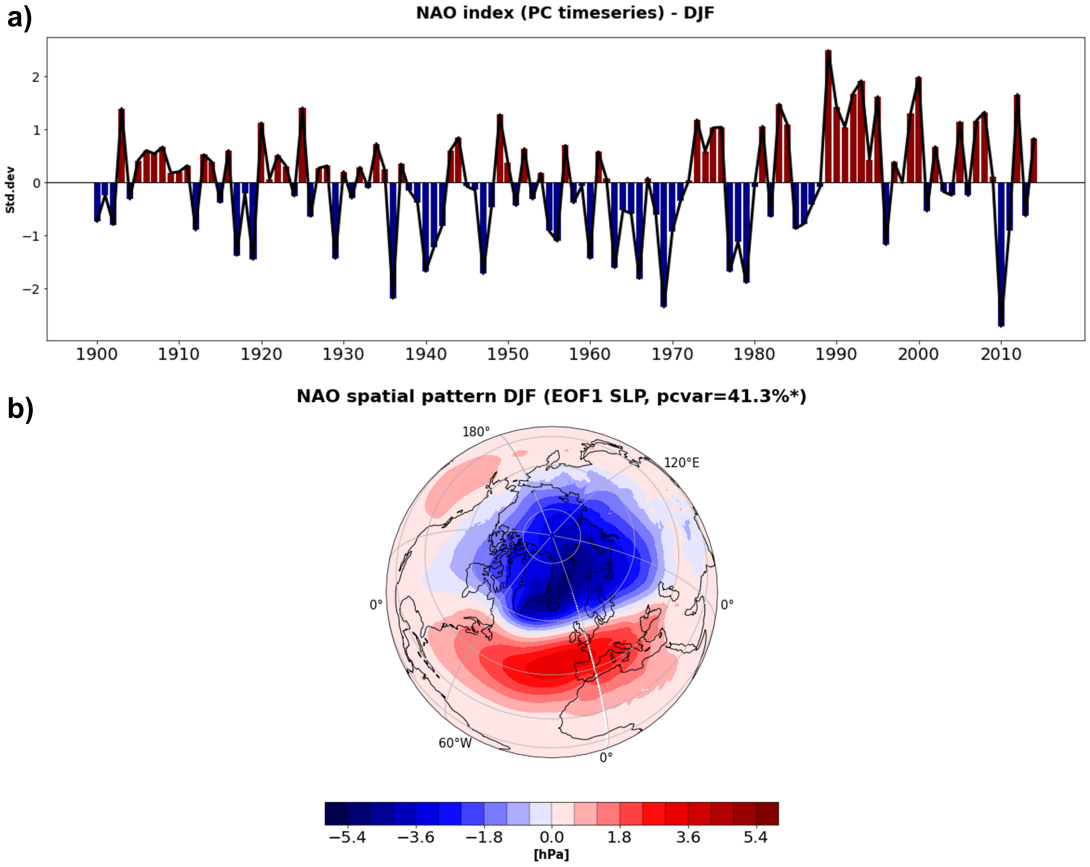


**Figure 2.6.:** North Atlantic Oscillation. (a) The NAO Index is shown as the PC time series of the leading EOF of mean winter (DJF) SLP anomalies over the North Atlantic region based on the ERA20C_ERA5 data set during 1900-2014. (b) Regression pattern of global DJF SLP anomalies on the NAO Index in (a).

Ingrained in mid-latitude dynamics, NAO signals emerge as barotropic phenomena driven by eddy-mean flow interactions (Feldstein and Franzke 2017; Lorenz and Hartmann 2003). These patterns span the atmospheric column and peak during winter storms. Studies also suggest tropospheric NAO links to the stratospheric polar vortex (Karpechko et al. 2017). Although it is considered a mode of internally-generated climate variability, external factors do impact NAO, and these include sea surface temperature anomalies (Baker et al. 2019), cryosphere-atmosphere coupling (Cohen et al. 2014; Screen et al. 2018), and external forcing like volcanic eruptions and solar activity (Gray et al. 2016; Ineson et al. 2011; Le Mouël et al. 2019; Swingedouw et al. 2017). While internal variability prevails, extensive observational records and simulations are needed to assess the forced component within NAO (IPCC 2021a).

- **The Pacific-North American (PNA) pattern:** The PNA is another prominent large-scale atmospheric circulation pattern that significantly impacts the climate of both the North Pacific and North America. It is characterized by four primary centers of action: a positive anomaly situated over the Aleutian Islands, a negative anomaly extending across the North Pacific, a positive anomaly positioned over western Canada, and a negative anomaly spanning the southeastern United States (Wallace and Gutzler 1981). Similar to NAO, the PNA pattern is defined as the leading EOF of area-weighted SLP anomalies over the region [20–85N, 120E–120W]. Figure 2.7 shows the PC time series (PNA index) from mean winter (DJF) anomalies (2.7a) and the corresponding regression pattern (2.7b). Depending on the signs of the anomalies, the PNA can manifest as either positive or negative. In a positive PNA phase, a stronger and northward-shifted jet stream prevails over the North Pacific, while a weaker and southward-shifted jet stream dominates over the eastern United States. Conversely, a negative PNA phase leads to the opposite atmospheric circulation pattern (Leathers et al. 1991; Wallace and Gutzler 1981). Moreover, the PNA plays a vital role in shaping precipitation patterns within the United States. During a positive PNA phase, wetter-than-normal conditions prevail over regions like the Pacific Northwest, northern Rockies, Great Lakes, and New England, while drier-than-normal conditions occur in California, the Southwest, and the Southeast. The opposite holds true for a negative PNA phase (Leathers et al. 1991; Wallace and Gutzler 1981).

- **The Pacific-South American (PSA) patterns:** The PSA modes stand out as prominent atmospheric circulation features within the Southern Hemisphere (Mo and Ghil 1987). The PSA, similar in certain aspects to the PNA pattern (Wallace and Gutzler 1981), is characterized by an atmospheric Rossby wave train that extends from south-eastern Australia to Argentina. However, distinctively, the PSA modes, namely PSA1 and PSA2, are defined by two patterns rather than one, forming the second and third EOFs of SLP anomalies across the Southern Hemisphere. Notably, the first EOF mode corresponds to the Southern Annular Mode (SAM) which explains most of variability over the Southern hemisphere. PSA1 and PSA2 are closely linked, as they exist in quadrature, and together

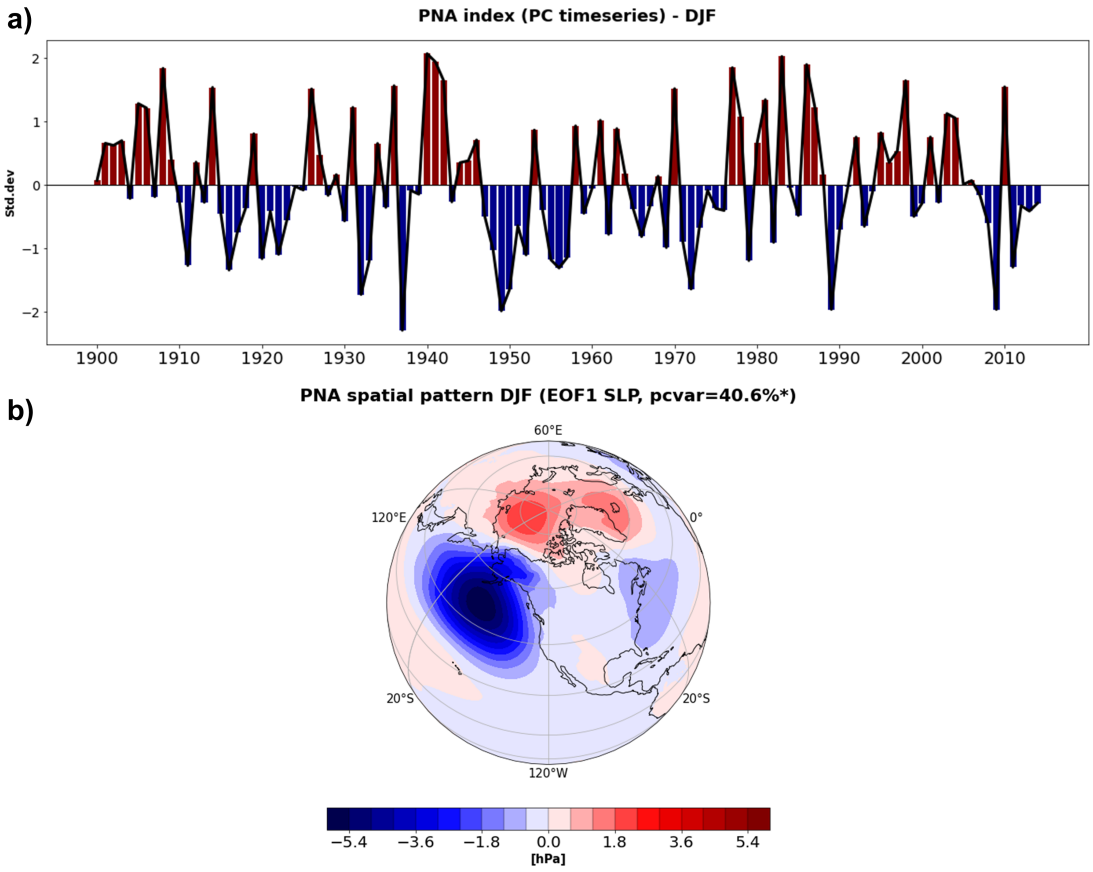


**Figure 2.7.:** Similar to 2.6 but for the Pacific North American pattern. (a) The PNA Index is shown as the PC time series of the leading EOF of mean winter (DJF) SLP anomalies over the North Pacific and North American region. (b) Regression pattern of DJF SLP anomalies on the PNA Index in (a).

constitute the wave train phenomena. 2.8, shows the PSA1 pattern, i.e. the second EOFs of area-weighted SLP anomalies south of 20S. The temporal manifestation of PSA modes ranges from intraseasonal to decadal scales. The PSA patterns exert significant influence in several domains, notably atmospheric blocking events (Renwick and Revell 1999), South American rainfall variability (Mo and Paegle 2001), warming trends over West Antarctica and the Antarctic Peninsula (Marshall and Thompson 2016), and Antarctic precipitation variability (Marshall et al. 2017).

### Coupled modes of variability

The modes above are considered to be outcomes of atmospheric processes. These patterns still emerge as fundamental modes of variability even when the bottom boundaries are held constant in extended simulations of atmospheric GCMs. Although contributions from tropical forcing are evident, especially during certain seasons, the dynamics of the atmosphere alone play the dominant role in the formation of the PNA PSA and NAO patterns. This section introduces coupled climate variability, which involves diverse interactions between the atmosphere and other components of the Earth system. In certain situations, these inter-

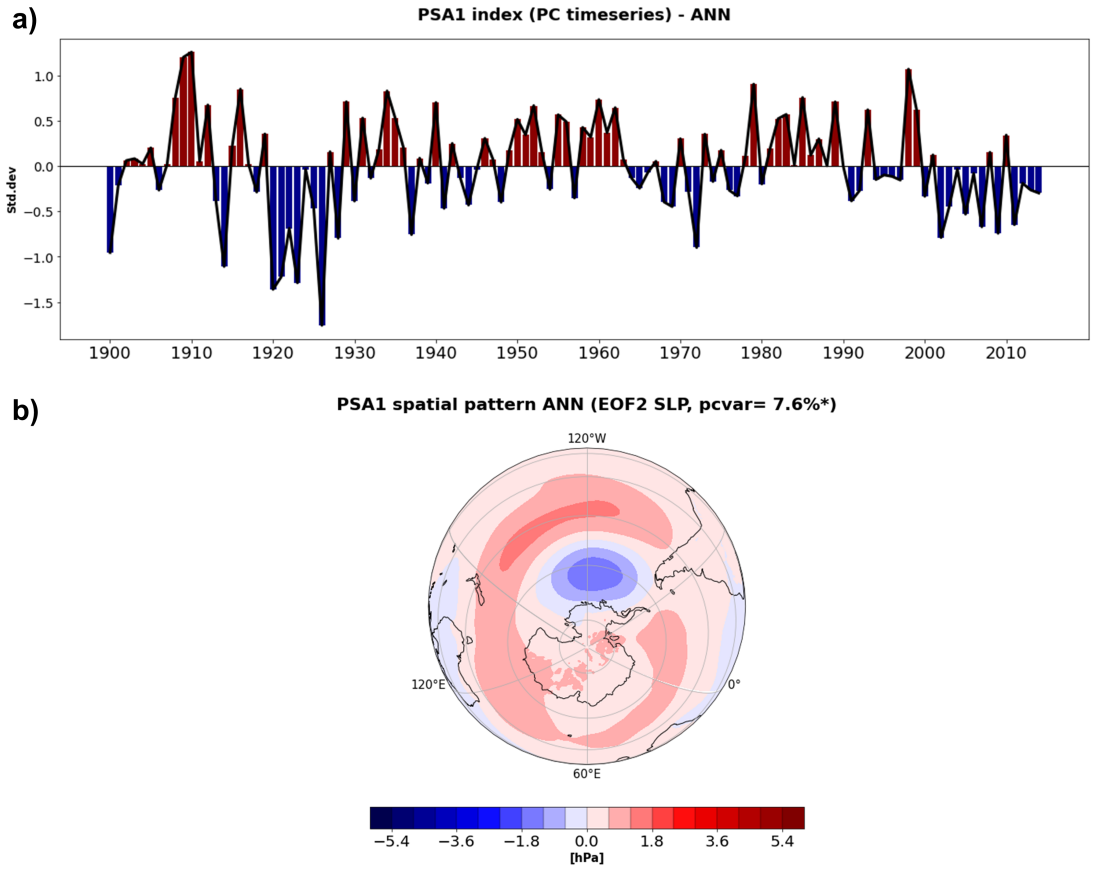


**Figure 2.8.:** Similar to 2.6 but for the Pacific South America mode 1. (a) The PSA1 Index is shown as the linearly detrended PC time series associated with second EOF of area-weighted SLP anomalies south of 20S. (b) Regression pattern of annually averaged (ANN) SLP anomalies on the PSA1 Index in (a).

actions can give rise to modes of variability that possess distinct characteristics compared to the variability that the atmosphere generates independently through its internal dynamics. This indicates that when the atmosphere is coupled to the rest of the Earth's system, it can result in complex patterns that might not arise solely from its inherent processes. The patterns showcased below are part of diagnostic results derived from the Extended Reconstructed Sea Surface Temperature version 5 (ERSSTv5), a dataset managed and provided by the NOAA.

- **El Niño - Southern Oscillation (ENSO):** ENSO is the most prominent coupled ocean–atmosphere phenomenon that reveals the intricate interplay between the equatorial Pacific's SSTs, wind patterns, and global climate dynamics. ENSO's central feature involves the oscillation between abnormal warming (El Niño) and cooling (La Niña) of the central/eastern equatorial Pacific SSTs, accompanied by shifts in overlaying winds and precipitation patterns (Neelin et al. 1998; Philander 1990; Wang 2018). This climatic phenomenon predominantly unfolds on interannual time scales and serves as a key mode of tropical variability (Trenberth et al. 2002). ENSO's significance extends beyond its localized occurrence as it holds substantial influence over global surface temperatures (Pan and Oort 1983; Trenberth et al. 2002) and drives climate predictability at seasonal to

interannual scales (Philander 1990; Smith et al. 2012). ENSO indices are among the most carefully monitored metrics used by meteorological institutes worldwide due to ENSO's profound implications for environmental dynamics. ENSO's influence is evident in its coupling of equatorial Pacific SST and SLP anomalies. El Niño events, in particular, are marked by weakened easterly trade winds, reduced equatorial cold tongue, diminished marine biosphere productivity, and alterations in sea level gradients (Neelin et al. 1998; Wang 2018). The shift in rainfall distribution during El Niño, impacting the ITCZ and global atmospheric patterns, also underscores ENSO's far-reaching influence (Neelin et al. 1998; Wang 2018). ENSO's monitoring involves a range of indices, such as the Niño3 and Niño3.4 regions' SST anomaly (SSTA) and the Southern Oscillation Index (SOI) based on normalized SLP anomalies (Troup 1965). The diversity of ENSO indices arises from the complex nature of its events, exhibiting variations in magnitude, spatial structure, and seasonal timing (L'Heureux et al. 2017; Pepler 2016). This thesis utilizes the most commonly used index for ENSO, the Niño3.4 index which is defined through area-averaged monthly SSTAs over the Niño3.4 region [5N–5S, 170–120W]. Figure 2.9 shows the Niño3.4 index for the historical 1900-2014 period (2.9a) and the regression of global SSTAs onto the Niño3.4 index during all El Niño winters (2.9b) and all La Niña winters (2.9c) during the same period (see caption of 2.9).

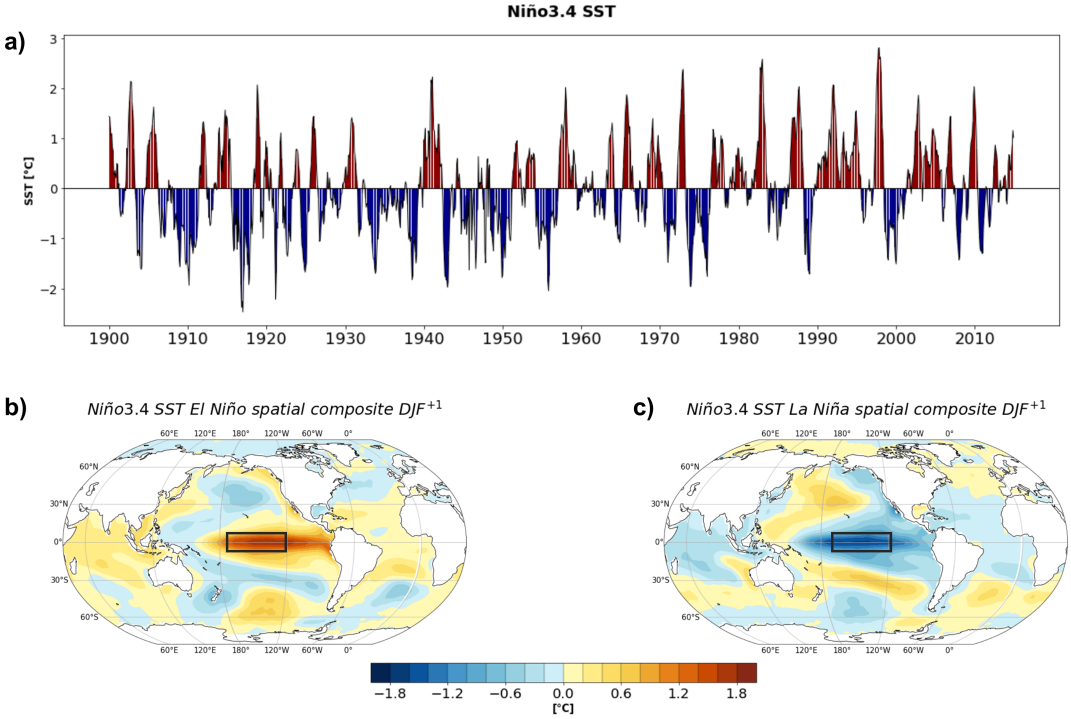


**Figure 2.9.:** ENSO 1900-2014 time series and spatial composites from CVDP-LE diagnostics (see 3.4) using ERSSTv5 data. a) Monthly SSTA time series in the Nino3.4 region (5N–5S, 170–120W, region outlined by the black rectangle in b and c). b) Global maps of linearly detrended SST based on compositing all El Niño events (23) using +1 standard deviation threshold of the linearly detrended December Niño3.4 SST Index during the winter of the following year an event is defined. c) Same as b) but based on compositing all La Niña events (19) using a -1 standard deviation threshold.

ENSO's remarkable predictability, surpassing the usual weather forecast limits, stems from slowly evolving SSTAs. These anomalies persist from summer through winter, allowing skilled predictions using statistical or coupled atmosphere–ocean models (Philander 1990; Smith et al. 2012). These forecasts extend to a variety of variables, offering valuable insights into seasonal conditions and their repercussions for various aspects of society and the environment.

- **The Pacific Decadal Variability (PDV):** Also known as the Pacific Decadal Oscillation (PDO), PDV reveals itself as an integral mode of internal variability that broadly shapes the North Pacific region. The name "Pacific (inter)Decadal Oscillation" (PDO), which Mantua et al. 1997 used to describe the predominate PDV pattern, is at the center of this discourse. This type of variability, which alternates between positive and negative phases (2.10a), has observable effects on the ecosystems of the North Pacific and the Northern Hemisphere's climate. The PDV index, hereupon synonymous with the PDO index, serves as a quantifiable representation of this decadal variability pattern. Here, the PDV index is defined as the standardized PC time series of the leading EOF associated with area-weighted SST anomalies over the North Pacific region [20–70°N, 110°E–100°W] after subtracting the global mean (70°N–60°S), effectively detrending the data (see 2.10a; (Mantua et al. 1997)). By regressing the global SSTAs onto the PC time series, a "horseshoe" pattern is visible in the North Pacific (2.10b). This pattern is prominent during the positive phase of PDV, which is associated with anomalously cool SSTAs in the central North Pacific surrounded by anomalously warm SSTAs along the North American west coast (2.10b). On the other hand, during a negative PDV phase, the pattern is reversed with warmer SSTAs in the central North Pacific and cooler along the North American west coast. The exceptional winter in 1976-1977, was later referred to as "regime shift" as the alteration, initially highlighted by (Nitta and Yamada 1989; Trenberth 1990), unveiled a noticeable change in the mean state of winter SLP in the North Pacific. In the subsequent years, the exploration of interdecadal changes in the Pacific accelerated, with the 1990s witnessing a surge in research endeavors uncovering mechanisms behind the PDV (Arblaster et al. 2002; Mantua et al. 1997; Meehl et al. 2009; Power et al. 1999; Zhang et al. 1997). Scientists noticed substantial changes in the North Pacific biota during that time, which (Ebbesmeyer et al. 1991) assessed using a combined analysis of meteorological and biological data. Building upon these seminal findings, (Miller et al. 1994) methodically outlined the resulting climatic changes and attributed them to the regime shift. With its far-reaching implications, PDV stands as a key element of decadal climate variability, influencing ecosystems and climatic processes both regionally and globally.

- **The Atlantic Multidecadal Variability (AMV):** Also known as the Atlantic Multidecadal Oscillation (AMO), AMV is a notable climatic mode manifesting slow SST fluctuations extending across decades within the North Atlantic Ocean. This intricate phenomenon reveals itself through basin-scale SSTAs, reflecting interactions with the

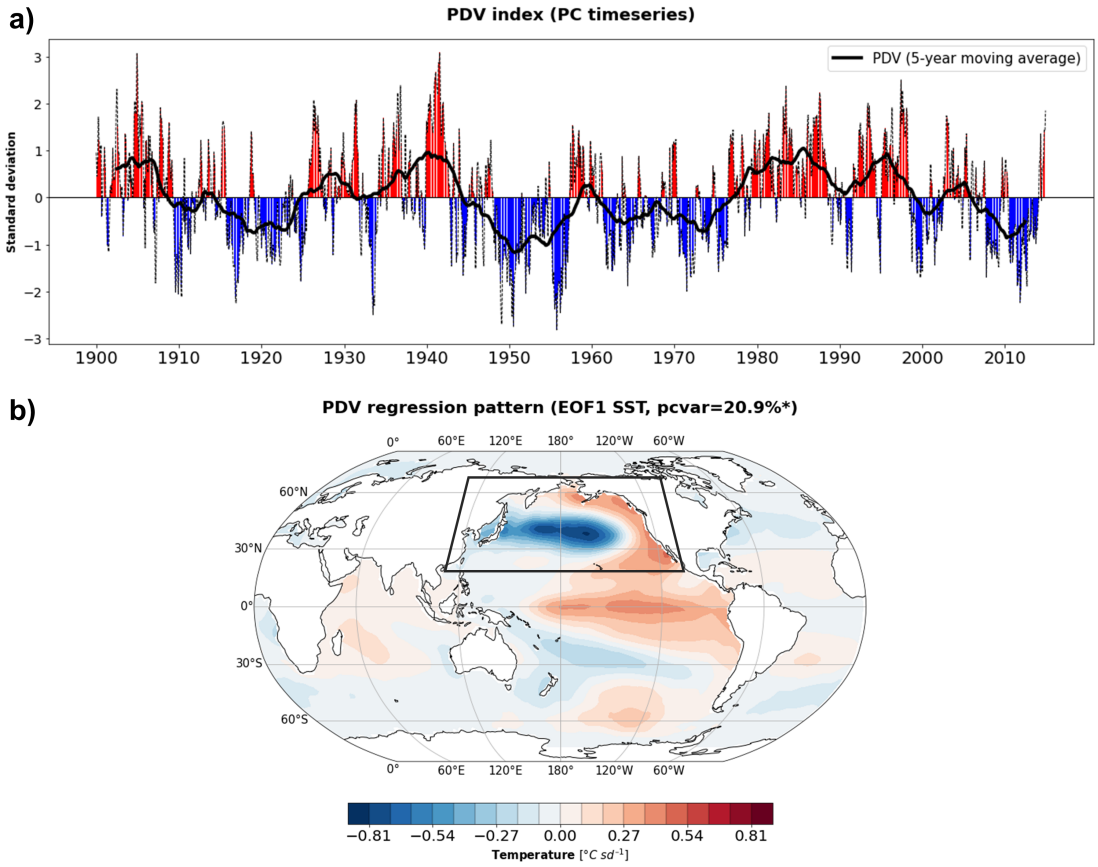


**Figure 2.10.:** Pacific Decadal Variability. (a) Principle component (PC) time series associated with the leading EOF of monthly SST anomalies over the North Pacific (after removing the global mean SST anomaly) based on the ERSSTv5 data set during 1900–2014; showing the unsmoothed record (red and blue) and the 5-year moving average (black line). (b) Regression pattern of global SST anomalies onto the PC time series in (a).

atmosphere over approximately 70-year cycles (Deser et al. 2010). Additionally, the AMV imprints are illustrated through heat content and density perturbations within the subsurface ocean, specifically linked to fluctuations in the Atlantic Meridional Overturning Circulation (AMOC) and related oceanic processes (Zhang 2017). To analyze AMV signals, various approaches have been employed to disentangle the externally forced influences from the observed SST data. These encompass linear detrending methodologies as well as statistical techniques using both observation-based and model-based approaches (Frajka-Williams et al. 2017; Frankcombe et al. 2015; Trenberth and Shea 2006). To represent its time evolution here, the AMV index is defined as monthly SST anomalies averaged over the North Atlantic region (0–60°N, 80–0°W) after subtracting the global mean (60°N–60°S) to effectively detrend the data and reduce the externally forced signal (Trenberth and Shea 2006). The AMV time series reconstructed from reanalysis data of the 1900-2014 period is shown below in 2.10a, with the black line denoting the smoothed version representing the slow-fluctuating multidecadal internal variability component. The distinctive positive phase of AMV entails anomalous

warming enveloping the entire North Atlantic region (IPCC 2021a). This warming is particularly pronounced in the subpolar gyre, along the sea ice margins in the Labrador Sea and Greenland/Barents Sea, and to a lesser extent in the subtropical North Atlantic (2.11b). Simultaneously, cooler SST anomalies appear over the South Atlantic and along the Pacific cold tongue, a pattern analogous to PDV. Inter-basin interconnections are clearly visible in AMV-related SSTAs (2.11b), highlighting the intricate network of teleconnections that connect nearby ocean basins, tropical and extratropical regions, as well as land and ocean domains.

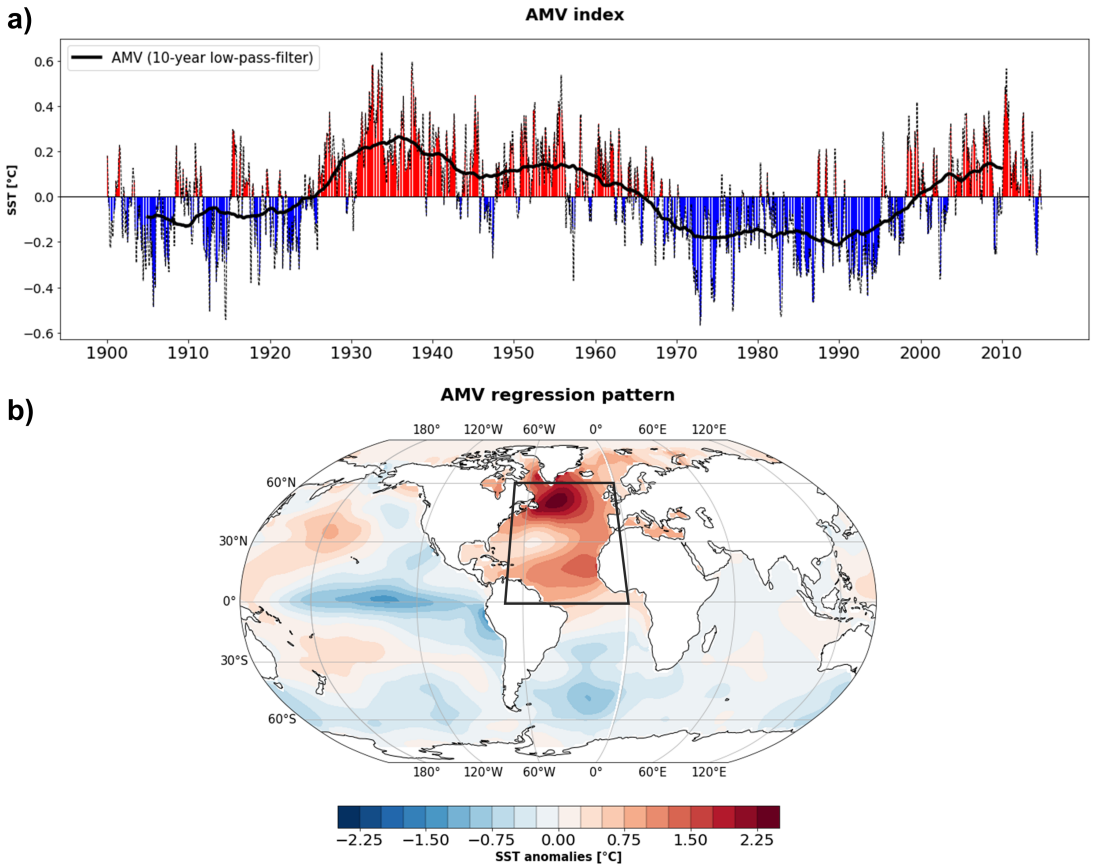


**Figure 2.11.:** Similar to 2.10 but for the Atlantic Multidecadal Variability. (a) The AMV Index, defined as the average monthly SST anomaly over the North Atlantic region (0–60N, region outlined by the black rectangle) minus the global mean monthly SST anomaly (red and blue). The black line depicts the 10-year low-pass-filtered time series representing the natural component of variability. (b) Regression pattern of global monthly SST anomalies (after removing the global mean SST anomaly) on the AMV Index in (a).

- **Tropical Atlantic variability:** The tropical Atlantic climate exhibits two dominant modes of variability on interannual to decadal time scales: the **Atlantic Zonal Mode (AZM)**, also colloquially referred to as the Atlantic Niño, and the **Atlantic Meridional Mode (AMM)**. These modes exert a substantial influence on climate patterns across various temporal scales, ranging from sub-seasonal to multi-year durations. The context of this thesis primarily emphasizes the tropical North Atlantic region in the study of these

modes. The AZM reaches its mature phase during the boreal summer upwelling season, characterized by maximum SSTAs in the eastern equatorial Atlantic. It is often analogous to the Pacific El Niño (Foltz et al. 2019; Keenlyside et al. 2007; Lübbecke and McPhaden 2017; Zebiak and Cane 1993). In contrast, the AMM operates on longer timescales and exhibits its peak influence during the boreal spring. It is identified by a cross-equatorial SST gradient with opposite signs in the northern and southern portions of the Atlantic Ocean. Both the AMM and AZM exert significant control over the ITCZ and related wind patterns, thereby significantly shaping climate patterns in adjacent and remote regions. The AMM primarily arises from air-sea heat fluxes and exhibits a thermodynamic nature (Chang et al. 2000; Foltz 2010). AZM and AMM constitute the primary and secondary patterns of tropical Atlantic variability. These modes can be characterized using spatial averages. The AZM is quantified by SST anomalies averaged over the equatorial Atlantic region (3°S–3°N, 0°–20°W). The AMM can be defined as the difference between normalized SSTAs averaged over the tropical North Atlantic (TNA) and tropical South Atlantic (TSA). The regression of SST anomalies onto the AMM time series (1958-2019) is shown in 2.11, adapted from IPCC 2021a, and where the black outline represents the region for the EOF definition while the cyan boxes represent the TNA and TSA regions. Hereupon, the TNA index is defined as the area-weighted monthly SSTAs over the north Tropical Atlantic region (5.5–23.5 N, 58 W–15 W) (Enfield et al. 1999). Furthermore, it is worth noting that this thesis places a particular emphasis on the TNA

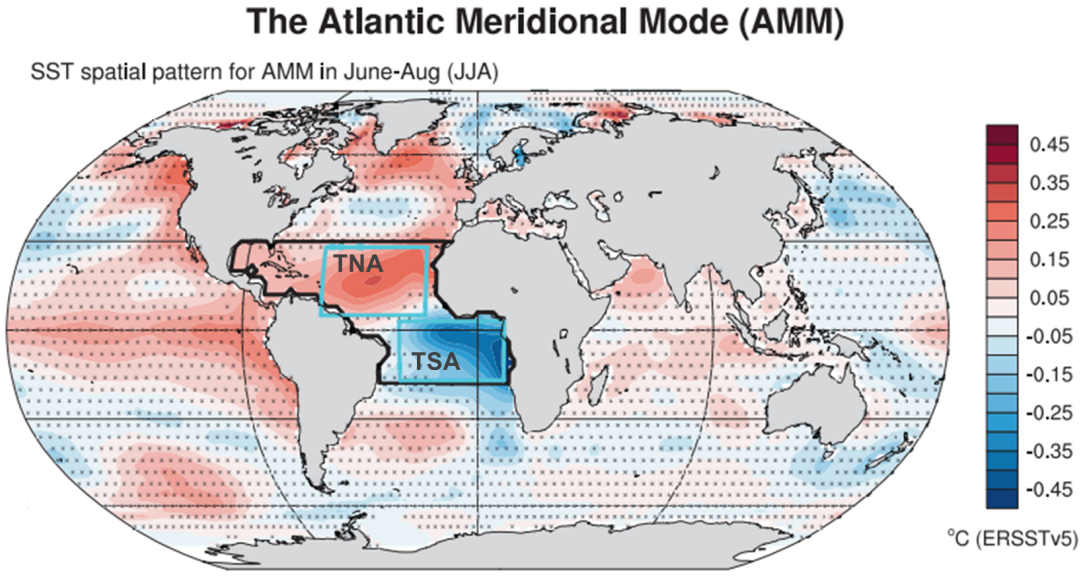


**Figure 2.12.:** Visualization of SSTAs regressed onto the AMM time series (not shown). The AMM during June–July–August (JJA), as represented by the standardized SST difference between the TNA region and the TSA region of the tropical Atlantic Ocean, as indicated by the cyan boxes. Additionally, the AMM is also estimated as the leading EOF over the tropical Atlantic Ocean (the region enclosed by the black box); here for the period spanning 1958 to 2019 using ERSSTv5 data. Figure adapted from IPCC 2021a.

due to recent studies indicating a potential interplay between tropical North Atlantic

and tropical Pacific variability at interannual time scales (Ham et al. 2013b; Ham et al. 2013a; Wang et al. 2017a). This teleconnection appears to be modulated over decadal time scales by the phases of the AMV (Wang et al. 2017a) and is further influenced by the increasing rate in global warming (Dong et al. 2014).

- **Madden–Julian Oscillation (MJO):** The MJO represents the predominant mode of tropical intra-seasonal variability, exhibiting a temporal scale ranging from 20 to 90 days (Madden 1986). It is considered as a fundamental driver of regional climatic changes and predictability on the sub-seasonal timescale, encompassing durations ranging from weeks to months (Madden and Julian 1994; Vitart 2017; Wheeler et al. 2017; Zhang 2013). This atmospheric phenomenon manifests as planetary-scale disturbances, characterized by zonal wavenumbers spanning 1 to 3, impacting atmospheric pressure, wind patterns, cloud formations, and precipitation. These disturbances predominantly propagate eastward along the equatorial belt at an average velocity of approximately 5 $m.s^{-1}$ (Roxy et al. 2019). More precisely, the MJO manifests as alternating zones of suppressed and enhanced convection, intricately linked to an anomalous zonal overturning circulation within the atmosphere (Zhang 2013).

  The MJO derives its variability from internal ocean-atmosphere processes that operate throughout the year. However, it exhibits distinct seasonality, with more pronounced signals during boreal winter. In contrast, during boreal summer, the centers of convective activity associated with the MJO migrate away from the equator, typically to latitudes between 10°N and 20°N. Concurrently, they propagate northward into the Asian monsoon region (Madden 1986; Yasunari 1980). The MJO's impacts can also extend beyond the seasonal context. Even though an index for the MJO is not explicitly used the results to be presented in this dissertation (Chapters 4 and 5), this oscillation plays an important role in shaping the timing and intensity of ENSO events, monsoons, tropical cyclones, and other related atmospheric phenomena (Lybarger and Stan 2019; Zhang et al. 2001).

  There are additional modes of climate variability with significant regional and global impacts. For example, the **Indian Ocean Dipole (IOD)** is the prominent mode of climate variability in the Indian Ocean. Positive IOD is characterized by negative SSTAs in the southeast equatorial Indian Ocean and weak positive anomalies in the western region. During negative IOD, this pattern is reversed, with positive SSTAs in the southeast and negative anomalies in the west (Zheng et al. 2010).

  Within the broader context of climate variability, modes like AMV and PDV, exert distinct modulations on global surface temperature trends across (multi-)decadal intervals since pre-industrial times. However, quantifying their individual influences remains challenging due to their intertwined nature and the potential effects of external forcing (Tung and Zhou 2013; Wu et al. 2011). Therefore, it is important to consider that, at the essence of climate variability lies the distinction between internally-generated climate

variability and externally-forced variability, both of which play integral roles in shaping Earth's climate and producing distinctive modes of climate variability.

### 2.2.2. Externally-forced variability

#### Natural forcing

Changes in the sun's emission, including variations in the intensity of solar radiation across different timescales, can externally induce climate variability. The sun's radiation changes are linked to interconnected phenomena such as sunspots, faculae, and flares, which arise periodically in the sun's active zones. Sunspots are colder regions that break the photosphere's typical convection pattern and are accompanied by high magnetic fields. Faculae, on the other hand, are hotter areas that emit strong magnetic fields and are frequently encountered in association with sunspots. Flares are powerful bursts of high-energy radiation and particles from the sun's outer atmosphere, accompanied by magnetic fields and strong motions (Wallace and Hobbs 2006a). Solar activity follows an approximately 11-year cycle, during which these phenomena occur in a sequence known as the solar cycle. The sun's emissions vary with this cycle, and during active phases, disturbances like sunspots, faculae, and flares are more frequent. Solar energy heats the Earth's surface, with about half in the visible short-wave part and the rest mostly in the near-infrared part of the electromagnetic spectrum. The Earth's surface absorbs a significant portion of this energy, warming the land and ocean. The atmosphere also plays a role in the exchange of energy, with GHGs trapping heat, known as the natural greenhouse effect (Masson-Delmotte et al. 2021). This effect allows a temperature near the Earth's surface of about 14°C, while radiating the excess heat back into space (Masson-Delmotte et al. 2021). However, the human emissions of $CO_2$, discussed in the next section, enhanced this effect to unprecedented levels. Radiative forcing refers to the change in net downward radiative flux at the tropopause or top-of-atmosphere due to an imposed perturbation relative to a reference state (usually pre-industrial, Masson-Delmotte et al. 2021). Natural external forcings, like variations in solar radiation or volcanic aerosols, can lead to natural variations in radiative forcing, either positive (warming) or negative (cooling), prompting the climate system to restore equilibrium. With their impact on the atmosphere, volcanic eruptions can cause externally imposed climatic fluctuation. While the geothermal energy released during volcanism has little impact on global heat balance, the climatic consequences of eruptions are principally driven by the formation of sulfate aerosols from ejected sulfur dioxide ($SO_2$). These volcanic particles are removed from the troposphere by cloud droplets in a matter of weeks. Major eruptions, on the other hand, that send plumes into the lower stratosphere, can have a considerable impact on the Earth's climate (Masson-Delmotte et al. 2021; Robock 2000). Volcanic eruptions can also inject large amounts of water vapor into the stratosphere. Water vapor is a GHG that can enhance the warming effect of other gases, but it can also form polar stratospheric clouds that catalyze ozone depletion (Solomon et al. 2010). Since sulfate particles in the stratosphere deflect solar energy, both direct and total solar radiation reaching the Earth's surface are reduced. This scattering effect causes a brief drop in global-mean surface

air temperature (Masson-Delmotte et al. 2021; Wallace and Hobbs 2006a). The warming of the lower stratosphere due to aerosol absorption is another consequence of volcanic eruptions. The cooling effect of volcanic eruptions on the Earth's surface lasts longer than the lifetime of stratospheric particles (Masson-Delmotte et al. 2021; Robock 2000; Solomon et al. 2010). This is due to the involvement of the ocean mixed layer, which has a high heat capacity. Heat fluxes between the ocean surface and the atmosphere respond to temperature differences induced by aerosols, dampening the cooling impact of the atmosphere. When aerosols disperse, insolation patterns normalize, the ocean mixed layer gradually recovers lost heat, and global-mean surface air temperature eventually returns to normal (Masson-Delmotte et al. 2021; Robock 2000). Clouds also influence the Earth's energy balance, both absorbing and emitting infrared radiation. The net effect of clouds in the current climate is a slight cooling, as their reflection of solar radiation compensates for their greenhouse effect (Masson-Delmotte et al. 2021).

#### Human-induced changes

The emission of GHGs and aerosols from human activities, such as the combustion of fossil fuels and biomass burning, has significantly impacted the composition of the atmosphere. Moreover, human-made halogen compounds, like chlorofluorocarbons (CFCs), not only contribute to radiative forcing but also deplete the stratospheric ozone layer. In addition to that, land use due to urbanization, deforestation, and agricultural practices alter the physical and biological properties of the Earth's surface, leading to changes in the radiative forcing and potential impacts on regional and global climate (Masson-Delmotte et al. 2021). Over the past thousand years, GHG concentrations remained relatively stable. However, since the Industrial Revolution in the mid-18th century, the concentration of GHGs increased significantly. Particularly, the concentration of $CO_2$, has risen from 278 parts per million (ppm) in 1750 to about 420 ppm at the time of writing this thesis (Masson-Delmotte et al. 2021; NOAA 2021). This increase is unquestionably anthropogenic, as confirmed by the changing isotopic composition of atmospheric $CO_2$. Other radiatively active compounds, such as methane ($CH_4$) and nitrous oxide ($N_2O$), are also experiencing a continuous increase, primarily attributed to extensive agricultural and industrial activities. The IPCC AR6 (Masson-Delmotte et al. 2021) puts things into context: the report says that from 2011 to 2020, the Earth's surface temperature was increased by 1.1ºC compared to the late 19th-century baseline predating the industrial revolution. This temperature is unprecedented in the past 100,000 years. In a historical context stretching back to 1850, each recent decade has successively recorded higher average temperatures, indicating a rapid warming phase unparalleled in the last two millennia (Masson-Delmotte et al. 2021).The concentration of GHGs in the atmosphere is experiencing a continual increase due to human-induced emissions. Presently, the levels of carbon dioxide are the highest observed in over 2 million years, while the concentrations of methane and nitrous oxide have not been this high for at least 800,000 years (Masson-Delmotte et al. 2021). The unprecedented rate at which the GHG concentration is increasing enhances the greenhouse effect, by increasing the opacity of the atmosphere. Ultimately, this results in even

higher absorption and emission of infrared radiation. The overall feedback effect amplifies the temperature increase, making the response of the climate system much more complex than a simple temperature rise (Masson-Delmotte et al. 2021). One of the most critical feedbacks in the climate system is the water vapor feedback. As atmospheric temperatures rise due to increased GHGs, the atmosphere can hold more water vapor, a potent GHG. This leads to a further increase in the greenhouse effect, trapping more heat in the atmosphere. The strength of the water vapor feedback has been a subject of concern and study, particularly regarding its impact on upper tropospheric humidity. The impact of aerosols on the radiative forcing is complex and varies in space and time. Aerosols scatter solar radiation back into space, resulting in a negative radiative forcing that might partially offset the enhanced greenhouse effect. However, aerosols have a short atmospheric lifetime, leading to inhomogeneous regional effects, complicating their overall impact on the climate system (Masson-Delmotte et al. 2021; Neelin 2010). Land-use change is recognized as a significant contributor to changing local, regional, and global climates. It alters the physical and biogeochemical properties of the land surface, affecting processes like albedo and greenhouse gas exchange between land and atmosphere. Urbanization, as a type of land use, creates urban heat islands and can influence long-term temperature records locally and globally (Masson-Delmotte et al. 2021; Neelin 2010). As mentioned earlier, to understand the climate system's response to these human-induced changes, numerical models based on established physical, chemical, and biological principles are used. These models help quantify the complex non-linear climate response, considering various coupled components of the climate system with different response times to perturbations.

### 2.2.3. Teleconnections: Atlantic - Pacific interactions

In atmospheric science, "teleconnection" refers to the interconnected changes observed in geographically distant climates, whether they occur simultaneously or with a time lag. Each of the modes introduced in 2.2.1 has its own principal center of variability: the North Atlantic for NAO and AMV, the tropical Pacific for ENSO, and the tropical/North Pacific for PDV. In terms of timescale, ENSO occurs on interannual timeframes, whereas PDV and AMV occur across decades. These oscillations coexist, but they interact and evolve over time, adding complexity to understanding their regional climatic implications. These interactions can even produce unexpected patterns, causing an oscillation's influence on regional climate to diverge from what was expected.

The intricate connections between the Atlantic and Pacific basins have been the focus of extensive research, spanning different timescales and revealing a range of influencing mechanisms (Latif and Grötzner 2000; McGregor et al. 2014; Meehl et al. 2016; Meehl et al. 2021a; Ruprich-Robert et al. 2017). These interactions involve complex processes through which one basin can influence the other and vice versa, leading to significant interannual-to-decadal climate variability in both regions. A tropical pathway for the Atlantic-Pacific connection is mainly driven by modifications in the Walker circulation that affect large-scale tropical weather

systems (Kucharski et al. 2007; McGregor et al. 2014; Nnamchi et al. 2015). Moreover, the connection between the two basins is also established through extratropical routes. For example, in the northern hemisphere, the PNA and NAO teleconnections not only link the Atlantic and Pacific basins but also exert considerable influence over Arctic sea ice responses (Galytska et al. 2023; Meehl et al. 2018; Polyakov and Johnson 2000) and shape European climate (Brönnimann 2007). Understanding these connections is essential for predicting and comprehending long-term climate patterns and their impacts on weather systems and ecosystems.

Previous investigations have shown a bidirectional relationship, where changes in one basin can impact the other, often mediated by the tropical Indian Ocean (Kumar et al. 2014; Levine et al. 2017; Li et al. 2016; Yang et al. 2020). Specifically, on the decadal timescale, (Meehl et al. 2021a) underscored how a positive AMV phase can lead to a negative PDV phase mainly through altered Walker circulation (Fig. 2.13a). During the subsequent decades, the negative PDV is found to drive a negative AMV. In addition to the Walker circulation, this interplay also involves the influence of convective heating and precipitation anomalies in the tropical Pacific, triggering connections to extratropical atmospheric variability modes like the PNA and PSA (Meehl et al. 2021a; Fig. 2.13b). On shorter timescales, a recent study by Park et al. 2023 explored inter-basin interactions between the Atlantic and Pacific, revealing how ENSO affects SSTAs of the north Tropical Atlantic (NTA; 0°–15°N) during spring and summer through both tropical and extratropical pathways. The TNA is a region of the Atlantic Ocean that is strongly influenced by the ENSO SST variability (Park et al., 2019). Atmospheric teleconnections connect ENSO and NTA on seasonal to interannual timescales. ENSO has been proven in studies to have an impact on SSTAs in the NTA during the spring and summer via both tropical and extratropical pathways (Park et al. 2023). SST variability in the NTA, on the other hand, has the potential to impact subsequent ENSO events over the following boreal winter by changing anomalous low-level zonal winds via atmospheric teleconnections over the equatorial western Pacific (Park and Li 2019; Park et al. 2023) Previous studies proposed similar mechanisms for the ENSO teleconnection to SSTAs over the TNA region (i.e. 5.5°–23.5°N, overlapping with the 0°–15°N NTA region). Due to their overlapping spatial projection, in the context of cross-basin interactions, both TNA and NTA regions capture the interplay between the Atlantic and the Pacific. However, in this thesis, the TNA index is used to represent the tropical Atlantic variability as it separates the northern part of the AMM, in contrast with the NTA which includes regions where the AZM and TSA are defined (see 2.2.1). According to previous studies, we can summarize mechanisms connecting Atlantic and Pacific tropical SSTs as follows:

- **The impact of ENSO on tropical Atlantic:**
    1. **Extratropical Rossby wave train:** this mechanism involves an atmospheric wave train (PNA-related) that propagates from the North Pacific to the North Atlantic, modulating the strength of the Azores anticyclone (NAO-related) and the trade winds in winter. This affects the latent heat flux and the mixed layer depth in the TNA region, affecting SST anomalies in spring (Enfield and Mayer 1997).

2. **Atmospheric bridge:** this mechanism involves a change in the Atlantic Hadley circulation induced by the PWC, affecting the subtropical high pressure and the trade winds in winter. This also affects the latent heat flux and the mixed layer depth in the TNA region, leading to SST changes in spring (Klein et al. 1999).
3. **Tropospheric temperature mechanism:** involves an eastward propagation of a Kelvin wave front triggered by the ENSO heating anomaly in the tropical Pacific, influencing the upper-tropospheric temperature and moist convection in the tropical Atlantic. This affects the shortwave radiation and the stability of the mixed layer in the TNA region, leading to SST anomalies in spring (Chiang and Sobel 2002; Chiang and Lintner 2005; Yulaeva and Wallace 1994).
4. **Remote Gill-type response:** another mechanism involving changes in the PWC is the secondary Gill-type response to the zonally compensated heat source over the Amazon basin following ENSO, proposed by (García-Serrano et al. 2017). This mechanism generates a baroclinic anticyclonic anomaly over the TNA region that weakens the trade winds and reduces evaporation and ocean mixing in spring (DeWeaver and Nigam 2002, 2004; Sasaki et al. 2015).

Note that the nature of these ENSO-driven teleconnections to the TNA is influenced by NAO and the AMM, which can either reinforce or dampen the relationship. During spring, warmer SSTs than usual are observed over the TNA region. This warmth leads to stronger convection; essentially, the vertical movement of warm, moist air that triggers clouds and precipitation (Ham et al. 2013b).

- **The impact of tropical Atlantic on ENSO:**
  1. **The Rossby wave response** to the west of the anomalous heat source over the TNA enhances the trade winds over the northeastern Pacific and cools the SST there (Ham et al. 2013a).
  2. **The Kelvin wave response** to the east of the anomalous heat source over the TNA interacts with the monsoonal westerly over the northern Indian Ocean and the Marititime Continenet and induces warm SST and positive heating anomaly there (Rong et al. 2010; Yu et al. 2016).
  3. **The wind–evaporation–SST–convection (WESC) feedback** over the northern Indian Ocean and Maritime continent further generates easterly anomalies over the equatorial western Pacific and triggers La Niña (Giannini et al. 2000; Jiang and Li 2021; Li et al. 2017).

**Regimes of Atlantic-Pacific interactions between 1950-2014**

The relationship between the TNA and ENSO has changed over time, with the influence of TNA on ENSO strengthening since the mid-1980s, linked to a positive phase shift of the AMV and/or human-caused warming (Meehl et al. 2021a; Park and Li 2019; Park et al.

2023). In contrast, the effect of ENSO on the TNA has decreased during the same period, leading to the identification of two contrasting regimes: a Pacific-driven regime from 1950 to the mid-1980s and an Atlantic-driven regime from the mid-1980s to 2014 (Meehl et al. 2021a; Park et al. 2023). These contrasting regimes span multiple decades and are crucial in understanding the inter-basin interactions between the Atlantic and Pacific Oceans. Figure 2.14, adapted from Park et al. 2023 explains how the Pacific and Atlantic basins interact in two contrasting ways, providing insights, into the mechanisms that shape the relationship between these basins. In Fig. 2.14a shows the Pacific-driven regime, which emphasizes the role of connections generated by ENSO across both extratropical regions. This leads to dipole patterns of SSTAs across the Atlantic ITCZ that resemble the AMM from spring to summer. As a result there is a contrast in precipitation along the ITCZ, where opposing reactions balance each other out in the Pacific. This scenario reduces the influence of the Atlantic on the Pacific. On the hand, Fig. 2.14b illustrates an Atlantic-driven regime where ENSO's impact on the Atlantic is weakened. During this period, internal variations in circulation within the basin play a significant role in shaping monopole SSTA field resembling patterns seen in NAO-like atmospheric circulation. This monopole SSTA is accompanied by an overall enhancement of precipitation in the tropical Atlantic, leading to the modulation of zonal winds. As a result, signals originating in the tropical Atlantic are propagated to the tropical Pacific, exerting a modulatory impact on ENSO events. Lead-lag correlation during the 1948-2020 revealed, according to Park and Li 2019; Park et al. 2023, that the Pacific basin influence on the Atlantic is more easily established than vice versa.

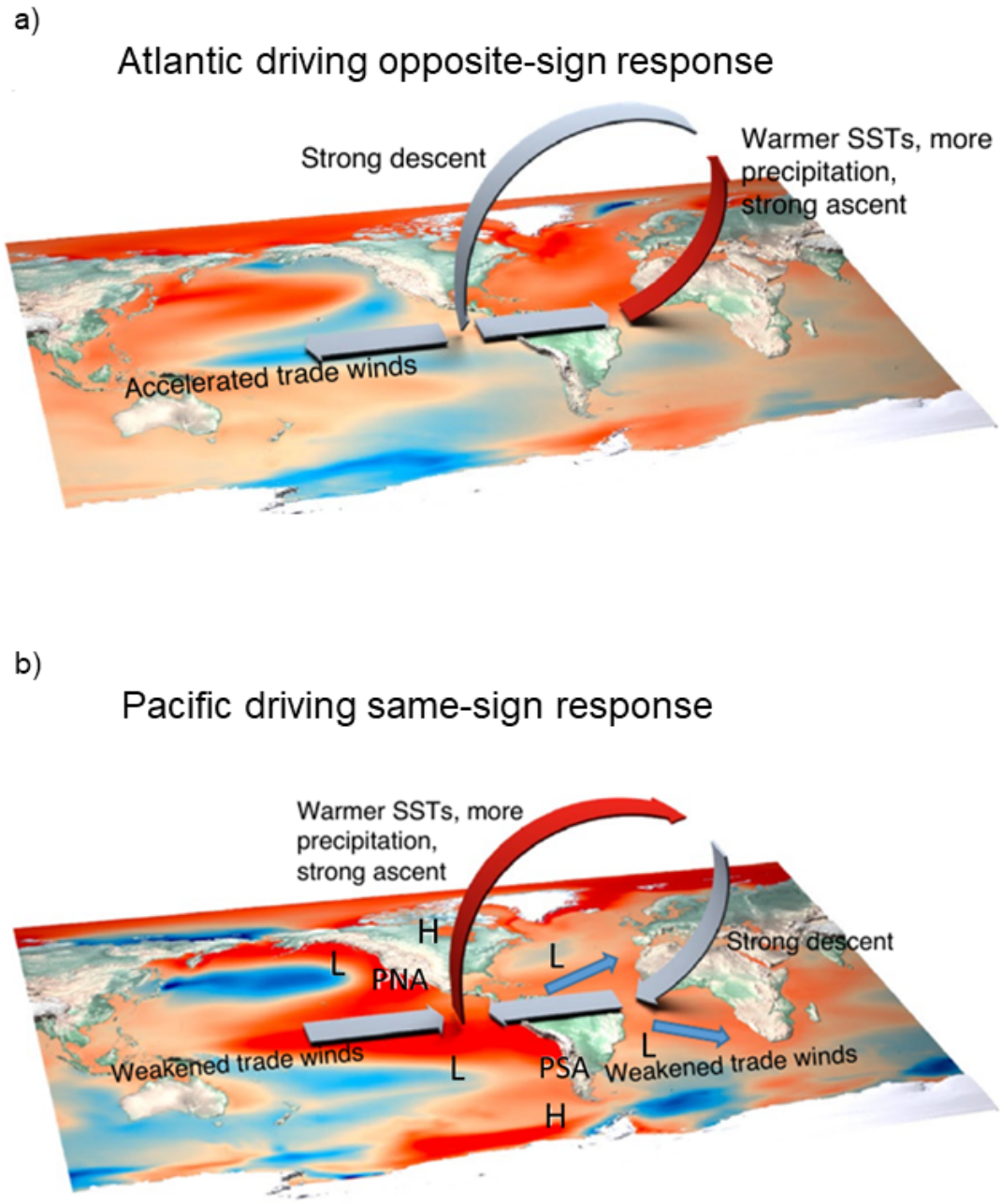


**Figure 2.13.:** Atlantic-Pacific interactions on decadal timescales. a) Schematic illustrating how a positive AMV leads to an opposing negative response in PDV-associated SSTs within the tropical Pacific. This phenomenon primarily occurs through the influence of the tropical Walker circulation. Background SST similar to pattern in 2.11. b) Similar representation to panel a, except in this scenario, a positive PDV in the tropical Pacific corresponds to a positive AMV in the tropical Atlantic. This interaction is driven by both the tropical Walker circulation and extratropical teleconnections. These teleconnections arise from positive anomalies in precipitation and convective heating in the tropical Pacific which result in the formation of a specific PNA pattern across North America, characterized by a sequence of anomalous low–high–low SLP patterns (L—H—L), and a comparable PSA pattern across South America. Background SST similar to pattern in 2.10. Figure adapted with permission from Meehl et al. 2021a.

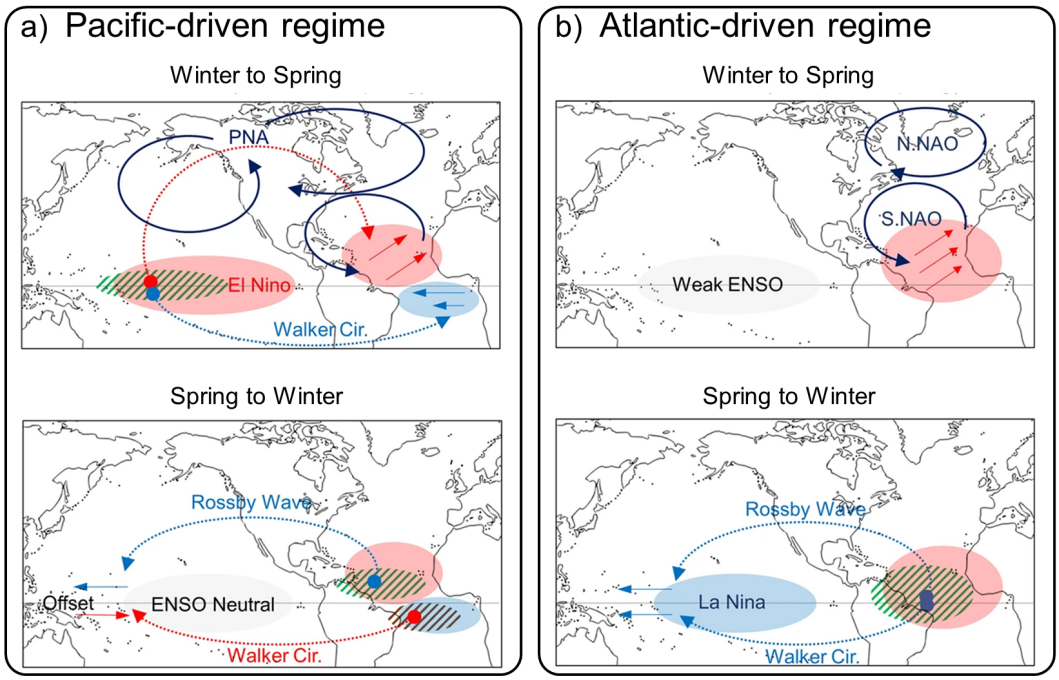


**Figure 2.14.:** Diagram depicting the inter-basin interactions between the Pacific and Atlantic. a) The formation of a tropical Atlantic mode throughout winter to late spring, and its impact on the tropical Pacific from late spring to the next winter in the Pacific-driven regime (e.g. 1950–1983). The red, blue, and gray shadings represent SSTA warming, cooling, and normal conditions, respectively. Dark blue solid arrows represent low-level atmospheric circulation associated with PNA and NAO. The dotted red and blue arrows represent atmospheric teleconnections that cause warming and cooling of the underlying SSTAs, respectively. The straight red and blue arrows represent unusual low-level winds. The green and brown hatching lines indicate increased and decreased precipitation, respectively. b) is analogous to (a), but for the Atlantic-driven regime (e.g. 1985–2014). Figure adapted from Park et al. 2023.

# 3. Methodology and data sources

## 3.1. Coupled Model Intercomparison Project Phase 6 (CMIP6)

To facilitate a nuanced understanding of the complex interactions introduced in the previous Chapter, this thesis employs ESMs from the most recent phase of CMIP, Phase 6 (CMIP6, Eyring et al. 2016). Historical CMIP6 simulations are driven by a range of forcings, both natural (e.g., solar and volcanic) and anthropogenic (e.g., GHGs, aerosols, and land-use changes), covering the period from 1850 to 2014. The scope of our analyses, however, is confined to the sub-periods 1900-2014 (Chapter 4) and 1950-2014 (Chapter 5). In the context of enhanced model sophistication and carefully curated datasets, the study gains additional rigor by utilizing large ensembles of CMIP6 historical runs. Despite persistent debates around the "signal-to-noise paradox" within the domain of climate modeling (Chylek et al. 2020; Klavans et al. 2021; Klavans et al. 2022; Sato et al. 2018; Scaife and et al. 2014; Smith et al. 2019; Wang et al. 2017a), large ensembles have proven instrumental in delineating observed climatic trends and attributing anthropogenic influences therein (Borchert et al. 2021; Deser and Phillips 2023; Deser 2020; Klavans et al. 2022; Meehl et al. 2013; Menary et al. 2020; Tebaldi et al. 2021). Such ensembles afford a robust sampling of internal model variability and facilitate the assessment of changes driven by external forcings (Borchert et al. 2021; Deser and Phillips 2023; Klavans et al. 2022; Menary et al. 2020). Consequently, these large ensembles serve as an invaluable tool for this thesis, providing comprehensive coverage of historical natural and anthropogenic external forcings. Furthermore, this thesis does not only utilize historical simulations; more specifically, Chapter 5 also incorporates a CMIP6 pre-industrial control simulation to represent conditions prior to the large-scale industrialization that began in 1850. Additionally, an ensemble of pacemaker simulations, where equatorial Pacific SSTs have been adjusted to observed values, is utilized to scrutinize Atlantic-Pacific interactions in Chapter 5. Each section provides further details on the specific models employed for the analyses.

## 3.2. Reanalysis and observational datasets

In general, models are frequently compared to observational or reanalysis datasets (based on observations) in order to test their realism. Observations encompass a wide range of climate variables, such as temperature, precipitation, sea level, and atmospheric composition, gathered through instruments, satellites, and ground-based measurements. Reanalysis datasets merge observations from various sources, including weather stations, satellites, and ocean buoys, with the aid of sophisticated data assimilation techniques. Reanalyses offer a compre-

hensive, spatiotemporally consistent picture of the Earth's climate system, with the advantage of extending back in time. The iterative process of model evaluation and refinement is central to advancing the fidelity of ESMs, enabling more accurate climate projections, and ultimately enhancing our understanding of the Earth's intricate climate system. More details on the different observational and reanalysis datasets used in this thesis are presented in the respective Chapters 4–5.

## 3.3. Empirical orthogonal function (EOFs)

Effective analysis of complex nonlinear dynamic systems requires interpreting high-dimensional datasets with spatiotemporal correlations (Chang and Chao 2014; Hannachi et al. 2007). To tackle this, reducing correlated variables to fewer unobserved ones is common (Bjornsson and Venegas 1997; Chang and Chao 2014; Navarra and Simoncini 2010). However, challenges like regional dependencies, data gaps, and nonlinearity arise (Kondrashov and Ghil 2006; Xu 2016). A principal component analysis (PCA) based on EOFs is a powerful spatiotemporal statistical approach that stands out for addressing such challenges (Jolliffe 1990). However, unlike traditional statistical tests, there is no predefined probability distribution or underlying physical principles guiding EOF analysis. Instead, it partitions a field into mathematically orthogonal modes, often interpreted as atmospheric or oceanographic structures. This technique uncovers dominant patterns by decomposing them into distinct spatial and temporal modes (Bjornsson and Venegas 1997; Jolliffe 1990). This method enhances signal-to-noise ratio and quantifies variations (Uwamahoro et al. 2019), playing a pivotal role in prediction, estimation, and detection (Kim and North 1997). It adapts to data without a priori information, making it data-driven and easy to implement, with extensions for different data types (Chang and Chao 2014; Hannachi et al. 2007; Neha and Pasari 2022). Typically, EOFs are deduced by computing the eigenvalues and eigenvectors of a spatially weighted anomaly covariance matrix of a given field. The spatial weighting is typically based on quantities like the cosine of latitude, or the more suitable square-root of cosine of latitude. The set of equations for the PCA analysis can be found in textbooks about statistical methods used in atmospheric sciences, e.g. (Wilks 2011). Eigenvalues offer insights into the proportion of variance accounted for by each mode, although sampling issues might blur their distinctiveness. A heuristic from North 1984 provides insights into discerning distinctive eigenvalues. Physical interpretation of EOFs might face two challenges: the orthogonality constraint and domain-dependent patterns. Real-world systems often lack orthogonality, and the patterns' existence might be contingent on the chosen geographical domain. Nevertheless, despite these limitations, classical EOF analysis remains valuable (Shea 2023, last access: 15 September 2023). The utility of EOFs have been demonstrated through the examples of the PC time series and regression patterns of some of the main modes of climate variability discussed in Section 2.2.1 (e.g. NAO, PNA,PSA1, PDV). Furthermore, deriving indices and spatial patterns of major modes using

EOF analysis has been an essential part in the preprocessing and analysis underlined in both Chapter 4 & Chapter 5.

## 3.4. Diagnostics for climate variability analysis

In order to scrutinize crucial aspects of inherent climate fluctuations, the study in Chapter 4 utilizes the CVDP-LE (Phillips et al. 2020), an analytical framework developed by NCAR. This framework is designed to specifically analyze large ensemble climate model outputs, offering a range of diagnostics for calculating key indices of coupled ocean-atmosphere and large-scale atmospheric climate variability, such as the ones discussed in Section 2.2.1. The package also provides the capability for evaluating these model-based diagnostics against benchmark observational databases on both temporal and spatial scales. The CVDP-LE diagnostics used in Chapter 4, are publicly available in the form of NetCDF files through the Climate Variability and Change Working Group (CVCWG) CVDP-LE Data Repository affiliated with the Community Earth System Model (CESM). Within this section, the modes of interest are AMV, PDV, PNA and PSA1, discussed in detail earlier in Section 2.2.1.

## 3.5. Time-series causal discovery

In climate science, traditional statistical methods have limitations in capturing causal relationships among variables. These limitations necessitate alternative methodologies capable of identifying and interpreting causal mechanisms. The methodology in this thesis aims to address this need. According to Pearl and Mackenzie, causal inference is the science of discovering how things affect each other in the real world based on the idea that we can use data and logic to discover the causal relationships among variables, and to answer questions about what would happen if we intervene or change some of the variables (Pearl and Mackenzie 2018). Causal inference goes beyond the traditional statistical methods that only measure associations or correlations, and aims to reveal the underlying mechanisms and structures that produce the observed phenomena. In the realm of causal inference, we refer to causal discovery as the process of reconstructing a full causal graph from data and underlying assumptions, translating the causal relationships among variables (Pearl and Mackenzie 2018; Peters et al. 2017). In climate research, understanding the causal relationships behind observed phenomena is crucial. While commonly used techniques like Pearson correlation and linear regression models are useful for identifying associations between variables, they fall short when it comes to uncovering the underlying causes driving these relationships (Runge et al. 2015). Pearson correlation, for instance, can mistakenly identify connections between variables due to confounding factors or autocorrelation. Granger causality (Granger 1969), which accounts for autocorrelation, has been applied to detect climate system teleconnections, revealing statistically robust relationships supported by physical mechanisms. However, it has limitations, primarily detecting lagged causal dependencies and potentially spurious causal

links in low-resolution data. Additionally, the traditional bivariate form of Granger causality cannot handle common drivers (Bathiany et al. 2018; Runge et al. 2014; Runge et al. 2019a). This is where the causal discovery method used in this thesis brings an advantage. Such methods make use of general assumptions about underlying processes to fully account for common causes and reconstruct causal relationships among multiple variables. They provide a valuable means of gaining deeper insights into causal processes and can be viewed as an interpretable technique within the field of machine learning (Xu et al. 2020). In the domain of time series causal discovery within complex dynamical systems, the objective is to statistically estimate causal connections, including their temporal lags. This is particularly relevant for climatic teleconnections, which manifest over varying time scales. The task can be complicated due to the high dimensionality of the variables and their interconnected nature. In systems with multiple variables, such as regional climate indices, correlations can result from multiple factors including autocorrelation within the series, or because of common drivers. Effective causal discovery aims to enhance the identification of true causal links while minimizing false positives (Runge et al. 2019b). These methods are valuable for gaining insights into the underlying physical processes, enhancing predictive models, and providing reliable estimates of causal strengths.

### 3.5.1. PCMCI+ algorithm

One widely employed framework for causal discovery is the conditional independence-based approach. This method relies on several key assumptions, including time-order, causal sufficiency, the Causal Markov condition, and faithfulness. It utilizes iterative conditional independence testing and has found application in various climate research areas (Bathiany et al. 2018; Di Capua et al. 2020; Ebert-Uphoff and Deng 2012; Runge et al. 2014; Runge et al. 2019a) including exploring pathways of teleconnections (Galytska et al. 2023; **Karmouche** et al. 2023a; Kretschmer et al. 2021), investigating cold-air outbreaks (Polkova et al. 2021) or conducting process-oriented climate model evaluations (**Karmouche** et al. 2023a; Nowack et al. 2020). The Peter Clark Momentary Conditional Independence (PCMCI) algorithm is a powerful causal discovery tool for time series data, addressing some of the limitations of previous approaches like the naive adaptation of the PC algorithm (named after its authors, Peter Spirtes and Clark Glymour; Spirtes and Glymour 1991; Spirtes et al. 2000). PCMCI operates under specific assumptions, including the absence of contemporaneous causal influences and the assumption that the causal relationships remain stationary over time (Runge et al. 2019a). To facilitate the causal analyses within this framework, we utilize in Chapter 4 & Chapter 5 the Tigramite Python package (Runge 2022), an open-source tool [1] designed to efficiently estimate causal graphs from time series datasets and which includes implementations of different PC-based algorithms. Time series data poses unique challenges, notably autocorrelation, which can lead to ill-calibrated conditional independence tests and low detection power. PCMCI techniques address these issues to some extent by employing a specific selection of conditioning sets in

[1] Available at https://github.com/jakobrunge/tigramite (last accessed on 17 September 2023)

the independent tests that determine the presence or absence of an edge between a given pair of variables. PCMCI+, implemented through the Tigramite package, extends these capabilities of PCMCI by allowing for contemporaneous edges while maintaining rigorous control over causal cycles and latent confounders (Runge 2020). PCMCI+ comprises three phases as illustrated in Figure 3.1a:

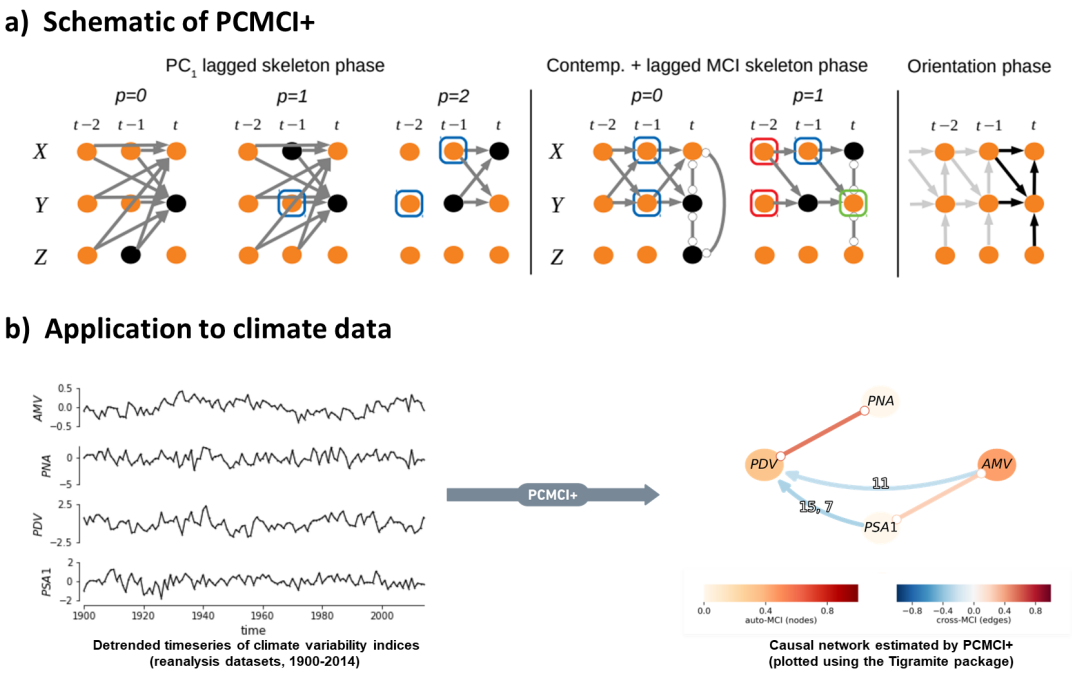


**Figure 3.1.:** a) Schematic illustrating the three phases of PCMCI+ algorithm applied to a time-dependent system given by the variables $X, Y, Z$. Details on each phase are explained in the text below. Panel (a) is adapted from Runge 2020. b) Application to real data. Constructing causal networks through the application of PCMCI+ to time series data of modes of climate variability from reanalysis datasets (left). In the causal network representation (right), each node corresponds to a variable (as seen in the left time series), with node color indicating the auto-correlation (representing self-links for each variable). The color of the links between nodes signifies the cross-MCI partial correlation value, which conveys both the sign and strength of the inferred causal relationship between two variables. Additionally, the time lag associated with lagged links (curved arrows) is denoted by small labels positioned on the links, while straight lines indicate instantaneous causal links occurring with no temporal delay. Panel (b) is adapted from **Karmouche** et al. 2023a

- **PC1 lagged phase (skeleton discovery):** In the context of a time-dependent system denoted as $X_t$, comprising $N$ variables $\mathbf{X_t} = (X_t^1, ..., X_t^N)$, the initial phase of skeleton discovery is initiated with the application of the PC1 Markov set discovery algorithm (Fig. 3.2a illustrates the case for $\mathbf{X_t} = X, Y, Z$). This algorithm, rooted in the PC algorithm (Spirtes et al. 2000), is employed on an initially fully connected graph. During each substep of the skeleton phase (indexed as $p$), starting at $p = 0$ and successively increasing $p$ in increments of one, the iterative PC1 procedure systematically examines each pair of lagged nodes (variables), represented as $(X_{t-\tau}^i, X_t^j)$, to determine their conditional independence in the presence of judiciously selected conditions derived from other lagged variables. Subsequently, if conditional independence is established, the algorithm

removes the adjacency linking these nodes. Notably, during this phase, the lagged conditions are instrumental in estimating, for each variable $X_t^j$, an encompassing set of lagged parents, denoted as $\widehat{\mathcal{B}}t^-(Xt^j)$, which subsequently guide the orientation of adjacencies in a time-sequential manner (left panels in Fig. 3.2a). However, it's important to note that this phase may still contain spurious connections arising from autocorrelation and false positives. Effectively addressing these challenges is handled in the next phase.

- **Momentary conditional independence (MCI) phase, contemporaneous and lagged:** The primary objective of this phase is to conduct conditional independence tests to further refine the skeleton discovery of causal relationships by eliminating spurious connections. This is done through a series of MCI tests, which employ partial correlation as the underlying statistical tool to examine the null hypothesis:

$$X_{t-\tau}^i \perp\!\!\!\perp X_t^j | \mathcal{S}, \widehat{\mathcal{B}}_t^-(X_t^j) \setminus \{X_{t-\tau}^i\}, \widehat{\mathcal{B}}_{t-\tau}^-(X_{t-\tau}^i) \tag{3.1}$$

  These tests assess the conditional independence of variables $X_{t-\tau}^i$ and $X_t^j$ with respect to a set of variables denoted as $\mathcal{S}$, conditioned on the lagged conditions $\widehat{\mathcal{B}}_t^-(X_t^j)$, and the time-shifted lagged conditions of $X_{t-\tau}^i$ previously acquired during the initial phase $\widehat{\mathcal{B}}_{t-\tau}^-(X_{t-\tau}^i)$. This iterative process encompasses subsets $\mathcal{S}$ from the set $\mathbf{X_t}$, representing contemporaneous adjacencies. The computed partial correlation tests yield a $t$-statistic and the degrees of freedom for these tests are determined by the effective sample size, calculated as

$$n - 2 - |\mathcal{S}, \widehat{\mathcal{B}}_t^-(X_t^j)) \setminus \{X_{t-\tau}^i\}, \widehat{\mathcal{B}}_{t-\tau}^-(X_{t-\tau}^i)\}|$$

  The outcome of this phase is a causal graph characterized by both lagged and contemporaneous connections (central panels in Fig. 3.2a). Subsequently, the algorithm enters a collider orientation phase, which further refines the orientation of contemporaneous links.

- **Orientation (Collider) Phase:** This phase is predicated on identifying unshielded triples of the form $X_{t-\tau}^i - X_t^k - X_t^j$, where $\tau \geq 0$. If $X_t^k$ does not belong to the separating set $\mathcal{S}$, which establishes the conditional independence between $X_{t-\tau}^i$ and $X_t^j$, the triple is oriented as $X_{t-\tau}^i \rightarrow X_t^k \leftarrow X_t^j$. The orientation process continues, ensuring that the resultant graph remains acyclic (right panel in Fig. 3.2a), adhering to predefined rules (R1-R3, as outlined in Runge 2020).

Various attributes of the derived causal relationships can be discerned directly from the network (right panel in Fig. 3.2b). These include the directionality, sign, and magnitude of the cross-MCI values, as well as the time lags, denoted by $\tau$, associated with each link. Each node in the network is indicative of a time series and its color represents its auto-correlation. Similarly, the color of the links translates the sign and strength of the corresponding causal relationship. Lagged relationships are depicted by curved arrows, annotated with small labels showing the time lags. If multiple significant time lags are identified for a single link,

the label will display them sorted by strength. The resulting graph encompasses directed lagged and contemporaneous links, along with unoriented adjacencies. These unoriented adjacencies may indicate either Markov equivalence, where collider and orientation rules are inapplicable (o-o), or conflicting adjacencies, a result of rule conflicts stemming from finite sample issues (x-x). The strength of the links can be estimated in various ways, such as standardized (causal) regression coefficients (Runge et al. 2015; Runge 2021). In Figure 3.1b and the results in Chapter 4, the link strengths are shown as MCI partial correlation values (cross-MCI) corresponding to the aforementioned conditional independence test statistic. In next section's proof of concept (Section 3.5.2) and Chapter 5, we quantify link strengths using standardized regression coefficients, as outlined in Runge et al. 2015, employing a linear mediation model based on the original parents identified by PCMCI+. More specifically, we assess the influence of each variable $X_t^j$ on its respective parents, $pa(X_t^j)$. Subsequently, the regression coefficients associated with each parent provide a link coefficient that holds a causal interpretation within the given assumptions. Assuming the variables $X$ and $Y$ are represented by their time series and considering a time lag $\tau$, under the assumption of causal sufficiency and the appropriateness of the linear model, the link coefficient (referred to as link coeff.) for $X_{t-\tau} \rightarrow Y_t$, explains how the expected value of $Y_t$ (measured in standard deviation units) will change following a one standard deviation change in $X_{t-\tau}$.

A comprehensive explanation of the original PCMCI methodology and its PCMCI+ extension, complete with their corresponding pseudo-code, proofs substantiating their asymptotic consistency, and empirical validations, can be located in the works by Runge et al. 2019b and Runge 2020, respectively. These scholarly contributions also discuss the foundational assumptions that underlie the interpretability of the identified connections within a causal context. It is imperative to highlight that, given the potential influence of latent confounding factors, the causal graphs generated by these methodologies strictly pertain to the variables under examination. The application of more sophisticated approaches (Gerhardus and Runge 2020), tailored to handle latent variables, would significantly compromise the reliability of causal graph inferences, particularly when dealing with the constrained sample sizes characteristic of the climatic research studies presented in this thesis.

### 3.5.2. Proof of concept: the 1997/1998 El Niño

The analysis and results in this section's proof of concept are part of a recently submitted paper to *Earth System Dynamics* (**Karmouche** et al. 2023b) where the author of this thesis was the first author and led the study, the writing of the manuscript, and performed all the analysis.

The ENSO phenomenon (described in Section 2.2.1) has been a subject of intense scientific interest due to its profound impacts on global climate patterns. Among the ENSO events, the El Niño of 1997/1998 stands out as one of the most powerful and influential episodes in recorded history. The processes and feedbacks involved with this event are relatively well understood and documented (Lengaigne et al. 2003; McPhaden 1999). Thus, as a proof of concept for our methodology, we apply causal discovery to analyze this event and to

physically interpret it in the context of well-known processes. This will provide insight to point toward the causal analysis in this paper of the less well-understood interactions between the Pacific and the Atlantic. Through the application of the PCMCI+ causal discovery algorithm, we identify potential cause-and-effect relationships among the selected variables, shedding light on the intricate interactions that contributed to the onset and intensification of the 1997/1998 El Niño event. Candidate variables for this case study, which have been used in previous studies (Lengaigne et al. 2003; McPhaden 1999; Neelin et al. 1998; Trenberth 1997; Wang 2018) and thus applied here include SSTAs over the Niño3.4 region (SST Niño3.4), precipitation anomalies over the central Pacific (Precip CPAC), the wind stress over the west Pacific ($\text{Wind}_{\text{Stress}}$ WPAC), the Pacific east-west SLP anomaly gradient ($\text{SLP}_{\text{grad}}$ EPAC-WPAC), and the depth of the thermocline in the eastern Pacific ($\text{Tcline}_{\text{Depth}}$ EPAC). We extract these variables as monthly averages between January 1995 and December 1999 from the National Center for Environmental Prediction-National Center for Atmospheric Research reanalysis 1 (NCEP-NCAR-R1) dataset (Kalnay et al. 1996), the Hadley Centre Sea Ice and Sea Surface Temperature (HadISST) dataset (Rayner et al. 2003), and two reanalysis datasets from the ECMWF, namely, the Ocean Reanalysis System 5 (ORAS5) dataset[2] and ERA5 (Hersbach et al. 2023). This means that the PCMCI+ data frame in this section has a length of 60 time steps (months) with 5 variables, which are listed in Table 3.1 with their respective details.

**Table 3.1.:** Climate variables used in the 1997/1998 El Niño case study carried out in **Karmouche** et al. 2023b

| **Variables (nodes)** | **Dataset** | **Definition** | **Region** |
|---|---|---|---|
| SST Niño3.4 | HadISST | SSTAs over the Niño3.4 region [°C] | 5S – 5N, 170W – 120W |
| Precip CPAC | ERA5 | Central Pacific Precipitation Anomalies [m] | 5S – 5N, 170W – 120W |
| $\text{Wind}_{\text{Stress}}$ WPAC | ORAS5 | West Pacific Wind Stress Anomalies [$\text{N m}^{-2}$] | 5S – 5N, 140E – 170E |
| $\text{SLP}_{\text{grad}}$ EPAC-WPAC | NCEP Reanalysis 1 | East-West Sea Level Pressure Anomaly Gradient [Pa] | [5S – 5N, 100E – 160E] minus [5S – 5N, 100W – 160W] |
| $\text{Tcline}_{\text{Depth}}$ EPAC | ORAS5 | Depth of 20C Isotherm in the Eastern Pacific [m] | 5S – 5N, 150W – 120W |

The Tigramite package offers the ability to plot causal networks where nodes represent the time series associated with each climate variability index. Node colors indicate the coefficient of the self-links (auto-coefficient) for each time series, and the colors of the links (arrows) denote the linear link coefficients, with blue indicating opposite-sign (negative) inter-dependency and red indicating same-sign (positive) inter-dependency strength. The link-associated time lags

[2] Copernicus Climate Change Service, Climate Data Store 2021

are shown as small labels on the curved links. If a lagged link is detected more than once, the indicated lags are sorted by strength (sorted by the absolute value of the link coefficient). During this proof-of-concept section, we estimate dependencies only for lags between 1 and 3 months ($\tau_{min} = 1$, $\tau_{max} = 3$). This is due to data availability and also because the inter-dependencies happening on a daily-to-weekly timescale are not within the scope of this paper. For this ENSO study, the PCMCI+ algorithm detected causal links that can be summarized through the causal network shown in Figure 3.2. We show the time series of each variable next to each node shown in the causal network.

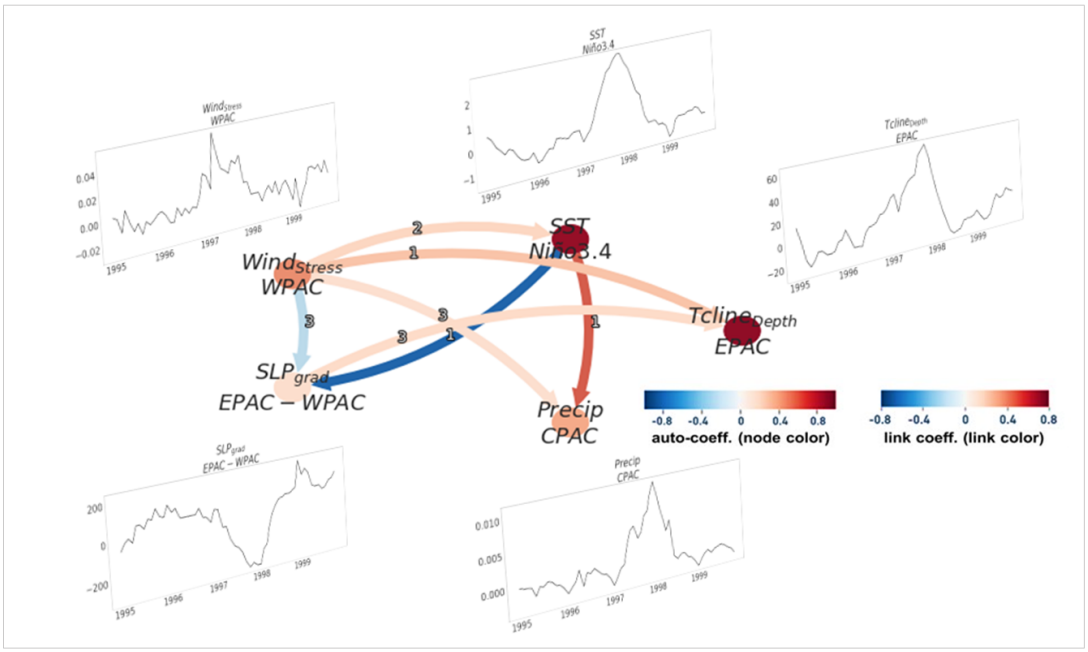


**Figure 3.2.:** Causal networks illustrating lagged causal connections among the variables outlined in Table 3.1 for the 1997-1998 El Niño event. These networks were constructed using the PCMCI+, applied to the detrended time series of each variable spanning from January 1995 to December 1999. Within these networks, nodes represent the time series corresponding to each climate variable (please refer to Table 3.1 for node labels and descriptions). Node colors signify the self-link coefficients for each time series (referred to as auto-coefficients, as indicated by the color bar), while the color of the links indicates the linear link coefficient (referred to as link coefficients, as indicated by the color bar). The time lags associated with the links are depicted as small labels on the links, with each unit representing a one-month interval. Figure adapted from **Karmouche** et al. 2023b.

The results obtained from the PCMCI+ algorithm confirm previous insights into the mechanisms leading to the 1997/1998 El Niño event by identifying significant causal links among the variables. One crucial node with multiple originating links is $\text{Wind}_{\text{Stress}}$ WPAC, indicating its central role in driving various aspects of the 1997/1998 El Niño phenomenon.

- **Causal Links Originating from $\text{Wind}_{\text{Stress}}$ WPAC:**
  1. $\text{Wind}_{\text{Stress}}$ WPAC $\rightarrow$ $\text{Tcline}_{\text{Depth}}$ EPAC: with a 1-month lag and as same-sign response. This link indicates that the westerly wind burst in the West Pacific contributed to an increase in the thermocline depth in the Eastern Pacific during the

following month (associated with an eastward propagating downwelling Kelvin wave in the ocean as previously documented (Lengaigne et al. 2003; McPhaden 1999; Wang and Picaut 2004).As the thermocline deepens in the east, upwelling brings up warmer water from the thickened thermocline, contributing to the warming of SSTs in the central and eastern equatorial Pacific.

2. $\text{Wind}_{\text{Stress}}$ WPAC → SST Niño3.4: with a 2-month lag and as same-sign response. This link indicates that as the wind stress over the West Pacific increases, it causes the SST anomalies over the Niño3.4 region to increase with a lag of 2 months. The deepening of the thermocline in the east and the reduction in the upwelling of colder waters further contribute to the anomalous warming of SSTs in the central and eastern equatorial Pacific.
3. $\text{Wind}_{\text{Stress}}$ WPAC → $\text{SLP}_{\text{grad}}$ EPAC-WPAC: with a 3-month lag and as opposite-sign response. This link indicates that the westerly wind burst in the West Pacific contributes to a three-month lagged decrease in the sea-level pressure gradient between the East and West Pacific. The decreasing SLP gradient means that the sea level pressures over the West Pacific become anomalously higher than those in the East Pacific, contributing to changes in atmospheric circulation and the thermocline depth.
4. $\text{Wind}_{\text{Stress}}$ WPAC → Precip CPAC: with a 3-month lag and as same-sign response. The link indicates that the anomalous increase in wind stress in the West Pacific contributes to an increase in Central Pacific precipitation after three months of the wind burst. Although no link originating from Precip CPAC was detected, the shift in precipitation patterns further amplifies the anomalous warming in the Niño3.4 region due to reduced upwelling and the Bjerknes feedback.

- **Causal Links Originating from SST Niño3.4:**
  1. SST Niño3.4 → Precip CPAC: with a 1-month lag and as same-sign response. This link means that the rising temperatures in the Central Pacific Niño3.4 region contributed to the increased rainfall over the same region after a one-month lag. The changes in precipitation patterns further affect the atmospheric and oceanic conditions, reinforcing the warming in the Niño3.4 region.
  2. SST Niño3.4 → $\text{SLP}_{\text{grad}}$ with a 1-month lag and as opposite-sign strong response. This link suggests that the rising temperatures over the Niño3.4 region greatly decrease the East-West sea-level pressure gradient. This reduction in the SLP gradient contributes as an indicator of a weakening of the PWC, further impacting atmospheric and oceanic conditions during the El Niño event.

- **Causal Link Originating from $\text{SLP}_{\text{grad}}$ EPAC-WPAC:**
  1. $\text{SLP}_{\text{grad}}$ EPAC-WPAC → $\text{Tcline}_{\text{Depth}}$ EPAC: with a 3-month lag and a same-sign response. This link suggests that the decreasing East Pacific SLP anomalies (compared

to the West Pacific), associated with both rising SSTs in the Niño3.4 region and the preceding increased Wind Stress over the West Pacific, contribute to a decrease in the thermocline depth over the East Pacific. However, this link's interpretation is tricky, as it suggests that the SLP gradient decreasing would cause the thermocline to become shallower after three months, which is opposite to the one-month lagged strong increase due to the West Pacific wind burst. This link color, on the other hand, suggests that the effect of $\text{Wind}_{\text{Stress}}$ WPAC $\rightarrow$ $\text{Tcline}_{\text{Depth}}$ EPAC is stronger in driving changes in the thermocline depth during the El Niño event than the 3-month lagged $\text{SLP}_{\text{grad}}$ EPAC-WPAC $\rightarrow$ $\text{Tcline}_{\text{Depth}}$ EPAC link.

To summarize, a causal analysis has been applied to the El Niño event of 1997/1998 to demonstrate the utility of such an analysis in quantifying the connections between physical processes. Previous results are confirmed by this causal analysis in that the westerly wind burst event in the western equatorial Pacific in March triggered an eastward traveling downwelling Kelvin wave in the ocean that deepened the thermocline in the east and shallowed it in the west. As SSTs warmed in the eastern equatorial Pacific, trade winds weakened. This weakening reduced the upwelling of cold, nutrient-rich waters in the eastern Pacific and instead brought up relatively warmer water from the thickened thermocline, contributing to the warming of SST in the Niño 3.4 region. The identified causal links align with the mechanisms involving the $\text{Wind}_{\text{Stress}}$ WPAC influencing thermocline depth, and leading to anomalous warming in the Niño3.4 region, in agreement with extensive previous studies (Hu et al. 2014; Lengaigne et al. 2003; McPhaden 1999; Wang and Picaut 2004). Furthermore, the East-West SLP anomalies and anomalous shifts in precipitation patterns are shown to be greatly affected by the SST variations in the central east Pacific as hypothesized, and this further contributes to the intensification and maintenance of the 1997/1998 El Niño event. Having demonstrated the utility of causal analysis in quantifying connections among phenomena governed by well-documented physical processes, we now extend our causal methodology to the evaluation of CMIP6 models in simulating decadal interactions between the Pacific and Atlantic Chapter 4 which are less comprehensively explored. We also apply the same methods to investigate the effect of external forcing on the connections between the Pacific and Atlantic SSTAs during the post-1950 historical period Chapter 5.

### 3.5.3. Network similarity quantification with $F_1$-Scores

This subsection is part of the already published article on *Earth System Dynamics* (**Karmouche et al. 2023a**), where the author of this thesis was the first author of the paper and led the writing and performed the data processing and analysis. To quantify the similarity between the resulting causal graphs (networks) from model simulations and those from observations (Chapter 4), we follow a similar modified $F_1$-score as in the methods by Nowack et al. 2020. The $F_1$-score ranges between 0 (no match) and 1 (perfect network match) and is based purely on the existence or non-existence of links in a network relative to a reference network. The $F_1$-score combines the statistical precision (P, fraction of links in model simulation network

that also occur in the reference network) and recall (R, fraction of links in the reference network that are detected in the model simulation network) and is defined as:

$$F_1 = \frac{2 \times P \times R}{P + R} \tag{3.2}$$

with

$$P = \frac{TP}{TP + FP}$$

and

$$R = \frac{TP}{TP + FN}$$

where $FP$ is the number of falsely detected links and $FN$ is the number of not detected links. We modify the definition as in Nowack et al. 2020 so that a link is considered a true positive ($TP$) if it is found with the same sign of MCI partial correlation as in the reference network. We further relax the time lag constraint by considering a $TP$ to exist if a link is found in a ±10 time-step interval compared to the lag in the reference network (i.e. $[min(\tau_{max},\ \tau+10),\ max(0,\ \tau-10)]$).

# 4. Regime-oriented causal model evaluation of Atlantic-Pacific Interactions in CMIP6

Among the key drivers of long-term climate variability are internal modes of variability, such as the PDV and AMV. These modes, characterized by alternating warm and cold phases (see Figures 2.10 and 2.11), exert significant influence on regional and global climate patterns over decadal to multidecadal timescales. Understanding the interplay between these modes and their effects on climate is of paramount importance in climate science. This research explores the complex relationships between the Atlantic and Pacific Oceans, with a focus on their responses to different stages of PDV and AMV. These modes exhibit unique characteristics, with PDV spanning the entirety of the Pacific basin's variability and AMV predominantly influencing the North Atlantic. Complementing this with previous literature discussed in Section 2.2.1, we introduce indices for PNA and PSA1 modes, both recognized as extratropical teleconnections and susceptibility influenced by the interplay between PDV and AMV. The ultimate goal is to identify the various causal fingerprints that arise from these interactions. To do so, we use a causal discovery process based on the PCMCI+, estimating these fingerprints in both observational reanalyses and state-of-the-art climate models. We conduct this research within multiple climatic regimes, each defined by the prevalent phases of PDV and AMV. The assessment of climate models' capability to reproduce the observed relationships is a key component of this research. Climate models, particularly those participating in CMIP6 (Eyring et al. 2016), are useful tools for forecasting future climatic scenarios. Hence, assessing their ability to recreate the observed causal links between PDV, AMV (and their teleconnections under different regimes) is significant for climate forecasts.

The work in this Chapter 4 (including text, figures and tables and supplementary material) is already published in (**Karmouche** et al. 2023a). For this paper, the author of this thesis led the writing, performed the data processing and analysis, prepared all figures and tables, and implemented the code[1] to reproduce this study with all figures and tables (**Karmouche** 2023). The author also contributed to the design and organization of the study and the interpretation of the results. This chapter is organized as follows: Section 4.1 describes the setup for the regime-oriented analysis (Section 4.1.1) and data (Section 4.1.2) that were used in this study. Section 4.2 start with a correlation analysis to compare the SST and SLP regression maps associated with the CMIP6-simulated time series of AMV, PDV, PNA and PSA to those from reanalysis data (Section 4.2.1). As the causal analysis only uses time series information

[1] https://github.com/EyringMLClimateGroup/karmouche23esd_CausalModelEvaluation_Modes, last access: 25.09.2023

of the calculated indices, this comes as a sanity check to measure the similarity between the observed and simulated spatial patterns associated with the index time series. This is followed by Section 4.2.2 where we show the causal networks from reanalysis data during different regimes. These serve as reference for the regime-oriented causal model evaluation in the subsequent Section 4.2.3. We discuss the results in Section 4.3 before closing the paper with a summary in Section 4.4. Figure 4.1 represents the different steps carried out during the regime-oriented causal model evaluation (see caption).

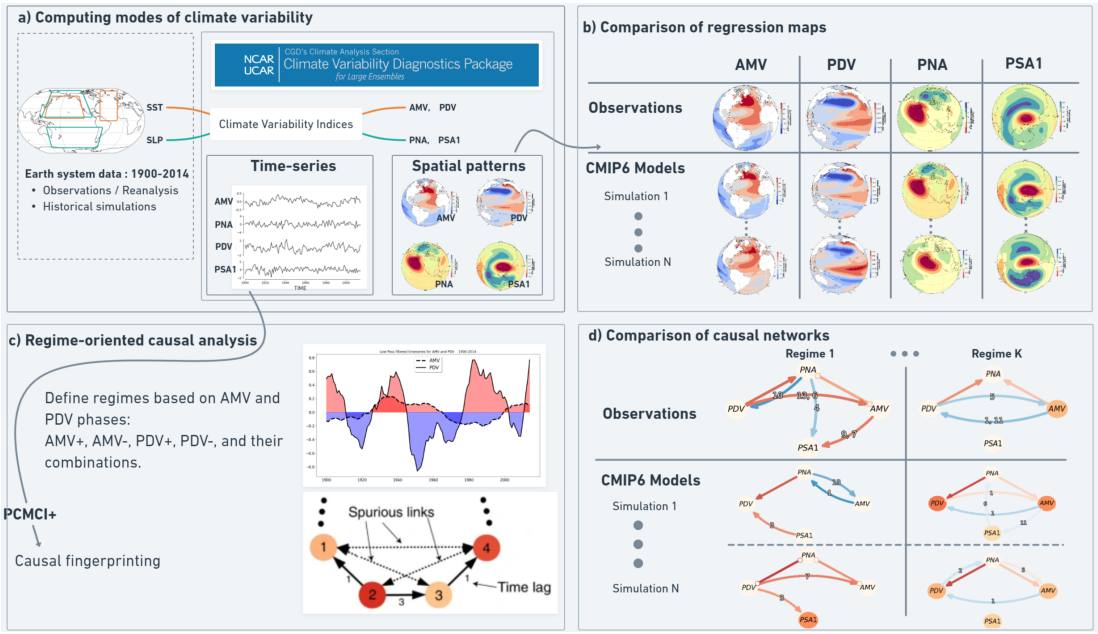


**Figure 4.1.:** Framework for the regime-oriented causal model evaluation. a) Gridded SST and SLP data used to calculate indices for AMV, PDV, PNA and PSA1 modes of climate variability. Diagnostics from the National Center for Atmospheric Research (NCAR) CVDP-LE produce the time series of these indices and their associated spatial patterns (regression maps). b) We first, as a sanity check, compare the CMIP6 model-simulated SST (for AMV and PDV) and SLP (for PNA, PSA1) regression maps to those from reanalysis before c) using the time series of the four indices for the regime-oriented causal analysis. Here we define different regimes depending on the sign of the 13-year low-pass filtered AMV and 11-year low-pass filtered PDV time series. For every regime we run PCMCI+ to estimate instantaneous and lagged links between nodes representing the time series of the indices calculated in (a) from the reanalyses and model data. In this schematic example, there are four indices, with node color indicating auto-correlation, and there is a causal link (solid black arrow) between index 2 and indices 1 and 3, and then there is a causal link between indices 3 and 4. The method identifies and removes spurious links (see black dashed arrows) between indices 1 and 4, or 2 and 4. Unitless representative time lags are labeled on each causal link, where index 1 lags index 2 by one time-step (depending on temporal resolution of the time series, here yearly), index 3 lags index 2 by three, and index 4 lags index 3 by one. Applying the method to the time series in (a) provides d) dataset- and regime-specific causal fingerprints in a similar format to the schematic in (c), which can be used for model evaluation and intercomparison. We calculate annual averages from the monthly time series of PDV and AMV provided by CVDP-LE. This way, the dataframe is fit for multi-year and decadal causal estimations. In addition to the subtraction of global mean temperatures in the CVDP-LE calculation of PDV and AMV, the causal networks are estimated after linearly detrending the time series of the four indices to ensure their stationarity. The estimated causal dependencies (links) are hence assumed to be a mixture of internal variability and time-varying anthropogenic forcing (mainly from aerosols). Figure adapted from **Karmouche** et al. 2023a.

Notably, the causal analysis involves annual averages computed from monthly PDV and AMV time series sourced from CVDP-LE (Phillips et al. 2020) with PNA and PSA1 originally extracted in yearly resolution (DJF and ANN, respectively). To ensure stationarity, the causal networks are estimated after linear detrending of the four index time series. Hence, for all results to be presented in this Chapter 4, we maintain the presumption that the calculated climate variability indices (eventually their spatial patterns and causal fingerprints) represent a mixed response of internally-generated variability and external aerosol forcing.

## 4.1. Methods and data

### 4.1.1. Set up for regime-oriented analysis

The teleconnections between the Pacific and Atlantic ocean basins are suggested to follow different regimes depending on the decadal phases that the AMV and PDV go through (Meehl et al. 2021a). In order to clearly identify the time periods of each phase, we smooth the time series data by applying 11-year and 13-year low-pass filters on PDV and AMV, respectively. Figure 4.2a shows the observed detrended low-pass filtered AMV and PDV time series used to specify the different phases and regimes for the masking before applying the PCMCI+ algorithm (the labeled regimes on the time series are only three out of the 10 we run the analysis over). First, running the analysis on the complete time period is intended to reveal the consistent causal dependencies throughout the complete historical time series Figure 3.1b. The resulting causal networks from the complete period do not, however, expose much information on the causal effects which are changing over shorter time periods depending on how the PDV and AMV are varying during those phases. In order to identify these phase-dependent causal dependencies, we perform the analysis on multiple shorter periods (regimes) by selecting the time-steps that represent either the positive (warm) or negative (cold) phases based on the low-pass filtered indices, with AMV+(-) for when the value of low-pass filtered AMV is positive (negative), and the same for PDV+(-). We further split these regimes into combinations of warm and cold PDV and AMV phases (PDV+/AMV+, PDV+/AMV-, PDV-/AMV+, PDV-/AMV-). Additionally, since some regimes are too short to reveal any dependencies, we also opted to run the analysis for an 'In-Phase' regime that sums the PDV+/AMV+ and PDV-/AMV- periods. The remaining time-steps would then consist of the 'Out-of-Phase' regime for the period where the two low-pass filtered indices have opposite signs (PDV+/AMV- and PDV-/AMV+).

This means that in addition to running it on the complete period, we apply the PCMCI+ algorithm on 10 different shorter time periods (within the original 1900-2014 period) for each dataset (see Figure 4.2a for reanalysis data). Figure 4.2b shows how we use the regimes defined in Figure 4.2a to mask the time series before applying the PCMCI+ method. This is shown for PDV+ and PDV- regimes as example. For each case, the gray shaded parts of the time series are masked periods, i.e. only the black shaded periods (see time series in Figure 4.2b) are considered. We show in Appendix Table A.4 to Table A.10, the number of years per regime for

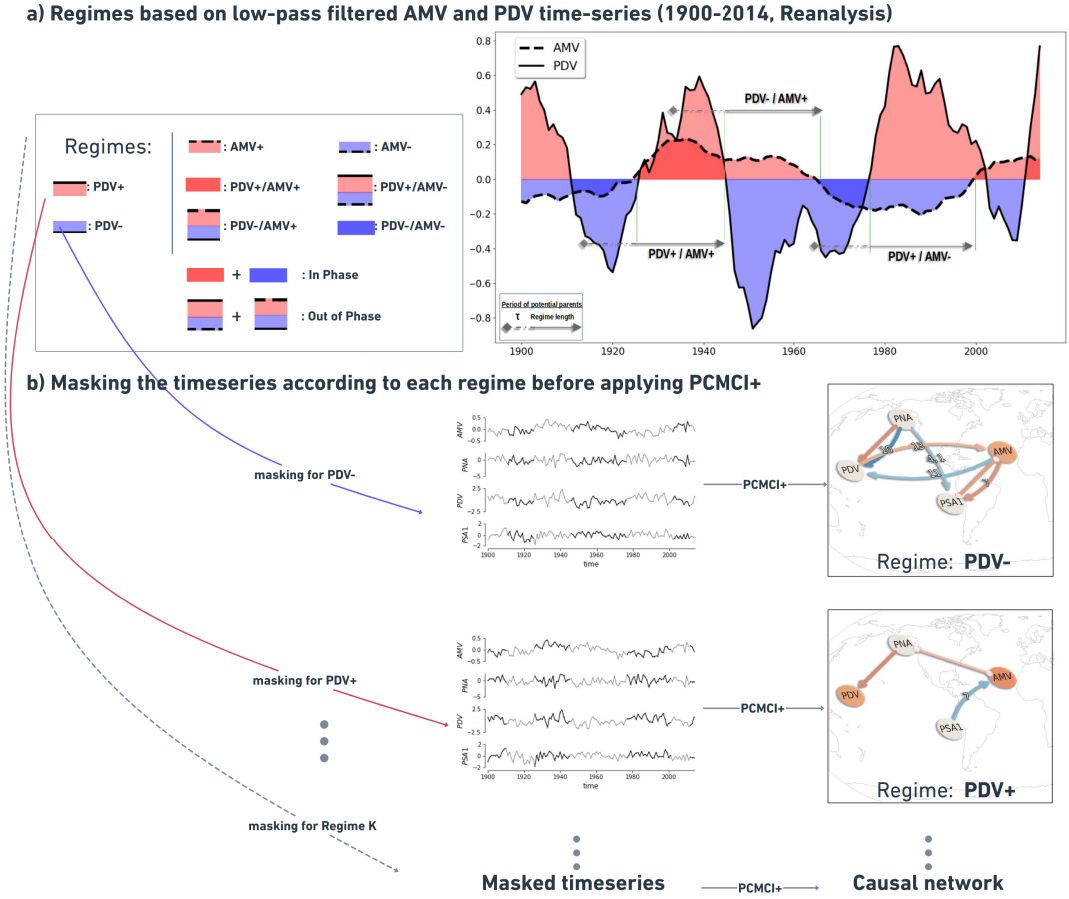


**Figure 4.2.:** a) PDV and AMV time series calculated by CVDP-LE diagnostics on ERSSTv5 data are smoothed using 11 and 13-year low-pass filters, respectively. 10 regimes are defined (see table on the left) in addition to the 1900-2014 complete period. The PCMCI+ algorithm is applied on unfiltered (non-smoothed) PDV, AMV, PNA, PSA1 yearly detrended time series that are masked according to the periods that define each regime. The right arrows on the smoothed time series represent unmasked periods from three out of 10 regimes (PDV+/AMV+, PDV-/AMV+, and PDV+/AMV-). b) The regimes identified in (a) are used to mask the non-smoothed (but detrended) index time series before applying PCMCI+. Here, for example, we show how we mask the data according to the PDV- (top) and PDV+ (bottom) regimes. The grey shaded periods are masked and thus not considered during the PCMCI+ analysis. Note that the masking here refers to variables at time point $X_t^j$ while their lagged parents can originate also from a masked period (gray shaded). This setting is referred to as `mask_type='y'` in Tigramite. Consequently, applying PCMCI+ on differently-masked time series produces different causal networks (network in top vs network in bottom) Figure adapted from **Karmouche** et al. 2023a

each dataset analysed. Nonetheless, it should be stated that the results of the regime-oriented causal analysis account for potential errors related to the sampling of the data. A study from (Smirnov and Bezruchko 2012) demonstrated, using a variety of examples, how sampling at lower intervals can produce large "spurious" results. We note that the low-pass filtered indices are used only to extract the time periods that constitute each regime. We remove any linear trend that might be present in the data prior to applying the causal discovery algorithm. In this way, the effects of external forcings are reduced. The four indices (AMV, PNA, PDV, PSA1) to which PCMCI+ is applied are represented by detrended yearly unfiltered (not smoothed)

time series (see Figure 4.2b). It is worth noting that the PCMCI+ algorithm is sensitive to the masking, and this is controlled through the mask_type='y' setting in the Tigramite software package. The grey-shaded periods on the time series represent masked time-steps Figure 4.2b, i.e., these periods are not considered during the causal analysis. Different regimes result in distinct causal networks as shown in the figure. For the parameterization of the PCMCI+ algorithm, we chose a maximum time lag ($\tau_{\max}$) of 15 years (15 time-steps), conforming with our annual data points. The significance level ($\alpha_{\text{pc}}$) for the MCI partial correlation tests is configured at 0.05.

### 4.1.2. Data

The data utilized in this study are derived from climate variability diagnostic results for the period 1900-2014, as provided by the CVDP-LE (see Sect. 3.4). The ERSSTv5 is selected as the reference data for assessing PDV and AMV indices and spatial regression maps (Figures 2.10 and 2.11). Alternatively, for the PNA and PSA1 modes (Figures 2.7 and 2.8), we refer to the SLP data from ERA20C-ERA5. The reference data serve for comparison to evaluate how indices generated using a selection of 12 Large Ensemble CMIP6 historical models reproduce the observed spatial patterns and causal dependencies. The list of CMIP6 large ensemble models (with the number of realizations per model) is provided in Table 4.1.

We note that in the spatial correlation analysis in the next section, monthly averages are used for AMV and PDV as that is the time resolution originally provided by the CVDP-LE for these modes. The diagnostic package does not produce monthly fields for the PNA and PSA1, so we use winter means (DJF) and all-year annual means (ANN), respectively. We found that most model simulations show weak correlations with reanalysis data for the annually averaged PNA (ANN, not shown) compared to the winter averaged PNA (DJF, Table 4.2). Hence, we chose winter means instead of annual means for PNA to reduce any seasonal bias within the simulated spatial patterns. The spatial patterns do not depend much on the time resolution (yearly or monthly) of the data, as they are all calculated on the whole 1900-2014 period. Prior to applying the causal discovery algorithm (PCMCI+), however, we yearly averaged the AMV and PDV time series (computed based on monthly means by the CVDP-LE). This way we unify the time resolution of our data to fit the causal analysis by using the yearly resolution to investigate connections on long timescales.

## 4.2. Results

### 4.2.1. Comparison of simulated and observed spatial patterns

To accompany the causal analysis, initial steps involve calculating pattern correlations $r$ between each simulation's SST and SLP regression maps and those derived from reanalysis over the entire 1900-2014 period (refer to PDV, AMV, PNA and PSA1 regression maps in Section 2.2.1). This is to quantify the similarity between the observed and simulated spatial

**Table 4.1.:** List of CMIP6 large ensemble (LE) historical simulations used in regime-oriented causal model evaluation (**Karmouche** et al. 2023a)

| **Dataset** | | **Components** | | **N° realisations used** | **References** |
|---|---|---|---|---|---|
| **CMIP6 LE** | **Institute** | **Atmosphere model** | **Ocean model** | | |
| ACCESS-ESM1-5 | CSIRO | HadGAM2 | ACCESS-OM2 | 10 | Ziehn et al. 2019 |
| CESM2 | NCAR | CAM6 | POP2 | 11 | Wieners et al. 2019b |
| CNRM-ESM2-1 | CNRM | Arpege 6.3 | NEMO3.6 | 10 | Seferian 2018 |
| CanESM5 | CCCma | CanAM5 | NEMO3.4.1 | 65 | Swart et al. 2019 |
| EC-Earth3 | EC-Earth | IFS cy36r4 | NEMO3.6 | 20 | Döscher et al. 2022 |
| GISS-E2-1-H | NASA | GISS-E2.1 | HYCOM Ocean | 23 | Kelley et al. 2020 |
| INM-CM5-0 | INM | INM-AM5-0 | INM-OM5 | 10 | Volodin et al. 2019 |
| IPSL-CM6A-LR | IPSL | LMDZ | NEMO-OPA | 32 | Boucher et al. 2018 |
| MIROC6 | JAMSTEC, AORI, NIES,R-CCS | CCSR AGCM | COCO4.9 | 50 | Shiogama et al. 2019 |
| MPI-ESM1-2-LR | MPI-M | ECHAM6.3 | MPIOM1.63 | 10 | Wieners et al. 2019a |
| NorCPM1 | NorESM Climate modeling Consortium | CAM-OSLO4.1 | MICOM1.1 | 30 | Bethke et al. 2019 |
| UKESM1-0-LL | Met Office Hadley Centre | MetUM-HadGEM3-GA7.1 | NEMO-HadGEM3-GO6.0 | 18 | (Tang et al. 2019) |

patterns for each of the four modes of climate variability we are to analyse. The purpose is to check if the CMIP6-simulated indices have spatial expressions that resemble those of indices calculated from reanalysis datasets. To introduce a benchmark of model performance, we calculate a Mean Score for each single simulation by taking the average of the four $r$ values (after applying a Fisher z-transform).

To look closer at how the spatial correlation values spread across every large ensemble and how they differ from one climate variability mode to another, Figure 4.3 provides a color-coded box-plot showing the distribution of these spatial correlation values, and their respective averages across every Large Ensemble of CMIP6 simulations used in the analysis. It depicts the similarity between the observed (reference maps in Figures 2.7, 2.8, 2.10 and 2.11) and the simulated patterns from the regression maps for the four modes, with values approaching 1 indicating a better simulation of the patterns associated with the observed modes.

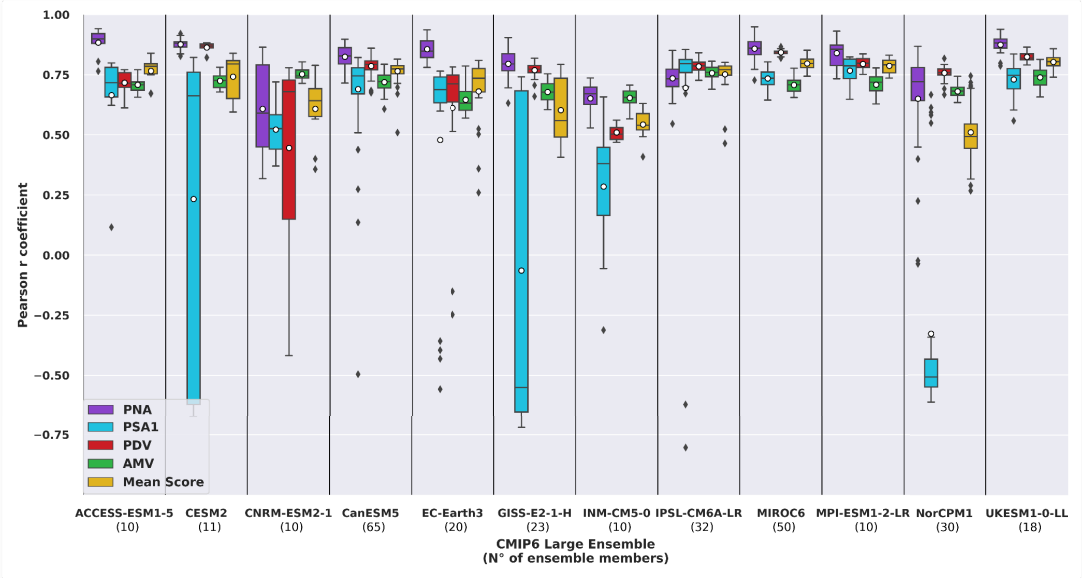


**Figure 4.3.:** Box-and-whisker plot illustrating the distribution of Pearson $r$ pattern correlation values for historical CMIP6 large ensembles. The number of ensemble members within each model is indicated in parentheses on the x-axis. Each box's lower boundary represents the first quartile ($Q1$) or 25th percentile, and the upper boundary signifies the third quartile ($Q3$) or 75th percentile. The horizontal line within the box indicates the median value ($Q2$) or 50th percentile. The span of the box, from $Q1$ to $Q3$, denotes the interquartile range (IQR). The lower and upper whiskers extend from the box to the minimum and maximum values, calculated as $Q1 - 1.5 \times \text{IQR}$ and $Q3 + 1.5 \times \text{IQR}$, respectively. Outliers are represented by black dots. Correlation values for PNA, PSA1, PDV, and AMV are color-coded in purple, cyan, red, and green, respectively. Yellow boxes indicate the Mean Score, calculated as the average of the four $r$ values after applying a Fischer z-transform. The white dots signify the mean values. Figure from **Karmouche** et al. 2023a.

Sorted by the ensemble average mean score of every CMIP6 large ensemble, Table 4.2 provides a view of the distribution (in the form of minimum, mean, maximum) of spatial correlation values for every mode and their Mean Score for every CMIP6 large ensemble model. It can be seen from Figure 4.3 and Table 4.2, based on the ensemble average mean score, that most models perform quite well in simulating the observed geographical patterns of the four

indices with pattern correlations mostly above 0.75. The UKESM1-0-LL (0.80), MIROC6 (0.80), MPI-ESM1-2-LR (0.79), ACCESS-ESM1-5 (0.77) and CanESM5 (0.77) outperform the other CMIP6 large ensembles in terms of recreating the spatial patterns of the four selected modes of climate variability. The number of ensemble members within every large ensemble has no apparent effect on the spread of the *r* value distribution across the models. For example, UKESM1-0-LL and MIROC6 with 18 and 50 realizations respectively, share similar narrow interquartile ranges (IQR, the width between the 3rd and 1st quartiles) of *r* values for the four climate variability spatial patterns. Appendix Table A.1 shows the distribution of Pearson *r* correlation between observed and simulated spatial patterns of PNA, PSA1, PDV, and AMV from a 10th, 50th, 90th percentile perspective. Looking only at the mean score spread, Table A.1 shows the 10th-90th percentile value range is 0.78-0.83 for UKESM1-0-LL, and 0.77-0.82 for MIROC6. This means that most members of these two model ensembles agree between each other and show high spatial similarity with observations when simulating the four modes. It can be concluded that the models generally do a good job in simulating the geographical patterns of the different modes but with different precision. Although the models with high mean scores tend to display high pattern correlations with observations for the four modes of climate variability, the white scatter points on Figure 4.3 imply that they simulate the PNA (purple) atmospheric mode slightly better than its South Pacific counterpart, the PSA1 (cyan) when compared to the ERA20C-ERA5 reference patterns. These high scoring models, notably UKESM1-0-LL, MPI-ESM1-2-LR, MIROC6, CanESM5 and IPSL-CM6A-LR also, on average, simulate better PDV (red) monthly spatial patterns compared to AMV (green), with ERSSTv5 as a reference dataset for the 1900-2014 period. The mean scores of Community Earth System Model (CESM)2, GISS-E2-1-H and NorCPM1 are strongly affected by the low correlation coefficients obtained for the PSA1 mode (cyan boxes). The 50th percentile bar on the cyan box for CESM2 suggests that there are more members with PSA1 patterns resembling the observed ones. The opposite is true for the GISS-E2-1-H model which contains less realizations with similar PSA1 patterns as those from reanalysis. The length of the cyan box for NorCPM1 indicate that most members fail to represent the spatial patterns of PSA1.

**Table 4.2.:** Pearson *r* correlations between the simulated (CMIP6 large ensemble) and observed (ERA20C-ERA5, ERSSTv5) spatial patterns of PNA, PSA1, PDV and AMV over the 1900-2014 period. Models are sorted according to the average mean score (column in bold; descending order).

| CMIP6 LE | Mean Score | | | PNA (DJF) | | | PSA1 (ANN) | | | PDV (monthly) | | | AMV (monthly) | | |
|---|---|---|---|---|---|---|---|---|---|---|---|---|---|---|---|
| | min | **mean** | max | min | mean | max | min | mean | max | min | mean | max | min | mean | max |
| UKESM1-0-LL | 0.74 | **0.80** | 0.86 | 0.79 | 0.87 | 0.94 | 0.56 | 0.73 | 0.84 | 0.79 | 0.82 | 0.86 | 0.66 | 0.74 | 0.81 |
| MIROC6 | 0.74 | **0.80** | 0.85 | 0.73 | 0.86 | 0.95 | 0.64 | 0.73 | 0.80 | 0.82 | 0.84 | 0.87 | 0.66 | 0.71 | 0.78 |
| MPI-ESM1-2-LR | 0.74 | **0.79** | 0.83 | 0.73 | 0.84 | 0.93 | 0.65 | 0.77 | 0.82 | 0.75 | 0.80 | 0.84 | 0.63 | 0.71 | 0.78 |
| ACCESS-ESM1-5 | 0.67 | **0.77** | 0.84 | 0.76 | 0.88 | 0.94 | 0.12 | 0.67 | 0.80 | 0.61 | 0.72 | 0.77 | 0.66 | 0.71 | 0.77 |
| CanESM5 | 0.51 | **0.77** | 0.81 | 0.71 | 0.82 | 0.90 | -0.50 | 0.69 | 0.82 | 0.67 | 0.79 | 0.86 | 0.61 | 0.72 | 0.79 |
| IPSL-CM6A-LR | 0.46 | **0.75** | 0.80 | 0.55 | 0.73 | 0.85 | -0.80 | 0.70 | 0.86 | 0.73 | 0.78 | 0.84 | 0.69 | 0.76 | 0.81 |
| CESM2 | 0.59 | **0.74** | 0.84 | 0.83 | 0.88 | 0.92 | -0.67 | 0.23 | 0.82 | 0.82 | 0.86 | 0.88 | 0.68 | 0.72 | 0.78 |
| EC-Earth3 | 0.26 | **0.68** | 0.81 | 0.78 | 0.86 | 0.94 | -0.56 | 0.48 | 0.76 | -0.25 | 0.61 | 0.78 | 0.57 | 0.65 | 0.79 |
| CNRM-ESM2-1 | 0.36 | **0.61** | 0.79 | 0.32 | 0.61 | 0.86 | 0.37 | 0.52 | 0.72 | -0.42 | 0.45 | 0.78 | 0.71 | 0.75 | 0.80 |
| GISS-E2-1-H | 0.41 | **0.60** | 0.79 | 0.63 | 0.80 | 0.90 | -0.72 | -0.06 | 0.74 | 0.66 | 0.77 | 0.82 | 0.60 | 0.68 | 0.75 |
| INM-CM5-0 | 0.41 | **0.54** | 0.63 | 0.53 | 0.65 | 0.74 | -0.31 | 0.28 | 0.66 | 0.47 | 0.51 | 0.56 | 0.57 | 0.65 | 0.71 |
| NorCPM1 | 0.27 | **0.51** | 0.74 | -0.04 | 0.65 | 0.87 | -0.61 | -0.33 | 0.67 | 0.67 | 0.76 | 0.82 | 0.63 | 0.68 | 0.74 |

Along with the release of the CVDP-LE (Phillips et al. 2020), CESM's CVCWG freely distributes results from several CMIP simulations including the CMIP6 1900-2014 historical simulations, from which data used in this analysis have been downloaded. The results include a pattern correlation summary with 11 key spatial metrics of oceanic and atmospheric modes of variability. Similar to the mean score we introduced in the spatial correlation analysis above, the CVDP-LE provides a mean score averaging the pattern correlations of the 11 metrics used. Although the pattern correlation mean score we calculated is not exactly the same as the one provided by the CVDP-LE tool because the number of indices used is different (four vs 11), the highest-scoring CMIP6 large ensembles from Table 4.2 (UKESM1-0-LL, MIROC6 and MPI-ESM1-2-LR) were also the highest scoring ensembles according to the pattern correlation summary provided on the tool's repository (Phillips et al. 2020). Moreover, one simulation from the UKESM1-0-LL ensemble, the r19i1p1f2 realization, was found to obtain the highest mean score based on both the pattern correlation values[2] published by CVDP-LE authors (Phillips et al. 2020), as high as 0.88 using 11 indices whereas our calculations in Table A.2 shows 0.86 using 4 indices for the same realization.

### 4.2.2. Regime-oriented causal analysis of observations and reanalyses

Several mechanisms are hypothesized to contribute to PDV and AMV. PDV is initially considered as a mode of internal climate variability (Meehl et al. 2021b). However, previous research indicates possible external contributions in the form of solar (Meehl et al. 2009), greenhouse gas (Dong et al. 2014; Fang et al. 2014; Meehl et al. 2009) or volcanic and anthropogenic aerosol forcings (Maher et al. 2015; Smith et al. 2016; Takahashi and Watanabe 2016; Wang et al. 2012). This means that the fingerprint of any possible external forcing acting as a confounder is embedded in the time series information of the extracted indices of the modes of climate variability used in this study. The linear detrending we perform prior to applying PCMCI+ will at least partially reduce such effects. However, as mentioned before, the subtraction of the global mean temperature for PDV and AMV and the linear detrending of all time series do not address local, nonlinear effects, which could be related to the aerosol forcing that varies over time and space. It is then important to recall that in this paper, the indices do not represent a fully isolated internal variability component but rather a mixture of naturally-occurring internal variability and nonlinear effects of external forcing, mainly in the form of aerosol forcing.

PCMCI+ is applied first to the indices of PDV, AMV, PNA and PSA1 calculated from reanalysis data, as a proxy for observations, to reveal any causal dependencies between the modes depicted by the observed time series information. As it is assumed that the nature of teleconnections between the different climate variability modes can vary over decadal timescales depending on the different phases these modes go through, we mask years of data (as discussed in Figure 4.2) to reveal the causal structures during specific periods (regimes)

[2] https://webext.cgd.ucar.edu/Multi-Case/CVDP-LE_repository/CMIP6_Historical_1900-2014/metrics.html, last access: 21.09.2023

in time. Reference causal networks obtained by running PCMCI+ on reanalysis data for the different regimes are shown in

The results show that the causal dependencies (links) between the four modes of climate variability (nodes) change from one regime to another. Starting from an analysis on the complete period (115 years, upper left panel in Figure 4.4, and see Table A.3 for exact cross-MCI values of the complete period causal graph) PCMCI+ reveals four different links: An 11-year lagged negative (link arrow is curved and blue) AMV→PDV link (cross-MCI = -0.25) showing that the opposite sign effect on PDV caused by AMV is lagged by a decade (e.g. positive AMV tends to produce negative PDV about a decade later). Therefore, this link can be interpreted as lagged opposite sign SST anomaly changes over the Pacific in response to SST anomaly changes over the Atlantic. The same causal graph features a strong positive (0.53) contemporaneous PDV—PNA link (i.e. link line is straight) suggesting PDV is strongly associated to PNA. In addition, the complete period graph implies weak South Pacific teleconnections of both AMV and PDV which are represented by a positive contemporaneous AMV— PSA1 (0.25) link and a lagged PSA1→PDV link. The latter ( PSA1→PDV link) is detected positive at 7 years (0.23) and negative at 15 years (-0.31). As explained in Section 3.5.1, if a lagged link is found at more than one time lag, the causal graph shows the link at the lag when it is most significant (i.e higher absolute cross-MCI value) and labels the other time lags after a comma ( $|-0.31|$ vs $|0.23|$ in this case, thus the "15, 7" label on the PSA1→PDV link; see upper left panel in Figure 4.4).

The complete period graph in the upper left in Figure 4.4 is useful to show the causal dependencies happening throughout the whole observational record used. However, this methodology can also be used to look at specific regimes to notice the change in dependencies arising from the physical state of the Atlantic and Pacific basins during those time periods. For example, the causal graphs from PDV+ and PDV- regimes indicate that direct decadal AMV—PDV interactions occur only during the PDV- regime (third row, left panel in Figure 4.4), whereas during the PDV+ regime (second row, left panel in Figure 4.4) we find a contemporaneous atmospheric teleconnection from PNA to both AMV and PDV. This difference could be explained by the fact that the PDV- regime comprises two important Atlantic variability events: the 1920s AMV phase-switch from negative to positive (see dashed lines showing low-pass AMV in Figure 4.2a) and the subsequent switch from positive back to negative during late 1960s.

The regime-oriented nature of this causal analysis provides for a separation of signals, for example delineating the PDV+ regime that depends on the AMV phase during those 59 years (second row panels in Figure 4.4). The short length of time series, in addition to the time-varying aerosol forcing during such regimes, can lead to inconclusive causal estimations. The PDV-/AMV- panel at the right of the third row in Figure 4.4 (25 years) shows strongly auto-correlated AMV and PSA1 patterns but no apparent links between any of the four variables. However, these short regimes might also reveal interesting causal relations that are not apparent when analysing longer periods. This is the case for the causal graph from the 25 years of the PDV+/AMV+ regime (central panel in Figure 4.4), which is the only one to

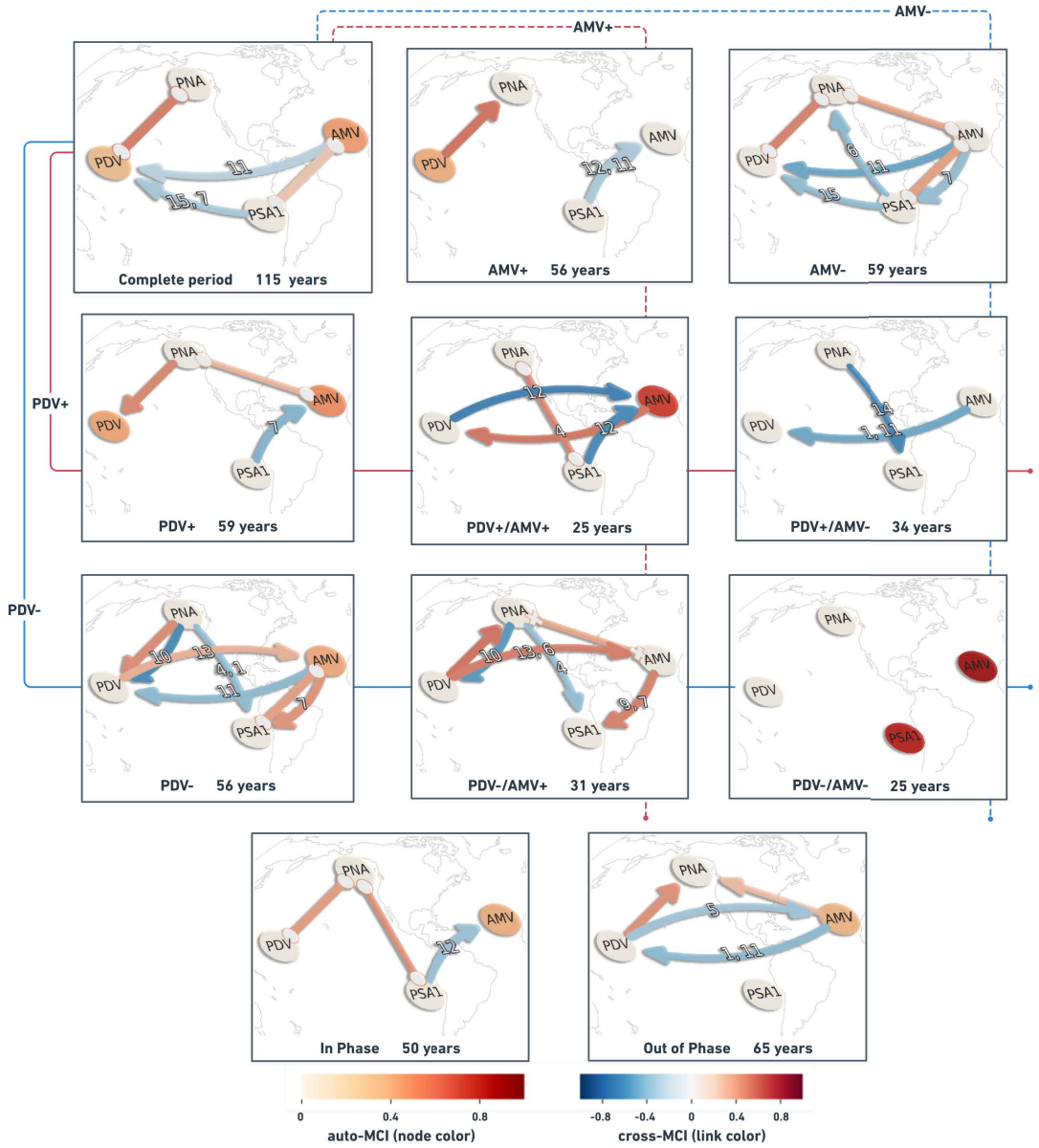


**Figure 4.4.:** Causal networks calculated with PCMCI+ from reanalysis data for the complete 1900-2014 period (upper left panel) and the different regimes. Nodes represent the time series associated with each climate variability index (see node labels) masked according to the predefined regimes. Node colours indicate the level of autocorrelation (auto-MCI) as the self-links of each node with darker red indicating stronger autocorrelations (color bar at lower left) while the color of the arrows (termed "links" here) denotes the inter-dependency strength (cross-MCI) with blue indicating opposite-sign (or negative) inter-dependency and red indicating same-sign (or positive) inter-dependency strength (color bar at lower right). Small labels on the curved links indicate the link-associated time lags (unit = 1 year). Straight links show contemporaneous inter-dependencies happening with no time lag (i.e. $\tau < 1$). Each network is sub-labeled with its respective regime name and the total number of unmasked years (time-steps) that characterize that regime (label and number of years at bottom of each panel). Lines going through the panels are to help visualize which combinations make up the regimes. Solid lines are for PDV, dashed for AMV. Red for warm (+), blue for cold (-) phases (e.g. PDV+/AMV- regime panel has a solid red line and dashed blue line going through it). Figure from **Karmouche** et al. 2023a.

feature a strong negative PDV→AMV link and a positive AMV→PDV link with comparable strength. Since the causal parents that drive the variables (other variables or the same one at different past time-steps) can originate from a masked period with respect to $\tau_{max}$, it implies, for example, that the strong 12-year lagged negative PDV→AMV causal link estimated during the PDV+/AMV+ regime (second row, central panel in Figure 4.4), might have fingerprints originating from a previous regime.

The limitation presented by the fact that some regimes might be too short to detect any causal links (e.g. PDV-/AMV-, 25 years) is overcome when introducing causal graphs for In-Phase and Out-of-Phase regimes (panels in the bottom of Figure 4.4). As explained in Section 4.1.1, the In-Phase regime is made up of the time-steps where AMV and PDV happen to be on the same phase (PDV+/AMV+ and PDV-/AMV-) while the Out-of-Phase regime is composed of time-steps where the two modes are on opposite phases (PDV+/AMV- and PDV-/AMV+), resulting in longer regime periods. We detect the negative lagged direct AMV→PDV and PDV→AMV only during the Out-of-Phase regime with a strong positive extra-tropical PDV→PNA teleconnection and a weaker AMV→PNA teleconnection. The In-Phase regime features a fast (zero lag) PDV teleconnection to PNA, PNA connection to PSA1, and a 12-year lagged PSA1→AMV link. As finite sample errors can lead to false positives as well as false negatives (missing links), it is difficult to attribute a physical explanation to every detected link. Though here both are thought to be driven by tropical precipitation and heating anomalies, we refrain from assigning any processes that might be behind the direct PNA— PSA1 causal links due the lack of knowledge regarding possible direct links between the North Pacific and South Pacific extra-tropics.

Through observations of the long-term variability patterns and pacemaker simulations of Atlantic and Pacific ocean basins, Meehl et al. 2021a explain how positive AMV could produce an opposite-sign response, mainly through the atmospheric Walker circulation, leading to negative PDV, and then the negative PDV subsequently contributing a same-sign response in the Atlantic driving the AMV from positive to negative phase. This mutual contrasting response from one basin to the other can be interpreted through the blue (negative cross-MCI) lagged AMV→PDV links and the reddish (positive cross-MCI) lagged PDV→AMV links in the causal networks in Figure 4.4. The results in Figure 4.4 show that the lagged AMV→PDV causal link has been estimated over the complete period and during five out of the 10 regimes (AMV-, PDV-, PDV+/AMV+, PDV+/AMV-, Out-of-Phase). During four of these regimes, the link can be interpreted as a lagged opposite-sign effect of AMV on PDV (blue curved link). The study of Meehl et al. 2021a suggests that in addition to the tropical Walker circulation, positive convective heating and precipitation anomalies in the tropical Pacific establish extra-tropical teleconnections to PNA and PSA which contribute to the same-sign effect of PDV on AMV. The causal graph from the 31 years of the PDV-/AMV+ regime (third row, middle panel in Figure 4.4) shows two possible pathways for this same-sign effect of PDV on AMV. During that regime, PCMCI+ estimates a strong positive 13- and 6-year lagged PDV→AMV link (the 13-year lagged link was also found during the 56 years of the PDV- regime) but also shows a positive PDV→PNA—AMV contemporaneous teleconnection where PNA seems to mediate

the same-sign effect of PDV on AMV. Therefore, this analysis presents additional evidence that AMV (although potentially affected by a forced aerosol signal) might serve as a predictor of decadal variability over the Pacific (hence for PDV) and eventually the other way around (Chikamoto et al. 2015; d'Orgeville and Peltier 2007; Johnson et al. 2020; Zhang and Delworth 2007).

An earlier study from (Zhang and Delworth 2007) proposed a mechanism in which positive (negative) AMO would lead to high (low) SLP anomalies over the North Pacific and eventually a positive (negative) PNA pattern. This weakening (strengthening) of the Aleutian low associated with the PNA pattern projects onto the multidecadal mode of variability over the North Pacific. The response of North Pacific SST to the anomalous PNA pattern induced by AMO is hypothesised to be lagged due to Rossby wave propagation and gyre adjustment where the authors found a 3-year lag when using a model simulation compared to a 12-year lag when they analysed the observed pattern. The extra-tropical contributions of PNA and PSA1 on the mutual PDV—AMV interactions can be concluded from causal graphs constructed during different regimes (see Figure 4.4). AMV-, PDV+, PDV-/AMV+ and Out-of-Phase are all regimes that suggest mutual Atlantic-Pacific connections can be established via PNA. The causal networks from the complete period and AMV- regime show that these inter-basin connections can also happen through PSA1.

Previous research also showed that components of the PDV can be forced by tropical Pacific variability and/or driven by atmospheric stochastic forcing which are both closely tied to Aleutian low variability associated with the PNA pattern (Johnson et al. 2020; Newman et al. 2016). This literature finding on the PDV—PNA teleconnection validates the contemporaneous PDV—PNA causal link estimated by PCMCI+ during most regimes (all except PDV+/AMV+ and PDV-/AMV-; see causal networks in Figure 4.4) with a strong positive cross-MCI value. The link is directed in some regimes (straight links with arrowhead, e.g. during PDV+ regime) while it is unoriented during other regimes (straight links with no arrowheads, e.g. during AMV- regime). A 10-year lagged negative PNA→PDV link appears during the PDV- regime in Figure 4.4 (and during PDV-/AMV+) which suggests that an extra-tropical teleconnection to PNA might have the opposite effect during longer time lags.

Generally, lags ranging from interannual (1 to 5 years, Meehl et al. 2021a; Wu et al. 2011) to decadal (12 to 17 years, Chylek et al. 2014; Wu et al. 2011) timescales have been proposed by previous studies for Atlantic-Pacific interactions which fall in the same range of time lags at which causal links have been estimated by PCMCI+ in this study.

### 4.2.3. Regime-oriented causal analysis of CMIP6 large ensembles

With the overall high level of fidelity that several models show in simulating the spatial patterns of at least the major modes of climate variability presented in this paper (see Figure 4.3), it is crucial to test whether these simulations also account for the possible lagged causal pathways between these different modes. To benchmark the dependency structures in model simulations, the simulated causal graphs are compared to those from reanalysis datasets (

ERSSTv5 for PDV and AMV, ERA20C-ERA5 for PNA and PSA1). The constructed causal graphs from the previous section illustrate the connections occurring between the different modes of climate variability during different regimes, as estimated from reanalysis data. Relative to reanalysis, we consider the causal graphs from Figure 4.4 as reference for the CMIP6 model evaluation to be demonstrated in this section.

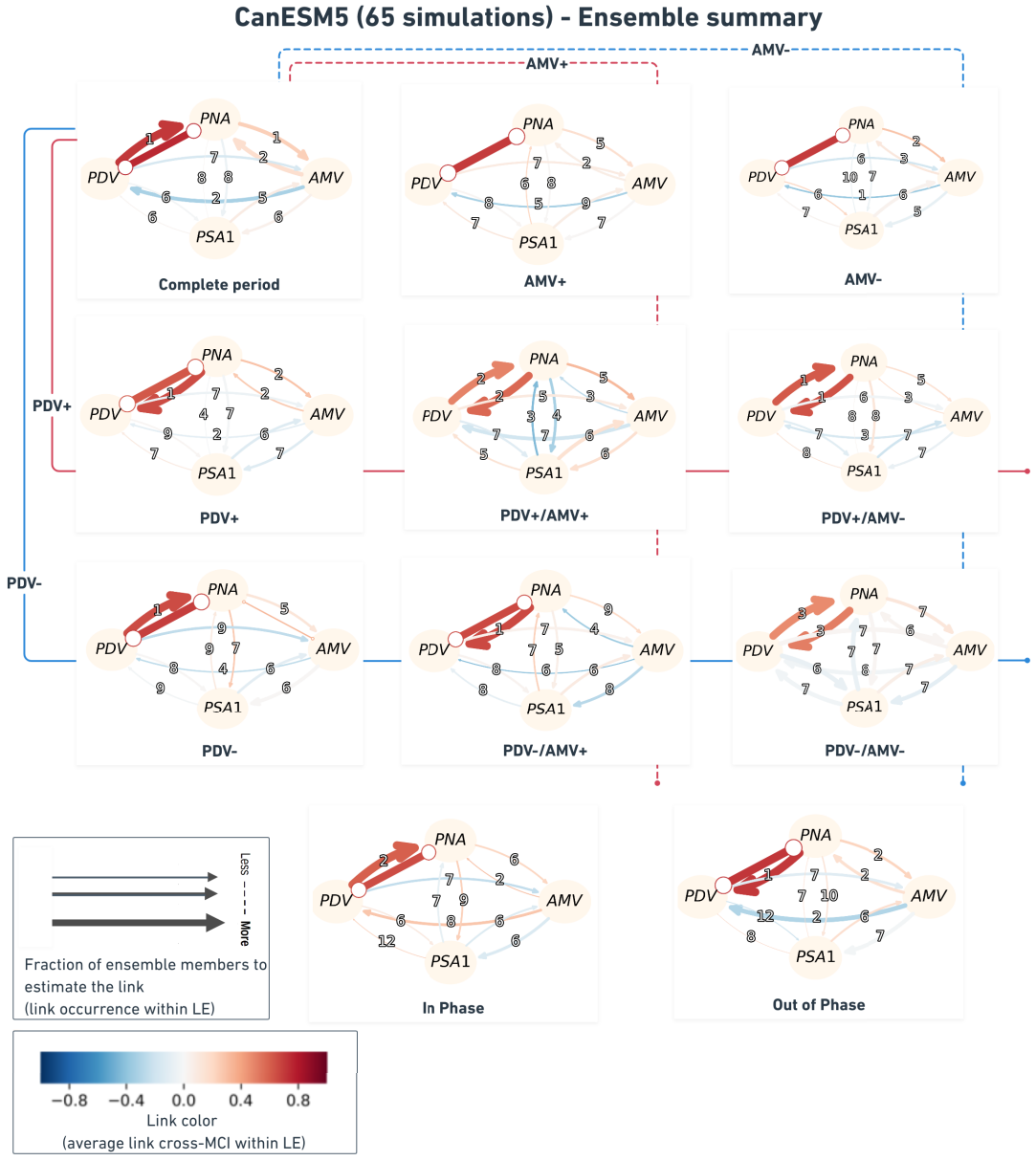


**Figure 4.5.:** Ensemble summary of the CanESM5 large ensemble model. Similar to Figure 4.4, but aggregating causal networks from 65 realizations. The link width here shows the fraction of ensemble members that feature that link relative to the total ensemble size (here 65); i.e. the thicker the link, the more ensemble members were found to estimate it during that specific regime. Link colors here translate the mean cross-MCI value among the ensemble members that estimated such link (color bar at lower left). Links of very light color are those that ensemble members agree little on their partial correlation sign. The link labels indicate the average time lag (rounded to the nearest integer) at which the link is estimated among the fraction of ensemble members that find such link. Figure from **Karmouche** et al. 2023a.

The exact same PCMCI+ setting used in the section above (see Section 4.2.2) is applied for time series indices calculated from every realization of the CMIP6 models listed in Table 4.1. In Section 4.2.1, we found that, overall, the spatial patterns of these simulated indices compare fairly well to the observed ones (Figure 4.3, Table 4.2). The purpose of this section is to show how the causal fingerprints in these simulations compare to those observed. For every realization, the analysis is run for the complete period in addition to the 10 different regimes, similar to the regime-oriented setting on reanalysis data in the section above. As the PDV and AMV phases occur in model simulations at different time periods than those in reanalysis (due to randomly generated internal variability and time-varying forcing caused mainly by aerosols), models need not show similar networks for the same periods as in observations. However, we can assess the degree of similarity in the causal fingerprint that these simulations hold within their modeled dynamics. The results of every realization during every regime are compared to the reference networks from reanalysis data during that regime.

To illustrate results from an individual model, we aggregate causal networks from 65 realizations from the CanESM5 model in Figure 4.5. This figure shows networks with links of variable thickness indicating that some links are found in most ensemble members during that specific regime (thick links, e.g. PDV—PNA in most regimes) compared to other links (thinner links, e.g. PDV→AMV in most regimes) which were detected only by a small fraction of ensemble members. The thicker the link, the more agreement between members of the same ensemble in detecting that specific link. We also label the links with the rounded mean lag at which they are detected in the ensemble members. The link color in this ensemble summary (Figure 4.5) is informative of the level of agreement between ensemble members in estimating that causal link with the same sign. The clearer the shade of blue (negative) or red (positive), the better agreement between ensemble members in simulating the link with the same sign. For example, the color of AMV—PNA links in most regimes (although mostly estimated by few members during each regime, i.e. relatively thin links; see Figure 4.5) tend towards reddish shades suggesting that the CanESM5 members, in which such links were estimated, agree that the causal link is of positive sign. This can be translated to the positive (negative) AMV driving positive (negative) PNA and vice versa. This can be seen on all causal networks in Figure 4.5, except the ones from PDV+/AMV+ and PDV-/AMV+ regimes indicating that in a few of the CanESM5 realizations, AMV would induce an opposite sign response on PNA (see thin blue AMV→PNA links on PDV+/AMV+ and PDV-/AMV+ causal graphs in Figure 4.5).

Other than the PDV—PNA links (estimated by most ensemble members during all regimes), the occurrence of a link in the CanESM5 model seems to vary from one regime to another. This is less true for the complete period, the In-Phase and the Out-of-Phase regimes. The complete period ensemble causal graph distinctly shows AMV—PNA interactions as same-sign causal links between the two modes. The same graph (upper left panel in Figure 4.5) also shows a clear blue AMV→PDV link, demonstrating the opposite-sign response driven by AMV on PDV, similar to the one featuring in the complete period causal graph from reanalysis data (upper left in Figure 4.4). The color and width (thickness) of this AMV→PDV link in the

complete period graph in Figure 4.5 (upper left panel) suggest that the link was estimated with negative cross-MCI values by a considerable fraction of CanESM5 simulations.

A more evident network similarity is evinced during the Out-of-Phase regime. Both the graph from reanalysis (Figure 4.4, Out-of-Phase) and the CanESM5 ensemble graph (Figure 4.5, Out-of-Phase) display a short lagged (1-year lag and 2-year mean lag, respectively) opposite-sign (blue, negative cross-MCI) AMV→PDV causal link. Moreover, the two graphs (Out-of-Phase causal networks in Figure 4.4 and Figure 4.5) suggest a same-sign (red, positive cross-MCI value) contemporaneous and short-lagged (1 year) PDV—PNA causal links, and weaker same-sign (lower positive cross-MCI values) AMV—PNA links. The latter links are instantaneous in the reanalysis data but lagged in CanESM5. However, the short mean lag (2 years) in the simulated CanESM5 Out-of-Phase graphs imply that several members estimate a contemporaneous link.

The CanESM5 ensemble causal graph during the In-Phase regime at the bottom of Figure 4.5 demonstrates the advantage of using large ensembles. While the reanalysis graph during this regime suggests only PDV—PNA and lagged PSA1→AMV teleconnections (with a debatable contemporaneous PNA— PSA1 link), the CanESM5 ensemble graph displays a clear same-sign lagged AMV→PDV link with a third of its ensemble members simulating such a dependency. Despite the fact that the positive AMV→PDV link is not detected in reanalysis during the In-Phase regime (Figure 4.4, In-Phase regime causal graph), literature supports this contrasting effect estimated by CanESM5 model data (Meehl et al. 2021a; Wu et al. 2011). Model simulations can therefore explain causal dynamics between modes of climate variability that might not definitively appear when analysing observations. There is less doubt about the agreement between members of the CanESM5 ensemble, and also when compared to reanalysis, about the occurrence of an AMV→PDV link with an opposite sign during the Out-of-Phase regime.

Ensemble summary plots are calculated for all CMIP6 large ensembles from Table 4.1 but we only chose to display them for CanESM5 in Figure 4.5. The ensemble summary of causal networks from reanalysis data and the 12 CMIP6 models for the complete 1900-2014 period, Out-of-phase and In-Phase regimes are shown in appendix Figs. A1-A3 respectively. In order to measure the level of similarity between observed and individual ensemble member networks across all the CMIP6 models, $F_1$-scores are computed for every realisation and every regime. The results reveal that most CMIP6 Large Ensembles show better network (causal graph) similarity with reanalysis reference networks during the Out-of-Phase regime, compared to the networks drawn during the other regimes and/or the complete period. The whisker plot in Figure 4.6a shows the distribution of $F_1$-scores across the CMIP6 large ensembles for the complete period (light blue boxes), the In-Phase regime (dark blue) and the Out-of-Phase regime (green). The range of scores during the other regimes (not shown) was found to be much lower compared to the scores during the regimes shown in Figure 4.6a. The white scatter points show that on average, CESM2, CanESM5, MIROC6 and MPI-ESM1-2-LR large ensembles clearly display better network similarity with observations during the Out-of-Phase regime. The highest scores during this regime (0.92) belong to members of CanESM5

and MIROC6 large ensembles (see location markers on whisker plot). Figure 4.6b compares Out-of-Phase causal graphs from these highest-scoring realizations (and their low-pass filtered AMV, PDV time series) to those from reanalysis. The networks in Figure 4.6b agree on the 1-year lagged AMV→PDV link. The positive contemporaneous PDV—PNA link is directed differently in reanalysis and CanESM5 r11i1p2f1, but unoriented in CanESM5 r17i1p2f1 and MIROC6 r20i1p1f1. The Out-of-Phase graphs from these realizations also agree on a same-sign contemporaneous AMV—PNA dependency, with a lower cross-MCI value (weaker) than that of the PDV—PNA connection.

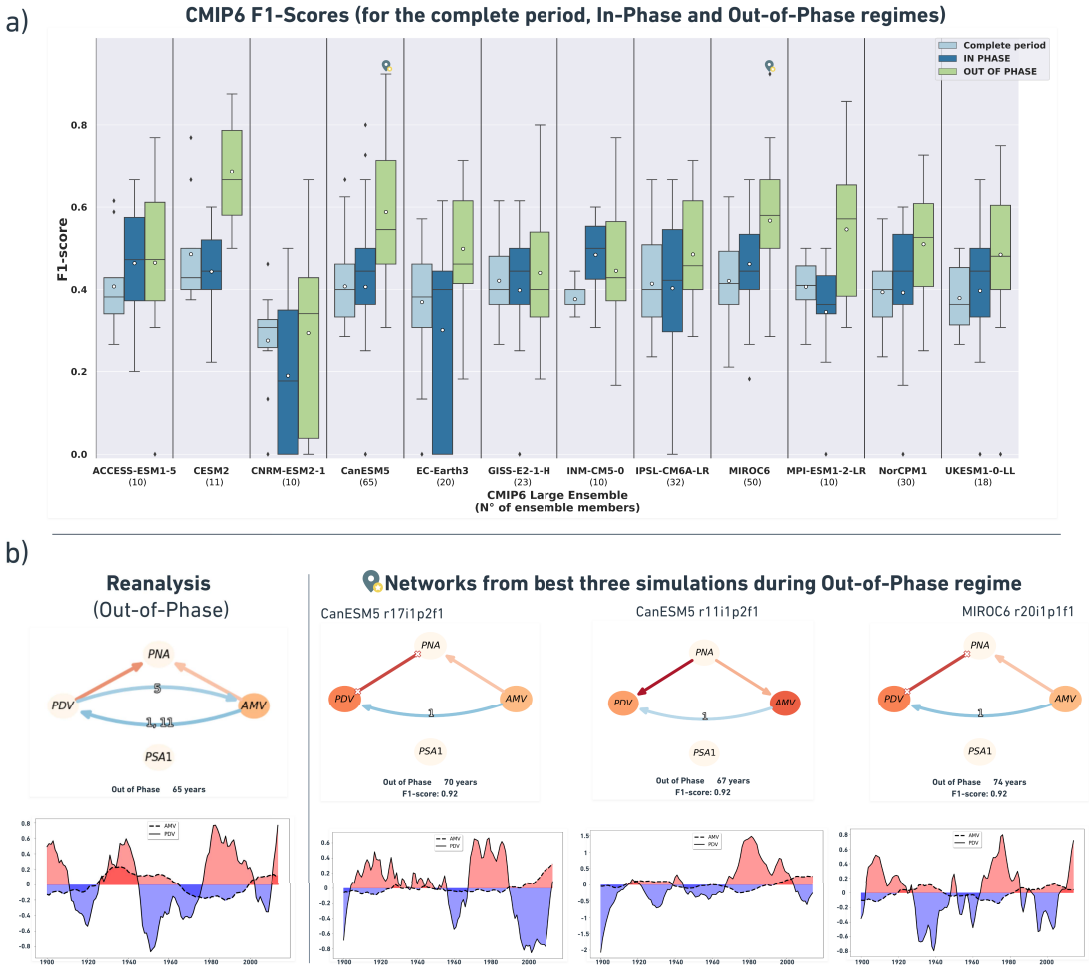


**Figure 4.6.:** a) Whisker plot showing the distribution of $F_1$-scores across the CMIP6 large ensembles for the causal analysis for: the complete period (light blue boxes), the In-Phase regime (dark blue boxes) and the Out-of-Phase regime (green boxes). White scatter points denote the mean large ensemble $F_1$-scores. b) Reference causal network estimated from reanalysis during the Out-of-Phase regime (left, with low-pass AMV and PDV time series below) compared to networks and time series from three CMIP6 simulations (right, with simulated low-pass AMV and PDV time series below each network) with the best network similarity i.e. highest $F_1$-score. Figure from (**Karmouche** et al. 2023a).

In Figure 4.7 we perform intra- and cross-model network comparisons for the complete period and long regimes. This is done by computing $F_1$-scores with every single realization as a reference. Averaging the $F_1$-scores by ensemble produces an $F_1$-matrix for every regime

in the form of heat maps translating the degree of similarity (the redder the color, the greater the similarity) in causal dynamics between members of the same large ensemble (boxes on the main diagonal) and pairwise causal similarity between different large ensembles (boxes outside the main diagonal). Every grid box on the heat maps shows how the corresponding CMIP6 model from the axis on top (see model names on x-axis top of every panel) compares to the reference corresponding CMIP6 model (see model names on y-axis left of each panel). We exclude the short regimes (PDV+/AMV+, PDV+/AMV-, PDV-/AMV+ and PDV-/AMV-) from this comparison as the PCMCI+ results during these regimes tend to be inconclusive (i.e. the regimes are too short to estimate any causal link for several simulations from different models). The heat maps show that CNRM-ESM2-1 large ensemble clearly stands out as the most dissimilar model during most regimes. This is seen in the third row and third column (from top to bottom, left to right) of each heat map ($F_1$-matrix of every regime) in Figure 4.7 indicating the lowest $F_1$-scores (yellow and white lines on the heat maps; see also color-bar). The model does not only have the lowest level of agreement with other ensembles but also shows poor accordance within its own members. Generally, the other CMIP6 models exhibit better network similarity during longer regimes (Complete period, AMV+, AMV-, PDV+, PDV-, In-Phase, Out-of-Phase). Members of CESM2 large ensemble strongly agree between each other in terms of causal fingerprints displayed during the analysis on the complete period; this is shown by the dark red box on the second row and second column of the complete period heat map ($F_1$-matrix). The INM-CM5-0 large ensemble shows low average $F_1$-scores during the PDV+ and Out-of-Phase regimes, but it surprisingly shows the most agreement between its own ensemble realizations during the complete period, AMV-, PDV- and the In-Phase regimes (see dark red grid boxes in the center of heat maps of these regimes on Figure 4.7). This implies that the INM-CM5-0 ensemble might involve mostly simulations where PDV and AMV are in the same phase.

The skill of CESM2, CanESM5, MIROC6 and MPI-ESM1-2-LR in recreating the observed causal pathways of the Out-of-Phase regime is also manifested through the better similarity the members of these models show when compared to each other. The heat maps ($F_1$-matrices in Figure 4.7) serve to distinguish models with similar causal dynamics. The specified range of internal variability within realizations of the same ensemble (combined with the model-simulated time-varying aerosol forcing) can also be inferred by comparing one large ensemble to itself.

## 4.3. Discussion

Previous research already suggested the improvement in simulation of dominant modes of climate variability throughout the different phases of the CMIP archive (Eyring et al. 2021b; Fasullo et al. 2020). Although, in general, models are able to capture the spatial patterns of these modes, CMIP6 revealed discrepancies in the skill these large ensemble simulations display when recreating the observed modes. Some models perform very well, while there

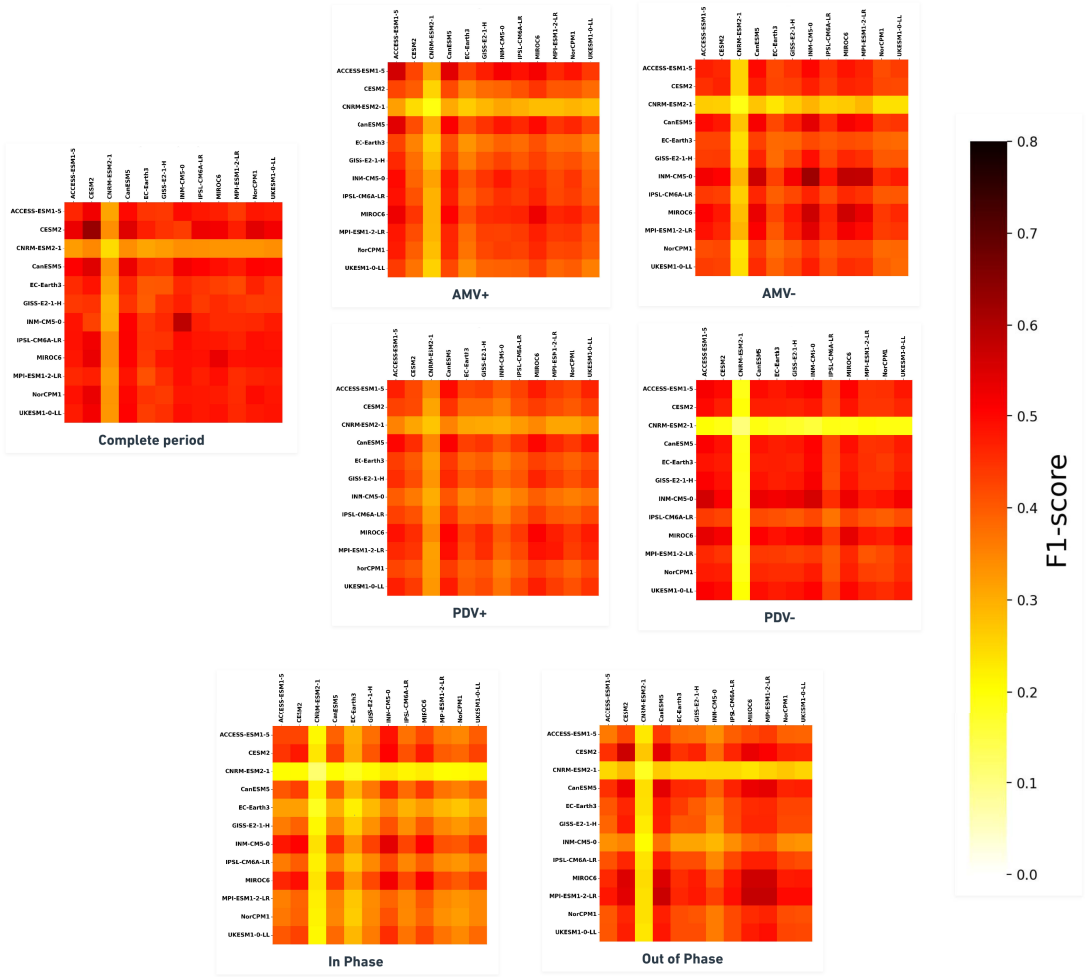


**Figure 4.7.:** Matrices of average $F_1$-scores for pair-wise network comparisons between ensemble members of 12 CMIP6 large ensembles during every regime. Boxes on the main diagonal translate the level of similarity between members of a single CMIP6 ensemble. Boxes outside the main diagonal show the similarity between realizations of a CMIP6 large ensemble compared to realizations from another CMIP6 large ensemble (taking every realization as a reference at a time, before averaging across every large ensemble). The redder the grid box, the better causal network similarity it translates when comparing realizations of the corresponding CMIP6 model (x-axis coordinate name on top of each panel) to causal networks from the corresponding reference CMIP6 model (y-axis coordinate on the left of each panel). The matrices for the short regimes (PDV+/AMV+, PDV+/AMV-, PDV-/AMV+ and PDV-/AMV-) are not shown as their results are not conclusive since PCMCI+ fails to estimate any causal networks for several members of different ensembles. Figure from (**Karmouche** et al. 2023a).

is still room for improvement for others. This conclusion is illustrated through results of the pattern correlations in Section 4.2.1 and the wide range of comparison metrics produced and published by the CVDP-LE authors (Phillips et al. 2020). The ability of CMIP6 large ensembles to recreate the spatial patterns of modes of climate variability does not, however, ensure that they simulate the connections between those modes. Relative to the reference networks from reanalysis datasets during the Out-of-Phase regime, CESM2, CanESM5, MIROC6 and MPI-ESM1-2-LR large ensembles display the highest degree of similarity. During the analysis of the complete 1900-2014 period, a considerable fraction of simulations belonging to these

CMIP6 models estimates an opposite-sign response from AMV to PDV (represented by blue AMV→PDV links, see Figure A.1). The clear occurrence of this opposite-sign response in several CMIP6 large ensembles (notably, CESM2, CanESM5, MIROC6 and MPI-ESM1-2-LR) shows that these models realistically simulate the mechanisms that connect Atlantic and Pacific modes of SST variability. The direct connection between the Atlantic and Pacific basins involves mainly the tropical Walker circulation and its associated SST, evaporation, wind and SLP changes where rising temperatures in the Atlantic Ocean can cause a cooling effect similar to La Niña in the equatorial Pacific (Kucharski et al. 2016; Li et al. 2016; McGregor et al. 2014; Meehl et al. 2021a; Ruprich-Robert et al. 2021). Moreover, these CMIP6 large ensembles were found to also simulate most spatial patterns with high correlation coefficients. On the other hand, other large ensembles such as the UKESM1-0-LL and ACCESS-ESM1-5, despite their high correlation with the observed spatial patterns, do not exhibit the same level of similarity when comparing their causal networks to the reference networks. This discrepancy might be due to the difference in external time-varying aerosol forcing with respect to random internally-generated variability.

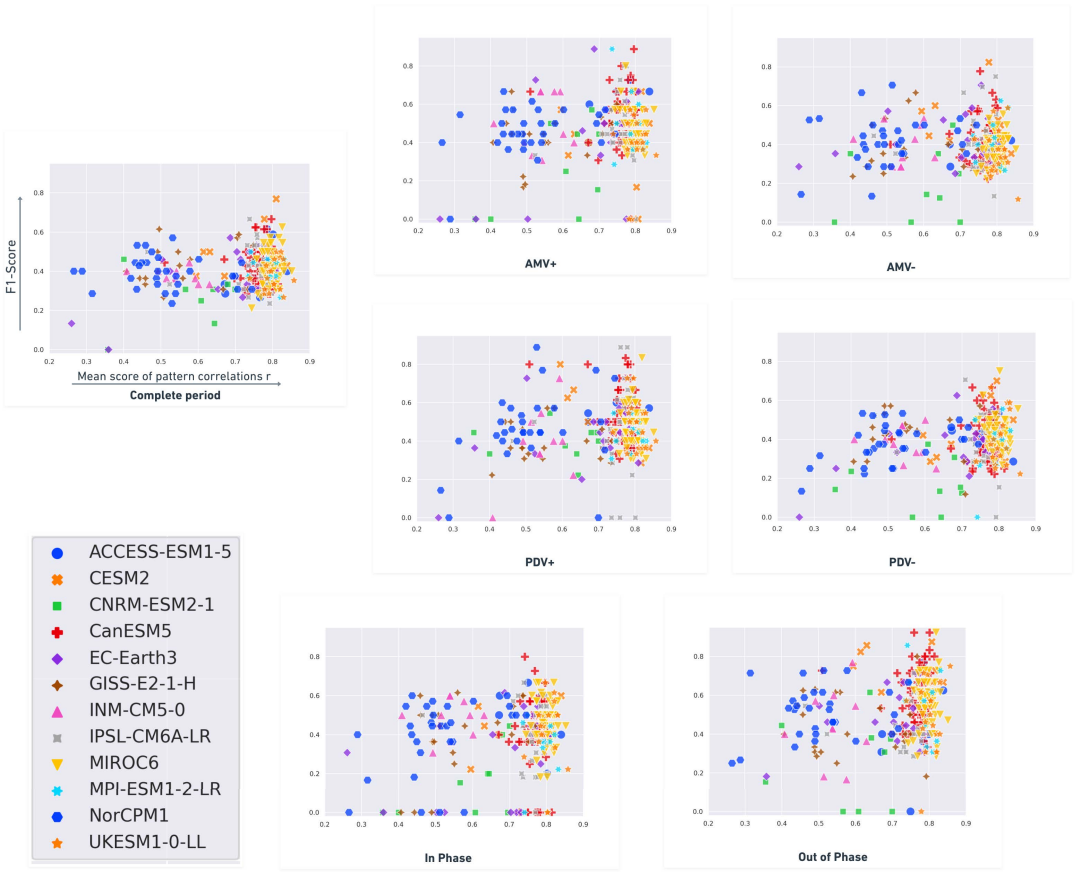


**Figure 4.8.:** Scatter plots: $R_{coef}$ mean score (spatial correlation with reanalysis, x-axis) vs $F_1$-score (network similarity with respect to reanalysis, y-axis) during the different regimes. Spatial correlation values do not change from one regime to another; these are the same mean scores calculated from the Pearson $r$ coefficients of the four modes in Section 4.2.1 over the 1900-2014 period. Similar to Figure 4.7, scatter plots are shown only for the long regimes. Figure from (**Karmouche** et al. 2023a).

In Figure 4.8 we plot the $F_1$-scores for all realizations (color- and marker-coded by CMIP6 ensemble, see legend) for the long regimes with respect to the mean-score of $r$ spatial correlations from Section 4.2.1. Similar to Figure 4.7, we choose not to show the scatter plots for the short regimes. As the mean-scores of spatial correlations are the same for all regimes (computed between the regression maps on the whole 1900-2014 time series of the indices), how high (low) a single scatter point can get during a certain regime reveals its causal network similarity (dissimilarity) with reanalysis during that regime. The scatter points closer to the top right corner of each plot belong to realizations which simulate better the spatial patterns and causal fingerprints of reanalysis. Considering only the complete period panel (upper left in Figure 4.8), the upper right corner of this panel shows mainly realizations from CESM2 (orange crosses), MIROC6 (yellow triangles), CanESM5 (red plus signs) models. From the same panel, we can notice, for example, that the UKESM1-0-LL realizations (orange 5-pointed stars) have great spatial pattern similarity with reanalysis. These UKESM1-0-LL realizations, however, do not show high similarity when comparing their causal fingerprint to that concluded from reanalysis data. The same can be said about MPI-ESM1-2-LR realizations (cyan 6-pointed stars) which, in spite of their high level of skill in recreating the spatial regression patterns of the four modes of climate variability, fail to obtain $F_1$-scores as high as those from CESM2, CanESM5 or MIROC6 during most regimes. Only during the AMV+ and Out-of-Phase regimes that very few MPI-ESM1-2-LR simulations exceed the 0.7 $F_1$-score bar. Overall, we can conclude that CESM2 (orange crosses), CanESM5 (red plus signs) and MIROC6 (yellow triangles) undoubtedly outperform other large ensembles in this evaluation. This is proven through the consistency that simulations from these two large ensembles show in resembling the observed causal fingerprints during the different regimes. Despite obtaining high spatial correlation coefficients, two members of the IPSL-CM6A-LR model (grey scatters) show the best network similarity with reanalysis during the PDV+ regime while three other members of this model show no similarity during the same regime.

It is worth mentioning that the number of realisations within an large ensemble appears to increase the chance of a model to comprise a simulation with similar dependency structures as those found in observations. The three simulations with the highest $F_1$-scores during the Out-of-Phase regime (see Figure 4.6) belong to either CanESM5 or MIROC6 which are the large ensembles with the highest number of realisations (65 and 50 ensemble members, respectively). This is likely related to the number of realizations needed to capture similar random internal variability to the one observed in reanalysis data. This is less valid for the CESM2 model, which with only 11 realizations, contains simulations with high $F_1$-scores during most regimes shown in Figure 4.8. In general, modeling centers previously contributed only a small number of realizations to international climate change projection assessments [e.g., phase 5 of the CMIP Taylor et al. 2012]. As a result, model-associated errors and internal climate variability remained difficult, if not impossible, to disentangle (Kay et al. 2015). In this paper, as CMIP6 includes large ensemble models, we overcome this sampling problem by using at least 10 realizations per model (see Table 4.1). In this way, we have a better estimate of the natural internal variability and the externally forced part. The larger the ensemble size, the

more likely that the observed internal variability falls within the plausible internal variability range simulated by that particular large ensemble model realizations. However, despite the improvement of CMIP6 models in capturing the different modes of climate variability (Fasullo et al. 2020), recent studies already pointed to persisting tropical Atlantic biases that knew little or no improvement compared to CMIP5 (Farneti et al. 2022; Richter and Tokinaga 2020). These biases certainly affect the simulation of Atlantic variability within CMIP6 models as they project additional uncertainties on the AMV-related causal dynamics and spatial patterns. Moreover, previous research showed that, on the decadal timescale, Atlantic mean SST biases in CMIP5 models are directly related to the variability of trade winds over the region (Kajtar et al. 2018). McGregor et al. 2018 found that the addition of the CMIP5 Atlantic bias leads to enhanced descending motion trends in the western and eastern Pacific, and a reduced trend in the central Pacific. The same study found that the observed northward migration of the Intertropical Convergence Zone (ITCZ) is absent when introducing CMIP5 Atlantic bias.

The spatial pattern correlation analysis (Figure 4.3), the resulting $F_1$-scores with respect to reanalysis (Figure 4.6a), and the CMIP6 pair-wise network comparisons (Figure 4.7) call for the need to investigate the coupling attributes and the simulated internal variability in the CNRM-ESM2-1 ensemble, as its realizations clearly fail to reproduce the observed spatial patterns and causal links between modes of climate variability compared to other CMIP6 large ensembles. The relatively large distribution of spatial correlation values for the simulated PNA and PDV modes (see purple and red boxes of CNRM-ESM2-1 in Figure 4.3), suggest spatial disagreement between the realizations of CNRM-ESM2-1 model regarding the expressed PNA and PDV patterns. This might be the result of a relatively large distribution of forced PNA and/or PDV trends. This can be supported by the time series metrics provided by CVDP-LE which reveal that, among the models analysed in this paper (see Table 4.1), CNRM-ESM2-1 holds the largest $10^{th}$-to-$90^{th}$ percentile range of linear PDV trends (-0.89 per 115 years to 1.18 per 115 years) during the 1900-2014 period. These values can be found on the PDV time series ensemble summary figure as part of the historical 1900-2014 CMIP6 variability diagnostic results[3] distributed by the CVDP-LE authors (Phillips et al. 2020). Considering that the model only counts 10 realizations, the large $10^{th}$-to-$90^{th}$ percentile range reveals that the forced PDV trend can be significantly different from one CNRM-ESM2-1 simulation to another. This translates not only to the dissimilarity in terms of spatial PDV patterns within the ensemble members but most probably leads to very different causal dynamics too. The latter can be seen through the causal networks in Appendix Figures A.1–A.2 where CNRM-ESM2-1 simulations hardly agree on the sign of the PDV—PNA links (appearing with lighter shades of red) compared to the other CMIP6 models (where PDV—PNA links appear with darker shades of red).

In the present work we defined regimes explicitly based on the phases of PDV and AMV. There are also methods to agnostically extract underlying regimes and their corresponding

[3] https://webext.cgd.ucar.edu/Multi-Case/CVDP-LE_repository/CMIP6_Historical_1900-2014/pdv_timeseries_mon.summary.png, last access: 21.09.2023

causal graphs from time series (Saggioro et al. 2020), but these are not reliable for the small sample sizes in combination with the high dimensionality of the present datasets.

## 4.4. Summary

Applying PCMCI+ to reanalysis data revealed that the direct decadal opposite-sign response from AMV to PDV, described by Meehl et al. 2021a occurs not only during the analysis of the complete 1900-2014 period (with 11-year time lag), but also during several specified regimes: PDV- (11-year lag), AMV- (11-year lag), PDV+/AMV- (1- and 11-year lags), and when PDV and AMV are out of phase (1- and 11-year lags). These regimes vary from 34-year long (for PDV+/AMV-) to 65-year long (for Out-of-Phase). For the shorter PDV+/AMV+ regime (25-year long) we detect a positive same-sign response from AMV to PDV with a 4-year time delay. The causal networks constructed from the reanalyses datasets have also revealed the same-sign response from PDV to AMV during two regimes: PDV- (59-year long) and PDV-/AMV+ (31-years long). In other words, the regime-oriented causal analysis indicates that AMV might serve as an early predictor of decadal variability over the Pacific. We also find an indirect connection between the Atlantic and Pacific, which is established via PNA during AMV- and PDV+ regimes (both 59-year long), and during PDV-/AMV+. The latter is one of the two regimes that feature a same-sign response from PDV to AMV. An indirect connection between Atlantic and Pacific via the Pacific–South American Pattern is found during the complete 1900-2014 period, where AMV is positively linked with PSA1, but PSA1 has a negative lagged link to PDV. During AMV- regime, the causal graph shows opposite-sign AMV→PSA1→PDV lagged connections.

As an example for the regime-oriented causal analysis on CMIP6 models, we showed the CanESM5 ensemble averaged causal graphs which indicate that the opposite sign effect of AMV on PDV (blue AMV→PDV link) is recreated by several realizations (38 out of 65) during the Out-of-Phase regime, agreeing with the reanalysis results and literature findings (Johnson et al. 2020; Newman et al. 2016). Appendix Figure A.1 and Figure A.2 show that this opposite sign-lagged effect of AMV on PDV was clearly present in simulations belonging to CESM2 and MIROC6 ensembles (AMV→PDV links are clearly blue). The PDV teleconnection to PNA in the form of mutual same-sign response (positive cross-MCI links) was clearly present in most realizations of not only the CanESM5 model (Figure 4.5) but most of the CMIP6 large ensemble simulations analysed. This is true considering the exception of the CNRM-ESM2-1 simulations which show less agreement between each other on the sign of the PDV—PNA links (appearing with lighter shades of red in Figure A.1 and Figure A.2) compared to the other CMIP6 models.

The evaluation of the Large Ensembles from the CMIP6 archive presented in this paper unveiled how a model performs compared to other models in terms of simulating observed spatial patterns and causal pathways between modes of climate variability. Most CMIP6 models were found to score better during the Out-of-Phase regime, with CESM2, CanESM5,

MIROC6, and MPI-ESM1-2-LR as the best performers during this regime. We showed the importance of using large ensembles in causal model evaluation to address the sampling issue and explained possible causal pathways during specific regimes that might not appear in causal networks constructed from reanalysis data. Several CanESM5 realizations suggested a same-sign AMV→PDV link during the In-Phase regime. This link did not appear on the In-Phase regime causal graph reconstructed from reanalysis. This same sign response is nonetheless documented by previous research (Meehl et al. 2021a; Wu et al. 2011). The CanESM5 and MIROC6 models with the highest numbers of members were found to outperform other models in simulating observed causal patterns during the long regimes (see Figure 4.6a). Interestingly, the CESM2 model, with a relatively smaller ensemble size (11 realizations), was also found to display larger causal fingerprint similarity with reanalysis during the long regimes. The causal network similarity between different CMIP6 large ensemble models was also assessed throughout this paper. Simulations from CESM2, CanESM5 and MIROC6 models also largely resemble each other and those from the MPI-ESM1-2-LR model in terms of estimated causal networks during most regimes (Figure 4.7).

A deepened intra-model comparison remains essential to evaluate how realizations of the same model ensemble differ from one another. The 'ripf' identifier of every simulation within the CMIP6 large ensembles used in this study show that some large ensembles only include realizations (r) with the same initialization (i), physics (p) and forcing (f), while other large ensembles contain realizations with different physics or forcing. On that account, it is of high importance to inspect the documentation provided by modeling groups on the relevant realization attributes of their model ensemble.

Causal model evaluation is also helping to better understand remote contributions to internal variability over specific regions. As we are not subtracting the ensemble mean (representing the forced response), the causal links found when analyzing observational reanalysis and CMIP6 historical simulations are thus expected to include external forcing contributions, especially those from space and time-varying aerosol radiative forcing. It is therefore crucial to separate the internal variability component from the externally forced part to gain a better understanding on the effects of external forcings on Atlantic-Pacific interactions. Meehl et al. 2021a recently examined this effect through time series pacemaker experiments in which effects from all external forcings and/or aerosols only are removed. The approach and findings presented there motivated the follow-up study (Chapter 5 where an ensemble of pacemaker simulations and a pre-industrial control run are to be analyzed through causal discovery algorithms to reveal the impact of climate change on the teleconnections and interactions between major modes of climate variability. Overall, the regime-oriented causal model evaluation followed in this study has the potential of a powerful methodology that can be applied to a number of environment-related topics, offering tremendous insight to improve the understanding of the complex earth system and the state-of-the-art of climate modeling.

# 5. Changing effects of external forcing on Atlantic-Pacific interactions

Historical analyses in recent studies suggested connections between the Atlantic and Pacific basins underscoring the significance of processes such as the Walker circulation in forging these connections and present the mechanisms through which distinctive climate variability modes affect each other, engendering complex networks of interrelated impacts on global and regional climate variability (Kumar et al. 2014; Levine et al. 2017; Li et al. 2016; Meehl et al. 2016; Meehl et al. 2021a; Park et al. 2023; Ruprich-Robert et al. 2017; Yang et al. 2020). The discourse on the recent Walker circulation trends continues to be a subject of scholarly debate (DiNezio et al. 2013; Kociuba and Power 2015; Power and Kociuba 2011; Vecchi and Soden 2007). While some studies found internal variability playing an important role in explaining the recent strengthening of the Walker circulation (Chung et al. 2019), the role of the adjacent Atlantic ocean in modulating tropical Pacific variability cannot be sidelined, pointing to a potential anthropogenic influence on Atlantic SST warming and its consequences on Pacific variability (Klavans et al. 2022; Kucharski et al. 2011; McGregor et al. 2014; Watanabe and Tatebe 2019). In order to help with the separation of internal variability from external forcings, this section leverages large ensemble simulations which emerge as a powerful tool to unravel observed trends and facilitate the detection and attribution of anthropogenic climate change effects (Borchert et al. 2021; Deser and Phillips 2023; Klavans et al. 2022; Menary et al. 2020). The choice of CMIP6 large ensembles used to quantify the externally forced response, is based on the climate modes evaluation carried out in Chapter 4. To deepen this inquiry, this section narrows the scope of the thesis to examining teleconnections on a seasonal to interannual basis, differing from the yearly-interannual to decadal timescales investigated in the previous Chapter 4. Drawing upon the frameworks posited by Meehl et al. 2021a; Park et al. 2023, the study conducts a causal analysis of reanalysis data to scrutinize distinct teleconnection regimes within two historical phases: the Pacific-driven regime (1950-1983) and the Atlantic-driven regime (1985-2014). The utilization of Pacific pacemaker simulations facilitates the examination of the ENSO's impact on teleconnections in both the North Pacific and North Atlantic regions, encompassing analyses with and without the presence of externally induced signals. Complementing this, the study uses pre-industrial control run results to substantiate the inherent occurrence of Atlantic-Pacific interactions, devoid of anthropogenic external forcings.

The work in this Chapter 5 (including text, figures, and supplementary material), has been recently submitted to Earth System Dynamics journal (**Karmouche** et al. 2023b). Similar to

**Karmouche** et al. 2023a (on which Chapter 4 is based), the author of this thesis led the study, the writing of the manuscript, performed all the analysis and produced all figures and tables. The code to reproduce the study in this Chapter 5 (with all figures and tables) will be publicly available upon publication of the paper.

## 5.1. Data and methods

### 5.1.1. Indices

Candidate variables for the causal analysis of this Atlantic-Pacific study are chosen to represent the tropical and extra-tropical pathways connecting the tropical Pacific and the tropical North Atlantic (as discussed Section 2.2.3) and which involve ENSO, SSTAs over the Tropical North Atlantic (TNA) region, PNA, NAO and the PWC. Indices for these variables are chosen respectively as: the Niño3.4 index, the TNA index, the PNA index, the NAO index, and the PWC$u$ index. The PWC$u$ index is calculated as the monthly zonal wind (u component) anomaly at 925 hPa (or nearest available pressure level in simulations) over the region [6°N–6°S, 180°-150°E], following methods from Chung et al. 2019. Positive (negative) PWC$u$ values denote anomalous westerlies (easterlies) winds that imply a weakening (strengthening) of the PWC.

### 5.1.2. Observational and reanalyses datasets

To derive the SST-based indices in the Atlantic and Pacific (TNA and Niño3.4) during the documented historical period from 1950-2014, the HadISST dataset was employed (Rayner et al. 2003). Additionally, the SLP and the zonal wind component (u) at 925 hPa were derived from the NCEP-NCAR-R1 dataset (Kalnay et al. 1996) to derive indices for the atmospheric modes (NAO and PNA) and the Walker circulation over the Pacific (PWC$u$).

### 5.1.3. Pacific pacemaker simulations

To scrutinize the influences of ENSO on the Atlantic-Pacific interplay, a 10-member ensemble of the CESM2 model (Danabasoglu et al. 2020) was employed, where the SSTAs in the eastern tropical Pacific were prescribed according to ERSSTv5 data spanning 1880-2019. Analogous to the reanalysis datasets detailed in Section 5.1.2 above, the evaluation revolves around the period between 1950 and 2014. To retain the inherent state and discrepancies of the model, the SST nudging only encompassed the anomalies and not the total SST. The ensemble counts all CMIP6 evolving external and anthropogenic elements, representing historical forcings until 2014. The data extracted parallels that in reanalysis datasets, including surface temperature (TS), SLP, and U variables. Comprehensive details regarding the dataset are retrievable from the Climate Variability and Change Working Group (CVCWG) webpage[1].

[1] Accessible via https://www.cesm.ucar.edu/working-groups/climate/simulations/cesm2-pacific-pacemaker, DOI: 10.26024/gtrs-tf57, last access: 01.09.2023

### 5.1.4. Pre-industrial control run

To deepen the exploration of intermodal interactions in the Atlantic and Pacific basins in an unforced setting, 120 years of data drawn from the CESM2 pre-industrial control setup (representing the era preceding 1850, Eyring et al. 2016) was utilized. Specifically, we use data from the beginning of year 1000 to the end of year 1119. Similar to reanalysis and pacemaker simulations, this run incorporates monthly means of TS, SLP, and U variables. We use the CESM2 model for its remarkable simulation of ENSO characteristics (Capotondi et al. 2020; Chen et al. 2021; Danabasoglu et al. 2020; Deser et al. 2020) and also to facilitate the comparison with the pacemaker ensemble results.

### 5.1.5. Separating internal variability from the externally forced components

To isolate internal variability from the Pacific pacemaker simulations, we first calculate a multi-ensemble mean (MEM) for each variable, representing an estimate of the externally forced component. This is done by averaging three CMIP6 historical large ensemble means (with different numbers of ensemble members): CESM2 (11 members), MIROC6 (50 members), and UKESM1-0-LL (16 members). These models were chosen to represent the MEM, since they realistically simulate the spatiotemporal characteristics of the major modes of climate variability (notably ENSO and North Atlantic SST modes) during the historical period (Fasullo et al. 2020; **Karmouche** et al. 2023a; Phillips et al. 2020). It is noteworthy that these CMIP6 models were among the best-scoring large ensembles during the pattern correlation and causal model evaluation in the previous Chapter 4. Moreover, to detect changes in various climate phenomena, the required number of members in an ensemble simulation may differ. Forced changes in ocean heat content can be detected with only a few members, while changes in atmospheric circulation or extreme precipitation and temperature may need 20-30 members (Deser et al. 2012; Smith et al. 2022; Tebaldi et al. 2021). Detecting forced changes in the characteristics of internal variability, such as its amplitude, spatial pattern, and remote teleconnections, may require even larger ensembles (Deser and Phillips 2023; Milinski et al. 2019; O'Brien and Deser 2023; Smith et al. 2022). The idea behind estimating the forced response from three different large ensembles with different numbers of realizations is to reduce any biases originating from the model's own representation of CMIP6 forcing and/or from the ensemble size. Because each of the 10 members in the pacemaker ensemble is subjected to the same CMIP6 time-varying external forcing, we assume that MEM is the response to external forcing such as GHG-induced warming trends, solar radiation, volcanic activity, land use changes, and anthropogenic aerosols. Consequently, the discrepancies in each pacemaker simulation relative to MEM can be attributed to internal variability. Therefore, for a given variable $X$ ($X = SST, U, SLP$), we can express the separation in a pacemaker simulation $i$ as:

$$X_i = X_{\text{MEM}} + X_{\text{internal}(i)}, \qquad i = 1, 2, \ldots, 10 \tag{5.1}$$

where $X_{\text{MEM}}$ is the forced component estimated from the CMIP6 MEM and $X_{\text{internal}(i)}$ is the residual of the original $X_i$ minus the forced response $X_{\text{MEM}}$, which varies among different

members and shows the component associated with isolated internal variability. This is similar to methods from Wu et al. 2021, but using the CMIP6 MEM instead of the pacemaker ensemble mean to quantify the forced component.

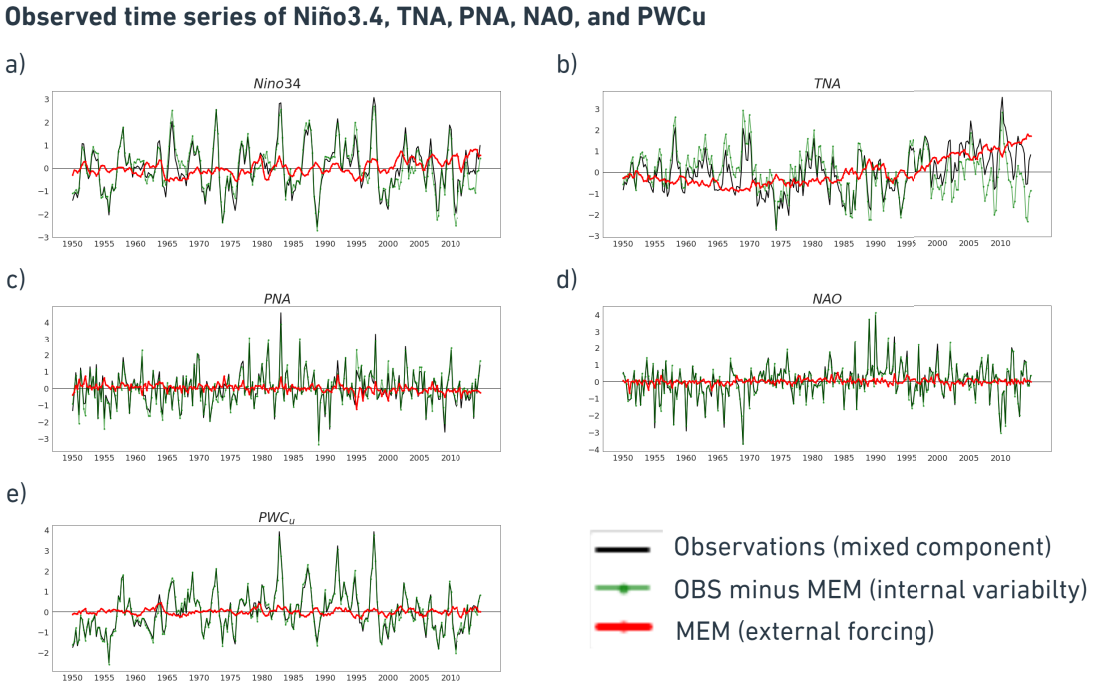


**Figure 5.1.:** Standardized seasonally averaged time series of a) Niño3.4, b) TNA, c) PNA, d) NAO, and e) PWC$u$ during the observed 1950-2014 period. Unit for the standard deviations are [°C] in a and b, [Pa] in c and d, and [m.s$^{-1}$] in e. The time series in black represent the mixed signal from indices calculated using HadISST (a,b) and NCEP-NCAR Reanalysis-1 (c-e). The time series in green are calculated after subtracting the CMIP6 external forcing represented by MEM following Equation (5.1). In each panel, the red line denotes the difference between the black and green line at each time step, representing the varying effect of subtracting MEM on each index. Figure from **Karmouche** et al. 2023b

To isolate the internal variability in observations and the pacemaker simulations following Equation (5.1) we subtract the MEM for SST, SLP, and U from observations and each pacemaker simulation before calculating the indices above. Figure 5.1 illustrates the standardized seasonally averaged time series of Niño3.4 (a), TNA (b), PNA (c), NAO (d), and PWC$u$ (e) indices from observations for the 1950-2014 period. For each index, the time series in black represents the original indices from HadISST (a,b) and NCEP-NCAR-R1 (c-e), as mixed signals including external forcing (non-linear trends). The time series in green show the indices after subtracting MEM (producing an isolated internal variability). The difference that denotes the effects of external forcing is shown in red. Based on 5.1, there are two indices that expose positive trends represented by external forcings, namely Niño3.4 (a) and TNA (b). The rest of the analyzed indices do not show distinctive trends nor significant effects of external forcing.

### 5.1.6. Application of PCMCI+

On the time resolution of the PCMCI+ data frames, we note that we use seasonally averaged time series of each index (TNA, Niño3.4, PNA, NAO, and PWC$u$) with four seasons (time steps) per year, as averages of January-February-March (JFM), April-May-June (AMJ), July-August-September (JAS), and October-November-December (OND). For the parameter settings of the PCMCI+ we set the maximum time lag to 8 time steps ($\tau_{max}$ = 8 [seasons]), meaning that we only investigate teleconnections within a maximum of two-year time lag. Additionally, we also look at contemporaneous links detected within the same season ($\tau_{min}$ = 0). These contemporaneous inter-dependencies that happen with no time lag (i.e., $\tau$<1) are shown as straight links on the causal networks (similar to Chapter 4). The significance threshold for MCI partial correlation analyses was established at 0.2, to account for the limited sample duration. As mentioned in Section 3.5.1, in this section we transform the cross-MCI to linear link coefficients (link coeff.) using the linear mediation model (similar to results shown in Figure 3.2). Note that the PCMCI+ resulting graphs may contain unoriented as well as conflicting links ("o-o" or "x-x" ) at lag zero (e.g. due to Markov equivalence and conflicting orientation rule applications). Here we orient these links to satisfy a (fully-oriented) Directed Acyclic Graph (DAG) based on the direction in which they most appeared in all instances of that particular contemporaneous link across the CESM2 pacemaker ensemble during each regime. The set of directions learned from the majority ruling is used to direct unoriented links during the reanalysis and the pre-industrial control runs as well. Such adjustment is practiced while ensuring no occurrence of contemporaneous cycles. A detailed description of the originally unoriented contemporaneous links, their occurrences, newly attributed directions, and the underpinning rationale for these orientations can be found in Table B.1 of the Appendix.

## 5.2. Results

### 5.2.1. Analysis of observational and reanalysis datasets

#### Observed correlation patterns

To demonstrate the relationships between Atlantic and Pacific SST modes and to estimate the effect of removing the externally forced signal (represented by MEM, for more details see Section 5.1.5) from the original SSTs, we first calculate Pearson's correlation between global SSTAs with SST-derived indices based on the original HadISST dataset.

Figure 5.2 displays the regression patterns of global SSTAs during two distinct regimes: the Pacific-driven 1950-1983 period (Figure 5.2a and b) and the Atlantic-driven 1985-2014 period (Figure 5.2c and d). The analysis in Figure 5.2 focuses on the relationship between SSTAs and two key climate indices (namely Niño3.4 and TNA indices) using the original SST signal, hypothesized to contain influences of both internal variability and external forcing (as discussed in Section 5.1.5 and seen in Section 5.1.1a and b). Figure 5.3, on the other hand, shows the same analysis but after isolating the internal variability component of the SST modes and

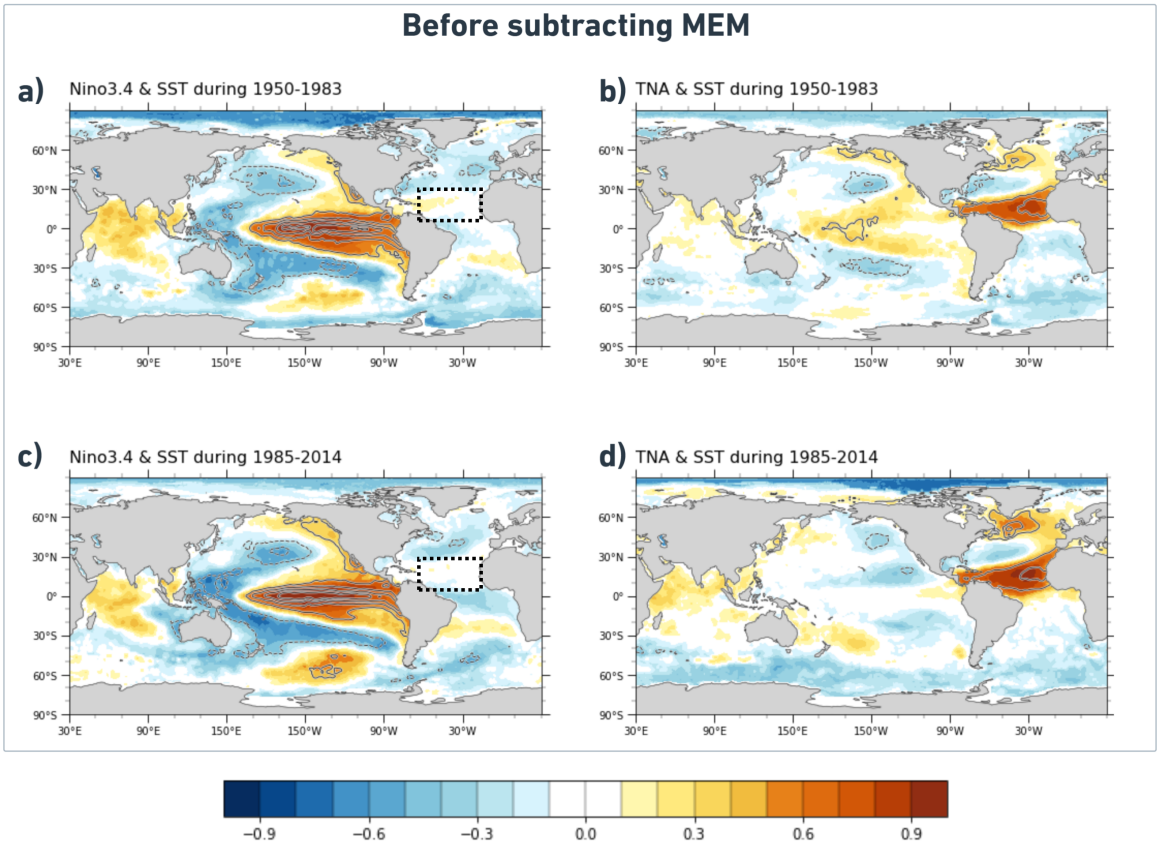


**Figure 5.2.:** Regression pattern of global SSTAs onto Niño3.4 index (a,c) and TNA index (b,d) during both periods: 1950-1983 (top) vs 1985-2014 (bottom). a) Pearson's correlation coefficients (shadings) and regression coefficients (contours) of detrended global SSTAs with the standardized Niño3.4 index based on HadISST data during 1950-1983. b) Same as (a) but showing the SSTAs correlation and regression with the standardized TNA index instead of Niño3.4. c) Same as (a) but for the 1985-2014 period. d) Same as (b) but for the 1985-2014 period. White-shaded areas indicate weak correlations (between -0.1 and 0.1). The contour interval is 0.2 (°C) with dashed (solid) contours indicating regions with negative (positive) regression coefficients. Global SSTAs are detrended by removing the global mean at each time step. For convenience, the dashed black box shows the considered TNA region. Figure from **Karmouche** et al. 2023b.

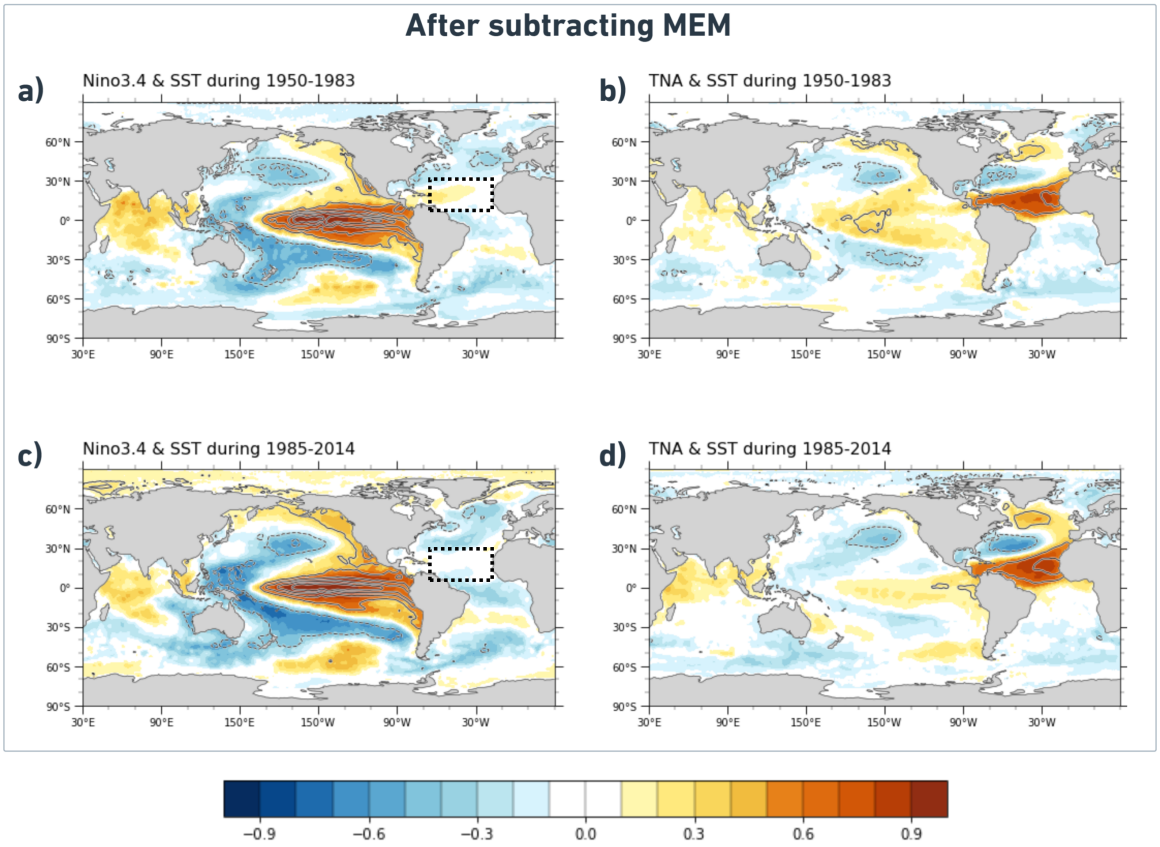


**Figure 5.3.:** Similar to Figure 5.2 but after removing the externally forced signal represented by MEM following Equation (5.1) (see methods Section 5.1.5). All SST fields have the CMIP6 MEM subtracted prior to calculating anomalies and performing the regressions. Figure from **Karmouche** et al. 2023b.

anomalies by subtracting MEM from the original SST fields following Equation (5.1). For both Figure 5.2 and Figure 5.3, the top panel (a) illustrates Pearson's correlation coefficients and regression coefficients between detrended global SSTAs and the standardized Niño3.4 index for the period 1950-1983, based on HadISST data. Similarly, the second panel (b) presents the same correlation and regression analysis but with the standardized TNA index instead of Niño3.4. The bottom panels (c) and (d) replicate the analyses from panels (a) and (b) but for the period 1985-2014. To visualize the impact of subtracting MEM, the reader can compare one panel from Figure 5.3 to its respective panel in Figure 5.2.

- **SSTAs regression onto the Niño3.4 index.** Before removing external forcing, during the 1950–1983 period (Figure 5.2a), we find weak correlations between the Niño3.4 index and SSTAs over most of the Atlantic with negative values extending from the European west coast and decaying north of the TNA region (black dashed box in Figure 5.2a). Within this TNA region, there are weak positive correlations extending from the Gulf of Mexico and decaying around the center of the TNA region. This positive relationship is consistent with several previous studies (Enfield and Mayer 1997; García-Serrano et al. 2017; Jiang and Li 2019; Klein et al. 1999) that suggest warm (cold) SSTAs develop over the TNA region and peak during the spring and summer following an El Niño (La Niña) winter (Park et al. 2023). These positive values vanish when analyzing the 1985-2014 period (Figure 5.2c), where the TNA region shows mainly values between -0.1 and 0.1 for the Niño3.4 index correlation with the SSTAs over that region (see the black dashed box in Figure 5.2c). In the North Pacific, both periods show positive correlations extending along the west coast of North America, and negative correlations in the central North Pacific. This horseshoe-like pattern is consistent throughout all SSTA-Niño3.4 regression maps (panels a and c in Figure 5.2 and Figure 5.3). Comparing Figure 5.3a to Figure 5.2a, we conclude that although the positive correlations of tropical Atlantic SSTAs with the Niño3.4 index slightly increased when subtracting MEM during the Pacific-driven 1950-1983 period, the impact of removing the externally forced signal is not pronounced. This conclusion also holds for the SSTA-Niño3.4 correlations during the 1985-2014 regime as there are no major differences between the TNA box (dashed box) in Figure 5.3c compared to the one in Figure 5.2c.

- **SSTAs regression onto the TNA index.** During the first period (1950-1983), the results suggest no major difference in the relationship between the TNA index and North Pacific SSTAs before and after removing external forcing. The correlation maps for the Pacific-driven regime (Figure 5.2b and 5.3b) show mainly positive values in the central equatorial Pacific and negative values in the central North and central South Pacific, similar to the symmetric horseshoe pattern observed from the Niño3.4 regressions shown in Figure 5.2a and 5.3a. Conversely, the subsequent 1985-2014 Atlantic-driven period, where externally forced warming projects greatly onto the Atlantic SST changes

(Klavans et al. 2021; Klavans et al. 2022; Mann et al. 2014), Figure 5.2d shows negative correlation values of TNA index with SSTAs over the eastern Tropical and North Pacific. However, the removal of the external forcing resulted in a strengthened dipole SSTA pattern over the North Atlantic and weak positive correlations over the central and eastern equatorial Pacific (Figure 5.3d). The removal of external forcing suppressed the negative relationship between the TNA index and SSTAs over the tropical and northeastern Pacific during the 1985-2014 period (Figure 5.3d). It is also important to highlight that the impact of external forcing is much more pronounced during 1985-2014, given the clear differences in the Pacific sector between the correlation maps in Figure 5.2d and 5.3d, and which falls in agreement with previous studies (Dong et al. 2014; Dong and McPhaden 2017; Kucharski et al. 2016; Meehl et al. 2013; Meehl et al. 2021a). This suggests that external forcing might have played a major role in the recent effect of the Atlantic on the Pacific. However, the nature of these connections remains unclear. Next, the causal discovery methodology will be applied to better quantify these connections to provide insights into the relevant physical processes.

**Causal networks**

To investigate the teleconnections during the two periods from a causal discovery perspective, Figure 5.4 demonstrates causal networks of Atlantic-Pacific teleconnections based on indices from Section 5.1.1 (Figure 5.1) from the Reanalyses datasets (Section 5.1.2). The left panels in Figure 5.4 (a,c) show the resulting causal networks during the 1950-1983 Pacific-driven period, while the panels on the right (b,d) show the networks for the 1985-2014 Atlantic-driven period. For each period, the panel on top (a,b) represents the original observed signal (corresponding to the black curve in Figure 5.1). The bottom panel shows the networks where indices have been calculated after subtracting the MEM, effectively isolating internal variability (corresponding to the green curve in Figure 5.1). In the bottom panels (c) and (d) the MEM is subtracted from the reanalyses before PCMCI+ is applied. Picturing Niño3.4, PNA and $PWC_u$ as variables representing the Pacific while TNA and NAO represent the Atlantic, we can, for example, look at how nodes from the Pacific basin are linked to each other and to the Atlantic ones, and vice-versa. As a general note, based on Figure 5.4 (all panels), we detect the extensively studied relationship of ENSO and PWC(Bayr et al. 2014; Trenberth 1997; Zhao and Allen 2019), illustrated through the strong positive contemporaneous causal connection from $PWC_u$ to the Niño3.4 ($PWC_u \rightarrow$Niño3.4 link). We confirm that positive values of $PWC_u$ indicate anomalously weak easterly winds associated with the weakening of PWC and the emergence of El Niño events. With PWC inextricably linked to Niño3.4, a conclusion solidified throughout the results in Sections 5.2.1 and 5.2.2, we consider causal links to and from a $PWC_u$ node to denote a causal relationship associated with ENSO. We also find a weak opposite sign causal response from $PWC_u$ to Niño3.4 at one season lag (Figure 5.4a and c).

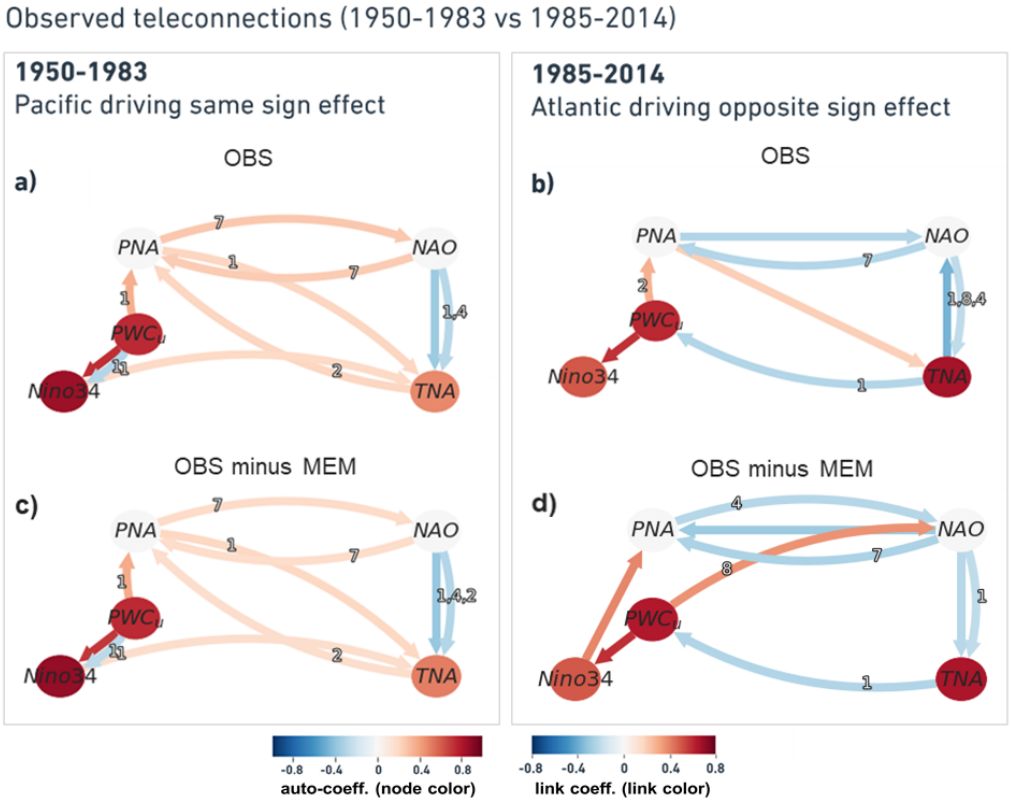


**Figure 5.4.:** Causal networks representing Atlantic-Pacific teleconnections for 1950-1983 (left column) vs 1985-2014 (right column) in the Reanalyses datasets. (a) Constructed by applying PCMCI+ on the standardized time series of the five seasonally averaged indices calculated from reanalysis datasets for the 1950-1983 period. Nodes represent the time series associated with each climate variability index (see node labels). Node colors indicate the auto-link coefficients (auto-coeff), and the color of the links denote the linear link coefficient (link coeff). The link-associated time lags (unit=1 season) are shown as small labels on the curved links. Straight links show contemporaneous inter-dependencies that happen with no time lag. (b) Same as (a) but for the 1985-2014 period. (c) same as (a), but with indices calculated after removing MEM. (d) Same as (c) but for the 1985-2014 period. Figure from **Karmouche et al. 2023b**

- **Pacific-driven regime (1950-1983)**: The Pacific-driven 1950-1983 is found to be dominated by a same-sign effect from ENSO on TNA through both tropical and extra-tropical routes. During an El Niño event, the weakened Walker circulation allows an eastward shift in the maximum convection center from the Maritime Continent to the central equatorial Pacific. This tropical convection triggers a poleward-propagating Rossby wave which extends into the midlatitudes, constituting the PNA pattern. This teleconnection linking the equatorial and extra-tropical Pacific is detected as a lagged positive causal link from PWC$_u$ to PNA during 1950-1983 (Figure 5.4a and c). The wave pattern associated with PNA contributes to the formation of an anomalous low-pressure center over the southeast United States and the Caribbean. The presence of the PNA pattern results in anomalous southwesterly winds over the TNA region. The negative rainfall anomaly over the western Pacific and the Atlantic region, caused by the reversed Walker circulation during El Niño, plays a role in inducing this anomalous low-pressure center

over the southeast United States. Additionally, the suppressed heating response in the Atlantic region, resembling the Gill-like pattern (Gill 1980; Matsuno 1966), also contributes to the development of anticyclonic circulation and southwesterly wind anomalies over the TNA region (García-Serrano et al. 2017; Jiang and Li 2019). The combined effect of these extratropical and tropical routes leads to southwesterly wind anomalies that weaken the northeasterly trade winds, reduce evaporation, and induce SSTA warming over the TNA region (Casselman et al. 2021; García-Serrano et al. 2017; Jiang and Li 2019; Meehl et al. 2021a; Park et al. 2023; Trenberth 1997; Wallace and Gutzler 1981). The two routes for the ENSO effect on TNA, which is enhanced during the 1950-1983 period, can be seen through the causal networks in Figure 5.4a and c showing two positive (lagged) links from the Pacific to TNA: PNA→TNA (1 season) and Niño3.4→TNA (1 season). The TNA→PNA link in Figure 5.4a and c is lagged by two seasons which might suggest that the warming over the TNA region contributes back to anomalous southwesterly winds and maintains the PNA pattern. The Pacific-driven regime's causal graphs show that after El Niño excites PNA, the latter appears to be mutually connected to the NAO with a 7-season lag (PNA→NAO and NAO→PNA links in Figure 5.4a and c). These links are however inconsistent with previous studies on the linkage between North Atlantic and North Pacific modes of atmospheric circulation and which suggest contemporaneous negative links between PNA and NAO. Honda et al. 2001 conducted a study on the period between 1979 and 1994 and discovered a negative correlation (-0.7) between the intensities of the Aleutian and Icelandic lows (low-pressure centers of the PNA and NAO, respectively). Song et al. 2009 concluded that the strongest negative correlations between PNA and NAO occur with no time lag and within a range of 10-day lags. By analyzing reanalysis datasets, Pinto et al. 2011 found no significant anti-correlation between PNA and NAO between 1950 and the mid-1970s, but this was clearly detected during the sub-period 1973–1994. A period of weak PNA-NAO coupling might explain the undetected contemporaneous PNA→NAO negative links during the Pacific-driven period. According to Soulard and Lin 2017, it is the absence of tropical forcing from ENSO that strengthens the relationship between PNA and NAO. On the other hand, observational uncertainty prior to the satellite era can also be a reason that lagged positive links were detected between NAO and PNA instead of contemporaneous negative links. On the Atlantic side, apart from the influence of ENSO and PNA on TNA, NAO is also found to impact the TNA SSTAs (contemporaneous negative NAO→TNA links in Figure 5.4a and c). The changes in pressure gradients between the Azores high and the Icelandic low can alter trade winds, heat fluxes, and SSTs. Reduced northeasterly trade winds contribute to trapping warm SSTAs over the TNA region as less latent heat is released into the atmosphere (Cassou and Terray 2001; Lee et al. 2008). We detect several causal connections between NAO and TNA where the NAO drives changes in TNA, not only contemporaneously but also lagged (NAO→TNA, Figure 5.4a and c). This negative relationship of the NAO index with TNA is seen through the negative NAO→TNA links in Figure 5.4a and c. Although

direct links connecting either Niño3.4 (or $PWC_u$) to NAO have not been detected during the Pacific-driven regime, the NAO is thought to affect the interplay between ENSO and TNA which is further complicated by the fact that ENSO can also influence the NAO through extratropical pathways (Casselman et al. 2021; Doblas-Reyes et al. 2017). If we consider the causal links that connect the SST modes (Niño3.4 and TNA) directly, or through $PWC_u$ and PNA, then these results support the hypothesis that it was the Pacific SSTs mainly driving the same sign response on the Atlantic SSTs between 1950 and 1983 (Meehl et al. 2021a; Park et al. 2023). Overall, comparing Figure 5.4a to c reveals a limited effect of external forcing during the first period as no major changes were detected in the causal graph after subtracting MEM.

- **Atlantic-driven regime (1985-2014)**: During the second period, the monopole SSTA pattern centered over the TNA region (shown in Figure 5.2d) suggests enhanced precipitation there. The Rossby wave energy associated with the enhanced precipitation propagates toward the subtropical Pacific. Combined with the modulated Walker circulation, this induces easterly wind anomalies over the equatorial Pacific, favoring the development of La Niña events (Ham et al. 2013b; Park et al. 2022; Park et al. 2023). This is illustrated in Figure 5.4b and d through the 1-season lagged TNA→$PWC_u$ negative link, an effect that evidently reaches the Niño3.4 node (strong $PWC_u$→Niño3.4 link). While the atmospheric bridge connecting the equatorial and the extra-tropical Pacific was detected as $PWC_u$→PNA links in Figure 5.4a-c, this was detected as a direct contemporaneous Niño3.4→PNA link when external forcing is removed during the second period (Figure 5.4d). Without external forcing, the NAO is found to drive small changes in TNA (Figure 5.4d). The contemporaneous TNA-NAO connection is found in the opposite direction during the externally forced Atlantic-driven regime (TNA→NAO, Figure 5.4b). The latter is also the strongest occurrence of TNA-NAO links among the results in Figure 5.4. The ENSO effect on TNA through the extratropical pathway is still detected when external forcing was not removed. This is seen in Figure 5.4b as a contemporaneous link from PNA to TNA in addition to an extratropical PNA teleconnection through $PWC_u$ anomalies (PNA→TNA and $PWC_u$→PNA links). This mild contemporaneous PNA→TNA link is suppressed when MEM is subtracted, in contrast to the appearance of a strong 8-season lagged $PWC_u$→NAO link (Figure 5.4d) inconsistent with the already proposed negative and short lagged ENSO-NAO relationship (Brönnimann et al. 2007; Brönnimann 2007). Contrary to the first period, the contemporaneous negative PNA connection to NAO (Honda et al. 2001; Pinto et al. 2011; Song et al. 2009) is detected during the second period (PNA→NAO in Figure 5.4b and NAO→PNA in Figure 5.4d). Song et al. 2009 explain the anti-correlation they found between day-to-day variability of the Aleutian low and Icelandic low being the result of the anomalous Rossby wave-breaking events associated with the PNA pattern. The paper shows that when the PNA is in a positive (negative) phase, there is more Rossby wave breaking

over the North Pacific (Atlantic), which can weaken or split the polar vortex over that region. This can then affect the jet stream and the storm tracks over the North Atlantic, leading to a negative (positive) NAO phase. Lagged negative causal PNA→NAO and NAO→PNA links are also detected during the 1985-2014 period.

**Summary on the effects of external forcings**

It appears from Figure 5.4 that external forcing does not have significant effects on the causal networks from the 1950-1983 regime (Figure 5.4c vs 5a), consistent with the SST correlation maps suggesting no major difference before and after subtracting MEM (Figure 5.2a vs 4a). Whereas for the following 1985-2014 period, changes were only detected in the tropical/extra-tropical pathways connecting Atlantic and Pacific. The difference between Figure 5.2d and Figure 5.3d hints at a major role played by the externally forced signal in the negative relationship between the TNA index and the tropical east Pacific SSTAs during the Atlantic-driven regime, which is not clearly detected by comparing causal graphs (Figure 5.4b vs Figure 5.4d). Namely, the causal networks show the effect of external forcing as in TNA causing changes in NAO and also in establishing the extra-tropical PNA connection to TNA with no seasonal lag. The latter connection is suppressed when external forcing was removed, in contrast to the appearance of a lagged $PWC_u$→NAO link (comparing Figure 5.4b and 5d). Most importantly, inconsistent with the correlation map in Figure 5.3d, the one-season lagged negative TNA→$PWC_u$ link was still detected, with similar strength (link coeff.), after removing the externally forced signal. It is important to note that this discrepancy, regarding the effect of removing MEM during 1985-2014, was less apparent during a sensitivity test we carried out. There, the analysis of the Atlantic-driven regime was started one year later (1986 instead of 1985) in the observational run and the respective causal graphs revealed that the negative sign response from TNA to PWC was not detected after removing MEM (Figure B.1), consistent with the correlation maps from 1985-2014. This further supports the already proposed studies indicating an increasing impact of external forcing on North Atlantic SSTA changes and the associated widespread effects during the most recent decades (He et al. 2023; Klavans et al. 2022; Murphy et al. 2017). In Appendix Figure B.1, the 8-season lagged $PWC_u$→NAO (featuring in Figure 5.4d) was detected before and after subtracting MEM.

The variability of ENSO's relationship to TNA from one regime to another is influenced by the decadal changes in the background mean state. A study by Park and Li 2019 found that the relationship between ENSO and TNA SST is non-stationary and depends on the phase of the AMV. Specifically, when AMV is trending to its negative phase, the impact of ENSO on TNA becomes amplified and has a more prolonged effect. This was the case during the 1950-1983 period when AMV was trending towards its negative phase. During the 1985-2014 period, AMV was trending back from a negative to a positive phase and the opposite was observed (reduced amplitude and shortened effect). The anomalously warm North Atlantic SSTAs during the positive AMV phase favor the strengthening of the PWC, which ultimately brings upwelled cold water to cool down the central equatorial pacific. The

specific contributions of internal variability to these regime changes remain unclear. Zhang et al. 2019 emphasizes the influence of the thermohaline circulation, particularly the Atlantic Meridional Overturning Circulation (AMOC), on the multidecadal changes in Atlantic SSTs. Whereas for the interannual fluctuations, the paper suggests they are primarily driven by wind-induced changes in turbulent heat fluxes. On the other hand, a series of recent papers (Bellucci et al. 2017; Booth et al. 2012; Klavans et al. 2022; Mann et al. 2014; Watanabe and Tatebe 2019) show growing evidence of an increasing effect of external forcing on the AMV and its lead/lag association with the AMOC. This suggests that internal variability and external radiative forcing contribute to the decadal SST variations over the Atlantic (Klavans et al. 2022; Meehl et al. 2016; Meehl et al. 2021a; Park et al. 2019; Park et al. 2023).

### 5.2.2. Causal analysis of Pacific pacemaker simulations

To scrutinize the potential causal dependencies between the modes, we use a 10-member ensemble of the CESM2 Pacific pacemaker simulations (see Section 5.1.3) where Eastern Tropical SSTAs have been nudged towards observed values (maintaining ENSO evolution, Figure 5.5a). The rest of the coupled model is free to evolve resulting in different climate variations outside the nudging region depending on the single realizations' own initial conditions. The range of possible outcomes for Atlantic SSTAs is then governed by contributions from internal variability, CMIP6 time-varying external forcing, and the potential cross-basin contributions from the Pacific according to the model's dynamics. The variations of the TNA index in the pacemaker simulations are compared in Figure 5.5b to observations (see legend top right), before and after removing the CMIP6 time-evolving external forcing (MEM).

Figure 5.6 is similar to Figure 5.4 but shows causal networks based on an ensemble summary of CESM2 Pacific pacemaker simulations. The causal networks are aggregated based on 10 pacemaker realizations. In the four panels (a-d), we apply the PCMCI+ on the time series of each simulation before aggregating. The link width indicates the number of simulations that feature that link (for reference, the width of the link between PNA and NAO in Figure 5.6a shows the maximum width, equivalent to 10 simulations, and the link between Niño3.4 and TNA shows the minimum width, equivalent to 2 simulations). In other words, the more ensemble members were found to estimate the link during that particular run, the thicker the link appeared. The mean link coefficient value averages all coefficients of that link's instances and the link labels denote the median time lag at which they were detected. The node color translates the average auto-link coefficient of each time series among the pacemaker ensemble. In Figure 5.6c and d, the MEM is subtracted from every simulation before the causal discovery algorithm is applied. For simplicity, we directed contemporaneous links based on the most frequent direction in which they are detected within the ensemble (treating each period and scenario separately). We also only took into account links with absolute value coefficients above the arbitrary threshold of 0.1.

The prominent feature of the causal analysis on the Pacific pacemaker simulations before removing external forcing (Figure 5.6a and b) is the ability to distinguish a Pacific-driven period

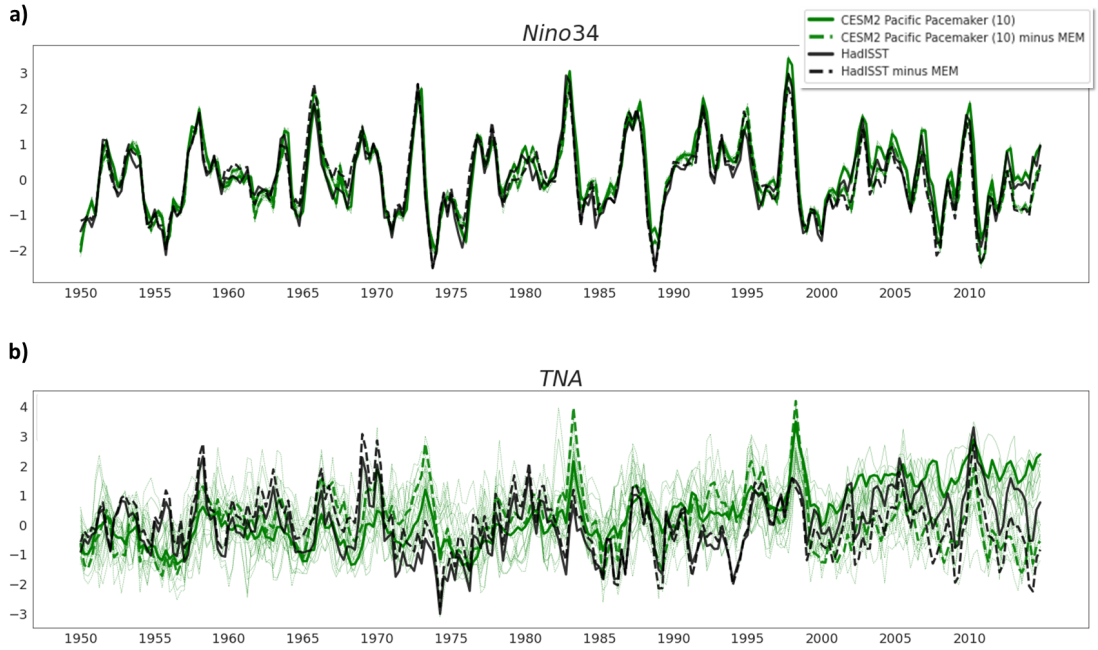


**Figure 5.5.:** Standardized indices from the Pacific pacemaker ensemble (10 members) with observations (HadISST) for Niño3.4 (a) and TNA (b). Black solid (dashed) lines denote observed time series from HadISST data before (after) multi-ensemble mean (MEM) subtraction. Green solid (dashed) lines depict the CESM2 Pacific pacemaker ensemble average before (after) MEM subtraction. Adapted from **Karmouche** et al. 2023b.

as opposed to an Atlantic-driven one. Similar to observations, the regression and correlation maps in Figures 5.2 and 5.3, and previously introduced literature (Meehl et al. 2021a; Park et al. 2023), the causal networks in Figure 5.6 also show the 1950-1983 period was dominated by the equatorial Pacific SSTAs driving a same-sign effect on the tropical North Atlantic SSTAs and triggering a negative-sign response from the Atlantic onto the Pacific during the subsequent 1985-2014 period (via TNA→ $PWC_u$). This is illustrated during the first period through the links originating from the Niño3.4 (and/or the PWC) node and reaching the Atlantic modes (NAO and/or TNA nodes) either directly (e.g. PWC – TNA) or potentially through PNA (Niño3.4 → PNA → NAO, Figure 5.6a-c). Both the results from the reanalysis (Figure 5.4a) and those from the pacemaker ensemble (Figure 5.6a) show positive causal Niño3.4→TNA links and/or $PWC_u$→TNA during the Pacific-driven 1950-1983 regime. When MEM is subtracted during this regime (Figure 5.6c), contemporaneous PNA→TNA links were also estimated. This means that both the tropical and extra-tropical routes for ENSO effect on TNA are detected during the Pacific-driven regime (Figure 5.6a and c). The 1985-2014 period knows a decay of the extra-tropical pathway (no PNA→TNA link in Figure 5.6b) and shows that several ensemble members detect rather the negative TNA→$PWC_u$ link, which is consistent with the causal network from reanalysis (Figure 5.4b). The thick line of the TNA→$PWC_u$ connection in Figure 5.6b suggests that most of the CESM2 pacemaker simulations with nudged observed SSTAs in the equatorial Pacific simulate the opposite-sign response from the Atlantic to the

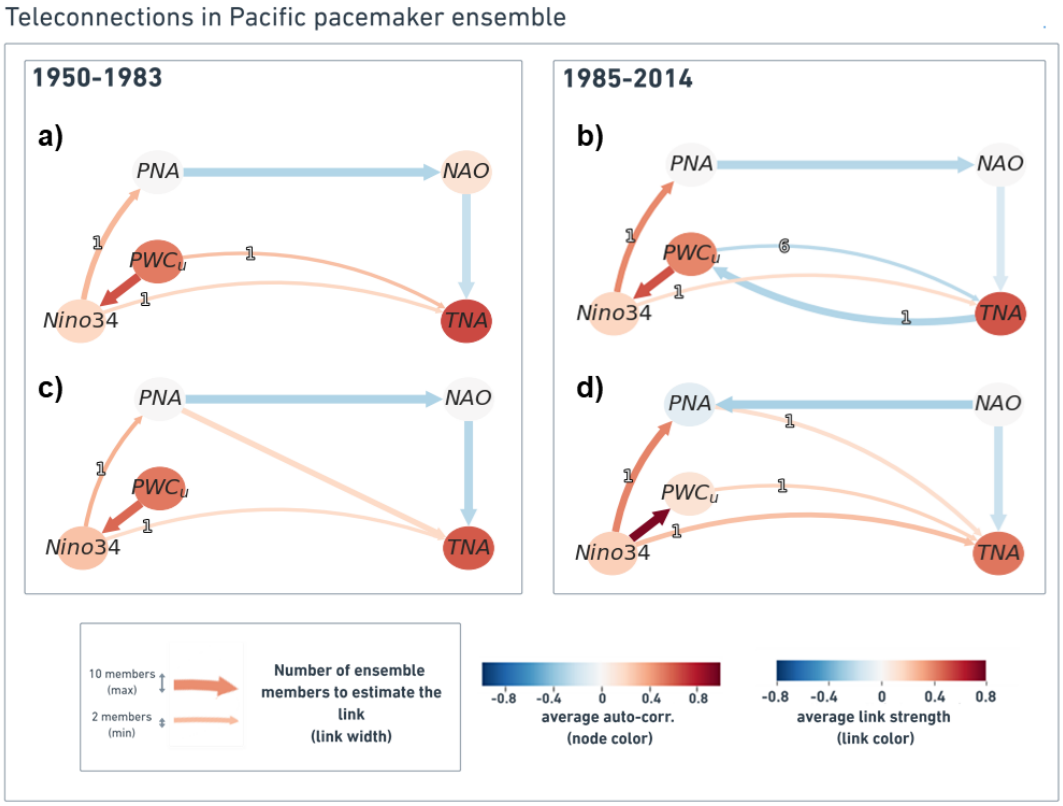


**Figure 5.6.:** Ensemble summary causal networks and time series from Pacific pacemaker simulations (1950-1983 vs 1985-2014). In panels (a-d), we apply the PCMCI+ on the time series of each simulation before aggregating the 10 causal networks into one. The link width shows the number of simulations that feature that link. The link color shows the mean value of link coefficients averaged over the ensemble members. The node color translates the average auto-coefficient of each time series among the pacemaker ensemble. The link labels provide the median time latency (rounded to the closest integer) for all ensemble members that detect a particular link. In (c) and (d) the MEM is subtracted from every simulation before PCMCI+ is applied. The link labels provide the median time latency (rounded to the closest integer) for all ensemble members that detect a particular link. Figure from **Karmouche** et al. 2023b

Pacific during the Atlantic-driven 1985-2014 regime before subtracting MEM. In the meantime, the positive-sign impact from the Pacific on the Atlantic (via either Niño3.4 or PWC on TNA) was detected by at least two members in each experiment. For example, the Niño3.4→TNA link appears in the four experiments (all panels in Figure 5.6). This link is more evident when MEM is subtracted during the second period as Figure 5.6d shows more ensemble members to simulate the link (thicker Niño3.4→TNA link) compared to Figure 5.6b. The simulations from the pacemaker ensemble agree greatly with the proposed contemporaneous negative PNA relationship to NAO (Honda et al. 2001). This was mostly detected as contemporaneous PNA→NAO links in Figure 5.6a-c and as NAO→PNA in Figure 5.6d. As can be seen from Figure 5.6, the similarities with the causal networks from observational data (Figure 5.4) entail an important role of ENSO (in combination with external forcing) in shaping SST variability over the Atlantic. While the PNA-NAO connection is found positive and lagged in observations during the 1950-1983 period (Figure 5.4a and c), it is detected as a negative contemporaneous

connection in most pacemaker simulations. Removing external forcing for the Pacific-driven 1950-1983 regime did not have a significant effect in the case of reanalysis and the same for the pacemaker ensemble except for the vanishing $PWC_u$→TNA link. The relationship between ENSO and PNA is, however, detected by fewer simulations when removing external forcing, and it is illustrated in Figure 5.6c by a thinner and weaker (on average) positive Niño3.4→PNA link compared to the one in Figure 5.6a.

The importance of both ENSO and external forcing is further manifested during the 1985-2014 period through the emergence of the negative sign effect from the Atlantic (TNA) on the Pacific (Niño3.4 through PWC), similar to the observations (Figure 5.4b). On the other hand, when subtracting MEM from the pacemaker simulations, more members show the positive Niño3.4→TNA link (Figure 5.6d) while the significant negative TNA→ $PWC_u$ link is not detected (Figure 5.6d vs. b). We recall that this is different in the causal networks from the observed 1985-2014, which feature the negative TNA→$PWC_u$ before and after subtracting the MEM (Figure 5.4b and d). This apparent effect of external forcing being the main driver of an Atlantic-driven regime during the second period is nevertheless implied by the results from the correlation/regression analysis in the previous section (Figure 5.3d vs (Figure 5.2d) and the sensitivity test in Supplementary Figure B.1. Subtracting external forcing during the most recent period resulted in a change in the direction of the link between $PWC_u$ and Niño3.4 and the link between NAO and PNA. As the directions of contemporaneous links were decided by majority rule (the most frequent direction of a particular lag-zero link among all ensemble members during a specific run), Figure 5.6d shows that more ensemble members detected those links in the opposite direction (Niño3.4 → $PWC_u$ and NAO→PNA).

The observed Niño3.4 time series in Figure 5.5a is similar to the pacemaker ensemble mean (because SSTAs over the Niño region are nudged towards observed values; small differences, most likely originating from observational uncertainty, ERSSTv5 vs HadISST). The pacemaker ensemble mean TNA (green lines in Figure 5.5b) implies an important role of ENSO in shaping SSTAs over the Atlantic, possibly through combining internal variability processes and modulating the effects of external forcing. Despite several discrepancies between the observed and the pacemaker-simulated TNA indices during the years following major volcanic eruptions (e.g. the early 1990s) and during important El Niño / La Niña events (e.g. 1997–1998), the pacemaker ensemble follows similar variations to the observed TNA through most of the 1950 to early 2000s period (green solid and dashed lines compared to black lines). The fact that prescribing SSTAs only in the equatorial Pacific resulted in TNA SSTAs similar to observations emphasizes the role of ENSO in the Atlantic-Pacific interactions and undermines the role of internal variability in driving SST variability over the Atlantic during most of the analyzed period. Literature suggests that ENSO (Maher et al. 2015; Maher et al. 2018) and its decadal imprint, PDV (Allen et al. 2014; Dong et al. 2014), have contributions from external drivers, especially volcanic and anthropogenic aerosols. Other studies show that recent periods of global warming hiatus are the results of anthropogenic aerosols modulating the phase of PDV rather than canceling out other warming effects (Kaufmann et al. 2011; Smith et al. 2016). The results in Figure 5.6 also suggest that the coupling between Atlantic and Pacific SSTs is moderately

strong in the CESM2 model during Niño events, explaining the appearance of Niño3.4→TNA (and/or $PWC_u$→TNA) links in all causal networks on Figure 5.6 (a-d). This also explains the large discrepancies between the pacemaker ensemble mean (lines in green) and observations (lines in black) in Figure 5.5b during significant El Niño years. The main difference between the reanalysis and pacemaker causal networks remains during the Atlantic-driven regime after removing external forcing. Figure 5.5b shows increasing differences between the observed and the pacemaker-simulated TNA after the year 2000. This difference might be due to the overestimation of the 1998-2013 global warming rate in CMIP6 climate models (Fyfe et al. 2021; McBride et al. 2021; Smith and Forster 2021; Smith et al. 2021; Tokarska et al. 2020a; Tokarska et al. 2020b), and inherently in MEM. Different factors contributing to such overestimation in CMIP6 have been proposed including the high equilibrium climate sensitivity (ECS) that results in too strong warming responding to anthropogenic GHGs or too weak cooling responding to aerosols (IPCC 2013; Schlund et al. 2020; Smith and Forster 2021; Tokarska et al. 2020a; Wei et al. 2021). According to Wei et al. 2021, ECS only plays a partial role in the failure of most CMIP6 models in simulating the early 2000s global warming slowdown. Instead, the authors attribute the discrepancy between observed and CMIP6-simulated warming trends mostly to the models' deficiencies in simulating major modes of internal variability at interannual, interdecadal, and multidecadal scales, thus excluding their potential effects (e.g. the cooling effect of PDV switching to a negative phase in the early 2000s).

The different sources of external forcing, the overestimation of most recent warming trends, and the coincidence of volcanic eruptions with ENSO events complicate the attribution of external contributions to the Atlantic-Pacific interactions during the last decades of the historical record. To further test whether the observed teleconnections (including a change in the regime of Atlantic-Pacific interactions) would arise only from internal climate variability, the next section presents results from a pre-industrial control run of the CESM2 model.

### 5.2.3. Causal analysis of pre-industrial control run

Given 120 years of unforced simulation, we use the CESM2 pre-industrial run to analyze the causal connections between the Atlantic and Pacific during their different states.

Figure 5.7a shows the long-term state of the two basins through the smoothed time series of AMV (solid; red and blue) and PDV (dashed; pink and light blue) indices from 120 years of CESM2 pre-industrial control simulation, precisely from the start of the year 1000 to the end of 1119. We define three 40-year periods (160 seasons each) and we reconstruct a causal network for each that represents the connections between the Atlantic and Pacific basins. We investigate such periods the same way we did for reanalysis data and the Pacific pacemaker simulations (Section 5.2.1 and Section 5.2.2, respectively), focusing on the links between the Atlantic and Pacific modes. The causal graphs initially displayed several links of different link strengths. Here in Figure 5.7b, we show only the strongest links (with absolute value link coefficients above the arbitrary threshold of 0.15; i.e. enhanced link colors).

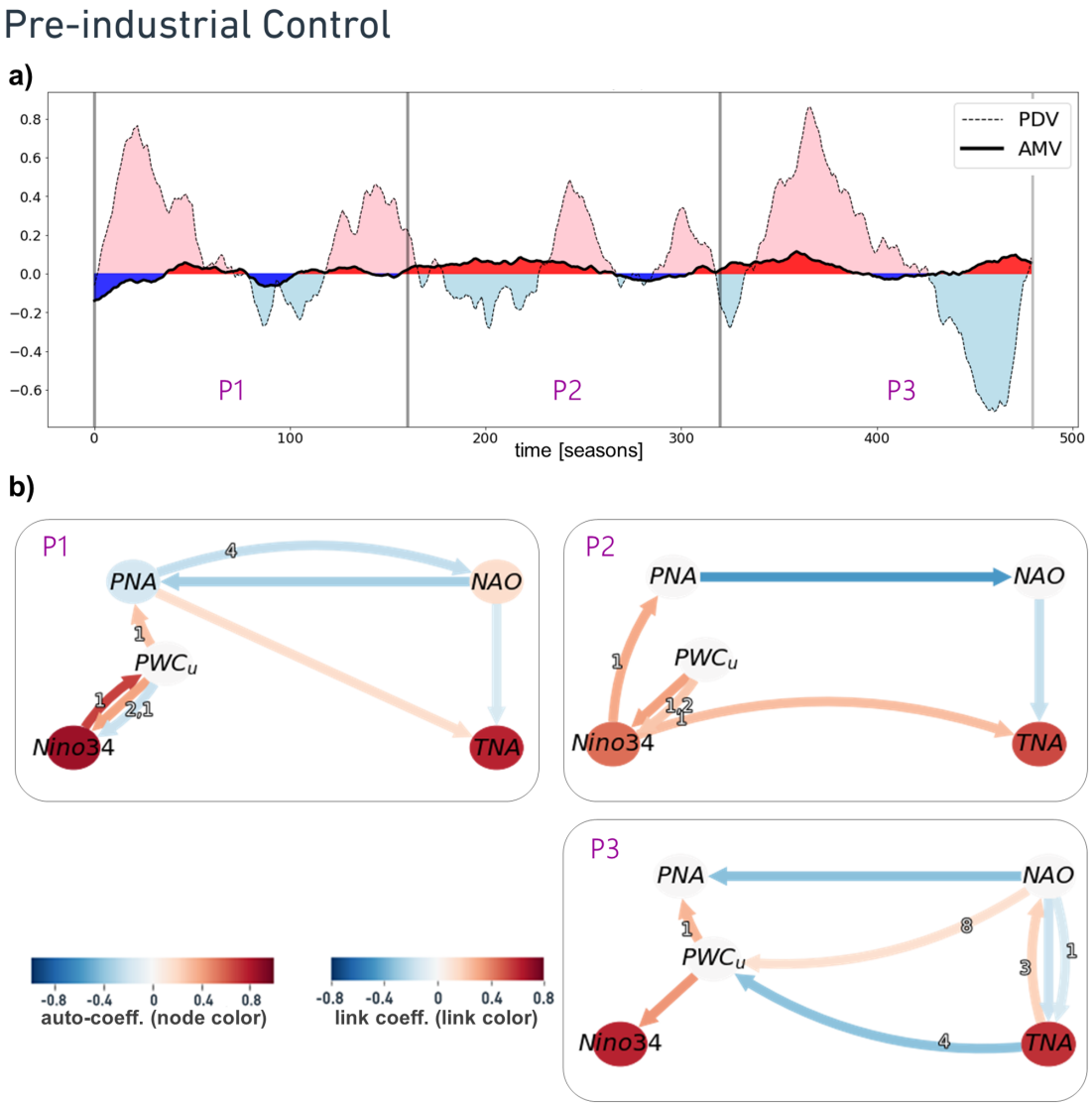


**Figure 5.7.:** CESM2 pre-industrial control simulation. a) Smoothed AMV and PDV indices (10-year low-pass filtered) illustrating the decadal internal variability over the Atlantic and Pacific for 120 years (480 time steps [seasons]). We divide the time series into three 40-year periods (labelled P1, P2 and P3; 160 seasons each), which express different states of AMV and PDV. b) For every period (P1-3) selected in panel (a), we show the respective causal network, similar to reanalysis data (Figure 5.4) and pacemaker simulations (Figure 5.6). Figure from **Karmouche** et al. 2023b

1. The first 40-year period in Figure 5.7a (P1) corresponds to PDV mainly in a positive phase while AMV is trending from a negative to a neutral state. During this period Niño3.4 SST changes were found to strongly affect the PWC-associated zonal winds (1 season lagged positive Niño3.4→PWC$_u$ link; P1 in Figure 5.7b). These wind-induced changes are detected to affect extra-tropical PNA mode with a 1-season lag (positive PWC$_u$→PNA). The PNA changes are detected to be affected by NAO changes as well (NAO→PNA). The causal graph shows that the Pacific was contributing to tropical North Atlantic SSTA changes mainly through the extra-tropical pathway, detected as a contemporaneous positive PNA→TNA link, where the lower pressure center at the

southeastern lobe of the PNA pattern reduces the Atlantic northeasterlies, trapping warm water over the TNA region.

2. The second period (P2 in Figure 5.7a) illustrates a mostly positive AMV (trending negative towards the end of P2) while the PDV switches from a negative to a positive phase. The causal graph (P2 in Figure 5.7b) features a positive Niño3.4→PNA link and a strong negative contemporaneous PNA→NAO link. The ENSO-induced changes are also found to contribute to the TNA SST anomalies (positive Niño3.4→TNA link). Both tropical (Niño3.4→TNA) and extra-tropical (Niño3.4→PNA→NAO→TNA) routes suggest the Pacific was mainly driving the Atlantic during this period.

3. The third period (P3 in Figure 5.7a) shows PDV trending from a strong positive phase to a strong negative phase while the AMV curve shows mainly positive SSTAs. The corresponding causal graph (P3 in Figure 5.7b) shows that the warm TNA SSTAs strongly contributed to La Niña conditions over the Pacific through strengthening the PWC (strong negative 4-season lagged TNA→$PWC_u$ link), cooling the Pacific on the decadal timescale (see PDV during P3 in Figure 5.7a). The warming SST trends in the Atlantic favor a strengthened PWC which ultimately cools the SSTs over the Niño3.4 due to enhanced upwelling. The effect of the Atlantic on the Pacific during this period is manifested in the extra-tropics as well where NAO is found to strongly contribute to PNA variability (contemporaneous NAO→PNA link).

The PNA→NAO connection is stronger in P2 compared to the NAO→PNA links in P1 and P3. The relatively weak magnitudes of PDV anomalies during P2 (compared to P1 and P3; Fig, 8a) suggest reduced ENSO amplitude and hence limited ENSO-like tropical forcing during that period (despite the lagged Niño3.4→PNA). The absence of strong El Niño forcing might explain the strength of the PNA connection to NAO in P2, as suggested by Lin and Derome 2004; Soulard and Lin 2017.

Drawing conclusions from the pre-industrial run analysis, it is evident that:

- Pacific-driven and Atlantic-driven regimes, and the phase switch between them, happen naturally in the absence of anthropogenic forcing.

- This does not reject the possibility that human-induced forcing contributed greatly to at least the observed 1985-2014 changes.

- The strength, direction, and lags of the cross-basins' seasonal-to-interannual interactions are modulated by the long-term state of the two basins (PDV and AMV).

## 5.3. Discussion and Conclusions

Conventional regression and correlation methods offered indications of a regime shift in the Atlantic-Pacific interactions during the observed historical 1950-2014 period (Meehl et al.

2021a; Park et al. 2023). The correlation maps also showed that external forcing (represented by CMIP6 MEM) likely played a major role in setting the negative sign for the relationship between the TNA index and north tropical Pacific SSTAs during the Atlantic-driven 1985-2014 period (Figure 5.3d vs (Figure 5.2d). However, these approaches could not explore the underlying pathways of these effects, which causal graphs provide by uncovering intricate causal relationships.

Based on causal graphs derived from reanalysis data and Pacific pacemaker simulations before separating the externally forced signal (a and b in Figure 5.4 and Figure 5.6), we find the Pacific's same sign influence on Atlantic during 1950-1983, aligning with prior reports (Meehl et al. 2021a; Park et al. 2023). Estimated positive links from Niño3.4 (or $PWC_u$) to TNA represent the tropical pathway where El Niño and the modified Walker Circulation prompt equatorial Atlantic anticyclonic activity, weakening trade winds, and warming tropical North Atlantic as a result of reduced evaporation. Other pathways recognized through PNA and NAO have also been detected. Positive causal links Niño3.4 (or $PWC_u$)→PNA and PNA→TNA highlight the extra-tropical path for the Pacific-induced effect on TNA. El Niño-associated Rossby wave propagation enhances Southeast United States low-pressure center (positive PNA phase), weakening North Atlantic trade winds and promoting TNA warming (García-Serrano et al. 2017; Jiang and Li 2019; Klein et al. 1999). The transition from a Pacific-driven to an Atlantic-driven regime is evident in reanalysis and Pacific pacemaker simulations. During 1985-2014, causal graphs reveal lagged negative TNA→PWC links, denoting intensifying easterly trade winds affecting ENSO. Proposed mechanisms involve Rossby wave energy generated by enhanced precipitation over anomalously warm TNA region, impacting subtropical Pacific and causing easterly wind anomalies and La Niña-like cooling (Park and Li 2019; Park et al. 2022; Wang et al. 2017b). Similar to reanalysis data, Pacific pacemaker simulations distinguish Pacific and Atlantic-driven regimes in SST responses (directly or via PWC). In the meantime, pacemaker-simulated SLP-based indices denote negative contemporaneous NAO-PNA relationship during 1950-1983 and 1985-2014. Notably, reanalysis identified positive 7-season lagged causal links during the first period, for which mechanisms are unclear.

The study involved separating external forcing from internal variability by subtracting CMIP6 MEM, yielding insights into external forcing's impact on Pacific-Atlantic interactions. Although MEM removal had modest effects on Pacific-driven regime causal graphs (panel c vs. a; Figure 5.4 and Figure 5.6), pronounced impacts emerged in the following period (panel b vs. d; Figure 5.4 and Figure 5.6), aligning with correlation and regression maps (Figure 5.3d vs. Figure 5.2d). During the Atlantic-driven era (1985-2014), reanalysis graphs highlighted TNA's strong contribution to same-season NAO changes (Figure 5.4b), reversed after MEM subtraction (Figure 5.4d). Additionally, a shift in the extra-tropical route linking the Pacific and Atlantic was observed during that period. Importantly, a negative TNA to ENSO response (via PWC) persisted despite MEM removal. In contrast, aggregated pacemaker graphs underscored external forcing's primary role in the Atlantic-driven regime, as evidenced by the vanishing TNA to PWC link and the emergence of Pacific-driven causal links after external forcing was removed. We note that the discrepancy between reanalysis and pacemaker aggre-

gated causal graphs regarding the effect of subtracting MEM during 1985-2014 lessened when conducting a sensitivity test. Initiating the Atlantic-driven regime a year later (1986 instead of 1985) in the reanalysis yielded no detected negative TNA→PWC$_u$ link after MEM removal (Supplementary Figure B.1), in line with correlation maps and aggregated pacemaker graphs for 1985-2014. A major role played by external forcing in the negative effect of TNA on ENSO falls in agreement with recent studies highlighting an increasing impact of external forcing on North Atlantic SSTAs and associated effects in recent decades (He et al. 2023; Klavans et al. 2022; Murphy et al. 2017). This brings additions to the debate over the attribution of the recently observed strengthening of the PWC, i.e. we suggest external forcing contributions modulated by the Atlantic might have amplified the recent PWC strengthening, in contrast with previous studies suggesting a dominant role of internal variability (Chung et al. 2019). Major disparities between observed and CESM2 pacemaker-simulated TNA indices (during the Atlantic-driven period) were discussed in Section 5.2.2 and attributed to the extensively investigated post-2000s warming overestimation in CMIP6 (Fyfe et al. 2021; Smith and Forster 2021; Smith et al. 2021; Tokarska et al. 2020a). The pacemaker-simulated TNA index ( Figure 5.5b) time series revealed a moderately strong coupling in the CESM2 model between Atlantic and Pacific SSTs, resulting in major differences in magnitude with the observed TNA following important El Niño events. This might explain the appearance of Niño3.4→TNA (and/or PWC$_u$→TNA) links in all aggregated causal networks in Figure 5.6 (a-d).

The analysis of the historical record (1950-2014) suggests external forcing's potential contributions, yet doesn't exclude the role of internal variability driven by the Pacific and Atlantic long-term states (PDV and AMV). To explore Atlantic-Pacific internal variability interactions in unforced conditions, we utilized 120 years from the CESM2 pre-industrial control run, divided into three 40-year periods. During two periods (P1 and P2), the causal graphs underscore the Pacific's impact on TNA variability through the tropical and extra-tropical pathways. Whereas for the third period (P3), characterized by a predominantly positive AMV and a significant PDV phase switch, a robust lagged negative TNA→PWC$_u$ link was evident, similar to Atlantic-driven regime causal graphs in reanalysis (Figure 5.4b and d) and pacemaker simulations with externally forced signal (Figure 5.6b). The lag for the TNA effect on PWC differs between the pre-industrial control run (four seasons in P3) and observations/pacemaker ensemble (one season). In short, our pre-industrial control analysis indicates that both contrasting response regimes arise naturally without anthropogenic external forcing, influenced by the long-term states of the Pacific and Atlantic basins.

Throughout this study, causal discovery revealed varying signs and lags for the links between PNA and NAO. Earlier research proposed a robust negative correlation between Aleutian and Icelandic lows only during specific historical sub-periods (e.g., mid-1970s to mid-1990s; Honda et al. 2001; Pinto et al. 2011). This might clarify the absence of contemporaneous negative PNA→NAO links during the causal analysis for the Pacific-driven 1950-1983 era in reanalysis (Figure 5.4a and c), where lagged positive connections were observed. However, prior studies haven't outlined mechanisms for such multi-season lagged positive associations. Conversely, the simultaneous negative PNA-NAO link was consistently identified across pace-

maker and pre-industrial control runs. This link could be the result of Rossby wave-breaking events connecting PNA to opposite NAO phases (Song et al. 2009) or simply because, particularly in certain seasons, the two modes are spatially overlapping projections of the same variability pattern, connecting the Aleutian and Icelandic lows (Soulard and Lin 2017).

In a concluding remark, the authors would like to highlight that causal discovery is a powerful tool to assess the physical mechanisms of Atlantic-Pacific interactions. However, a careful selection of the potential variables representing the analyzed mechanisms and the length of the time series are crucial for a robust application of causal analysis and reliable interpretation of detected connections. We experienced issues such that the algorithm rejected/added some connections when the analyzed period was prolonged or shortened and/or shifted by a few years. Therefore in order to make credible conclusions based on the application of causal discovery, it is important to accurately determine the causal assumptions, clarify the correct confounding variables, and analyze the interactions at their most relevant time scales to achieve robust results.

Finally, this study from **Karmouche** et al. 2023b, aims to enhance our understanding of the teleconnections between the Atlantic and Pacific oceans and their variability under different regimes. The findings emphasize the significance of external forcing, particularly in the most recent regime, and highlight the roles of ENSO, tropical and extra-tropical pathways, and internal variability in shaping SST variability over the Atlantic on seasonal to interannual timescales. Further research is warranted to refine our knowledge of these complex interactions and improve model simulations to capture the observed teleconnections more accurately. External forcing represented by the CMIP6 MEM has contributions from natural (e.g. solar radiation, volcanic eruptions) and anthropogenic sources (e.g. aerosols, GHGs) with time and space-varying effects, hence, we encourage further analysis using simulations with single external forcing sources (e.g. aerosol-only or GHG-only simulations) to increase the understanding and attribution of the observed changes in the climate system.

# 6. Conclusion

## 6.1. Main Summary

Various modes of natural climate variability that are driven by internal mechanisms within the Earth system exert significant influence on regional and global climate patterns over decadal to multidecadal timescales. Building upon the foundational scientific background, including ocean-atmosphere interactions and Earth system modeling (Chapter 2), and the robust methodologies and data sources outlined in Chapter 3, this thesis focused on the interplay between these modes and their effects over different timescales. In the study carried out in Chapter 4, a deep analysis was undertaken to assess the performance of various CMIP6 models in replicating observed spatial patterns of the major modes of Atlantic-Pacific climate variability and the underlying causal structures that connect them. The pattern correlation analysis revealed that models such as UKESM1-0-LL, MPI-ESM1-2-LR, MIROC6, CanESM5, and IPSL-CM6A-LR exhibited noteworthy fidelity in replicating the observed spatial patterns of various climate modes, notably performing well in reproducing the spatial patterns of PDV and PNA modes for the period 1900-2014, using ERSSTv5 as a reference.

The regime-oriented (depending on the phases of PDV and AMV) causal analysis of realizations from CESM2, CanESM5, and MIROC6 revealed their superior causal network similarity with reanalysis data. Furthermore, the analysis underscored the ability of climate models to score better F1-scores when AMV and PDV are out-of-phase. The evaluation highlighted that larger ensemble sizes, seen in models like CanESM5 (65) and MIROC6 (50), were beneficial in increasing the likelihood of simulating similar causal fingerprints (dependency structures) as the ones learned from observations and reanalysis; this feature is attributed to a better capture of internal variability by larger ensembles (Kay et al. 2015). It is noteworthy however that despite its smaller size, the CESM2 ensemble, counting only 11 members, demonstrated robust causal network agreement not only with respect to reanalysis but also between its own realizations. Transitioning to Chapter 5, the focus shifted to an analytical exploration of the changing effects of external forcing on Atlantic-Pacific interactions on shorter seasonal-to-interannual timescales, particularly focusing on two regimes between 1950 and 2014. The separation of internal variability from the forced component utilized three of the well-performing large ensembles learned from the pattern correlations and the causal model evaluation of the previous chapter. The analysis brought to light the existence of Pacific-driven (1950-1983) and Atlantic-driven (1985-2014) subperiods, as demonstrated by the causal networks from observational and reanalysis data sets, further supporting findings from recent studies utilizing different analytical approaches (Meehl et al. 2021a; Park et al. 2023). The causal analysis

offered a deeper understanding of the changing dependencies in the northern hemisphere Atlantic-Pacific sector during the two periods. In particular, the results spotlighted the critical role of tropical and extra-tropical routes in the same sign effect of ENSO on tropical north Atlantic SSTAs. While the effect of ENSO on the Atlantic was predominant during the first analyzed period (1950-1983), the most recent period 1985-2014 was marked by the emergence of an opposite sign response, this time by TNA on ENSO through modifications of the PWC. A critical analysis was undertaken to compare the results from observations/reanalysis with those from Pacific pacemaker simulations, revealing significant insights into the role of anthropogenic external forcing, especially in the most recent decades. The CESM2 pacemaker simulation results suggest that human-induced external forcing substantially contributed to the opposite sign effect of north Atlantic warming on tropical Pacific SST variability. A similar causal analysis utilizing 120 years from a pre-industrial control run, simulating the climate system before large-scale industrialization, highlights the importance of internal variability fluctuations on decadal timescales in modulating the interplay between interannual climate variability modes over the Atlantic and Pacific oceans, even in the absence of anthropogenic forcing. The study advocates for further research, focusing on individual external forcing sources to precisely attribute the observed changes in the climate system, aiming for a future enriched with informed and precise climate projections.

## 6.2. Outlook

As we face unprecedented climate changes, the need for a deeper understanding of the complex dynamics of the climate system, including both natural and human-induced external forcings, has never been more critical. The analysis of CMIP6 models carried out in the preceding chapters stands as testimony to this urgent requirement. Building on the insights gained from this dissertation, there is a significant opportunity to enhance the accuracy and sophistication of climate models. The use of large ensembles, as demonstrated in the research, can facilitate a more nuanced understanding of climate dynamics, including a detailed exploration of various climate components such as radiation-aerosol-cloud dynamics and the behavior of the cryosphere. Furthermore, the complex interactions between the ocean and the atmosphere, which play a crucial role in determining weather patterns and climate dynamics on different timescales, warrant closer scrutiny. Future research should aim to unravel the intricate feedback mechanisms that govern these interactions. A holistic approach, integrating research across different domains of climate science, is imperative for more accurate climate change projections. This entails a comprehensive study of external forcings and various long-term internal variability regimes. Moreover, a broader perspective is advocated, one that expands beyond Atlantic-Pacific interconnections to encapsulate global modes of variability. It is here that the utility of new causal discovery approaches comes to light, offering a pathway to combine spatial information with time series causal discovery, thereby enhancing our spatiotemporal understanding of global climate dynamics. In an era marked by a rapid

escalation in the frequency and intensity of extreme climate events, the predictability of the climate system has never been more critical. These climatic aberrations pose immense socio-economic challenges and disturb ecological systems globally, underscoring the urgency for refined scientific insights into the changing teleconnections that forge our climate system. Improved climate models have potential applications in various areas, including policy-making, disaster readiness, and the development of mitigation strategies, contributing to the foundation for building sustainable, climate-resilient societies. Integrating climate science with socio-economic models is also a key area, facilitating the creation of strategies to anticipate and navigate the challenges posed by changing climate conditions.

# Appendix

## A. Supplementary Materials for Chapter 4

As of Chapter 4, all figures and tables here in Appendix A are published in **Karmouche** et al. 2023a.

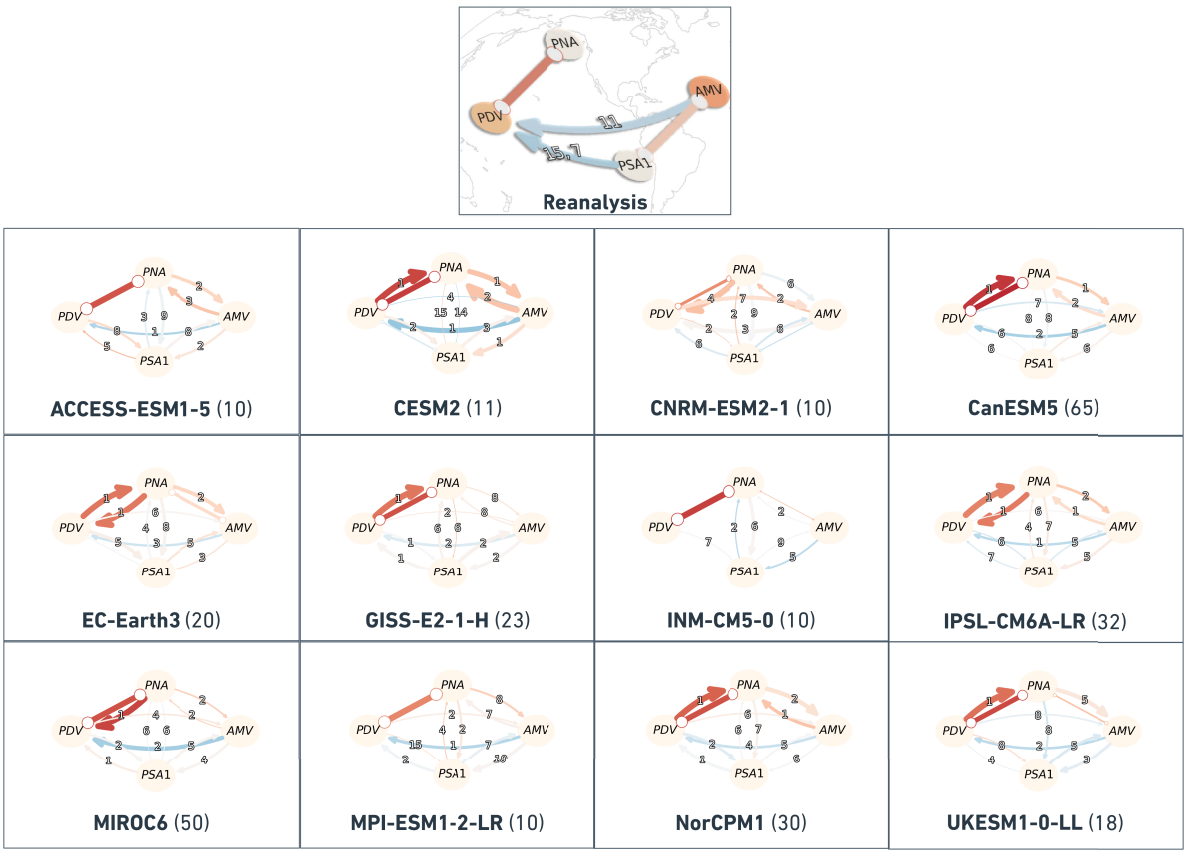


**Figure A.1.: Similar to Figure 4.5 but for the 12 CMIP6 models during the *complete 1900-2014 period*. Each panel has a label stating the model name and the number of ensemble members between parenthesis. The auto-MCI values were not taken into consideration.**

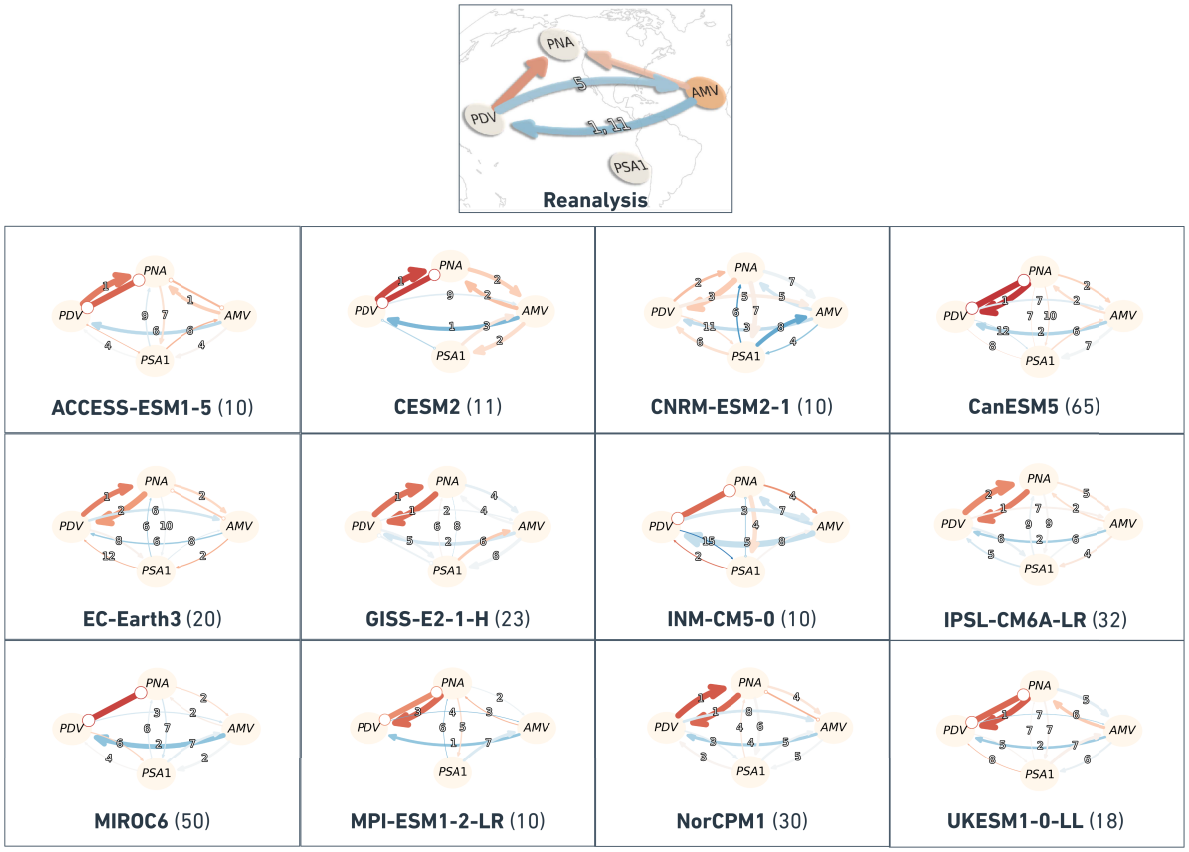


**Figure A.2.: Similar to Figure 4.5 but for the 12 CMIP6 models during the *Out-of-Phase regime*. Each panel has a label stating the model name and the number of ensemble members between parenthesis. The auto-MCI values were not taken into consideration.**

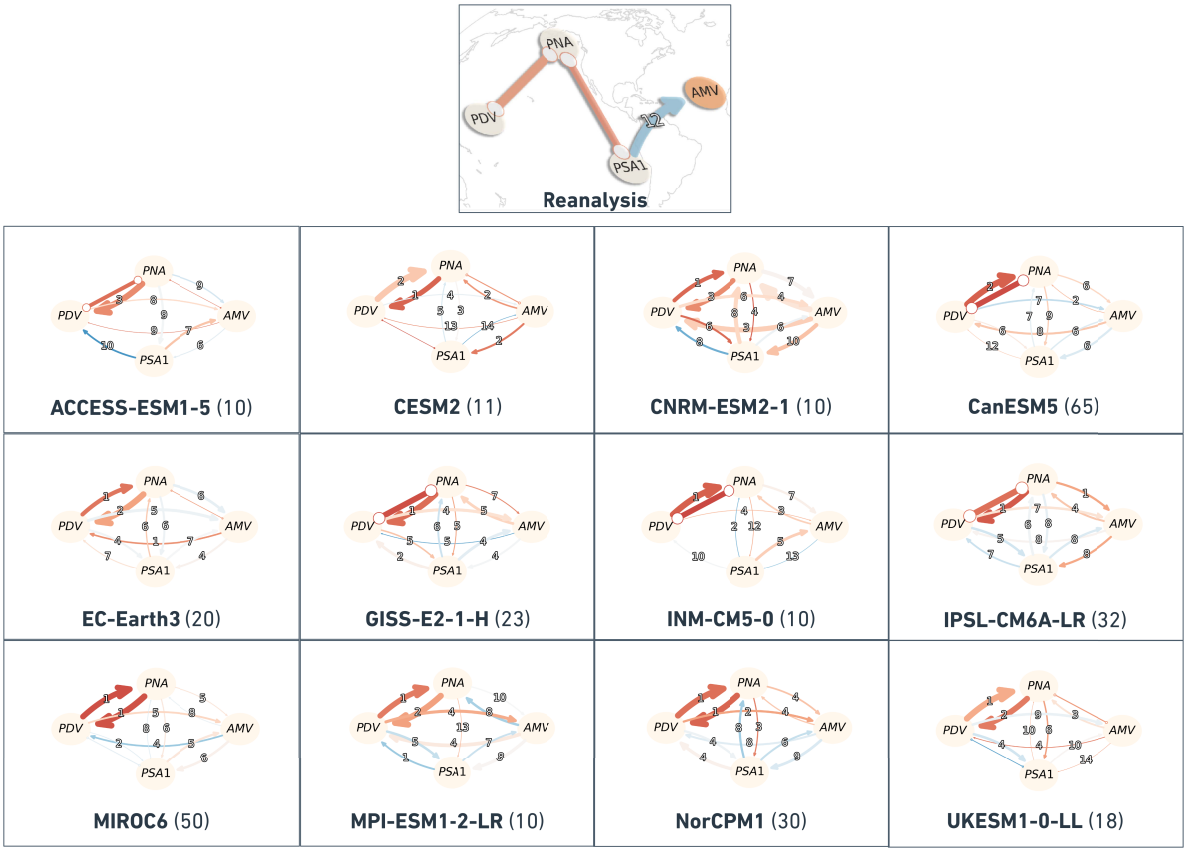


**Figure A.3.: Similar to Figure 4.5 but for the 12 CMIP6 models during the *In-Phase regime*. Each panel has a label stating the model name and the number of ensemble members between parenthesis. The auto-MCI values were not taken into consideration.**

**Table A.1.:** Distribution of Pearson *r* correlation values between the simulated (CMIP6 LE) and observed (ERA20C_ERA5, ERSSTv5) spatial patterns of PNA, PSA1, PDV, AMV and their Mean Score over the 1900-2014 period. Sorted by Alphabetical order.

| CMIP6 LE | Percentile | PNA (DJF) | PSA1 (ANN) | PDV (monthly) | AMV (monthly) | Mean Score |
|---|---|---|---|---|---|---|
| ACCESS-ESM1-5 | 10th | 0.80 | 0.57 | 0.68 | 0.67 | 0.67 |
| | 50th | 0.90 | 0.72 | 0.71 | 0.71 | 0.78 |
| | 90th | 0.93 | 0.79 | 0.77 | 0.75 | 0.80 |
| CESM2 | 10th | 0.84 | -0.64 | 0.82 | 0.68 | 0.61 |
| | 50th | 0.88 | 0.66 | 0.87 | 0.73 | 0.79 |
| | 90th | 0.91 | 0.77 | 0.88 | 0.77 | 0.82 |
| CNRM-ESM2-1 | 10th | 0.38 | 0.39 | -0.06 | 0.73 | 0.40 |
| | 50th | 0.59 | 0.53 | 0.68 | 0.74 | 0.64 |
| | 90th | 0.84 | 0.63 | 0.77 | 0.79 | 0.71 |
| CanESM5 | 10th | 0.76 | 0.56 | 0.75 | 0.68 | 0.73 |
| | 50th | 0.83 | 0.75 | 0.79 | 0.72 | 0.77 |
| | 90th | 0.88 | 0.81 | 0.82 | 0.76 | 0.80 |
| EC-Earth3 | 10th | 0.81 | -0.40 | 0.45 | 0.58 | 0.49 |
| | 50th | 0.85 | 0.69 | 0.71 | 0.63 | 0.73 |
| | 90th | 0.92 | 0.75 | 0.77 | 0.71 | 0.79 |
| GISS-E2-1-H | 10th | 0.73 | -0.70 | 0.73 | 0.62 | 0.46 |
| | 50th | 0.79 | -0.55 | 0.77 | 0.68 | 0.56 |
| | 90th | 0.86 | 0.73 | 0.81 | 0.72 | 0.76 |
| INM-CM5-0 | 10th | 0.53 | -0.08 | 0.47 | 0.62 | 0.48 |
| | 50th | 0.67 | 0.38 | 0.50 | 0.66 | 0.54 |
| | 90th | 0.73 | 0.57 | 0.56 | 0.71 | 0.60 |
| IPSL-CM6A-LR | 10th | 0.66 | 0.70 | 0.75 | 0.72 | 0.72 |
| | 50th | 0.73 | 0.80 | 0.79 | 0.76 | 0.77 |
| | 90th | 0.82 | 0.84 | 0.81 | 0.79 | 0.80 |
| MIROC6 | 10th | 0.81 | 0.68 | 0.83 | 0.67 | 0.77 |
| | 50th | 0.86 | 0.73 | 0.84 | 0.71 | 0.80 |
| | 90th | 0.91 | 0.78 | 0.85 | 0.74 | 0.82 |
| MPI-ESM1-2-LR | 10th | 0.76 | 0.70 | 0.75 | 0.64 | 0.74 |
| | 50th | 0.86 | 0.79 | 0.80 | 0.72 | 0.79 |
| | 90th | 0.93 | 0.82 | 0.83 | 0.77 | 0.82 |
| NorCPM1 | 10th | 0.38 | -0.58 | 0.72 | 0.64 | 0.41 |
| | 50th | 0.72 | -0.51 | 0.76 | 0.68 | 0.49 |
| | 90th | 0.82 | 0.58 | 0.79 | 0.72 | 0.70 |
| UKESM1-0-LL | 10th | 0.83 | 0.65 | 0.80 | 0.68 | 0.78 |
| | 50th | 0.88 | 0.75 | 0.82 | 0.74 | 0.80 |
| | 90th | 0.91 | 0.79 | 0.86 | 0.79 | 0.83 |

**Table A.2.:** Pearson correlation values obtained using 18 UKESM1-0-LL simulation, with respect to the observed (ERA20C_ERA5, ERSSTv5) spatial patterns of PNA, PSA1, PDV, AMV and their Mean Score over the 1900-2014 period. Sorted by mean score.

| UKESM1-0-LL Ensemble member | PNA (DJF) | PSA1 (ANN) | PDV (monthly) | AMV (monthly) | **Mean Score** |
|---|---|---|---|---|---|
| r19i1p1f2 | 0.91 | 0.84 | 0.86 | 0.80 | 0.86 |
| r6i1p1f3 | 0.89 | 0.75 | 0.86 | 0.78 | 0.83 |
| r3i1p1f2 | 0.90 | 0.76 | 0.85 | 0.76 | 0.83 |
| r14i1p1f2 | 0.94 | 0.75 | 0.82 | 0.68 | 0.82 |
| r2i1p1f2 | 0.88 | 0.78 | 0.84 | 0.75 | 0.82 |
| r1i1p1f2 | 0.87 | 0.81 | 0.82 | 0.78 | 0.82 |
| r11i1p1f2 | 0.91 | 0.68 | 0.81 | 0.76 | 0.81 |
| r8i1p1f2 | 0.90 | 0.78 | 0.79 | 0.70 | 0.80 |
| r17i1p1f2 | 0.80 | 0.76 | 0.84 | 0.81 | 0.80 |
| r7i1p1f3 | 0.86 | 0.78 | 0.82 | 0.72 | 0.80 |
| r4i1p1f2 | 0.90 | 0.67 | 0.82 | 0.73 | 0.80 |
| r16i1p1f2 | 0.86 | 0.75 | 0.81 | 0.72 | 0.79 |
| r10i1p1f2 | 0.88 | 0.74 | 0.83 | 0.66 | 0.79 |
| r9i1p1f2 | 0.89 | 0.56 | 0.82 | 0.77 | 0.79 |
| r18i1p1f2 | 0.88 | 0.60 | 0.82 | 0.76 | 0.78 |
| r5i1p1f3 | 0.85 | 0.75 | 0.81 | 0.68 | 0.78 |
| r13i1p1f2 | 0.84 | 0.71 | 0.80 | 0.74 | 0.78 |
| r12i1p1f2 | 0.79 | 0.67 | 0.80 | 0.68 | 0.74 |

**Table A.3.:** Cross-MCI and auto-MCI values calculated by PCMCI+ from reanalysis timeseries data for the complete 1900-2014 period. Values are relative to the complete period causal graph shown in Figure 3.1b (right panel) and Figure 4.4 (upper left panel). The table presents the cross-MCI (cross-correlation) values denoting the sign and strength of the causal link between node $i$ and node $j$ for lags between 0 and $\tau_{max}$. In bold are the highest absolute cross-MCI values for that specific link (detected within the statistical significance threshold, $\alpha_{pc} \leq 0.05$) and for which links are apparent on the causal graphs. The values are rounded to two decimal places.

| $i$ | time lag $\tau$ / $j$ | 0 | 1 | 2 | 3 | 4 | 5 | 6 | 7 | 8 | 9 | 10 | 11 | 12 | 13 | 14 | 15 |
|---|---|---|---|---|---|---|---|---|---|---|---|---|---|---|---|---|---|
| **AMV** | AMV | 0.00 | 0.45 | 0.22 | 0.14 | 0.17 | 0.21 | 0.18 | 0.18 | 0.09 | 0.11 | 0.05 | 0.05 | 0.18 | 0.09 | 0.03 | 0.05 |
| | PNA | 0.18 | -0.20 | -0.06 | 0.01 | -0.13 | -0.11 | -0.17 | -0.04 | 0.01 | -0.04 | -0.13 | -0.18 | -0.17 | -0.19 | -0.16 | -0.06 |
| | PDV | -0.04 | -0.18 | -0.16 | -0.07 | -0.12 | -0.15 | -0.16 | -0.18 | -0.06 | -0.13 | -0.21 | **-0.25** | 0.02 | -0.18 | -0.06 | -0.11 |
| | PSA1 | **0.25** | -0.05 | -0.01 | -0.06 | -0.10 | -0.11 | -0.12 | -0.05 | -0.06 | -0.00 | -0.02 | -0.07 | -0.04 | -0.08 | -0.00 | 0.08 |
| **PNA** | AMV | 0.18 | -0.05 | -0.02 | -0.03 | -0.09 | -0.12 | -0.07 | 0.03 | -0.05 | 0.01 | 0.01 | -0.04 | 0.05 | 0.07 | 0.03 | 0.03 |
| | PNA | 0.00 | 0.06 | 0.05 | 0.04 | -0.04 | 0.10 | 0.02 | 0.00 | -0.06 | -0.11 | 0.03 | -0.14 | -0.01 | -0.06 | -0.11 | 0.05 |
| | PDV | **0.53** | -0.07 | 0.10 | -0.05 | -0.04 | 0.14 | 0.16 | -0.02 | -0.18 | -0.10 | -0.02 | 0.01 | 0.00 | -0.07 | -0.17 | -0.02 |
| | PSA1 | 0.11 | -0.09 | 0.06 | -0.12 | -0.08 | -0.01 | -0.03 | -0.05 | -0.13 | 0.00 | -0.13 | -0.11 | 0.12 | -0.12 | -0.10 | 0.13 |
| **PDV** | AMV | -0.04 | -0.03 | -0.01 | -0.04 | -0.09 | -0.15 | -0.09 | -0.05 | 0.00 | -0.02 | 0.02 | 0.02 | 0.01 | 0.10 | 0.12 | 0.14 |
| | PNA | **0.53** | 0.17 | 0.09 | 0.04 | 0.21 | 0.21 | 0.05 | -0.02 | -0.08 | -0.08 | 0.06 | 0.00 | -0.01 | -0.02 | -0.10 | -0.07 |
| | PDV | 0.00 | 0.33 | 0.18 | 0.07 | 0.18 | 0.18 | 0.08 | 0.02 | -0.12 | -0.01 | 0.09 | 0.11 | 0.02 | -0.09 | -0.21 | -0.15 |
| | PSA1 | -0.07 | 0.11 | 0.14 | 0.02 | 0.03 | 0.07 | 0.00 | -0.17 | -0.13 | -0.06 | -0.12 | -0.09 | -0.07 | -0.03 | -0.09 | 0.03 |
| **PSA1** | AMV | **0.25** | -0.09 | 0.15 | -0.09 | -0.07 | -0.07 | -0.06 | -0.21 | -0.16 | -0.14 | -0.19 | -0.17 | -0.16 | -0.20 | -0.19 | -0.15 |
| | PNA | 0.11 | -0.10 | 0.18 | -0.10 | 0.04 | 0.06 | 0.04 | 0.21 | 0.01 | 0.07 | -0.10 | 0.11 | 0.11 | -0.01 | -0.17 | -0.09 |
| | PDV | -0.07 | 0.03 | 0.11 | -0.01 | 0.02 | 0.09 | 0.09 | **0.23** | 0.08 | -0.07 | -0.13 | -0.07 | -0.08 | -0.10 | -0.21 | **-0.31** |
| | PSA1 | 0.00 | 0.04 | 0.18 | 0.03 | 0.19 | 0.04 | 0.10 | -0.02 | -0.16 | 0.02 | -0.09 | 0.01 | -0.09 | -0.19 | -0.19 | 0.01 |

**Table A.4.:** Number of years for every regime for: Reanalysis and CMIP6 simulations 1-40.

| | Complete Period | AMV+ | AMV- | PDV+ | PDV- | In-Phase | Out-of-Phase | PDV+/AMV+ | PDV+/AMV- | PDV-/AMV+ | PDV-/AMV- |
|---|---|---|---|---|---|---|---|---|---|---|---|
| Reanalysis | 115 | 56 | 59 | 59 | 56 | 50 | 65 | 25 | 34 | 31 | 25 |
| ACCESS-ESM1-5_r5i1p1f1 | 115 | 51 | 64 | 60 | 55 | 82 | 33 | 39 | 21 | 12 | 43 |
| ACCESS-ESM1-5_r1i1p1f1 | 115 | 57 | 58 | 63 | 52 | 71 | 44 | 38 | 25 | 19 | 33 |
| ACCESS-ESM1-5_r9i1p1f1 | 115 | 57 | 58 | 66 | 49 | 44 | 71 | 26 | 40 | 31 | 18 |
| ACCESS-ESM1-5_r2i1p1f1 | 115 | 57 | 58 | 63 | 52 | 31 | 84 | 18 | 45 | 39 | 13 |
| ACCESS-ESM1-5_r8i1p1f1 | 115 | 53 | 62 | 65 | 50 | 59 | 56 | 31 | 34 | 22 | 28 |
| ACCESS-ESM1-5_r7i1p1f1 | 115 | 64 | 51 | 68 | 47 | 53 | 62 | 35 | 33 | 29 | 18 |
| ACCESS-ESM1-5_r10i1p1f1 | 115 | 69 | 46 | 58 | 57 | 36 | 79 | 24 | 34 | 45 | 12 |
| ACCESS-ESM1-5_r4i1p1f1 | 115 | 56 | 59 | 59 | 56 | 42 | 73 | 21 | 38 | 35 | 21 |
| ACCESS-ESM1-5_r3i1p1f1 | 115 | 68 | 47 | 54 | 61 | 35 | 80 | 21 | 33 | 47 | 14 |
| ACCESS-ESM1-5_r6i1p1f1 | 115 | 51 | 64 | 48 | 67 | 48 | 67 | 16 | 32 | 35 | 32 |
| CESM2_r1i1p1f1 | 115 | 74 | 41 | 61 | 54 | 44 | 71 | 32 | 29 | 42 | 12 |
| CESM2_r8i1p1f1 | 115 | 54 | 61 | 54 | 61 | 47 | 68 | 20 | 34 | 34 | 27 |
| CESM2_r2i1p1f1 | 115 | 62 | 53 | 42 | 73 | 29 | 86 | 9 | 33 | 53 | 20 |
| CESM2_r6i1p1f1 | 115 | 63 | 52 | 67 | 48 | 21 | 94 | 18 | 49 | 45 | 3 |
| CESM2_r10i1p1f1 | 115 | 66 | 49 | 50 | 65 | 41 | 74 | 21 | 29 | 45 | 20 |
| CESM2_r11i1p1f1 | 115 | 50 | 65 | 54 | 61 | 39 | 76 | 14 | 40 | 36 | 25 |
| CESM2_r7i1p1f1 | 115 | 65 | 50 | 51 | 64 | 27 | 88 | 14 | 37 | 51 | 13 |
| CESM2_r3i1p1f1 | 115 | 64 | 51 | 58 | 57 | 53 | 62 | 30 | 28 | 34 | 23 |
| CESM2_r5i1p1f1 | 115 | 58 | 57 | 56 | 59 | 37 | 78 | 18 | 38 | 40 | 19 |
| CESM2_r9i1p1f1 | 115 | 62 | 53 | 57 | 58 | 10 | 105 | 7 | 50 | 55 | 3 |
| CESM2_r4i1p1f1 | 115 | 55 | 60 | 65 | 50 | 35 | 80 | 20 | 45 | 35 | 15 |
| CNRM-ESM2-1_r11i1p1f2 | 115 | 44 | 71 | 61 | 54 | 74 | 41 | 32 | 29 | 12 | 42 |
| CNRM-ESM2-1_r4i1p1f2 | 115 | 53 | 62 | 56 | 59 | 28 | 87 | 11 | 45 | 42 | 17 |
| CNRM-ESM2-1_r1i1p1f2 | 115 | 70 | 45 | 59 | 56 | 32 | 83 | 23 | 36 | 47 | 9 |
| CNRM-ESM2-1_r5i1p1f2 | 115 | 54 | 61 | 56 | 59 | 99 | 16 | 47 | 9 | 7 | 52 |
| CNRM-ESM2-1_r7i1p1f2 | 115 | 63 | 52 | 54 | 61 | 70 | 45 | 36 | 18 | 27 | 34 |
| CNRM-ESM2-1_r9i1p1f2 | 115 | 51 | 64 | 65 | 50 | 43 | 72 | 22 | 43 | 29 | 21 |
| CNRM-ESM2-1_r10i1p1f2 | 115 | 54 | 61 | 54 | 61 | 59 | 56 | 26 | 28 | 28 | 33 |
| CNRM-ESM2-1_r3i1p1f2 | 115 | 56 | 59 | 53 | 62 | 82 | 33 | 38 | 15 | 18 | 44 |
| CNRM-ESM2-1_r8i1p1f2 | 115 | 65 | 50 | 76 | 39 | 50 | 65 | 38 | 38 | 27 | 12 |
| CNRM-ESM2-1_r2i1p1f2 | 115 | 54 | 61 | 64 | 51 | 59 | 56 | 31 | 33 | 23 | 28 |
| CanESM5_r15i1p1f1 | 115 | 59 | 56 | 61 | 54 | 45 | 70 | 25 | 36 | 34 | 20 |
| CanESM5_r11i1p1f1 | 115 | 49 | 66 | 66 | 49 | 28 | 87 | 14 | 52 | 35 | 14 |
| CanESM5_r1i1p2f1 | 115 | 60 | 55 | 64 | 51 | 37 | 78 | 23 | 41 | 37 | 14 |
| CanESM5_r19i1p2f1 | 115 | 56 | 59 | 46 | 69 | 39 | 76 | 13 | 33 | 43 | 26 |
| CanESM5_r26i1p2f1 | 115 | 51 | 64 | 63 | 52 | 49 | 66 | 24 | 39 | 27 | 25 |
| CanESM5_r33i1p2f1 | 115 | 62 | 53 | 56 | 59 | 65 | 50 | 34 | 22 | 28 | 31 |
| CanESM5_r31i1p2f1 | 115 | 65 | 50 | 61 | 54 | 61 | 54 | 36 | 25 | 29 | 25 |
| CanESM5_r13i1p2f1 | 115 | 61 | 54 | 55 | 60 | 39 | 76 | 20 | 35 | 41 | 19 |
| CanESM5_r29i1p2f1 | 115 | 55 | 60 | 56 | 59 | 28 | 87 | 12 | 44 | 43 | 16 |

**Table A.5.:** Number of years for every regime for: Reanalysis and CMIP6 simulations 41-80.

| | Complete Period | AMV+ | AMV- | PDV+ | PDV- | In-Phase | Out-of-Phase | PDV+/AMV+ | PDV+/AMV- | PDV-/AMV+ | PDV-/AMV- |
|---|---|---|---|---|---|---|---|---|---|---|---|
| Reanalysis | 115 | 56 | 59 | 59 | 56 | 50 | 65 | 25 | 34 | 31 | 25 |
| CanESM5_r22i1p2f1 | 115 | 58 | 57 | 55 | 60 | 40 | 75 | 19 | 36 | 39 | 21 |
| CanESM5_r23i1p1f1 | 115 | 47 | 68 | 51 | 64 | 71 | 44 | 27 | 24 | 20 | 44 |
| CanESM5_r6i1p1f1 | 115 | 70 | 45 | 60 | 55 | 33 | 82 | 24 | 36 | 46 | 9 |
| CanESM5_r2i1p2f1 | 115 | 48 | 67 | 48 | 67 | 25 | 90 | 3 | 45 | 45 | 22 |
| CanESM5_r38i1p2f1 | 115 | 65 | 50 | 68 | 47 | 50 | 65 | 34 | 34 | 31 | 16 |
| CanESM5_r19i1p1f1 | 115 | 63 | 52 | 65 | 50 | 37 | 78 | 25 | 40 | 38 | 12 |
| CanESM5_r37i1p2f1 | 115 | 45 | 70 | 63 | 52 | 41 | 74 | 17 | 46 | 28 | 24 |
| CanESM5_r24i1p1f1 | 115 | 59 | 56 | 56 | 59 | 44 | 71 | 22 | 34 | 37 | 22 |
| CanESM5_r4i1p1f1 | 115 | 65 | 50 | 62 | 53 | 40 | 75 | 26 | 36 | 39 | 14 |
| CanESM5_r25i1p1f1 | 115 | 55 | 60 | 57 | 58 | 65 | 50 | 31 | 26 | 24 | 34 |
| CanESM5_r22i1p1f1 | 115 | 61 | 54 | 55 | 60 | 57 | 58 | 29 | 26 | 32 | 28 |
| CanESM5_r12i1p1f1 | 115 | 60 | 55 | 56 | 59 | 63 | 52 | 32 | 24 | 28 | 31 |
| CanESM5_r23i1p2f1 | 115 | 49 | 66 | 64 | 51 | 48 | 67 | 23 | 41 | 26 | 25 |
| CanESM5_r13i1p1f1 | 115 | 53 | 62 | 66 | 49 | 44 | 71 | 24 | 42 | 29 | 20 |
| CanESM5_r4i1p2f1 | 115 | 54 | 61 | 63 | 52 | 50 | 65 | 26 | 37 | 28 | 24 |
| CanESM5_r27i1p2f1 | 115 | 54 | 61 | 55 | 60 | 32 | 83 | 13 | 42 | 41 | 19 |
| CanESM5_r10i1p2f1 | 115 | 61 | 54 | 65 | 50 | 63 | 52 | 37 | 28 | 24 | 26 |
| CanESM5_r16i1p2f1 | 115 | 59 | 56 | 59 | 56 | 47 | 68 | 25 | 34 | 34 | 22 |
| CanESM5_r18i1p2f1 | 115 | 47 | 68 | 49 | 66 | 45 | 70 | 13 | 36 | 34 | 32 |
| CanESM5_r32i1p2f1 | 115 | 59 | 56 | 61 | 54 | 17 | 98 | 11 | 50 | 48 | 6 |
| CanESM5_r17i1p1f1 | 115 | 49 | 66 | 62 | 53 | 28 | 87 | 12 | 50 | 37 | 16 |
| CanESM5_r14i1p2f1 | 115 | 56 | 59 | 52 | 63 | 41 | 74 | 17 | 35 | 39 | 24 |
| CanESM5_r5i1p1f1 | 115 | 51 | 64 | 68 | 47 | 34 | 81 | 19 | 49 | 32 | 15 |
| CanESM5_r24i1p2f1 | 115 | 56 | 59 | 49 | 66 | 50 | 65 | 20 | 29 | 36 | 30 |
| CanESM5_r30i1p2f1 | 115 | 49 | 66 | 58 | 57 | 38 | 77 | 15 | 43 | 34 | 23 |
| CanESM5_r14i1p1f1 | 115 | 54 | 61 | 55 | 60 | 54 | 61 | 24 | 31 | 30 | 30 |
| CanESM5_r21i1p1f1 | 115 | 53 | 62 | 63 | 52 | 27 | 88 | 14 | 49 | 39 | 13 |
| CanESM5_r16i1p1f1 | 115 | 70 | 45 | 56 | 59 | 27 | 88 | 19 | 37 | 51 | 8 |
| CanESM5_r36i1p2f1 | 115 | 51 | 64 | 59 | 56 | 33 | 82 | 14 | 45 | 37 | 19 |
| CanESM5_r3i1p1f1 | 115 | 51 | 64 | 65 | 50 | 49 | 66 | 25 | 40 | 26 | 24 |
| CanESM5_r8i1p1f1 | 115 | 65 | 50 | 51 | 64 | 27 | 88 | 14 | 37 | 51 | 13 |
| CanESM5_r7i1p2f1 | 115 | 43 | 72 | 50 | 65 | 58 | 57 | 18 | 32 | 25 | 40 |
| CanESM5_r6i1p2f1 | 115 | 50 | 65 | 64 | 51 | 67 | 48 | 33 | 31 | 17 | 34 |
| CanESM5_r25i1p2f1 | 115 | 60 | 55 | 43 | 72 | 62 | 53 | 25 | 18 | 35 | 37 |
| CanESM5_r20i1p1f1 | 115 | 54 | 61 | 61 | 54 | 42 | 73 | 21 | 40 | 33 | 21 |
| CanESM5_r5i1p2f1 | 115 | 61 | 54 | 61 | 54 | 35 | 80 | 21 | 40 | 40 | 14 |
| CanESM5_r39i1p2f1 | 115 | 61 | 54 | 51 | 64 | 33 | 82 | 15 | 36 | 46 | 18 |
| CanESM5_r11i1p2f1 | 115 | 52 | 63 | 57 | 58 | 48 | 67 | 21 | 36 | 31 | 27 |
| CanESM5_r2i1p1f1 | 115 | 60 | 55 | 58 | 57 | 25 | 90 | 14 | 44 | 46 | 11 |
| CanESM5_r15i1p2f1 | 115 | 59 | 56 | 62 | 53 | 72 | 43 | 39 | 23 | 20 | 33 |

**Table A.6.:** Number of years for every regime for: Reanalysis and CMIP6 simulations 81-120.

| | Complete Period | AMV+ | AMV- | PDV+ | PDV- | In-Phase | Out-of-Phase | PDV+/AMV+ | PDV+/AMV- | PDV-/AMV+ | PDV-/AMV- |
|---|---|---|---|---|---|---|---|---|---|---|---|
| Reanalysis | 115 | 56 | 59 | 59 | 56 | 50 | 65 | 25 | 34 | 31 | 25 |
| CanESM5_r9i1p2f1 | 115 | 53 | 62 | 55 | 60 | 49 | 66 | 21 | 34 | 32 | 28 |
| CanESM5_r1i1p1f1 | 115 | 58 | 57 | 60 | 55 | 39 | 76 | 21 | 39 | 37 | 18 |
| CanESM5_r12i1p2f1 | 115 | 59 | 56 | 61 | 54 | 59 | 56 | 32 | 29 | 27 | 27 |
| CanESM5_r18i1p1f1 | 115 | 56 | 59 | 52 | 63 | 57 | 58 | 25 | 27 | 31 | 32 |
| CanESM5_r28i1p2f1 | 115 | 45 | 70 | 51 | 64 | 47 | 68 | 14 | 37 | 31 | 33 |
| CanESM5_r20i1p2f1 | 115 | 55 | 60 | 60 | 55 | 34 | 81 | 17 | 43 | 38 | 17 |
| CanESM5_r10i1p1f1 | 115 | 49 | 66 | 55 | 60 | 59 | 56 | 24 | 31 | 25 | 35 |
| CanESM5_r17i1p2f1 | 115 | 50 | 65 | 56 | 59 | 45 | 70 | 18 | 38 | 32 | 27 |
| CanESM5_r35i1p2f1 | 115 | 57 | 58 | 54 | 61 | 68 | 47 | 32 | 22 | 25 | 36 |
| CanESM5_r3i1p2f1 | 115 | 46 | 69 | 63 | 52 | 62 | 53 | 28 | 35 | 18 | 34 |
| CanESM5_r21i1p2f1 | 115 | 54 | 61 | 56 | 59 | 41 | 74 | 18 | 38 | 36 | 23 |
| CanESM5_r7i1p1f1 | 115 | 58 | 57 | 53 | 62 | 18 | 97 | 7 | 46 | 51 | 11 |
| CanESM5_r8i1p2f1 | 115 | 64 | 51 | 67 | 48 | 36 | 79 | 26 | 41 | 38 | 10 |
| CanESM5_r40i1p2f1 | 115 | 56 | 59 | 63 | 52 | 26 | 89 | 15 | 48 | 41 | 11 |
| CanESM5_r9i1p1f1 | 115 | 42 | 73 | 63 | 52 | 46 | 69 | 18 | 45 | 24 | 28 |
| CanESM5_r34i1p2f1 | 115 | 51 | 64 | 58 | 57 | 20 | 95 | 7 | 51 | 44 | 13 |
| EC-Earth3_r22i1p1f1 | 115 | 42 | 73 | 60 | 55 | 45 | 70 | 16 | 44 | 26 | 29 |
| EC-Earth3_r6i1p1f1 | 115 | 61 | 54 | 48 | 67 | 28 | 87 | 11 | 37 | 50 | 17 |
| EC-Earth3_r23i1p1f1 | 115 | 62 | 53 | 55 | 60 | 30 | 85 | 16 | 39 | 46 | 14 |
| EC-Earth3_r3i1p1f1 | 115 | 44 | 71 | 58 | 57 | 33 | 82 | 10 | 48 | 34 | 23 |
| EC-Earth3_r17i1p1f1 | 115 | 50 | 65 | 57 | 58 | 46 | 69 | 19 | 38 | 31 | 27 |
| EC-Earth3_r19i1p1f1 | 115 | 54 | 61 | 55 | 60 | 56 | 59 | 25 | 30 | 29 | 31 |
| EC-Earth3_r12i1p1f1 | 115 | 43 | 72 | 59 | 56 | 47 | 68 | 17 | 42 | 26 | 30 |
| EC-Earth3_r20i1p1f1 | 115 | 54 | 61 | 59 | 56 | 46 | 69 | 22 | 37 | 32 | 24 |
| EC-Earth3_r10i1p1f1 | 115 | 62 | 53 | 53 | 62 | 20 | 95 | 10 | 43 | 52 | 10 |
| EC-Earth3_r18i1p1f1 | 115 | 45 | 70 | 61 | 54 | 21 | 94 | 6 | 55 | 39 | 15 |
| EC-Earth3_r24i1p1f1 | 115 | 56 | 59 | 72 | 43 | 43 | 72 | 28 | 44 | 28 | 15 |
| EC-Earth3_r9i1p1f1 | 115 | 58 | 57 | 57 | 58 | 46 | 69 | 23 | 34 | 35 | 23 |
| EC-Earth3_r1i1p1f1 | 115 | 61 | 54 | 59 | 56 | 47 | 68 | 26 | 33 | 35 | 21 |
| EC-Earth3_r14i1p1f1 | 115 | 59 | 56 | 69 | 46 | 103 | 12 | 58 | 11 | 1 | 45 |
| EC-Earth3_r16i1p1f1 | 115 | 61 | 54 | 37 | 78 | 27 | 88 | 5 | 32 | 56 | 22 |
| EC-Earth3_r7i1p1f1 | 115 | 55 | 60 | 50 | 65 | 30 | 85 | 10 | 40 | 45 | 20 |
| EC-Earth3_r4i1p1f1 | 115 | 54 | 61 | 54 | 61 | 37 | 78 | 15 | 39 | 39 | 22 |
| EC-Earth3_r21i1p1f1 | 115 | 59 | 56 | 68 | 47 | 64 | 51 | 38 | 30 | 21 | 26 |
| EC-Earth3_r2i1p1f1 | 115 | 64 | 51 | 56 | 59 | 51 | 64 | 28 | 28 | 36 | 23 |
| EC-Earth3_r25i1p1f1 | 115 | 59 | 56 | 66 | 49 | 82 | 33 | 46 | 20 | 13 | 36 |
| GISS-E2-1-H_r2i1p5f1 | 115 | 55 | 60 | 60 | 55 | 46 | 69 | 23 | 37 | 32 | 23 |
| GISS-E2-1-H_r1i1p5f1 | 115 | 63 | 52 | 68 | 47 | 42 | 73 | 29 | 39 | 34 | 13 |
| GISS-E2-1-H_r1i1p1f2 | 115 | 58 | 57 | 55 | 60 | 50 | 65 | 24 | 31 | 34 | 26 |
| GISS-E2-1-H_r8i1p1f1 | 115 | 62 | 53 | 70 | 45 | 73 | 42 | 45 | 25 | 17 | 28 |

**Table A.7.:** Number of years for every regime for: Reanalysis and CMIP6 simulations 121-160.

| | Complete Period | AMV+ | AMV- | PDV+ | PDV- | In-Phase | Out-of-Phase | PDV+/AMV+ | PDV+/AMV- | PDV-/AMV+ | PDV-/AMV- |
|---|---|---|---|---|---|---|---|---|---|---|---|
| Reanalysis | 115 | 56 | 59 | 59 | 56 | 50 | 65 | 25 | 34 | 31 | 25 |
| GISS-E2-1-H_r4i1p1f2 | 115 | 48 | 67 | 61 | 54 | 26 | 89 | 10 | 51 | 38 | 16 |
| GISS-E2-1-H_r7i1p1f1 | 115 | 49 | 66 | 53 | 62 | 77 | 38 | 32 | 21 | 17 | 45 |
| GISS-E2-1-H_r5i1p1f1 | 115 | 61 | 54 | 53 | 62 | 55 | 60 | 27 | 26 | 34 | 28 |
| GISS-E2-1-H_r9i1p1f1 | 115 | 56 | 59 | 67 | 48 | 50 | 65 | 29 | 38 | 27 | 21 |
| GISS-E2-1-H_r1i1p3f1 | 115 | 56 | 59 | 63 | 52 | 48 | 67 | 26 | 37 | 30 | 22 |
| GISS-E2-1-H_r4i1p3f1 | 115 | 59 | 56 | 66 | 49 | 48 | 67 | 29 | 37 | 30 | 19 |
| GISS-E2-1-H_r6i1p1f1 | 115 | 61 | 54 | 57 | 58 | 57 | 58 | 30 | 27 | 31 | 27 |
| GISS-E2-1-H_r3i1p1f1 | 115 | 62 | 53 | 56 | 59 | 65 | 50 | 34 | 22 | 28 | 31 |
| GISS-E2-1-H_r2i1p3f1 | 115 | 57 | 58 | 58 | 57 | 48 | 67 | 24 | 34 | 33 | 24 |
| GISS-E2-1-H_r10i1p1f1 | 115 | 58 | 57 | 51 | 64 | 52 | 63 | 23 | 28 | 35 | 29 |
| GISS-E2-1-H_r5i1p3f1 | 115 | 54 | 61 | 54 | 61 | 33 | 82 | 13 | 41 | 41 | 20 |
| GISS-E2-1-H_r2i1p1f2 | 115 | 50 | 65 | 53 | 62 | 72 | 43 | 30 | 23 | 20 | 42 |
| GISS-E2-1-H_r4i1p1f1 | 115 | 59 | 56 | 63 | 52 | 61 | 54 | 34 | 29 | 25 | 27 |
| GISS-E2-1-H_r2i1p1f1 | 115 | 48 | 67 | 64 | 51 | 53 | 62 | 25 | 39 | 23 | 28 |
| GISS-E2-1-H_r3i1p1f2 | 115 | 65 | 50 | 50 | 65 | 26 | 89 | 13 | 37 | 52 | 13 |
| GISS-E2-1-H_r3i1p5f1 | 115 | 47 | 68 | 55 | 60 | 69 | 46 | 28 | 27 | 19 | 41 |
| GISS-E2-1-H_r3i1p3f1 | 115 | 59 | 56 | 61 | 54 | 77 | 38 | 41 | 20 | 18 | 36 |
| GISS-E2-1-H_r1i1p1f1 | 115 | 62 | 53 | 51 | 64 | 62 | 53 | 30 | 21 | 32 | 32 |
| GISS-E2-1-H_r5i1p1f2 | 115 | 53 | 62 | 61 | 54 | 33 | 82 | 16 | 45 | 37 | 17 |
| INM-CM5-0_r2i1p1f1 | 115 | 60 | 55 | 55 | 60 | 72 | 43 | 36 | 19 | 24 | 36 |
| INM-CM5-0_r6i1p1f1 | 115 | 60 | 55 | 58 | 57 | 63 | 52 | 33 | 25 | 27 | 30 |
| INM-CM5-0_r9i1p1f1 | 115 | 54 | 61 | 57 | 58 | 46 | 69 | 21 | 36 | 33 | 25 |
| INM-CM5-0_r8i1p1f1 | 115 | 60 | 55 | 45 | 70 | 84 | 31 | 37 | 8 | 23 | 47 |
| INM-CM5-0_r4i1p1f1 | 115 | 60 | 55 | 56 | 59 | 53 | 62 | 27 | 29 | 33 | 26 |
| INM-CM5-0_r7i1p1f1 | 115 | 61 | 54 | 59 | 56 | 41 | 74 | 23 | 36 | 38 | 18 |
| INM-CM5-0_r5i1p1f1 | 115 | 60 | 55 | 49 | 66 | 24 | 91 | 9 | 40 | 51 | 15 |
| INM-CM5-0_r1i1p1f1 | 115 | 52 | 63 | 63 | 52 | 56 | 59 | 28 | 35 | 24 | 28 |
| INM-CM5-0_r10i1p1f1 | 115 | 55 | 60 | 55 | 60 | 79 | 36 | 37 | 18 | 18 | 42 |
| INM-CM5-0_r3i1p1f1 | 115 | 60 | 55 | 56 | 59 | 53 | 62 | 27 | 29 | 33 | 26 |
| IPSL-CM6A-LR_r9i1p1f1 | 115 | 55 | 60 | 54 | 61 | 44 | 71 | 19 | 35 | 36 | 25 |
| IPSL-CM6A-LR_r15i1p1f1 | 115 | 69 | 46 | 60 | 55 | 30 | 85 | 22 | 38 | 47 | 8 |
| IPSL-CM6A-LR_r6i1p1f1 | 115 | 71 | 44 | 61 | 54 | 29 | 86 | 23 | 38 | 48 | 6 |
| IPSL-CM6A-LR_r28i1p1f1 | 115 | 63 | 52 | 65 | 50 | 63 | 52 | 38 | 27 | 25 | 25 |
| IPSL-CM6A-LR_r31i1p1f1 | 115 | 65 | 50 | 55 | 60 | 45 | 70 | 25 | 30 | 40 | 20 |
| IPSL-CM6A-LR_r25i1p1f1 | 115 | 51 | 64 | 58 | 57 | 60 | 55 | 27 | 31 | 24 | 33 |
| IPSL-CM6A-LR_r27i1p1f1 | 115 | 64 | 51 | 58 | 57 | 49 | 66 | 28 | 30 | 36 | 21 |
| IPSL-CM6A-LR_r30i1p1f1 | 115 | 57 | 58 | 55 | 60 | 51 | 64 | 24 | 31 | 33 | 27 |
| IPSL-CM6A-LR_r24i1p1f1 | 115 | 59 | 56 | 55 | 60 | 59 | 56 | 29 | 26 | 30 | 30 |
| IPSL-CM6A-LR_r5i1p1f1 | 115 | 62 | 53 | 60 | 55 | 61 | 54 | 34 | 26 | 28 | 27 |
| IPSL-CM6A-LR_r22i1p1f1 | 115 | 58 | 57 | 52 | 63 | 79 | 36 | 37 | 15 | 21 | 42 |

**Table A.8.:** Number of years for every regime for: Reanalysis and CMIP6 simulations 161-200.

| | Complete Period | AMV+ | AMV- | PDV+ | PDV- | In-Phase | Out-of-Phase | PDV+/AMV+ | PDV+/AMV- | PDV-/AMV+ | PDV-/AMV- |
|---|---|---|---|---|---|---|---|---|---|---|---|
| Reanalysis | 115 | 56 | 59 | 59 | 56 | 50 | 65 | 25 | 34 | 31 | 25 |
| IPSL-CM6A-LR_r26i1p1f1 | 115 | 56 | 59 | 65 | 50 | 48 | 67 | 27 | 38 | 29 | 21 |
| IPSL-CM6A-LR_r8i1p1f1 | 115 | 57 | 58 | 59 | 56 | 37 | 78 | 19 | 40 | 38 | 18 |
| IPSL-CM6A-LR_r14i1p1f1 | 115 | 63 | 52 | 54 | 61 | 42 | 73 | 22 | 32 | 41 | 20 |
| IPSL-CM6A-LR_r10i1p1f1 | 115 | 60 | 55 | 52 | 63 | 45 | 70 | 21 | 31 | 39 | 24 |
| IPSL-CM6A-LR_r16i1p1f1 | 115 | 54 | 61 | 62 | 53 | 45 | 70 | 23 | 39 | 31 | 22 |
| IPSL-CM6A-LR_r4i1p1f1 | 115 | 64 | 51 | 56 | 59 | 53 | 62 | 29 | 27 | 35 | 24 |
| IPSL-CM6A-LR_r20i1p1f1 | 115 | 51 | 64 | 56 | 59 | 62 | 53 | 27 | 29 | 24 | 35 |
| IPSL-CM6A-LR_r1i1p1f1 | 115 | 56 | 59 | 57 | 58 | 54 | 61 | 26 | 31 | 30 | 28 |
| IPSL-CM6A-LR_r3i1p1f1 | 115 | 48 | 67 | 52 | 63 | 45 | 70 | 15 | 37 | 33 | 30 |
| IPSL-CM6A-LR_r7i1p1f1 | 115 | 51 | 64 | 48 | 67 | 44 | 71 | 14 | 34 | 37 | 30 |
| IPSL-CM6A-LR_r13i1p1f1 | 115 | 65 | 50 | 54 | 61 | 56 | 59 | 30 | 24 | 35 | 26 |
| IPSL-CM6A-LR_r19i1p1f1 | 115 | 52 | 63 | 56 | 59 | 85 | 30 | 39 | 17 | 13 | 46 |
| IPSL-CM6A-LR_r23i1p1f1 | 115 | 50 | 65 | 59 | 56 | 36 | 79 | 15 | 44 | 35 | 21 |
| IPSL-CM6A-LR_r18i1p1f1 | 115 | 53 | 62 | 52 | 63 | 34 | 81 | 12 | 40 | 41 | 22 |
| IPSL-CM6A-LR_r29i1p1f1 | 115 | 47 | 68 | 56 | 59 | 44 | 71 | 16 | 40 | 31 | 28 |
| IPSL-CM6A-LR_r2i1p1f1 | 115 | 54 | 61 | 48 | 67 | 35 | 80 | 11 | 37 | 43 | 24 |
| IPSL-CM6A-LR_r11i1p1f1 | 115 | 56 | 59 | 61 | 54 | 52 | 63 | 27 | 34 | 29 | 25 |
| IPSL-CM6A-LR_r32i1p1f1 | 115 | 53 | 62 | 62 | 53 | 54 | 61 | 27 | 35 | 26 | 27 |
| IPSL-CM6A-LR_r21i1p1f1 | 115 | 63 | 52 | 59 | 56 | 35 | 80 | 21 | 38 | 42 | 14 |
| IPSL-CM6A-LR_r17i1p1f1 | 115 | 50 | 65 | 60 | 55 | 39 | 76 | 17 | 43 | 33 | 22 |
| IPSL-CM6A-LR_r12i1p1f1 | 115 | 57 | 58 | 54 | 61 | 66 | 49 | 31 | 23 | 26 | 35 |
| MIROC6_r35i1p1f1 | 115 | 46 | 69 | 55 | 60 | 38 | 77 | 12 | 43 | 34 | 26 |
| MIROC6_r32i1p1f1 | 115 | 64 | 51 | 55 | 60 | 46 | 69 | 25 | 30 | 39 | 21 |
| MIROC6_r40i1p1f1 | 115 | 58 | 57 | 56 | 59 | 47 | 68 | 23 | 33 | 35 | 24 |
| MIROC6_r20i1p1f1 | 115 | 60 | 55 | 60 | 55 | 41 | 74 | 23 | 37 | 37 | 18 |
| MIROC6_r11i1p1f1 | 115 | 58 | 57 | 58 | 57 | 33 | 82 | 17 | 41 | 41 | 16 |
| MIROC6_r44i1p1f1 | 115 | 66 | 49 | 59 | 56 | 54 | 61 | 32 | 27 | 34 | 22 |
| MIROC6_r4i1p1f1 | 115 | 46 | 69 | 57 | 58 | 42 | 73 | 15 | 42 | 31 | 27 |
| MIROC6_r13i1p1f1 | 115 | 59 | 56 | 67 | 48 | 39 | 76 | 25 | 42 | 34 | 14 |
| MIROC6_r3i1p1f1 | 115 | 51 | 64 | 62 | 53 | 56 | 59 | 27 | 35 | 24 | 29 |
| MIROC6_r46i1p1f1 | 115 | 63 | 52 | 49 | 66 | 47 | 68 | 22 | 27 | 41 | 25 |
| MIROC6_r9i1p1f1 | 115 | 60 | 55 | 57 | 58 | 42 | 73 | 22 | 35 | 38 | 20 |
| MIROC6_r14i1p1f1 | 115 | 58 | 57 | 61 | 54 | 58 | 57 | 31 | 30 | 27 | 27 |
| MIROC6_r15i1p1f1 | 115 | 42 | 73 | 60 | 55 | 41 | 74 | 14 | 46 | 28 | 27 |
| MIROC6_r21i1p1f1 | 115 | 59 | 56 | 63 | 52 | 49 | 66 | 28 | 35 | 31 | 21 |
| MIROC6_r38i1p1f1 | 115 | 59 | 56 | 57 | 58 | 25 | 90 | 13 | 44 | 46 | 12 |
| MIROC6_r31i1p1f1 | 115 | 57 | 58 | 58 | 57 | 62 | 53 | 31 | 27 | 26 | 31 |
| MIROC6_r16i1p1f1 | 115 | 64 | 51 | 73 | 42 | 50 | 65 | 36 | 37 | 28 | 14 |
| MIROC6_r29i1p1f1 | 115 | 63 | 52 | 65 | 50 | 55 | 60 | 34 | 31 | 29 | 21 |
| MIROC6_r2i1p1f1 | 115 | 44 | 71 | 48 | 67 | 51 | 64 | 14 | 34 | 30 | 37 |

**Table A.9.:** Number of years for every regime for: Reanalysis and CMIP6 simulations 201-240.

| | Complete Period | AMV+ | AMV- | PDV+ | PDV- | In-Phase | Out-of-Phase | PDV+/AMV+ | PDV+/AMV- | PDV-/AMV+ | PDV-/AMV- |
|---|---|---|---|---|---|---|---|---|---|---|---|
| Reanalysis | 115 | 56 | 59 | 59 | 56 | 50 | 65 | 25 | 34 | 31 | 25 |
| MIROC6_r34i1p1f1 | 115 | 61 | 54 | 47 | 68 | 69 | 46 | 31 | 16 | 30 | 38 |
| MIROC6_r1i1p1f1 | 115 | 70 | 45 | 53 | 62 | 52 | 63 | 30 | 23 | 40 | 22 |
| MIROC6_r39i1p1f1 | 115 | 64 | 51 | 54 | 61 | 57 | 58 | 30 | 24 | 34 | 27 |
| MIROC6_r8i1p1f1 | 115 | 52 | 63 | 61 | 54 | 68 | 47 | 33 | 28 | 19 | 35 |
| MIROC6_r42i1p1f1 | 115 | 57 | 58 | 57 | 58 | 59 | 56 | 29 | 28 | 28 | 30 |
| MIROC6_r27i1p1f1 | 115 | 74 | 41 | 60 | 55 | 73 | 42 | 46 | 14 | 28 | 27 |
| MIROC6_r26i1p1f1 | 115 | 66 | 49 | 55 | 60 | 42 | 73 | 24 | 31 | 42 | 18 |
| MIROC6_r17i1p1f1 | 115 | 55 | 60 | 59 | 56 | 49 | 66 | 24 | 35 | 31 | 25 |
| MIROC6_r48i1p1f1 | 115 | 56 | 59 | 66 | 49 | 69 | 46 | 38 | 28 | 18 | 31 |
| MIROC6_r6i1p1f1 | 115 | 53 | 62 | 57 | 58 | 45 | 70 | 20 | 37 | 33 | 25 |
| MIROC6_r30i1p1f1 | 115 | 57 | 58 | 53 | 62 | 53 | 62 | 24 | 29 | 33 | 29 |
| MIROC6_r49i1p1f1 | 115 | 54 | 61 | 63 | 52 | 52 | 63 | 27 | 36 | 27 | 25 |
| MIROC6_r5i1p1f1 | 115 | 58 | 57 | 68 | 47 | 57 | 58 | 34 | 34 | 24 | 23 |
| MIROC6_r41i1p1f1 | 115 | 64 | 51 | 57 | 58 | 46 | 69 | 26 | 31 | 38 | 20 |
| MIROC6_r23i1p1f1 | 115 | 56 | 59 | 55 | 60 | 46 | 69 | 21 | 34 | 35 | 25 |
| MIROC6_r12i1p1f1 | 115 | 54 | 61 | 55 | 60 | 42 | 73 | 18 | 37 | 36 | 24 |
| MIROC6_r10i1p1f1 | 115 | 57 | 58 | 67 | 48 | 37 | 78 | 23 | 44 | 34 | 14 |
| MIROC6_r24i1p1f1 | 115 | 62 | 53 | 56 | 59 | 51 | 64 | 27 | 29 | 35 | 24 |
| MIROC6_r33i1p1f1 | 115 | 55 | 60 | 66 | 49 | 38 | 77 | 22 | 44 | 33 | 16 |
| MIROC6_r7i1p1f1 | 115 | 57 | 58 | 58 | 57 | 26 | 89 | 13 | 45 | 44 | 13 |
| MIROC6_r36i1p1f1 | 115 | 74 | 41 | 59 | 56 | 42 | 73 | 30 | 29 | 44 | 12 |
| MIROC6_r28i1p1f1 | 115 | 57 | 58 | 56 | 59 | 46 | 69 | 22 | 34 | 35 | 24 |
| MIROC6_r37i1p1f1 | 115 | 62 | 53 | 62 | 53 | 63 | 52 | 36 | 26 | 26 | 27 |
| MIROC6_r47i1p1f1 | 115 | 61 | 54 | 48 | 67 | 44 | 71 | 19 | 29 | 42 | 25 |
| MIROC6_r19i1p1f1 | 115 | 50 | 65 | 59 | 56 | 62 | 53 | 28 | 31 | 22 | 34 |
| MIROC6_r18i1p1f1 | 115 | 56 | 59 | 55 | 60 | 48 | 67 | 22 | 33 | 34 | 26 |
| MIROC6_r22i1p1f1 | 115 | 65 | 50 | 49 | 66 | 35 | 80 | 17 | 32 | 48 | 18 |
| MIROC6_r43i1p1f1 | 115 | 67 | 48 | 57 | 58 | 31 | 84 | 20 | 37 | 47 | 11 |
| MIROC6_r50i1p1f1 | 115 | 58 | 57 | 47 | 68 | 26 | 89 | 8 | 39 | 50 | 18 |
| MIROC6_r25i1p1f1 | 115 | 57 | 58 | 55 | 60 | 49 | 66 | 23 | 32 | 34 | 26 |
| MIROC6_r45i1p1f1 | 115 | 70 | 45 | 59 | 56 | 32 | 83 | 23 | 36 | 47 | 9 |
| MPI-ESM1-2-LR_r2i1p1f1 | 115 | 62 | 53 | 55 | 60 | 66 | 49 | 34 | 21 | 28 | 32 |
| MPI-ESM1-2-LR_r10i1p1f1 | 115 | 54 | 61 | 50 | 65 | 51 | 64 | 20 | 30 | 34 | 31 |
| MPI-ESM1-2-LR_r3i1p1f1 | 115 | 59 | 56 | 64 | 51 | 58 | 57 | 33 | 31 | 26 | 25 |
| MPI-ESM1-2-LR_r5i1p1f1 | 115 | 64 | 51 | 61 | 54 | 42 | 73 | 26 | 35 | 38 | 16 |
| MPI-ESM1-2-LR_r8i1p1f1 | 115 | 59 | 56 | 51 | 64 | 57 | 58 | 26 | 25 | 33 | 31 |
| MPI-ESM1-2-LR_r7i1p1f1 | 115 | 50 | 65 | 68 | 47 | 23 | 92 | 13 | 55 | 37 | 10 |
| MPI-ESM1-2-LR_r9i1p1f1 | 115 | 60 | 55 | 58 | 57 | 65 | 50 | 34 | 24 | 26 | 31 |
| MPI-ESM1-2-LR_r4i1p1f1 | 115 | 64 | 51 | 55 | 60 | 48 | 67 | 26 | 29 | 38 | 22 |
| MPI-ESM1-2-LR_r6i1p1f1 | 115 | 52 | 63 | 61 | 54 | 58 | 57 | 28 | 33 | 24 | 30 |

**Table A.10.:** Number of years for every regime for: Reanalysis and CMIP6 simulations 241-289.

| | Complete Period | AMV+ | AMV- | PDV+ | PDV- | In-Phase | Out-of-Phase | PDV+/AMV+ | PDV+/AMV- | PDV-/AMV+ | PDV-/AMV- |
|---|---|---|---|---|---|---|---|---|---|---|---|
| Reanalysis | 115 | 56 | 59 | 59 | 56 | 50 | 65 | 25 | 34 | 31 | 25 |
| MPI-ESM1-2-LR_r1i1p1f1 | 115 | 64 | 51 | 66 | 49 | 57 | 58 | 36 | 30 | 28 | 21 |
| NorCPM1_r20i1p1f1 | 115 | 58 | 57 | 49 | 66 | 48 | 67 | 20 | 29 | 38 | 28 |
| NorCPM1_r19i1p1f1 | 115 | 54 | 61 | 58 | 57 | 27 | 88 | 12 | 46 | 42 | 15 |
| NorCPM1_r13i1p1f1 | 115 | 53 | 62 | 51 | 64 | 31 | 84 | 10 | 41 | 43 | 21 |
| NorCPM1_r29i1p1f1 | 115 | 56 | 59 | 53 | 62 | 52 | 63 | 23 | 30 | 33 | 29 |
| NorCPM1_r4i1p1f1 | 115 | 53 | 62 | 44 | 71 | 48 | 67 | 15 | 29 | 38 | 33 |
| NorCPM1_r18i1p1f1 | 115 | 59 | 56 | 58 | 57 | 40 | 75 | 21 | 37 | 38 | 19 |
| NorCPM1_r30i1p1f1 | 115 | 63 | 52 | 52 | 63 | 62 | 53 | 31 | 21 | 32 | 31 |
| NorCPM1_r27i1p1f1 | 115 | 52 | 63 | 65 | 50 | 44 | 71 | 23 | 42 | 29 | 21 |
| NorCPM1_r2i1p1f1 | 115 | 56 | 59 | 61 | 54 | 34 | 81 | 18 | 43 | 38 | 16 |
| NorCPM1_r5i1p1f1 | 115 | 57 | 58 | 47 | 68 | 55 | 60 | 22 | 25 | 35 | 33 |
| NorCPM1_r22i1p1f1 | 115 | 59 | 56 | 47 | 68 | 37 | 78 | 14 | 33 | 45 | 23 |
| NorCPM1_r3i1p1f1 | 115 | 56 | 59 | 65 | 50 | 48 | 67 | 27 | 38 | 29 | 21 |
| NorCPM1_r16i1p1f1 | 115 | 44 | 71 | 59 | 56 | 26 | 89 | 7 | 52 | 37 | 19 |
| NorCPM1_r17i1p1f1 | 115 | 66 | 49 | 48 | 67 | 35 | 80 | 17 | 31 | 49 | 18 |
| NorCPM1_r9i1p1f1 | 115 | 60 | 55 | 56 | 59 | 33 | 82 | 17 | 39 | 43 | 16 |
| NorCPM1_r8i1p1f1 | 115 | 46 | 69 | 52 | 63 | 55 | 60 | 19 | 33 | 27 | 36 |
| NorCPM1_r11i1p1f1 | 115 | 50 | 65 | 43 | 72 | 54 | 61 | 16 | 27 | 34 | 38 |
| NorCPM1_r6i1p1f1 | 115 | 65 | 50 | 64 | 51 | 54 | 61 | 34 | 30 | 31 | 20 |
| NorCPM1_r23i1p1f1 | 115 | 55 | 60 | 65 | 50 | 29 | 86 | 17 | 48 | 38 | 12 |
| NorCPM1_r1i1p1f1 | 115 | 57 | 58 | 70 | 45 | 44 | 71 | 28 | 42 | 29 | 16 |
| NorCPM1_r14i1p1f1 | 115 | 61 | 54 | 55 | 60 | 63 | 52 | 32 | 23 | 29 | 31 |
| NorCPM1_r21i1p1f1 | 115 | 54 | 61 | 50 | 65 | 33 | 82 | 11 | 39 | 43 | 22 |
| NorCPM1_r7i1p1f1 | 115 | 59 | 56 | 57 | 58 | 55 | 60 | 28 | 29 | 31 | 27 |
| NorCPM1_r10i1p1f1 | 115 | 64 | 51 | 56 | 59 | 87 | 28 | 46 | 10 | 18 | 41 |
| NorCPM1_r26i1p1f1 | 115 | 54 | 61 | 47 | 68 | 40 | 75 | 13 | 34 | 41 | 27 |
| NorCPM1_r25i1p1f1 | 115 | 65 | 50 | 63 | 52 | 67 | 48 | 40 | 23 | 25 | 27 |
| NorCPM1_r12i1p1f1 | 115 | 60 | 55 | 53 | 62 | 54 | 61 | 26 | 27 | 34 | 28 |
| NorCPM1_r24i1p1f1 | 115 | 58 | 57 | 56 | 59 | 43 | 72 | 21 | 35 | 37 | 22 |
| NorCPM1_r28i1p1f1 | 115 | 66 | 49 | 50 | 65 | 31 | 84 | 16 | 34 | 50 | 15 |
| NorCPM1_r15i1p1f1 | 115 | 67 | 48 | 45 | 70 | 65 | 50 | 31 | 14 | 36 | 34 |
| UKESM1-0-LL_r16i1p1f2 | 115 | 62 | 53 | 67 | 48 | 70 | 45 | 42 | 25 | 20 | 28 |
| UKESM1-0-LL_r3i1p1f2 | 115 | 63 | 52 | 58 | 57 | 54 | 61 | 30 | 28 | 33 | 24 |
| UKESM1-0-LL_r8i1p1f2 | 115 | 46 | 69 | 59 | 56 | 44 | 71 | 17 | 42 | 29 | 27 |
| UKESM1-0-LL_r14i1p1f2 | 115 | 57 | 58 | 59 | 56 | 73 | 42 | 37 | 22 | 20 | 36 |
| UKESM1-0-LL_r13i1p1f2 | 115 | 49 | 66 | 52 | 63 | 80 | 35 | 33 | 19 | 16 | 47 |
| UKESM1-0-LL_r11i1p1f2 | 115 | 71 | 44 | 56 | 59 | 12 | 103 | 12 | 44 | 59 | 0 |
| UKESM1-0-LL_r12i1p1f2 | 115 | 68 | 47 | 69 | 46 | 26 | 89 | 24 | 45 | 44 | 2 |
| UKESM1-0-LL_r9i1p1f2 | 115 | 59 | 56 | 54 | 61 | 46 | 69 | 22 | 32 | 37 | 24 |
| UKESM1-0-LL_r7i1p1f3 | 115 | 60 | 55 | 74 | 41 | 37 | 78 | 28 | 46 | 32 | 9 |
| UKESM1-0-LL_r17i1p1f2 | 115 | 50 | 65 | 68 | 47 | 35 | 80 | 19 | 49 | 31 | 16 |
| UKESM1-0-LL_r1i1p1f2 | 115 | 62 | 53 | 51 | 64 | 44 | 71 | 21 | 30 | 41 | 23 |
| UKESM1-0-LL_r5i1p1f3 | 115 | 65 | 50 | 50 | 65 | 72 | 43 | 36 | 14 | 29 | 36 |
| UKESM1-0-LL_r2i1p1f2 | 115 | 45 | 70 | 49 | 66 | 47 | 68 | 13 | 36 | 32 | 34 |
| UKESM1-0-LL_r10i1p1f2 | 115 | 47 | 68 | 51 | 64 | 47 | 68 | 15 | 36 | 32 | 32 |
| UKESM1-0-LL_r19i1p1f2 | 115 | 73 | 42 | 57 | 58 | 39 | 76 | 27 | 30 | 46 | 12 |
| UKESM1-0-LL_r18i1p1f2 | 115 | 48 | 67 | 66 | 49 | 41 | 74 | 20 | 46 | 28 | 21 |
| UKESM1-0-LL_r6i1p1f3 | 115 | 70 | 45 | 60 | 55 | 47 | 68 | 31 | 29 | 39 | 16 |
| UKESM1-0-LL_r4i1p1f2 | 115 | 56 | 59 | 63 | 52 | 52 | 63 | 28 | 35 | 28 | 24 |

# B. Supplementary Materials for Chapter 5

As of Chapter 5, all material herein (Appendix B) has been recently submitted to *Earth System Dynamics* (**Karmouche** et al. 2023b).

**Table B.1.:** Directing unoriented contemporaneous links based on most detected direction within a specific run among the 10 simulations of the CESM2 pacemaker ensemble (Figure 5.6).

| Unoriented Links | Instances | Direction | Ruling |
|---|---|---|---|
| PNA—NAO | Figure 5.4d | **NAO→PNA** | Most detected direction for "1985-2014 minus MEM" regime |
| Niño3.4—PNA | Figure 5.4d | **Niño3.4→PNA** | Based on the 1-season lagged instances in all regimes |
| Niño3.4—PWC$_u$ | P1 and P2 in Figure 5.7b | **PWC$_u$→Niño3.4** | Most detected direction in all regimes |

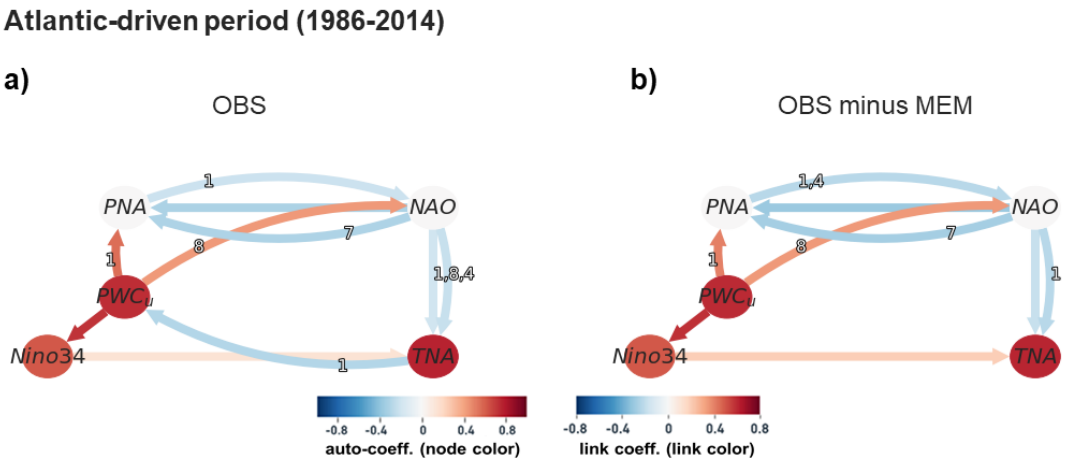


**Figure B.1.: Atlantic-driven regime starting in 1986 (instead of 1985) shows vanishing TNA→PWC$_u$ link when MEM is subtracted. a) Similar to Figure 5.4b but for 1986-2014. b) Similar to Figure 5.4d but for 1986-2014 period**

# List of Abbreviations

**CMIP** Coupled Model Intercomparison Project . . . 1

**$CO_2$** carbon dioxide . . . 6

**$CH_4$** methane . . . 31

**$N_2O$** nitrous oxide . . . 31

**$SO_2$** sulfur dioxide . . . 30

**ERSSTv5** Extended Reconstructed Sea Surface Temperature version 5 . . . 23

**HadISST** Hadley Centre Sea Ice and Sea Surface Temperature . . . 46

**NCEP-NCAR-R1** National Center for Environmental Prediction-National Center for Atmospheric Research reanalysis 1 . . . 46

**ESM** Earth system model . . . 12

**MEM** multi-ensemble mean . . . 89

**CVCWG** Climate Variability and Change Working Group . . . 76

**CESM** Community Earth System Model . . . 58

**ECMWF** European Centre for Medium-Range Weather Forecasts . . . 19

**ORAS5** Ocean Reanalysis System 5 . . . 46

**ESM** Earth system model . . . 12

**ITCZ** Intertropical Convergence Zone . . . 7

**GCM** general circulation model . . . 10

**GHG** greenhouse gas . . . 1

**IPCC** Intergovernmental Panel on Climate Change . . . 6

**NCAR** National Center for Atmospheric Research . . . 52

**PNA** Pacific-North American . . . 21

**PSA** Pacific-South American . . . 21

**NAO** North Atlantic Oscillation . . . 20

**EOF** empirical orthogonal function . . . 19

**NOAA** National Oceanic and Atmospheric Administration . . . 17

**AMOC** Atlantic Meridional Overturning Circulation . . . 26

| | | |
|---|---|---|
| **AZM** | Atlantic Zonal Mode | 27 |
| **AMM** | Atlantic Meridional Mode | 27 |
| **PCMCI** | Peter Clark Momentary Conditional Independence | 42 |
| **ERA20C-ERA5** | 20th Century Atmospheric Reanalysis extended with ERA5 | 19 |
| **IOD** | Indian Ocean Dipole | 29 |
| **PCA** | principal component analysis | 40 |
| **MJO** | Madden–Julian Oscillation | 29 |
| **SOI** | Southern Oscillation Index | 24 |
| **SST** | sea surface temperature | 14 |
| **SSTA** | SST anomaly | 24 |
| **SLP** | sea level pressure | 7 |
| **TNA** | Tropical North Atlantic | 76 |
| **AMV** | Atlantic Multidecadal Variability | 1 |
| **PDV** | Pacific Decadal Variability | 1 |
| **ENSO** | El Niño-Southern Oscillation | 1 |
| **CVDP-LE** | Climate Variability Diagnostic Package for Large Ensembles | 19 |
| **PWC** | Pacific Walker circulation | 17 |

# List of Figures

# List of Tables

# References


Allen, R. J., Norris, J. R., & Kovilakam, M. (2014). Influence of anthropogenic aerosols and the Pacific Decadal Oscillation on tropical belt width. *Nature Geoscience*, *7*(4), 270–274. https://doi.org/10.1038/ngeo2091

Arblaster, J., Meehl, G., & Moore, A. (2002). Interdecadal modulation of Australian rainfall. *Climate Dynamics*, *18*(6), 519–531.

Baker, H. S., Woollings, T., Forest, C. E., & Allen, M. R. (2019). The Linear Sensitivity of the North Atlantic Oscillation and Eddy-Driven Jet to SSTs. *Journal of Climate*, *32*(19), 6491–6511. https://doi.org/https://doi.org/10.1175/JCLI-D-19-0038.1

Bathiany, S., Dakos, V., Scheffer, M., & Lenton, T. M. (2018). Climate models predict increasing temperature variability in poor countries. *Science advances*, *4*(5), eaar5809.

Bayr, T., Dommenget, D., Martin, T., & Power, S. B. (2014). The eastward shift of the Walker circulation in response to global warming and its relationship to ENSO variability. *Clim. Dynam.*, *43*(9-10), 2747–2763. https://doi.org/10.1007/s00382-014-2091-y

Bellucci, A., Mariotti, A., & Gualdi, S. (2017). The role of forcings in the twentieth-century North Atlantic multidecadal variability: The 1940–75 North Atlantic cooling case study. *Journal of Climate*, *30*(18), 7317–7337. https://doi.org/10.1175/jcli-d-16-0301.1

Bethke, I., Wang, Y., Counillon, F., Kimmritz, M., Fransner, F., Samuelsen, A., Langehaug, H. R., Chiu, P.-G., Bentsen, M., Guo, C., Tjiputra, J., Kirkevåg, A., Oliviè, D. J. L., Seland, ?, Fan, Y., Lawrence, P., Eldevik, T., & Keenlyside, N. (2019). NCC NorCPM1 model output prepared for CMIP6 CMIP. https://doi.org/10.22033/ESGF/CMIP6.10843

Bjerknes, J. (1969). Atmospheric teleconnections from the equatorial Pacific. *Monthly weather review*, *97*(3), 163–172. https://doi.org/10.1175/1520-0493(1969)097<0163:atftep>2.3.co;2

Bjornsson, H., & Venegas, S. (1997). A manual for EOF and SVD analyses of climatic data. CCGCR Rep. 97-1, 52 pp. *Cent. for Clim. and Global Change Res., McGill Univ., Montreal, Que., Canada*.

Booth, B. B., Dunstone, N. J., Halloran, P. R., Andrews, T., & Bellouin, N. (2012). Aerosols implicated as a prime driver of twentieth-century North Atlantic climate variability. *Nature*, *484*(7393), 228–232. https://doi.org/10.1038/nature10946

Borchert, L. F., Koul, V., Menary, M. B., Befort, D. J., Swingedouw, D., Sgubin, G., & Mignot, J. (2021). Skillful decadal prediction of unforced southern European summer temperature variations. *Environ. Res. Lett.*, *16*, 104017. https://doi.org/10.1088/1748-9326/ac20f5

Boucher, O., Denvil, S., Levavasseur, G., Cozic, A., Caubel, A., Foujols, M.-A., Meurdesoif, Y., Cadule, P., Devilliers, M., Ghattas, J., Lebas, N., Lurton, T., Mellul, L., Musat, I., Mignot, J., & Cheruy, F. (2018). IPSL IPSL-CM6A-LR model output prepared for CMIP6 CMIP. https://doi.org/10.22033/ESGF/CMIP6.1534

Bridgman, H. A., & Oliver, J. E. (2006). *The Global Climate System: Patterns, Processes, and Teleconnections*. Cambridge University Press. https://doi.org/10.1017/CBO9780511817984

Brönnimann, S., Xoplaki, E., Casty, C., Pauling, A., & Luterbacher, J. (2007). ENSO influence on Europe during the last centuries. *Climate Dynamics*, *28*(2–3), 181–197. https://doi.org/10.1007/s00382-006-0175-z

Brönnimann, S. (2007). Impact of El Niño–Southern Oscillation on European climate. *Reviews of Geophysics*, *45*(3), RG3003. https://doi.org/10.1029/2006rg000199

Capotondi, A., Deser, C., Phillips, A. S., Okumura, Y., & Larson, S. M. (2020). ENSO and Pacific Decadal Variability in the Community Earth System Model Version 2 [e2019MS002022 2019MS002022]. *Journal of Advances in Modeling Earth Systems*, *12*(12), e2019MS002022. https://doi.org/https://doi.org/10.1029/2019MS002022

Casselman, J. W., Taschetto, A. S., & Domeisen, D. I. V. (2021). Nonlinearity in the Pathway of El Niño–Southern Oscillation to the Tropical North Atlantic. *Journal of Climate*, *34*(17), 7277–7296. https://doi.org/https://doi.org/10.1175/JCLI-D-20-0952.1

Cassou, C., & Terray, L. (2001). Oceanic forcing of the wintertime low-frequency atmospheric variability in the North Atlantic European sector: A study with the ARPEGE model. *Journal of Climate*, *14*(22), 4266–4291. https://doi.org/10.1175/1520-0442(2001)014<4266:ofotwl>2.0.co;2

Chang, P., Saravanan, R., & Ji, L. (2000). Tropical Atlantic seasonal predictability: The roles of El Niño remote influence and thermodynamic air-sea feedback. *Geophysical Research Letters*, *27*(16), 2545–2548.

Chang, E. T., & Chao, B. F. (2014). Analysis of coseismic deformation using EOF method on dense, continuous GPS data in Taiwan. *Tectonophysics*, *637*, 106–115.

Charney, J. G. (1947). Dynamics of long waves in a baroclinic westerly current. *Journal of Meteorology*, *4*(5), 135–162. https://doi.org/10.1175/1520-0469(1947)004<0135:DOLWIA>2.0.CO;2

Chen, D., Zhang, X., Li, T., Wang, B., & Liang, X. (2021). ENSO Dynamics in the E3SM-1-0, CESM2, and GFDL-CM4 Climate Models. *Journal of Climate*, *34*(23), 10193–10213. https://doi.org/10.1175/jcli-d-21-0355.1

Chiang, J. C., & Sobel, A. H. (2002). Tropical tropospheric temperature variations caused by ENSO and their influence on the remote tropical climate. *Journal of climate*, *15*(18), 2616–2631.

Chiang, J. C., & Lintner, B. R. (2005). Mechanisms of remote tropical surface warming during El Niño. *Journal of climate*, *18*(20), 4130–4149.

Chikamoto, Y., Timmermann, A., Luo, J.-J., Mochizuki, T., Kimoto, M., Watanabe, M., Ishii, M., Xie, S.-P., & Jin, F.-F. (2015). Skilful multi-year predictions of tropical trans-basin climate variability. *Nature communications*, *6*(1), 1–7.

Chung, E. S., Timmermann, A., Soden, B. J., & et al. (2019). Reconciling opposing Walker circulation trends in observations and model projections. *Nat. Clim. Chang.*, *9*(5), 405–412. https://doi.org/10.1038/s41558-019-0446-4

Chylek, P., Dubey, M. K., Lesins, G., Li, J., & Hengartner, N. (2014). Imprint of the Atlantic multi-decadal oscillation and Pacific decadal oscillation on southwestern US climate: Past, present, and future. *Climate dynamics*, *43*(1), 119–129.

Chylek, P., Folland, C., Klett, J. D., & Dubey, M. K. (2020). CMIP5 climate models overestimate cooling by volcanic aerosols. *Geophys. Res. Lett.*, *47*(3), e2020GL087047. https://doi.org/10.1029/2020GL087047

Clapeyron, M. C. (1834). Mémoire sur la puissance motrice de la chaleur. *Journal de l'École polytechnique*, *23*, 153–190.

Clausius, R. (1850). Ueber die bewegende Kraft der Wärme und die Gesetze, welche sich daraus für die Wärmelehre selbst ableiten lassen. *Annalen der Physik*, *155*, 500–524. https://doi.org/10.1002/andp.18501550403

Cohen, J., Screen, J. A., Furtado, J. C., Barlow, M., Whittleston, D., Coumou, D., Francis, J., Dethloff, K., Entekhabi, D., Overland, J., & Jones, J. (2014). Recent Arctic amplification and extreme mid-latitude weather. *Nature Geoscience*, *7*, 627–637.

Copernicus Climate Change Service, Climate Data Store. (2021). ORAS5 global ocean reanalysis monthly data from 1958 to present [data set] [Accessed on 20-07-2023]. https://doi.org/10.24381/CDS.67E8EEB7

Danabasoglu, G., Lamarque, J.-F., Bacmeister, J., Bailey, D. A., DuVivier, A. K., Edwards, J., Emmons, L. K., Fasullo, J., Garcia, R., Gettelman, A., Hannay, C., Holland, M. M., Large, W. G., Lauritzen, P. H., Lawrence, D. M., Lenaerts, J. T. M., Lindsay, K., Lipscomb, W. H., Mills, M. J., ... Strand, W. G. (2020). The Community Earth System Model Version 2 (CESM2) [data set] [e2019MS001916 2019MS001916]. *Journal of Advances in Modeling Earth Systems*, *12*(2), e2019MS001916. https://doi.org/10.1007/S00382-019-05031-5

Deser, C., Alexander, M. A., & Timlin, M. S. (2003). Understanding the persistence of sea surface temperature anomalies in midlatitudes. *Journal of Climate*, *16*(1), 57–72.

Deser, C., Alexander, M. A., Xie, S.-P., & Phillips, A. S. (2010). Sea Surface Temperature Variability: Patterns and Mechanisms. *Annual Review of Marine Science*, *2*, 115–143. https://doi.org/10.1146/annurev-marine-120408-151453

Deser, C., Phillips, A. S., Bourdette, V., & Teng, H. (2012). Uncertainty in climate change projections: the role of internal variability. *Climate dynamics*, *38*(3), 527–546. https://doi.org/10.1007/s00382-010-0977-x

Deser, C., Simpson, I. R., McKinnon, K. A., & Phillips, A. S. (2020). ENSO and Pacific Decadal Variability in the Community Earth System Model Version 2 (CESM2). *Journal of Advances in Modeling Earth Systems*, *12*(8), e2019MS002010.

Deser, C., & Phillips, A. S. (2023). A range of outcomes: the combined effects of internal variability and anthropogenic forcing on regional climate trends over Europe. *Nonlinear Processes in Geophysics*, *30*(1), 63–84. https://doi.org/10.5194/npg-30-63-2023

Deser, C. (2020). Certain uncertainty: The role of internal climate variability in projections of regional climate change and risk management. *Earth's Future*, *8*(12), e2020EF001854. https://doi.org/10.1029/2020ef001854

DeWeaver, E., & Nigam, S. (2002). Linearity in ENSO's atmospheric response. *Journal of Climate*, *15*(17), 2446–2461.

DeWeaver, E., & Nigam, S. (2004). On the forcing of ENSO teleconnections by anomalous heating and cooling. *Journal of climate*, *17*(16), 3225–3235.

Di Capua, G., Runge, J., Donner, R. V., van den Hurk, B., Turner, A. G., Vellore, R., Krishnan, R., & Coumou, D. (2020). Dominant patterns of interaction between the tropics and mid-latitudes in boreal summer: Causal relationships and the role of time-scales. *Weather and Climate Dynamics Discussions*, *2020*, 1–28.

DiNezio, P. N., Vecchi, G. A., & Clement, A. C. (2013). Detectability of changes in the Walker circulation in response to global warming. *J. Clim.*, *26*(10), 4038–4048. https://doi.org/10.1175/jcli-d-12-00531.1

Doblas-Reyes, F. J., García-Serrano, J., Cassou, C., Douville, H., & Giannini, A. (2017). Revisiting the ENSO Teleconnection to the Tropical North Atlantic. *Journal of Climate*, *30*(17), 6945–6957. https://doi.org/10.1175/jcli-d-16-0641.1

Dong, L., Zhou, T., & Chen, X. (2014). Changes of Pacific decadal variability in the twentieth century driven by internal variability, greenhouse gases, and aerosols. *Geophysical Research Letters*, *41*(23), 8570–8577. https://doi.org/10.1002/2014gl062269

Dong, L., & McPhaden, M. J. (2017). The role of external forcing and internal variability in regulating global mean surface temperatures on decadal timescales. *Environmental Research Letters*, *12*(3), 034011. https://doi.org/10.1088/1748-9326/aa5dd8

d'Orgeville, M., & Peltier, W. R. (2007). On the Pacific decadal oscillation and the Atlantic multidecadal oscillation: might they be related? *Geophysical Research Letters*, *34*(23).

Döscher, R., Acosta, M., Alessandri, A., Anthoni, P., Arsouze, T., Bergman, T., Bernardello, R., Boussetta, S., Caron, L.-P., Carver, G., Castrillo, M., Catalano, F., Cvijanovic, I., Davini, P., Dekker, E., Doblas-Reyes, F. J., Docquier, D., Echevarria, P., Fladrich, U., ... Zhang, Q. (2022). The EC-Earth3 Earth system model for the Coupled Model Intercomparison Project 6. *Geoscientific Model Development*, *15*(7), 2973–3020. https://doi.org/10.5194/gmd-15-2973-2022

Eady, E. T. (1949). Long waves and cyclone waves. *Tellus*, *1*(3), 33–52. https://doi.org/10.3402/tellusa.v1i3.8507

Ebbesmeyer, C. C., Cayan, D. R., McLain, D. R., Nichols, F. H., Peterson, D. H., & Redmond, K. T. (1991). 1976 step in the Pacific climate: forty environmental changes between 1968-1975 and 1977-1984.

Ebert-Uphoff, I., & Deng, Y. (2012). Causal discovery for climate research using graphical models. *Journal of Climate*, *25*(17), 5648–5665.

Enfield, D. B., & Mayer, D. A. (1997). Tropical Atlantic sea surface temperature variability and its relation to El Niño-Southern Oscillation. *Journal of Geophysical Research: Oceans*, *102*(C1), 929–945. https://doi.org/https://doi.org/10.1029/96JC03296

Enfield, D. B., Mestas-Nuñez, A. M., Mayer, D. A., & Cid-Serrano, L. (1999). How ubiquitous is the dipole relationship in tropical Atlantic sea surface temperatures? *Journal of Geophysical Research: Oceans*, *104*(C4), 7841–7848. https://doi.org/10.1029/1998jc900109

Eyring, V., Bony, S., Meehl, G. A., Senior, C. A., Stevens, B., Stouffer, R. J., & Taylor, K. E. (2016). Overview of the Coupled Model Intercomparison Project Phase 6 (CMIP6) experimental design and organization. *Geoscientific Model Development*, *9*(5), 1937–1958. https://doi.org/10.5194/gmd-9-1937-2016

Eyring, V., Cox, P. M., Flato, G. M., Gleckler, P. J., Abramowitz, G., Caldwell, P., Collins, W. D., Gier, B. K., Hall, A. D., Hoffman, F. M., et al. (2019). Taking climate model evaluation to the next level. *Nature Climate Change*, *9*(2), 102–110. https://doi.org/10.1038/s41558-018-0355-y

Eyring, V., Gillett, N., Achuta Rao, K., Barimalala, R., Barreiro Parrillo, M., Bellouin, N., Cassou, C., Durack, P., Kosaka, Y., McGregor, S., Min, S., Morgenstern, O., & Sun, Y. (2021a). Human Influence on the Climate System. In V. Masson-Delmotte, P. Zhai, A. Pirani, S. Connors, C. Péan, S. Berger, N. Caud, Y. Chen, L. Goldfarb, M. Gomis, M. Huang, K. Leitzell, E. Lonnoy, J. Matthews, T. Maycock, T. Waterfield, O. Yelekçi, R. Yu, & B. Zhou (Eds.), *Climate Change 2021: The Physical Science Basis. Contribution of Working Group I to the Sixth Assessment Report of the Intergovernmental Panel on Climate Change* (pp. 423–552). Cambridge University Press. https://doi.org/10.1017/9781009157896.005

Eyring, V., Gillett, N., Achutarao, K., Barimalala, R., Barreiro Parrillo, M., Bellouin, N., Cassou, C., Durack, P., Kosaka, Y., McGregor, S., et al. (2021b). Human Influence on the Climate System: Contribution of Working Group I to the Sixth Assessment Report of the Intergovernmental Panel on Climate Change. *IPCC Sixth Assessment Report*, 423–552. https://doi.org/10.1017/9781009157896.005

Fang, C., Wu, L., & Zhang, X. (2014). The impact of global warming on the Pacific Decadal Oscillation and the possible mechanism. *Advances in Atmospheric Sciences*, *31*(1), 118–130.

Farneti, R., Stiz, A., & Ssebandeke, J. B. (2022). Improvements and persistent biases in the southeast tropical Atlantic in CMIP models. *npj Climate and Atmospheric Science*, *5*(1), 1–11.

Fasullo, J. T., Phillips, A. S., & Deser, C. (2020). Evaluation of leading modes of climate variability in the CMIP archives. *Journal of Climate*, *33*(13), 5527–5545. https://doi.org/10.1175/jcli-d-19-1024.1

Feldstein, S. B., & Franzke, C. L. E. (2017). Atmospheric Teleconnection Patterns. In C. L. E. Franzke & T. J. O'Kane (Eds.), *Nonlinear and Stochastic Climate Dynamics* (pp. 54–104). Cambridge University Press. https://doi.org/10.1017/9781316339251.004

Flato, G. M., Marotzke, J., Abiodun, B., Braconnot, P., Chou, S. C., Collins, W. D., Cox, P., Driouech, F., Emori, S., Eyring, V., Forest, C., Gleckler, P., Guilyardi, E., Jakob, C., Kattsov, V., Reason, C., & Rummukainen, M. (2013). Evaluation of Climate Models. Cambridge University Press. https://www.ipcc.ch/site/assets/uploads/2018/02/WG1AR5_Chapter09_FINAL.pdf

Foltz, G. R., Brandt, P., Richter, I., Rodríguez-Fonseca, B., Hernandez, F., Dengler, M., Rodrigues, R. R., Schmidt, J. O., Yu, L., Lefevre, N., Da Cunha, L. C., McPhaden, M. J., Araujo, M., Karstensen, J., Hahn, J., Martín-Rey, M., Patricola, C. M., Poli, P., Zuidema, P., . . . Garcon, V. C. (2019). The tropical Atlantic observing system. *Frontiers in Marine Science*, *6*, 206. https://doi.org/10.3389/fmars.2019.00206

Foltz, M., Gregory R.and McPhaden. (2010). Interaction between the Atlantic meridional and Niño modes. *Geophysical Research Letters*, *37*(18), L18604. https://doi.org/10.1029/2010GL044001

Frajka-Williams, E., Beaulieu, C., & Duchez, A. (2017). Emerging negative Atlantic Multidecadal Oscillation index in spite of warm subtropics. *Scientific Reports*, *7*(1), 11224.

Frankcombe, L. M., England, M. H., Mann, M. E., & Steinman, B. A. (2015). Separating Internal Variability from the Externally Forced Climate Response. *Journal of Climate*, *28*(20), 8184–8202. https://doi.org/10.1175/JCLI-D-15-0069.1

Frankignoul, C., & Hasselmann, K. (1977). Stochastic Climate Models, Part 2, Application to Sea-Surface Temperature Anomalies and Thermocline Variability. *Tellus*, *29*, 289–305. https://doi.org/10.3402/tellusa.v29i4.11362

Fyfe, J. C., Kharin, V. V., Santer, B. D., Cole, J. N. S., & Gillett, N. P. (2021). Significant impact of forcing uncertainty in a large ensemble of climate model simulations. *Proceedings of the National Academy of Sciences*, *118*(24). https://doi.org/10.1073/pnas.2016549118

Galytska, E., Weigel, K., Handorf, D., Jaiser, R., Köhler, R., Runge, J., & Eyring, V. (2023). Evaluating Causal Arctic-Midlatitude Teleconnections in CMIP6 [e2022JD037978 2022JD037978]. *Journal of Geophysical Research: Atmospheres*, *128*(17), e2022JD037978. https://doi.org/https://doi.org/10.1029/2022JD037978

García-Serrano, J., Cassou, C., Douville, H., Giannini, A., & Doblas-Reyes, F. J. (2017). Revisiting the ENSO teleconnection to the tropical North Atlantic. *Journal of Climate*, *30*(17), 6945–6957. https://doi.org/10.1175/jcli-d-16-0641.1

Gerhardus, A., & Runge, J. (2020). High-recall causal discovery for autocorrelated time series with latent confounders. *Advances in Neural Information Processing Systems*, *33*, 12615–12625. https://doi.org/10.48550/ARXIV.2007.01884

Gettelman, A., & Rood, R. B. (2016). Components of the Climate System. In *Demystifying Climate Models* (pp. 13–22). Springer. https://doi.org/10.1007/978-3-662-48959-8_2

Giannini, A., Kushnir, Y., & Cane, M. A. (2000). Interannual variability of Caribbean rainfall, ENSO, and the Atlantic Ocean. *Journal of Climate*, *13*(2), 297–311.

Gill, A. E. (1980). Some simple solutions for heat-induced tropical circulation. *Quarterly Journal of the Royal Meteorological Society*, *106*(449), 447–462. https://doi.org/10.1002/qj.49710644905

Gill, A. E. (1982). *Atmosphere-Ocean Dynamics* (Vol. 30). Academic Press.

Goosse, H. (2015). *Climate System Dynamics and Modelling*. Cambridge University Press. https://doi.org/10.1017/CBO9781316018682

Granger, C. W. (1969). Investigating causal relations by econometric models and cross-spectral methods. *Econometrica: journal of the Econometric Society*, 424–438.

Gray, L. J., Woollings, T. J., Andrews, M., & Knight, J. (2016). Eleven-year solar cycle signal in the NAO and Atlantic/European blocking. *Quarterly Journal of the Royal Meteorological Society*, *142*(698), 1890–1903. https://doi.org/https://doi.org/10.1002/qj.2782

Ham, Y.-G., Kug, J.-S., & Park, J.-Y. (2013a). Two distinct roles of Atlantic SSTs in ENSO variability: North tropical Atlantic SST and Atlantic Niño. *Geophysical Research Letters*, *40*(15), 4012–4017. https://doi.org/10.1002/grl.50729

Ham, Y.-G., Kug, J.-S., Park, J.-Y., & Jin, F.-F. (2013b). Sea surface temperature in the north tropical Atlantic as a trigger for El Niño/Southern Oscillation events. *Nature Geoscience*, *6*(2), 112–116. https://doi.org/10.1038/ngeo1686

Hannachi, A., Jolliffe, I. T., & Stephenson, D. B. (2007). Empirical orthogonal functions and related techniques in atmospheric science: A review. *International Journal of Climatology: A Journal of the Royal Meteorological Society*, *27*(9), 1119–1152.

Hartmann, D. L. (1994). *Global Physical Climatology*. Academic.

Hasselmann, K. (1976). Stochastic climate models part I. Theory. *tellus*, *28*(6), 473–485.

He, C., Clement, A. C., Kramer, S. M., Cane, M. A., Klavans, J. M., Fenske, T. M., & Murphy, L. N. (2023). Tropical Atlantic multidecadal variability is dominated by external forcing. *Nature*, *622*(7983), 521–527. https://doi.org/10.1038/s41586-023-06489-4

Hersbach, H., Bell, B., Berrisford, P., Biavati, G., Horányi, A., Muñoz Sabater, J., Nicolas, J., Peubey, C., Radu, R., Rozum, I., Schepers, D., Simmons, A., Soci, C., Dee, D., & Thépaut, J.-N. (2023). ERA5 monthly averaged data on single levels from 1940 to present [Accessed on 18-07-2023]. https://doi.org/10.24381/CDS.F17050D7

Holton, J. R., & Hakim, G. J. (2012). *An Introduction to Dynamic Meteorology* (5th). Academic Press.

Honda, M., Nakamura, H., Ukita, J., Kousaka, I., & Takeuchi, K. (2001). Interannual seesaw between the Aleutian and Icelandic lows. Part I: Seasonal dependence and life cycle. *Journal of Climate*, *14*(6), 1029–1042. https://doi.org/10.1175/1520-0442(2001)014<1029:isbtaa>2.0.co;2

Houghton, J., Ding, Y., Griggs, D., Noguer, M., van der Linden, P., Dai, X., Maskell, K., & Johnson, C. (2001). *Climate Change 2001: The Scientific Basis* (I. W. G. I, Ed.). Cambridge University Press. https://www.ipcc.ch/site/assets/uploads/2018/03/TAR-01.pdf

Hu, S., Fedorov, A. V., Lengaigne, M., & Guilyardi, E. (2014). The impact of westerly wind bursts on the diversity and predictability of El Niño events: An ocean energetics perspective. *Geophysical research letters*, *41*(13), 4654–4663.

Hurrell, J. W., Kushnir, Y., Ottersen, G., & Visbeck, M. (2003). *An Overview of the North Atlantic Oscillation* (J. W. Hurrell, Y. Kushnir, G. Ottersen, & M. Visbeck, Eds.). American Geophysical Union. https://doi.org/10.1029/134GM01

Hurrell, J. W., & Deser, C. (2010). North Atlantic climate variability: the role of the North Atlantic Oscillation. *Journal of marine systems*, *79*(3-4), 231–244. https://doi.org/10.1016/j.jmarsys.2008.11.026

Ineson, S., Scaife, A. A., Knight, J. R., Manners, J. C., Dunstone, N. J., Gray, L. J., & Haigh, J. D. (2011). Solar forcing of winter climate variability in the Northern Hemisphere. *Nature Geoscience*, *4*, 753–757.

IPCC. (2013). *Climate Change 2013: The Physical Science Basis. Contribution of Working Group I to the Fifth Assessment Report of the Intergovernmental Panel on Climate Change* (T. F. Stocker, D. Qin, G.-K. Plattner, M. Tignor, S. K. Allen, J. Boschung, A. Nauels, Y. Xia, V. Bex, & P. M. Midgley, Eds.). Cambridge University Press.

IPCC. (2021a). Annex IV: Modes of Variability. In C. Cassou, A. Cherchi, & Y. Kosaka (Eds.), *Climate Change 2021: The Physical Science Basis* (pp. 2153–2192). Cambridge University Press. https://doi.org/10.1017/9781009157896.018

IPCC. (2021b). *Climate Change 2021: The Physical Science Basis. Contribution of Working Group I to the Sixth Assessment Report of the Intergovernmental Panel on Climate Change* (Vol. In Press). Cambridge University Press. https://doi.org/10.1017/9781009157896

Jiang, L., & Li, T. (2019). Relative roles of El Niño-induced extratropical and tropical forcing in generating Tropical North Atlantic (TNA) SST anomaly. *Climate Dynamics*, *53*(7-8), 3791–3804. https://doi.org/10.1007/s00382-019-04748-7

Jiang, L., & Li, T. (2021). Impacts of tropical North Atlantic and equatorial Atlantic SST anomalies on ENSO. *Journal of Climate*, *34*(14), 5635–5655.

Johnson, N. C., Amaya, D. J., Ding, Q., Kosaka, Y., Tokinaga, H., & Xie, S.-P. (2020). Multidecadal modulations of key metrics of global climate change. *Global and Planetary Change*, *188*, 103149.

Jolliffe, I. T. (1990). PRINCIPAL COMPONENT ANALYSIS: A BEGINNER'S GUIDE — I. Introduction and application. *Weather*, *45*(10), 375–382. https://doi.org/https://doi.org/10.1002/j.1477-8696.1990.tb05558.x

Kajtar, J. B., Santoso, A., McGregor, S., England, M. H., & Baillie, Z. (2018). Model underrepresentation of decadal Pacific trade wind trends and its link to tropical Atlantic bias. *Climate dynamics*, *50*(3), 1471–1484.

Kalnay, E., Kanamitsu, M., Kistler, R., Collins, W., Deaven, D., Gandin, L., Iredell, M., Saha, S., White, G., Woollen, J., Zhu, Y., Chelliah, M., Ebisuzaki, W., Higgins, W., Janowiak, J., Mo, K. C., Ropelewski, C., Wang, J., Leetmaa, A., ... Joseph, D. (1996). The NCEP/NCAR 40-Year Reanalysis Project. *Bulletin of the American Meteorological Society*, *77*(3), 437–472. https://doi.org/https://doi.org/10.1175/1520-0477(1996)077<0437:TNYRP>2.0.CO;2

**Karmouche**, **S.**, Galytska, E., Runge, J., Meehl, G. A., Phillips, A. S., Weigel, K., & Eyring, V. (2023a). Regime-oriented causal model evaluation of Atlantic–Pacific teleconnections in CMIP6. *Earth System Dynamics*, *14*(2), 309–344. https://doi.org/10.5194/esd-14-309-2023

**Karmouche**, **S.**, Galytska, E., Meehl, G. A., Runge, J., Weigel, K., & Eyring, V. (2023b). Changing effects of external forcing on Atlantic-Pacific interactions. *EGUsphere*, *2023*, 1–36. https://doi.org/10.5194/egusphere-2023-1861

**Karmouche, S.** (2023). Regime-oriented causal model evaluation of Atlantic-Pacific teleconnections in CMIP6 (v1.0) [Zenodo [code]].

Karpechko, A. Y., Hitchcock, P., Peters, D. H. W., & Schneidereit, A. (2017). Predictability of downward propagation of major sudden stratospheric warmings. *Quarterly Journal of the Royal Meteorological Society*, *143*(704), 1459–1470. https://doi.org/https://doi.org/10.1002/qj.3017

Kaufmann, R. K., Kauppi, H., Mann, M. L., & Stock, J. H. (2011). Reconciling anthropogenic climate change with observed temperature 1998–2008. *Proceedings of the National Academy of Sciences*, *108*(29), 11790–11793. https://doi.org/10.1073/pnas.1102467108

Kay, J. E., Deser, C., Phillips, A. S., Mai, A., Hannay, C., Strand, G., Arblaster, J. M., Bates, S., Danabasoglu, G., Edwards, J., et al. (2015). The Community Earth System Model (CESM) large ensemble project: A community resource for studying climate change in the presence of internal climate variability. *Bulletin of the American Meteorological Society*, *96*(8), 1333–1349.

Keenlyside, N. S., Latif, M., Jungclaus, J., Kornblueh, L., & Roeckner, E. (2007). Advancing decadal-scale climate prediction in the North Atlantic sector. *Nature*, *453*, 84–88. https://doi.org/10.1038/nature06921

Kelley, M., Schmidt, G. A., Nazarenko, L. S., Bauer, S. E., Ruedy, R., Russell, G. L., Ackerman, A. S., Aleinov, I., Bauer, M., Bleck, R., et al. (2020). GISS-E2. 1: Configurations and climatology. *Journal of Advances in Modeling Earth Systems*, *12*(8), e2019MS002025.

Kim, K.-Y., & North, G. R. (1997). EOFs of Harmonizable Cyclostationary Processes. *Journal of the Atmospheric Sciences*, *54*(19), 2416–2427. https://doi.org/https://doi.org/10.1175/1520-0469(1997)054<2416:EOHCP>2.0.CO;2

Klavans, J. M., Cane, M. A., Clement, A. C., & Murphy, L. N. (2021). NAO predictability from external forcing in the late 20th century. *npj Climate and Atmospheric Science*, *4*(1), 1–9. https://doi.org/10.1038/s41612-021-00177-8

Klavans, J. M., Clement, A. C., Cane, M. A., & Murphy, L. N. (2022). The Evolving Role of External Forcing in North Atlantic SST Variability over the Last Millennium. *Journal of Climate*, *35*(9), 2741–2758. https://doi.org/10.1175/jcli-d-21-0338.1

Klein, S. A., Soden, B. J., & Lau, N.-C. (1999). Remote sea surface temperature variations during ENSO: Evidence for a tropical atmospheric bridge. *Journal of climate*, *12*(4), 917–932. https://doi.org/10.1175/1520-0442(1999)012<0917:rsstvd>2.0.co;2

Kociuba, G., & Power, S. B. (2015). Inability of CMIP5 models to simulate recent strengthening of the Walker circulation: implications for projections. *J. Clim.*, *28*(1), 20–35. https://doi.org/10.1175/jcli-d-13-00752.1

Kondrashov, D., & Ghil, M. (2006). Spatio-temporal filling of missing points in geophysical data sets. *Nonlinear Processes in Geophysics*, *13*(2), 151–159. https://doi.org/10.5194/npg-13-151-2006

Kretschmer, M., Adams, S. V., Arribas, A., Prudden, R., Robinson, N., Saggioro, E., & Shepherd, T. G. (2021). Quantifying causal pathways of teleconnections. *Bulletin of the American Meteorological Society*, *102*(12), E2247–E2263.

Kucharski, F., Bracco, A., Yoo, J. H., & Molteni, F. (2007). Low-Frequency Variability of the Indian Monsoon–ENSO Relationship and the Tropical Atlantic: The "Weakening" of the 1980s and 1990s. *Journal of Climate*, *20*(16), 4255–4266. https://doi.org/10.1175/JCLI4254.1

Kucharski, F., Kang, I.-S., Farneti, R., & Feudale, L. (2011). Tropical Pacific response to 20th century Atlantic warming. *Geophysical Research Letters*, *38*(3). https://doi.org/10.1029/2010gl046248

Kucharski, F., Ikram, F., Molteni, F., Farneti, R., Kang, I.-S., No, H.-H., King, M. P., Giuliani, G., & Mogensen, K. (2016). Atlantic forcing of Pacific decadal variability. *Climate Dynamics*, *46*(7), 2337–2351. https://doi.org/10.1007/s00382-015-2705-z

Kumar, A., Jha, B., & Wang, H. (2014). Attribution of SST variability in global oceans and the role of ENSO. *Climate dynamics*, *43*(1–2), 209–220. https://doi.org/10.1007/s00382-013-1865-y

Latif, M., & Grötzner, A. (2000). The equatorial Atlantic oscillation and its response to ENSO. *Climate Dynamics*, *16*(2–3), 213–218. https://doi.org/10.1007/s003820050014

Le Mouël, J.-L., Lopes, F., & Courtillot, V. (2019). A Solar Signature in Many Climate Indices. *Journal of Geophysical Research: Atmospheres*, *124*(5), 2600–2619. https://doi.org/https://doi.org/10.1029/2018JD028939

Leathers, D. J., Yarnal, B., & Palecki, M. A. (1991). The Pacific/North American teleconnection pattern and United States climate. Part I: Regional temperature and precipitation associations. *Journal of Climate*, *4*(5), 517–528.

Lee, S.-K., Enfield, D. B., & Wang, C. (2008). Why do some El Niños have no impact on tropical North Atlantic SST? *Geophysical Research Letters*, *35*(16). https://doi.org/10.1029/2008gl034734

Lengaigne, M., Boulanger, J.-P., Menkes, C., Madec, G., Delecluse, P., Guilyardi, E., & Slingo, J. (2003). The March 1997 Westerly Wind Event and the Onset of the 1997/98 El Niño: Understanding the Role of the Atmospheric Response. *Journal of Climate*, *16*(22), 3622–3638. https://doi.org/10.1175/1520-0442(2003)016<3330:tmwwea>2.0.co;2

Levine, A. F., McPhaden, M. J., & Frierson, D. M. (2017). The impact of the AMO on multidecadal ENSO variability. *Geophysical Research Letters*, *44*(8), 3877–3886. https://doi.org/10.1002/2017gl072524

L'Heureux, M. L., Takahashi, K., Watkins, A. B., Barnston, A. G., Becker, E. J., Di Liberto, T. E., Gamble, F., Gottschalck, J., Halpert, M. S., Huang, B., et al. (2017). Observing and predicting the 2015/16 El Niño. *Bulletin of the American Meteorological Society*, *98*(7), 1363–1382.

Li, X., Xie, S.-P., Gille, S. T., & Yoo, C. (2016). Atlantic-induced pan-tropical climate change over the past three decades. *Nature Climate Change*, *6*(3), 275–279. https://doi.org/10.1038/nclimate2840

Li, T., Wang, B., Wu, B., Zhou, T., Chang, C.-P., & Zhang, R. (2017). Theories on formation of an anomalous anticyclone in western North Pacific during El Niño: A review. *Journal of Meteorological Research*, *31*(6), 987–1006.

Lin, H., & Derome, J. (2004). Nonlinearity of the extratropical response to tropical forcing. *Journal of climate*, *17*(13), 2597–2608. https://doi.org/10.1175/1520-0442(2004)017<2597:notert>2.0.co;2

Lorenz, D. J., & Hartmann, D. L. (2003). Eddy–Zonal Flow Feedback in the Northern Hemisphere Winter. *Journal of Climate*, *16*(8), 1212–1227. https://doi.org/https://doi.org/10.1175/1520-0442(2003)16<1212:EFFITN>2.0.CO;2

Lübbecke, J. F., & McPhaden, M. J. (2017). Symmetry of the Atlantic Niño mode. *Geophysical Research Letters*, *44*(2), 965–973. https://doi.org/https://doi.org/10.1002/2016GL071829

Lybarger, N. D., & Stan, C. (2019). Revisiting MJO, Kelvin waves, and El Niño relationships using a simple ocean model. *Climate Dynamics*, *53*(9-10), 6363–6377.

Madden, R. A., & Julian, P. R. (1994). Observations of the 40–50-day tropical oscillation—A review. *Monthly weather review*, *122*(5), 814–837.

Madden, R. A. (1986). Seasonal variations of the 40-50 day oscillation in the tropics. *Journal of Atmospheric Sciences*, *43*(24), 3138–3158.

Maher, N., McGregor, S., England, M. H., & Gupta, A. S. (2015). Effects of volcanism on tropical variability. *Geophysical Research Letters*, *42*(14), 6024–6033. https://doi.org/10.1002/2015gl064751

Maher, N., Matei, D., Milinski, S., & Marotzke, J. (2018). ENSO change in climate projections: forced response or internal variability? *Geophysical Research Letters*, *45*(20), 11–390. https://doi.org/10.1029/2018gl079764

Mann, M. E., Steinman, B. A., & Miller, S. K. (2014). On forced temperature changes, internal variability, and the AMO. *Geophysical Research Letters*, *41*(9), 3211–3219. https://doi.org/10.1002/2014gl059233

Mantua, N. J., Hare, S. R., Zhang, Y., Wallace, J. M., & Francis, R. C. (1997). A Pacific interdecadal climate oscillation with impacts on salmon production. *Bulletin of the american Meteorological Society*, *78*(6), 1069–1080. https://doi.org/10.1175/1520-0477(1997)078<1069:apicow>2.0.co;2

Marshall, G. J., & Thompson, D. W. (2016). The signatures of large-scale patterns of atmospheric variability in Antarctic surface temperatures. *Journal of Geophysical Research: Atmospheres*, *121*(7), 3276–3289.

Marshall, G. J., Thompson, D. W. J., & van den Broeke, M. R. (2017). The Signature of Southern Hemisphere Atmospheric Circulation Patterns in Antarctic Precipitation. *Geophysical Research Letters*, *44*(22), 11, 580–11, 589. https://doi.org/https://doi.org/10.1002/2017GL075998

Masson-Delmotte, V., Zhai, P., Pirani, A., Connors, S., Péan, C., Berger, S., Caud, N., Chen, Y., Goldfarb, L., Gomis, M., Huang, M., Leitzell, K., Lonnoy, E., Matthews, J., Maycock, T., Waterfield, T., Yelekçi, O., Yu, R., & Zhou, B. (2021). *Climate Change 2021: The Physical Science Basis. Contribution of Working Group I to the Sixth Assessment Report of the Intergovernmental Panel on Climate Change* (tech. rep.). Intergovernmental Panel on Climate Change.

Matsuno, T. (1966). Quasi-geostrophic motions in the equatorial area. *Journal of the Meteorological Society of Japan. Ser. II*, *44*(1), 25–43. https://doi.org/10.2151/jmsj1965.44.1_25

Matthews, T., Murphy, C., Wilby, R. L., & Harrigan, S. (2014). Stormiest winter on record for Ireland and UK. *Nature Climate Change*, *4*, 738–740. https://doi.org/10.1038/nclimate2336

McBride, L. A., Hope, A. P., Canty, T. P., Bennett, B. F., Tribett, W. R., & Salawitch, R. J. (2021). Comparison of CMIP6 historical climate simulations and future projected warming to an empirical model of global climate. *Earth System Dynamics*, *12*(2), 545–579. https://doi.org/10.5194/esd-12-545-2021

McGregor, S., Timmermann, A., Stuecker, M. F., England, M. H., Merrifield, M., Jin, F.-F., & Chikamoto, Y. (2014). Recent Walker circulation strengthening and Pacific cooling amplified by Atlantic warming. *Nature Climate Change*, *4*(10), 888–892. https://doi.org/10.1038/nclimate2330

McGregor, S., Stuecker, M. F., Kajtar, J. B., England, M. H., & Collins, M. (2018). Model tropical Atlantic biases underpin diminished Pacific decadal variability. *Nature Climate Change*, *8*(6), 493–498.

McPhaden, M. J. (1999). Genesis and evolution of the 1997-98 El Niño. *Science*, *283*(5404), 950–954. https://doi.org/10.1126/science.283.5404.950

Mechoso, C. R., An, S.-I., & Valcke, S. (2021). *Atmosphere-ocean Modeling: Coupling and Couplers*. World Scientific.

Meehl, G. A., Hu, A., & Santer, B. D. (2009). The mid-1970s climate shift in the Pacific and the relative roles of forced versus inherent decadal variability. *Journal of Climate*, *22*(3), 780–792. https://doi.org/10.1175/2008jcli2552.1

Meehl, G. A., Hu, A., Arblaster, J. M., Fasullo, J., & Trenberth, K. E. (2013). Externally forced and internally generated decadal climate variability associated with the Interdecadal Pacific Oscillation. *Journal of Climate*, *26*(18), 7298–7310. https://doi.org/10.1175/jcli-d-12-00548.1

Meehl, G. A., Hu, A., Santer, B. D., & Xie, S.-P. (2016). Contribution of the Interdecadal Pacific Oscillation to twentieth-century global surface temperature trends. *Nature Climate Change*, *6*(11), 1005–1008. https://doi.org/10.1038/nclimate3107

Meehl, G. A., Chung, C. T. Y., Arblaster, J. M., Holland, M. M., & Bitz, C. M. (2018). Tropical Decadal Variability and the Rate of Arctic Sea Ice Decrease. *Geophysical Research Letters*, *45*(20), 11, 310–11, 318. https://doi.org/10.1029/2018GL079989

Meehl, G. A., Hu, A., Castruccio, F., England, M. H., Bates, S. C., Danabasoglu, G., McGregor, S., Arblaster, J. M., Xie, S.-P., & Rosenbloom, N. (2021a). Atlantic and Pacific tropics connected by mutually interactive decadal-timescale processes. *Nature Geoscience*, *14*(1), 36–42. https://doi.org/10.1038/s41561-020-00669-x

Meehl, G. A., Teng, H., Capotondi, A., & Hu, A. (2021b). The role of interannual ENSO events in decadal timescale transitions of the Interdecadal Pacific Oscillation. *Climate Dynamics*, *57*(7), 1933–1951.

Menary, M. B., Robson, J., Allan, R. P., Booth, B. B. B., Cassou, C., Gastineau, G., & et al. (2020). Aerosol-forced AMOC changes in CMIP6 historical simulations. *Geophysical Research Letters*, *47*(14), e2020GL088166. https://doi.org/10.1029/2020GL088166

Meng, Q., Latif, M., Park, W., Keenlyside, N. S., Semenov, V. A., & Martin, T. (2012). Twentieth century Walker Circulation change: data analysis and model experiments. *Climate Dynamics*, *38*, 1757–1773. https://link.springer.com/article/10.1007/s00382-011-1047-8

Milinski, S., Maher, N., & Olonscheck, D. (2019). How large does a large ensemble need to be? *Earth System Dynamics*, *11*(4), 885–901. https://doi.org/10.5194/esd-11-885-2020

Miller, A. J., Cayan, D. R., Barnett, T. P., Graham, N. E., & Oberhuber, J. M. (1994). The 1976-77 climate shift of the Pacific Ocean. *Oceanography*, *7*(1), 21–26.

Mo, K. C., & Ghil, M. (1987). Statistics and Dynamics of Persistent Anomalies. *Journal of Atmospheric Sciences*, *44*(5), 877–902. https://doi.org/https://doi.org/10.1175/1520-0469(1987)044<0877:SADOPA>2.0.CO;2

Mo, K. C., & Paegle, J. N. (2001). The Pacific–South American modes and their downstream effects. *International Journal of Climatology*, *21*(10), 1211–1229. https://doi.org/https://doi.org/10.1002/joc.685

Murphy, L. N., Bellomo, K., Cane, M., & Clement, A. (2017). The role of historical forcings in simulating the observed Atlantic multidecadal oscillation. *Geophysical Research Letters*, *44*(4), 1847–1853. https://doi.org/10.1002/2016GL071337

Navarra, A., & Simoncini, V. (2010). *A Guide to Empirical Orthogonal Functions for Climate Data Analysis*. Springer Science  Business Media.

Neelin, J. D., Battisti, D. S., Hirst, A. C., Jin, F.-F., Wakata, Y., Yamagata, T., & Zebiak, S. E. (1998). ENSO theory. *J. Geophys. Res.*, *103*(C7), 14261–14290. https://doi.org/10.1029/97JC03424

Neelin, J. D. (2010). *Climate Change and Climate Modeling*. Cambridge University Press.

Neha & Pasari, S. (2022). A review of empirical orthogonal function (EOF) with an emphasis on the co-seismic crustal deformation analysis. *Natural Hazards*, *110*(1), 29–56.

Newman, M., Alexander, M. A., Ault, T. R., Cobb, K. M., Deser, C., Di Lorenzo, E., Mantua, N. J., Miller, A. J., Minobe, S., Nakamura, H., et al. (2016). The Pacific decadal oscillation, revisited. *Journal of Climate*, *29*(12), 4399–4427. https://doi.org/10.1175/JCLI-D-15-0508.1

Nitta, T., & Yamada, S. (1989). Recent warming of tropical sea surface temperature and its relationship to the Northern Hemisphere circulation. *Journal of the Meteorological Society of Japan. Ser. II*, *67*(3), 375–383.

Nnamchi, H. C., Li, J., Anyadike, R. N., Ilesanmi, I. A., Jin, F.-F., Nwofor, O. K., Lu, R., & Li, T. (2015). Thermodynamic controls of the Atlantic Niño. *Nature Communications*, *6*(1), 8895. https://doi.org/10.1038/ncomms9895

NOAA. (2021). Trends in Atmospheric Carbon Dioxide [Mauna Loa Observatory, Hawaii]. 1

North, G. R. (1984). Empirical Orthogonal Functions and Normal Modes. *Journal of Atmospheric Sciences*, *41*(5), 879–887. https://doi.org/https://doi.org/10.1175/1520-0469(1984)041<0879:EOFANM>2.0.CO;2

Nowack, P., Runge, J., Eyring, V., & Haigh, J. D. (2020). Causal networks for climate model evaluation and constrained projections. *Nature communications*, *11*(1), 1–11.

O'Brien, J. P., & Deser, C. (2023). Quantifying and understanding forced changes to unforced modes of atmospheric circulation variability over the North Pacific in a coupled model large ensemble. *Journal of Climate*, *36*(1), 19–37. https://doi.org/10.1175/jcli-d-22-0101.1

Pan, Y. H., & Oort, A. H. (1983). Global climate variations connected with sea surface temperature anomalies in the eastern equatorial Pacific Ocean for the 1958–73 period. *Monthly Weather Review*, *111*(6), 1244–1258.

Park, J.-H., & Li, T. (2019). Interdecadal modulation of El Niño–tropical North Atlantic teleconnection by the Atlantic multi-decadal oscillation. *Climate Dynamics*, *52*(9-10), 5345–5360. https://doi.org/10.1007/s00382-018-4452-4

Park, J.-H., Li, T., Yeh, S.-W., & Kim, H. (2019). Effect of recent Atlantic warming in strengthening Atlantic–Pacific teleconnection on interannual timescale via enhanced connection with the Pacific meridional mode. *Climate dynamics*, *53*(1–2), 371–387. https://doi.org/10.1007/s00382-018-4591-7

Park, J.-H., Kug, J.-S., Yang, Y.-M., Oh, H., Zhao, J., & Wu, Y. (2022). Role of the Climatological North Pacific High in the North Tropical Atlantic–ENSO Connection. *Journal of Climate*, *35*(20), 3215–3226. https://doi.org/10.1175/jcli-d-21-0933.1

Park, J.-H., Yeh, S.-W., Kug, J.-S., Yang, Y.-M., Jo, H.-S., Kim, H.-J., & An, S.-I. (2023). Two regimes of inter-basin interactions between the Atlantic and Pacific Oceans on interannual timescales. *npj Climate and Atmospheric Science*, *6*(1), 13. https://doi.org/10.1038/s41612-023-00332-3

Pearl, J., & Mackenzie, D. (2018). *The book of why: the new science of cause and effect* (1st). Basic books.

Peixoto, J. P., & Oort, A. H. (1992). *Physics of Climate*. American Institute of Physics.

Pepler, A. S. (2016). Seasonal climate summary southern hemisphere (summer 2015-16): strong El Niño peaks and begins to weaken. *Journal of Southern Hemisphere Earth Systems Science*, *66*(4), 361–379.

Peters, J., Janzing, D., & Schölkopf, B. (2017). *Elements of causal inference: foundations and learning algorithms*. The MIT Press.

Philander, S. G. (Ed.). (1990). *El Niño, La Niña, and the Southern Oscillation* (Vol. 46). Geophysical Fluid Dynamics Laboratory/NOAA, Princeton University.

Phillips, A. S., Deser, C., & Fasullo, J. (2014). Evaluating modes of variability in climate models. *Eos, Transactions American Geophysical Union*, *95*(49), 453–455.

Phillips, A. S., Deser, C., Fasullo, J., Schneider, D., & Simpson, I. (2020). Assessing Climate Variability and Change in Model Large Ensembles: A User's Guide to the "Climate

Variability Diagnostics Package for Large Ensembles", version 1. *version*, *1*, 0. https://doi.org/10.5065/H7C7-F961

Pinto, J. G., Reyers, M., & Ulbrich, U. (2011). The variable link between PNA and NAO in observations and in multi-century CGCM simulations. *Climate Dynamics*, *36*(1-2), 337–354. https://doi.org/10.1007/s00382-010-0770-x

Polkova, I., Afargan-Gerstman, H., Domeisen, D. I., King, M. P., Ruggieri, P., Athanasiadis, P., Dobrynin, M., Aarnes, Ø., Kretschmer, M., & Baehr, J. (2021). Predictors and prediction skill for marine cold-air outbreaks over the Barents Sea. *Quarterly Journal of the Royal Meteorological Society*, *147*(738), 2638–2656.

Polyakov, I. V., & Johnson, M. A. (2000). Arctic decadal and interdecadal variability. *Geophysical Research Letters*, *27*(24), 4097–4100. https://doi.org/10.1029/2000GL011909

Pond, S., & Pickard, G. L. (1983). *Introductory Dynamical Oceanography*. Pergamon.

Power, S., Casey, T., Folland, C., Colman, A., & Mehta, V. (1999). Inter-decadal modulation of the impact of ENSO on Australia. *Climate Dynamics*, *15*(5), 319–324.

Power, S. B., & Kociuba, G. (2011). What caused the observed twentieth-century weakening of the Walker circulation? *J. Clim.*, *24*(24), 6501–6514. https://doi.org/10.1175/2011jcli4101.1

Rayner, N., Parker, D. E., Horton, E., Folland, C. K., Alexander, L. V., Rowell, D., Kent, E. C., & Kaplan, A. (2003). Global analyses of sea surface temperature, sea ice, and night marine air temperature since the late nineteenth century. *Journal of Geophysical Research: Atmospheres*, *108*(D14). https://doi.org/10.1029/2002jd002670

Renwick, J. A., & Revell, M. J. (1999). Blocking over the South Pacific and Rossby Wave Propagation. *Monthly Weather Review*, *127*(10), 2233–2247. https://doi.org/https://doi.org/10.1175/1520-0493(1999)127<2233:BOTSPA>2.0.CO;2

Richter, I., & Tokinaga, H. (2020). An overview of the performance of CMIP6 models in the tropical Atlantic: mean state, variability, and remote impacts. *Climate Dynamics*, *55*(9), 2579–2601.

Robock, A. (2000). Volcanic eruptions and climate. *Reviews of geophysics*, *38*(2), 191–219.

Rong, X., Zhang, R., & Li, T. (2010). Impacts of Atlantic sea surface temperature anomalies on Indo-East Asian summer monsoon-ENSO relationship. *Chinese Science Bulletin*, *55*, 2458–2468.

Roxy, M., Dasgupta, P., McPhaden, M. J., Suematsu, T., Zhang, C., & Kim, D. (2019). Twofold expansion of the Indo-Pacific warm pool warps the MJO life cycle. *Nature*, *575*(7784), 647–651.

Runge, J., Petoukhov, V., & Kurths, J. (2014). Quantifying the strength and delay of climatic interactions: The ambiguities of cross correlation and a novel measure based on graphical models. *Journal of climate*, *27*(2), 720–739.

Runge, J., Petoukhov, V., Donges, J. F., Hlinka, J., Jajcay, N., Vejmelka, M., Hartman, D., Marwan, N., Paluš, M., & Kurths, J. (2015). Identifying causal gateways and mediators in complex spatio-temporal systems. *Nature communications*, *6*(1), 1–10. https://doi.org/10.1038/ncomms9502

Runge, J., Bathiany, S., Bollt, E., Camps-Valls, G., Coumou, D., Deyle, E., Glymour, C., Kretschmer, M., Mahecha, M. D., Muñoz-Marí, J., et al. (2019a). Inferring causation from time series in Earth system sciences. *Nature communications*, *10*(1), 1–13.

Runge, J., Nowack, P., Kretschmer, M., Flaxman, S., & Sejdinovic, D. (2019b). Detecting and quantifying causal associations in large nonlinear time series datasets. *Science advances*, *5*(11), eaau4996. https://doi.org/10.1126/sciadv.aau4996

Runge, J. (2020). Discovering contemporaneous and lagged causal relations in autocorrelated nonlinear time series datasets. *Conference on Uncertainty in Artificial Intelligence*, 1388–1397. https://doi.org/10.48550/ARXIV.2003.03685

Runge, J. (2021). Necessary and sufficient graphical conditions for optimal adjustment sets in causal graphical models with hidden variables. *Advances in Neural Information Processing Systems*, *34*, 15762–15773. https://doi.org/10.48550/ARXIV.2102.10324

Runge, J. (2022). jakobrunge/tigramite: Tigramite 5.0. https://doi.org/10.5281/zenodo.6247837

Ruprich-Robert, Y., Msadek, R., Castruccio, F., Yeager, S., Delworth, T., & Danabasoglu, G. (2017). Assessing the climate impacts of the observed Atlantic multidecadal variability using the GFDL CM2. 1 and NCAR CESM1 global coupled models. *Journal of Climate*, *30*(8), 2785–2810. https://doi.org/10.1175/jcli-d-16-0127.1

Ruprich-Robert, Y., Moreno-Chamarro, E., Levine, X., Bellucci, A., Cassou, C., Castruccio, F., Davini, P., Eade, R., Gastineau, G., Hermanson, L., et al. (2021). Impacts of Atlantic multidecadal variability on the tropical Pacific: a multi-model study. *npj climate and atmospheric science*, *4*(1), 1–11.

Saggioro, E., de Wiljes, J., Kretschmer, M., & Runge, J. (2020). Reconstructing regime-dependent causal relationships from observational time series. *Chaos: An Interdisciplinary Journal of Nonlinear Science*, *30*(11), 113115. https://doi.org/10.1063/5.0020538

Sasaki, W., Doi, T., Richards, K. J., & Masumoto, Y. (2015). The influence of ENSO on the equatorial Atlantic precipitation through the Walker circulation in a CGCM. *Climate Dynamics*, *44*, 191–202.

Sato, Y., Goto, D., Michibata, T., Suzuki, K., Takemura, T., Tomita, H., & Nakajima, T. (2018). Aerosol effects on cloud water amounts were successfully simulated by a global cloud-system resolving model. *Nat. Commun.*, *9*(1), 985. https://doi.org/10.1038/s41467-018-03379-6

Scaife, A. A., & et al. (2014). Skillful long-range prediction of European and North American winters. *Geophysical Research Letters*, *41*(7), 2514–2519. https://doi.org/10.1002/2014gl059637

Schlund, M., Lauer, A., Gentine, P., Sherwood, S. C., & Eyring, V. (2020). Emergent constraints on equilibrium climate sensitivity in CMIP5: do they hold for CMIP6? *Earth System Dynamics*, *11*(4), 1233–1258. https://doi.org/10.5194/esd-11-1233-2020

Screen, J. A., Deser, C., Smith, D. M., Zhang, X., Blackport, R., Kushner, P. J., Oudar, T., McCusker, K. E., & Sun, L. (2018). Consistency and discrepancy in the atmospheric response to Arctic sea-ice loss across climate models. *Nature Geoscience*, *11*, 155–163.

Seferian, R. (2018). CNRM-CERFACS CNRM-ESM2-1 model output prepared for CMIP6 CMIP. https://doi.org/10.22033/ESGF/CMIP6.1391

Shea, D. (2023). *Empirical Orthogonal Function (EOF) Analysis and Rotated EOF Analysis* [Accessed: 2023-09-18]. https://climatedataguide.ucar.edu/climate-data-tools-and-analysis/empirical-orthogonal-function-eof-analysis-and-rotated-eof-analysis

Shiogama, H., Abe, M., & Tatebe, H. (2019). MIROC MIROC6 model output prepared for CMIP6 ScenarioMIP. https://doi.org/10.22033/ESGF/CMIP6.898

Smirnov, D., & Bezruchko, B. (2012). Spurious causalities due to low temporal resolution: Towards detection of bidirectional coupling from time series. *EPL (Europhysics Letters)*, *100*(1), 10005. https://doi.org/10.1209/0295-5075/100/10005

Smith, D. M., Scaife, A. A., & Kirtman, B. P. (2012). What is the current state of scientific knowledge with regard to seasonal and decadal forecasting? *Environmental Research Letters*, *7*(1). https://doi.org/10.1088/1748-9326/7/1/015602

Smith, D. M., Booth, B. B., Dunstone, N. J., Eade, R., Hermanson, L., Jones, G. S., Scaife, A. A., Sheen, K. L., & Thompson, V. (2016). Role of volcanic and anthropogenic aerosols in the recent global surface warming slowdown. *Nature Climate Change*, *6*(10), 936–940. https://doi.org/10.1038/nclimate3058

Smith, D. M., Eade, R., Scaife, A. A., Caron, L.-P., Danabasoglu, G., DelSole, T. M., Delworth, T., Doblas-Reyes, F. J., Dunstone, N. J., Hermanson, L., Kharin, V., Kimoto, M., Merryfield, W. J., Mochizuki, T., Müller, W. A., Pohlmann, H., Yeager, S., & Yang, X. (2019). Robust skill of decadal climate predictions. *npj Climate and Atmospheric Science*, *2*, 13. https://doi.org/10.1038/s41612-019-0084-4

Smith, C. J., & Forster, P. M. (2021). Suppressed Late-20th Century Warming in CMIP6 Models Explained by Forcing and Feedbacks [e2021GL094948 2021GL094948]. *Geophysical Research Letters*, *48*(19), e2021GL094948. https://doi.org/https://doi.org/10.1029/2021GL094948

Smith, C. J., Harris, G. R., Palmer, M. D., Bellouin, N., Collins, W., Myhre, G., Schulz, M., Golaz, J.-C., Ringer, M., Storelvmo, T., et al. (2021). Energy budget constraints on the time history of aerosol forcing and climate sensitivity. *Journal of Geophysical Research: Atmospheres*, *126*(13), e2020JD033622. https://doi.org/10.1029/2020jd033622

Smith, D. M., Gillett, N. P., Simpson, I. R., Athanasiadis, P. J., Baehr, J., Bethke, I., Bilge, T. A., Bonnet, R., Boucher, O., Findell, K. L., Gastineau, G., Gualdi, S., Hermanson, L., Leung, L. R., Mignot, J., Müller, W. A., Osprey, S., Otterå, O. H., Persad, G. G., ... Ziehn, T. (2022). Attribution of multi-annual to decadal changes in the climate system: The Large Ensemble Single Forcing Model Intercomparison Project (LESFMIP). *Frontiers in Climate*, *4*. https://doi.org/10.3389/fclim.2022.955414

Solomon, S., Rosenlof, K. H., Portmann, R. W., Daniel, J. S., Davis, S. M., Sanford, T. J., & Plattner, G.-K. (2010). Contributions of stratospheric water vapor to decadal changes in the rate of global warming. *Science*, *327*(5970), 1219–1223. https://doi.org/10.1126/science.1182488

Song, J., Li, C., Zhou, W., & Pan, J. (2009). The linkage between the Pacific-North American teleconnection pattern and the North Atlantic Oscillation. *Advances in Atmospheric Sciences*, *26*(2), 229–239. https://doi.org/10.1007/s00376-009-0229-3

Soulard, N., & Lin, H. (2017). The spring relationship between the Pacific-North American pattern and the North Atlantic Oscillation. *Climate Dynamics*, *48*(1–2), 619–629. https://doi.org/10.1007/s00382-016-3098-3

Spirtes, P., & Glymour, C. (1991). An algorithm for fast recovery of sparse causal graphs. *Social science computer review*, *9*(1), 62–72.

Spirtes, P., Glymour, C. N., & Scheines, R. (2000). *Causation, prediction, and search*. MIT press.

Swart, N. C., Cole, J. N., Kharin, V. V., Lazare, M., Scinocca, J. F., Gillett, N. P., Anstey, J., Arora, V., Christian, J. R., Jiao, Y., Lee, W. G., Majaess, F., Saenko, O. A., Seiler, C., Seinen, C., Shao, A., Solheim, L., von Salzen, K., Yang, D., ... Sigmond, M. (2019). CCCma CanESM5 model output prepared for CMIP6 ScenarioMIP. https://doi.org/10.22033/ESGF/CMIP6.1317

Swingedouw, D., Mignot, J., Ortega, P., Khodri, M., Menegoz, M., Cassou, C., & Hanquiez, V. (2017). Impact of explosive volcanic eruptions on the main climate variability modes. *Global and Planetary Change*, *150*, 24–45. https://doi.org/10.1016/j.gloplacha.2017.01.006

Takahashi, C., & Watanabe, M. (2016). Pacific trade winds accelerated by aerosol forcing over the past two decades. *Nature Climate Change*, *6*(8), 768–772. https://doi.org/10.1038/nclimate2996

Tang, Y., Rumbold, S., Ellis, R., Kelley, D., Mulcahy, J., Sellar, A., Walton, J., & Jones, C. (2019). MOHC UKESM1.0-LL model output prepared for CMIP6 CMIP historical. https://doi.org/10.22033/ESGF/CMIP6.6113

Taylor, K. E., Stouffer, R. J., & Meehl, G. A. (2012). An overview of CMIP5 and the experiment design. *Bulletin of the American meteorological Society*, *93*(4), 485–498.

Tebaldi, C., Dorheim, K., Wehner, M., & Leung, R. (2021). Extreme Metrics and Large Ensembles. *Earth System Dynamics Discussions*, *2021*(4), 1–59. https://doi.org/10.5194/esd-12-1427-2021

Tokarska, K. B., Hegerl, G. C., Schurer, A. P., Forster, P. M., & Marvel, K. (2020a). Observational constraints on the effective climate sensitivity from the historical period. *Environmental Research Letters*, *15*(3), 034043. https://doi.org/10.1088/1748-9326/ab738f

Tokarska, K. B., Stolpe, M. B., Sippel, S., Fischer, E. M., Smith, C. J., Lehner, F., & Knutti, R. (2020b). Past warming trend constrains future warming in CMIP6 models. *Science Advances*, *6*(12), eaaz9549. https://doi.org/10.1126/sciadv.aaz9549

Trenberth, K. E., Caron, J. M., Stepaniak, D. P., & Worley, S. (2002). Evolution of El Niño–Southern Oscillation and global atmospheric surface temperatures. *Journal of Geophysical Research: Atmospheres*, *107*(D8), AAC–5.

Trenberth, K. E., & Shea, D. J. (2006). Atlantic hurricanes and natural variability in 2005. *Geophysical research letters*, *33*(12). https://doi.org/10.1029/2006gl026894

Trenberth, K. E. (1990). Recent observed interdecadal climate changes in the Northern Hemisphere. *Bulletin of the American Meteorological Society*, *71*(7), 988–993.

Trenberth, K. E. (1997). The definition of El Niño. *Bulletin of the American Meteorological Society*, *78*(12), 2771–2778. https://doi.org/10.1175/1520-0477(1997)078<2771:tdoeno>2.0.co;2

Troup, A. (1965). The 'southern oscillation'. *Quarterly Journal of the Royal Meteorological Society*, *91*(390), 490–506.

Tung, K.-K., & Zhou, J. (2013). Using data to attribute episodes of warming and cooling in instrumental records. *Proceedings of the National Academy of Sciences*, *110*(6), 2058–2063. https://doi.org/10.1073/pnas.1212471110

Uwamahoro, J. C., Habarulema, J. B., & Buresova, D. (2019). Highlights about the performances of storm-time TEC modelling techniques for low/equatorial and mid-latitude locations. *Advances in Space Research*, *63*(10), 3102–3118. https://doi.org/https://doi.org/10.1016/j.asr.2019.01.027

Vallis, G. K. (2006). *Atmospheric and Oceanic Fluid Dynamics*. Cambridge University Press.

Vallis, G. K. (2017). *Atmospheric and Oceanic Fluid Dynamics: Fundamentals and Large-Scale Circulation* (2nd ed.). Cambridge University Press. https://doi.org/10.1017/9781107588417

Vecchi, G. A., & Soden, B. J. (2007). Global warming and the weakening of the tropical circulation. *J. Clim.*, *20*(17), 4316–4340. https://doi.org/10.1175/jcli4258.1

Vitart, F. (2017). Madden—Julian Oscillation prediction and teleconnections in the S2S database. *Quarterly Journal of the Royal Meteorological Society*, *143*(706), 2210–2220.

Volodin, E., Mortikov, E., Gritsun, A., Lykossov, V., Galin, V., Diansky, N., Gusev, A., Kostrykin, S., Iakovlev, N., Shestakova, A., & Emelina, S. (2019). INM INM-CM5-0 model output prepared for CMIP6 CMIP piControl. https://doi.org/10.22033/ESGF/CMIP6.5081

Walker, G., & Bliss, E. (1932). World Weather V. *Memoirs of the Royal Meteorological Society*, *4*, 53–84.

Wallace, J. M., & Gutzler, D. S. (1981). Teleconnections in the geopotential height field during the Northern Hemisphere winter. *Monthly weather review*, *109*(4), 784–812. https://doi.org/10.1175/1520-0493(1981)109<0784:titghf>2.0.co;2

Wallace, J. M., & Hobbs, P. V. (2006a). 10 - Climate Dynamics. In J. M. Wallace & P. V. Hobbs (Eds.), *Atmospheric Science (Second Edition)* (Second Edition, pp. 419–465). Academic Press. https://doi.org/https://doi.org/10.1016/B978-0-12-732951-2.50015-6

Wallace, J. M., & Hobbs, P. V. (2006b). 7 - Atmospheric Dynamics. In J. M. Wallace & P. V. Hobbs (Eds.), *Atmospheric Science (Second Edition)* (Second Edition, pp. 271–311). Academic Press. https://doi.org/https://doi.org/10.1016/B978-0-12-732951-2.50012-0

Wang, C., & Picaut, J. (2004). Understanding ENSO physics—A review. *Earth's Climate: The Ocean–Atmosphere Interaction, Geophys. Monogr*, *147*, 21–48.

Wang, T., Otterå, O. H., Gao, Y., & Wang, H. (2012). The response of the North Pacific Decadal Variability to strong tropical volcanic eruptions. *Climate Dynamics*, *39*(12), 2917–2936.

Wang, J., Yang, B., Ljungqvist, F. C., Luterbacher, J., Osborn, T. J., Briffa, K. R., & Zorita, E. (2017a). Internal and external forcing of multidecadal Atlantic climate variability over the past 1,200 years. *Nat. Geosci.*, *10*(7), 512–517. https://doi.org/10.1038/ngeo2962

Wang, L., Yu, J.-Y., & Paek, H. (2017b). Enhanced biennial variability in the Pacific due to Atlantic capacitor effect. *Nature Communications*, *8*(1), 14887. https://doi.org/10.1038/ncomms14887

Wang, C. (2018). A review of ENSO theories. *National Science Review*, *5*(6), 813–825. https://doi.org/10.1093/nsr/nwy104

Watanabe, M., & Tatebe, H. (2019). Reconciling roles of sulphate aerosol forcing and internal variability in Atlantic multidecadal climate changes. *Climate Dynamics*, *53*(7), 4651–4665. https://doi.org/10.1007/s00382-019-04811-3

WCRP. (2022). *WCRP Coupled Model Intercomparison Project (CMIP)*. https://www.wcrp-climate.org/wgcm-cmip

Wei, M., Shu, Q., Song, Z., Song, Y., Yang, X., Guo, Y., Li, X., & Qiao, F. (2021). Could CMIP6 climate models reproduce the early-2000s global warming slowdown? *Science China Earth Sciences*, *64*(6), 853–865. https://doi.org/10.1007/s11430-020-9740-3

Wheeler, M. C., Kim, H.-J., Lee, J.-Y., & Gottschalck, J. C. (2017). Real-time forecasting of modes of tropical intraseasonal variability: The Madden-Julian and boreal summer intraseasonal oscillations. In *The Global Monsoon System: Research and Forecast* (pp. 131–138). World Scientific.

Wieners, K.-H., Giorgetta, M., Jungclaus, J., Reick, C., Esch, M., Bittner, M., Legutke, S., Schupfner, M., Wachsmann, F., Gayler, V., Haak, H., de Vrese, P., Raddatz, T., Mauritsen, T., von Storch, J.-S., Behrens, J., Brovkin, V., Claussen, M., Crueger, T., … Roeckner, E. (2019a). MPI-M MPI-ESM1.2-LR model output prepared for CMIP6 CMIP historical. https://doi.org/10.22033/ESGF/CMIP6.6595

Wieners, K.-H., Giorgetta, M., Jungclaus, J., Reick, C., Esch, M., Bittner, M., Legutke, S., Schupfner, M., Wachsmann, F., Gayler, V., Haak, H., de Vrese, P., Raddatz, T., Mauritsen, T., von Storch, J.-S., Behrens, J., Brovkin, V., Claussen, M., Crueger, T., … Roeckner, E. (2019b). NCAR CESM2 model output prepared for CMIP6 CMIP historical. https://doi.org/10.22033/ESGF/CMIP6.6595

Wilks, D. (2011). Chapter 12 - Principal Component (EOF) Analysis. In D. S. Wilks (Ed.), *Statistical Methods in the Atmospheric Sciences* (pp. 519–562, Vol. 100). Academic Press. https://doi.org/https://doi.org/10.1016/B978-0-12-385022-5.00012-9

Woollings, T., Czuchnicki, C., & Franzke, C. (2014). Twentieth century North Atlantic jet variability. *Quarterly Journal of the Royal Meteorological Society*, *140*(680), 783–791. https://doi.org/https://doi.org/10.1002/qj.2197

Wu, S., Liu, Z., Zhang, R., & Delworth, T. L. (2011). On the observed relationship between the Pacific Decadal Oscillation and the Atlantic Multi-decadal Oscillation. *Journal of oceanography*, *67*(1), 27–35.

Wu, M., Zhou, T., Li, C., Li, H., Chen, X., Wu, B., Zhang, W., & Zhang, L. (2021). A very likely weakening of Pacific Walker Circulation in constrained near-future projections. *Nature communications*, *12*(1), 6502. https://doi.org/10.1038/s41467-021-26693-y

Xu, G., Duong, T. D., Li, Q., Liu, S., & Wang, X. (2020). Causality learning: A new perspective for interpretable machine learning. *arXiv preprint arXiv:2006.16789*.

Xu, C. (2016). Reconstruction of gappy GPS coordinate time series using empirical orthogonal functions. *Journal of Geophysical Research: Solid Earth*, *121*(12), 9020–9033. https://doi.org/https://doi.org/10.1002/2016JB013188

Yang, Y.-M., An, S.-I., Wang, B., & Park, J. H. (2020). A global-scale multidecadal variability driven by Atlantic multidecadal oscillation. *National Science Review*, *7*(7), 1190–1197. https://doi.org/10.1093/nsr/nwz216

Yasunari, T. (1980). A quasi-stationary appearance of 30 to 40 day period in the cloudiness fluctuations during the summer monsoon over India. *Journal of the Meteorological Society of Japan. Ser. II*, *58*(3), 225–229.

Yu, J., Li, T., Tan, Z., & Zhu, Z. (2016). Effects of tropical North Atlantic SST on tropical cyclone genesis in the western North Pacific. *Climate Dynamics*, *46*, 865–877.

Yulaeva, E., & Wallace, J. M. (1994). The signature of ENSO in global temperature and precipitation fields derived from the microwave sounding unit. *Journal of climate*, *7*(11), 1719–1736.

Zebiak, S. E., & Cane, M. A. (1993). A Model El Niño-Southern Oscillation. *Monthly Weather Review*, *121*(11), 2962–2975.

Zhang, Y., Wallace, J. M., & Battisti, D. S. (1997). ENSO-like interdecadal variability: 1900–93. *Journal of climate*, *10*(5), 1004–1020.

Zhang, C., Hendon, H. H., Kessler, W. S., & Rosati, A. J. (2001). A workshop on the MJO and ENSO. *Bulletin of the American Meteorological Society*, *82*(5), 971–976.

Zhang, R., & Delworth, T. L. (2007). Impact of the Atlantic multidecadal oscillation on North Pacific climate variability. *Geophysical Research Letters*, *34*(23).

Zhang, R., Sutton, R., Danabasoglu, G., Kwon, Y.-O., Marsh, R., Yeager, S. G., Amrhein, D. E., & Little, C. M. (2019). A review of the role of the Atlantic meridional overturning circulation in Atlantic multidecadal variability and associated climate impacts. *Reviews of Geophysics*, *57*(2), 316–375. https://doi.org/10.1029/2019RG000644

Zhang, C. (2013). Madden–Julian oscillation: Bridging weather and climate. *Bulletin of the American Meteorological Society*, *94*(12), 1849–1870.

Zhang, R. (2017). On the persistence and coherence of subpolar sea surface temperature and salinity anomalies associated with the Atlantic multidecadal variability. *Geophysical Research Letters*, *44*(15), 7865–7875.

Zhao, X., & Allen, R. J. (2019). Strengthening of the Walker Circulation in recent decades and the role of natural sea surface temperature variability. *Environmental Research Communications*, *1*(2), 021003. https://doi.org/10.1088/2515-7620/ab0dab

Zheng, X.-T., Xie, S.-P., Vecchi, G. A., Liu, Q., & Hafner, J. (2010). Indian Ocean Dipole Response to Global Warming: Analysis of Ocean–Atmospheric Feedbacks in a Coupled Model.

*Journal of Climate*, *23*(5), 1240–1253. https://doi.org/https://doi.org/10.1175/2009JCLI3326.1

Ziehn, T., Chamberlain, M., Lenton, A., Law, R., Bodman, R., Dix, M., Wang, Y., Dobrohotoff, P., Srbinovsky, J., Stevens, L., Vohralik, P., Mackallah, C., Sullivan, A., O'Farrell, S., & Druken, K. (2019). CSIRO ACCESS-ESM1.5 model output prepared for CMIP6 CMIP. https://doi.org/10.22033/ESGF/CMIP6.2288

# Acknowledgments

Funding for this study was provided by the European Research Council (ERC) Synergy Grant "Understanding and Modeling the Earth System with Machine Learning (USMILE)" under the Horizon 2020 research and innovation program (Grant Agreement No. 855187) and the "Advanced Earth System Model Evaluation for CMIP (EVal4CMIP)" project funded by the Helmholtz Society. Additional funding came from the European Union's Horizon 2020 research and innovation programme under Grant Agreement 101003536 (ESM2025—Earth System Models for the Future). We acknowledge the World Climate Research Programme's (WCRP's) Working Group on Coupled Modelling (WGCM), and we express gratitude to the CMIP-participating climate-modeling groups and the CVCWG for publicly publishing their CESM2 pacemaker simulations. Computational resources of the Deutsches Klimarechenzentrum (DKRZ) granted by its Scientific Steering Committee (WLA) under project no. bd1083 were essential to this work. We also acknowledge the use of AI tools in formatting, spell-checking, and referencing tasks.

First and foremost, I extend my deepest gratitude to my supervisor, Prof. Dr. Veronika Eyring. Her wisdom, patience, and dedication to scientific excellence have guided my journey. She not only provided academic guidance but also fostered an environment of intellectual freedom, allowing me to grow as an independent researcher. Her support provided me the opportunity to visit workshops and conferences in Germany and abroad, allowing me to meet great people and collaborate with renowned scientists from all around the world.
Many thanks to all the co-authors I had the privilege of working with: Dr. Evgenia Galytska, Dr. Gerald A. Meehl, Dr. Jakob Runge, Dr. Adam S. Phillips, Dr. Katja Weigel, and Prof. Dr. Veronika Eyring for their invaluable contributions to my first-author papers.
Special recognition goes to Dr. Jakob Runge, the expert in causal discovery. My stays at his department at the German Aerospace Center (DLR) in Jena were extremely beneficial, offering a unique environment to deepen my understanding of the methods used in the thesis.
Needless to say, my sincere thanks go to Dr. Gerald (Jerry) A. Meehl, whose profound knowledge and contributions were necessary for the quality of work done during my PhD time. The discussions with Jerry always brought light to this research when it was most needed.
Particular appreciation is reserved for Evgenia Galytska and Katja Weigel, whose hands-on support and collaborative spirit were primordial to my work. Their expertise, feedback, and comments contributed immensely to refining the results presented in this thesis.
I extend heartfelt thanks to all my colleagues here at IUP and everyone at the DLR-EVA working

group in Oberpfaffenhofen. Their professional advice and helpful discussions have been indispensable during my doctoral research. Whereas all the shared moments in workshops and conference trips will be forever memorable.
A special acknowledgment to my friends in Morocco, Germany, and all around the world. Your friendship has been a constant source of support and inspiration.
Finally, I owe an eternal debt of gratitude to my parents, Mohammed and Nadia, and my brothers Yassine and Ismail, for their unconditional love and support, which have been my backbone throughout this journey.